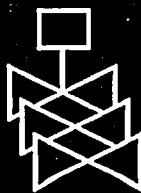
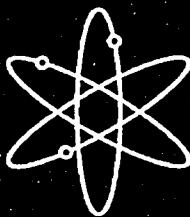


Corrosion Rate Measurements and Chemical Speciation of Corrosion Products Using Thermodynamic Modeling of Debris Components to Support GSI-191

Center for Nuclear Waste Regulatory Analyses

U.S. Nuclear Regulatory Commission
Office of Nuclear Regulatory Research
Washington, DC 20555-0001



AVAILABILITY OF REFERENCE MATERIALS IN NRC PUBLICATIONS

NRC Reference Material

As of November 1999, you may electronically access NUREG-series publications and other NRC records at NRC's Public Electronic Reading Room at <http://www.nrc.gov/reading-rm.html>. Publicly released records include, to name a few, NUREG-series publications; *Federal Register* notices; applicant, licensee, and vendor documents and correspondence; NRC correspondence and internal memoranda; bulletins and information notices; inspection and investigative reports; licensee event reports; and Commission papers and their attachments.

NRC publications in the NUREG series, NRC regulations, and *Title 10, Energy*, in the Code of *Federal Regulations* may also be purchased from one of these two sources.

1. The Superintendent of Documents
U.S. Government Printing Office
Mail Stop SSOP
Washington, DC 20402-0001
Internet: bookstore.gpo.gov
Telephone: 202-512-1800
Fax: 202-512-2250
2. The National Technical Information Service
Springfield, VA 22161-0002
www.ntis.gov
1-800-553-6847 or, locally, 703-605-6000

A single copy of each NRC draft report for comment is available free, to the extent of supply, upon written request as follows:

Address: Office of the Chief Information Officer,
Reproduction and Distribution
Services Section
U.S. Nuclear Regulatory Commission
Washington, DC 20555-0001
E-mail: DISTRIBUTION@nrc.gov
Facsimile: 301-415-2289

Some publications in the NUREG series that are posted at NRC's Web site address <http://www.nrc.gov/reading-rm/doc-collections/nureqs> are updated periodically and may differ from the last printed version. Although references to material found on a Web site bear the date the material was accessed, the material available on the date cited may subsequently be removed from the site.

Non-NRC Reference Material

Documents available from public and special technical libraries include all open literature items, such as books, journal articles, and transactions, *Federal Register* notices, Federal and State legislation, and congressional reports. Such documents as theses, dissertations, foreign reports and translations, and non-NRC conference proceedings may be purchased from their sponsoring organization.

Copies of industry codes and standards used in a substantive manner in the NRC regulatory process are maintained at—

The NRC Technical Library
Two White Flint North
11545 Rockville Pike
Rockville, MD 20852-2738

These standards are available in the library for reference use by the public. Codes and standards are usually copyrighted and may be purchased from the originating organization or, if they are American National Standards, from—

American National Standards Institute
11 West 42nd Street
New York, NY 10036-8002
www.ansi.org
212-642-4900

Legally binding regulatory requirements are stated only in laws; NRC regulations; licenses, including technical specifications; or orders, not in NUREG-series publications. The views expressed in contractor-prepared publications in this series are not necessarily those of the NRC.

The NUREG series comprises (1) technical and administrative reports and books prepared by the staff (NUREG-XXXX) or agency contractors (NUREG/CR-XXXX), (2) proceedings of conferences (NUREG/CP-XXXX), (3) reports resulting from international agreements (NUREG/IA-XXXX), (4) brochures (NUREG/BR-XXXX), and (5) compilations of legal decisions and orders of the Commission and Atomic and Safety Licensing Boards and of Directors' decisions under Section 2.206 of NRC's regulations (NUREG-0750).

DISCLAIMER: This report was prepared as an account of work sponsored by an agency of the U.S. Government. Neither the U.S. Government nor any agency thereof, nor any employee, makes any warranty, expressed or implied, or assumes any legal liability or responsibility for any third party's use, or the results of such use, of any information, apparatus, product, or process disclosed in this publication, or represents that its use by such third party would not infringe privately owned rights.

Corrosion Rate Measurements and Chemical Speciation of Corrosion Products Using Thermodynamic Modeling of Debris Components to Support GSI-191

Manuscript Completed: April 2005
Date Published: April 2005

Prepared by
V. Jain, X. He, Y.-M. Pan

Center for Nuclear Waste Regulatory Analyses
6220 Culebra Road
San Antonio, TX 78228-0510

B.P. Jain, NRC Project Manager

Prepared for
Division of Engineering Technology
Office of Nuclear Regulatory Research
U.S. Nuclear Regulatory Commission
Washington, DC 20555-0001
NRC Job Code N6061



ABSTRACT

This report documents thermodynamic simulations conducted to determine whether post loss-of-coolant-accident (LOCA) debris generation and consequent sump screen head loss in a pressurized water reactor containment can be affected by chemical interactions between the emergency core cooling system/containment spray water and exposed materials. Based on the measured corrosion rates, estimated exposed surface area, and exposure time, the thermodynamics simulations indicated that the formation of dominant solid phases was controlled by the presence of Nukon® low-density fiber insulation, aluminum, and concrete. The predicted dominant solid phases consisted of potentially amorphous silicate phases such as sodium aluminum silicate ($\text{NaAlSi}_3\text{O}_8$), calcium magnesium silicate [$\text{Ca}_2\text{Mg}_5\text{Si}_8\text{O}_{22}(\text{OH})_2$], calcium silicate (CaSiO_3), and silica (SiO_2). The results were based on the solid phases included in the thermodynamic simulation program database. The formation of actual solid phases may be different depending on the reaction kinetics. Although some constituents decreased proportionally with increasing time, the solid $\text{NaAlSi}_3\text{O}_8$ phase continued to be a dominant solid phase at all times. The formation of $\text{NaAlSi}_3\text{O}_8$ in the presence of alkaline solutions could lead to gel formation, which could result in clogging of containment area sump pump suction strainers. Thermodynamic simulations indicate that in alkaline simulated containment water at pH 10 there is no significant difference in corrosion product formation as high-temperature and pressure conditions during the initial stages of a LOCA event approach steady-state atmospheric pressure conditions. This report provides insight to and is useful in understanding the evolution of solution chemistry and the formation of solid phases in integrated chemical effects tests at the University of New Mexico.

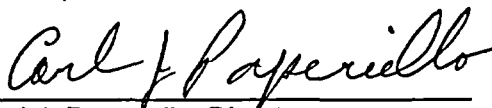
FOREWORD

The U.S. Nuclear Regulatory Commission (NRC) is engaged in research activities related to resolving Generic Safety Issue (GSI) 191, "Assessment of Debris Accumulation on PWR Sump Performance." During a review of those staff activities, the NRC's Advisory Committee on Reactor Safeguards (ACRS) raised a concern that products attributable to chemical interactions between the emergency core cooling system (ECCS)/containment spray water and exposed materials (such as metal surfaces, paint chips, and fiberglass insulation debris) could impede the performance of ECCS recirculation following a loss-of-coolant accident (LOCA) at a pressurized-water reactor (PWR).

In response to that concern, the NRC's Office of Nuclear Regulatory Research (RES) sponsored an integrated chemical effects test (ICET) program at the University of New Mexico, under the direction of Los Alamos National Laboratory. In addition, in order to (1) determine the need for a pressurized test loop for ICETs, (2) assess whether gelatinous products could form following a LOCA, (3) gain insights into important parameters, and (4) attempt to predict the ICET results, RES initiated the CNWRA study to perform computer-based thermodynamic simulations of chemical effects in a typical post-LOCA PWR containment environment. This model allows rapid and relatively inexpensive identification of the critical chemistry, time, temperature, pressure, and pH variables that affect chemical product formation.

This report documents the results of experiments to determine corrosion rates for metals and leaching rates for concrete and fiberglass, which were used as input parameters to the thermodynamic model. The report also identifies the assumptions and simplifications considered in the simulation modeling. One notable simplification is that the model does not consider reaction kinetics, which may affect the types and amounts of chemical species that form. However, these initial thermodynamic simulation results indicate that (1) chemical interactions could lead to the formation of gelatinous products following a LOCA, (2) the important parameters for solid formation include solution pH and temperature (among others), and (3) the presence of low-density fiber insulation, aluminum, and concrete influences the precipitation of chemical species.

This report also provides some initial understanding of the evolution of solution chemistry and the formation of solid phases in the ongoing ICET program. However, a better understanding of the impact of modeling assumptions and simplifications, including the effect of reaction kinetics, is necessary by comparing simulation results with ICET observations. The staff is conducting follow-on research to evaluate available analytical tools with the objective of gaining an understanding of their accuracies, uncertainties, and limitations within the sump environment. The insights gained in this report and recommendations from the follow-on research will assist the NRC staff in conducting safety reviews of licensees' responses to Generic Letter (GL) 2004-02, "Potential Impact of Debris Blockage on Emergency Recirculation During Design-Basis Accidents at Pressurized-Water Reactors," dated September 13, 2004.



Carl J. Papenello, Director
Office of Nuclear Regulatory Research
U.S. Nuclear Regulatory Commission

CONTENTS

Section	Page
ABSTRACT	iii
FOREWORD	v
FIGURES	ix
TABLES	xi
EXECUTIVE SUMMARY	xiii
ACKNOWLEDGMENTS	xvii
1 INTRODUCTION	1-1
2 CORROSION RATES OF DEBRIS COMPONENTS	2-1
2.1 Zinc	2-1
2.2 Aluminum	2-2
2.3 Carbon Steel	2-2
2.4 Copper	2-3
2.5 Concrete	2-4
2.6 Fiber Insulation	2-5
3 ESTIMATE OF DEBRIS COMPONENTS	3-1
4 ANALYSIS OF CORROSION PRODUCTS IN ALKALINE CONTAINMENT WATER USING THERMODYNAMIC SIMULATIONS	4-1
4.1 Effect of Temperature	4-1
4.2 Evolution of Solid and Aqueous Phases at 60 °C [140 °F]	4-4
5 SUMMARY	5-1
6 CONCLUSIONS	6-1
7 REFERENCES	7-1
APPENDIX A — CORROSION RATE MEASUREMENT METHODS FOR METALS	A-1
APPENDIX B — CORROSION RATE MEASUREMENTS FOR FIBER INSULATION GLASS AND CONCRETE	B-1
APPENDIX C — CHEMICAL SPECIATION, USING THERMODYNAMIC MODELING, DURING A REPRESENTATIVE LOSS-OF-COOLANT ACCIDENT EVENT (CNWRA 2004-07, REVISION 1)	C-1

FIGURES

Figure		Page
2-1	Relationship Between Release Rate and Temperature for Nukon® Low-Density Fiber Insulation Glass Between 60 and 110 °C [140 and 230 °F] at pH 7 and pH 10	2-6
4-1	Calculated Amount, in mol, of Predicted Potentially Amorphous Solid Phases Formed As a Function of Temperature in 0.259 M [2,800 ppm] Boron in Borated Alkaline Containment Solution at pH 10	4-3
4-2	Calculated Percent Predicted Solid Phases Formed As a Function of Temperature in 0.259 M [2,800 ppm] Boron in Borated Alkaline Containment Solution at pH 10 ..	4-3
4-3	Calculated Amount, in mol, of Predicted Solid Phases Formed As a Function of Time, in Hours, in 0.259 M [2,800 ppm] Borated Alkaline Containment Water	4-6
4-4	Calculated Percent Predicted Solid Phases Formed As a Function of Time in 0.259 M [2,800 ppm] Boron in Borated Alkaline Containment Water at pH 10	4-7
4-5	Calculated Sodium and Boron Concentrations, in mol/L, in Aqueous Phase As a Function of Time in 0.259 M [2,800 ppm] Borated Alkaline Containment Water in pH 10	4-9
4-6	Calculated Calcium and Silicon Concentrations, in mol/L, in Aqueous Phase As a Function of Time in 0.259 M [2,800 ppm] Borated Alkaline Containment Water in pH 10	4-9
4-7	Pourbaix Diagram for Aluminum in a pH 10 Borated Alkaline Solution at 60 °C [140 °F]	4-11
4-8	Pourbaix Diagram for Aluminum in a pH 10 Borated Alkaline Water Containing Silica at 60 °C [140 °F]	4-12

TABLES

Table	Page
1-1 Sources of Debris on the Sump Screen and Strainers	1-1
2-1 Measured Corrosion Rates for Debris Components in Borated Alkaline Containment Water at pH 10	2-1
2-2 Measured Corrosion Rates for Debris Components in Borated Alkaline Containment Water at pH 7	2-3
2-3 Constitution of Concrete Mixture	2-4
2-4 Major Components of Portland Cement	2-4
2-5 Leaching Rate of Calcium Oxide, Aluminum Oxide, and Silicon Dioxide from Concrete in Borated Alkaline Containment Water at pH 10	2-5
2-6 Analyzed Chemical Composition of Nukon® Fiber Insulation	2-7
2-7 Time Needed to Leach a 7- μm [0.28-mil]-Thick Nukon® Glass	2-7
3-1 Estimate of Release from Concrete Particulates	3-1
3-2 Estimation of Debris in pH 10 Borated Alkaline Containment Water Using Eq. 3-1 ..	3-2
3-3 Estimation of Debris in pH 10 Borated Alkaline Containment Water at 60 °C [140 °F] Using Eq. 3-1	3-3
4-1 pH and Redox Potential [Eh (V_{SHE})] of Borated Alkaline Containment Water with 0.259 M [2,800 ppm B] and 0.23 M [5,300 ppm Na] NaOH	4-2
4-2 Predicted Percent of Solid Phases at pH 10 Using OLI StreamAnalyzer®	4-4
4-3 Predicted Percent Element Distribution in Solid Phases at pH 10	4-4
4-4 Calculated Amount of Solid Phase Per Liter of Solution at pH 10, 60 °C [140 °F], at 32 Hours	4-5
4-5 pH and Redox Potential [Eh (V_{SHE})] of Simulated Containment Water with 0.259 M [2,800 ppm B] and 0.23 M [5,300 ppm Na] NaOH at 60 °C [140 °F]	4-6
4-6 Percent of Potentially Amorphous Solid Phases at 60 °C [140 °F], 101 kPa [1 atm], pH 10	4-7
4-7 Percent Element Distribution in Potentially Amorphous Solid Phases at 60 °C [140 °F], 101 kPa [1 atm] pH 10	4-8

EXECUTIVE SUMMARY

A loss-of-coolant-accident (LOCA) event causes rapid changes in the time-temperature-pressure-chemistry-pH conditions in the containment environment. Changes in the coolant chemistry are further complicated by interactions among materials typically present in the lower regions of the containment. These complex interactions require extensive and time-consuming experimentation to adequately analyze the potential for sump screen blockage caused by chemical precipitation. Thermodynamic simulations allow rapid and relatively inexpensive identification of critical variables from a large number of components present in the containment system during and following a LOCA event.

The primary objective of this study is to improve the predictive capability of the simulation model by reducing uncertainties in the corrosion rate values which underpin the data to the thermodynamic simulation program. An earlier study presented in Appendix C was based on available corrosion rate data in literature. This study, therefore, is focused on (i) determining the dissolution rate of Nukon® low-density fiberglass insulation and concrete in an alkaline solution at pH 10 in borated sodium hydroxide solution at 60, 90, and 110 °C [140, 194, and 230 °F]; (ii) determining corrosion rates for aluminum, copper, galvanized steel, and carbon steel in borated alkaline water at pH 10 at 60, 90, and 110 °C [140, 194, and 230 °F]; (iii) determining dissolution rate of Nukon® low-density fiberglass insulation and the corrosion rate of carbon steel in a borated trisodium phosphate solution at pH 7 at 60, 90, and 110 °C [140, 194, and 230 °F]; and (iv) thermodynamic modeling of the chemical speciation of plausible reaction products in coolant waters after a postulated LOCA event using experimentally determined corrosion rates.

Corrosion of galvanized steel, copper, aluminum, and carbon steel were measured using ASTM G59–97 (ASTM International, 2004a), and corrosion rates were calculated using ASTM G102–89 (ASTM International, 2004b) at 60, 90, and 110 °C [140, 194, and 230 °F] in borated {0.259 M [2,800 ppm] boron} alkaline containment water at pH 10. Corrosion rates for Nukon® glass and concrete were determined using ASTM C1220–98 (ASTM International, 2002) at 60, 90, and 110 °C [140, 194, and 230 °F] in borated {0.259 M [2,800 ppm] boron} alkaline containment water at pH 10 and in borated {0.259 M [2,800 ppm] boron} containment water at pH 7. A pH of 10 was adjusted by the addition of sodium hydroxide and a pH of 7 was adjusted by the addition of trisodium phosphate.

The thermodynamic simulations documented in this report were made using a thermodynamic simulator for evaluating aqueous chemical processes in industrial and environmental applications. Computational thermodynamics simulation calculations were conducted using StreamAnalyzer® Version 1.2 (OLI Systems, Inc., 2002a). Key chemical components involved in speciation simulation were copper, carbon steel, galvanized steel, aluminum, Nukon® low-density fiber insulation, and concrete. The amounts of corrosion products were determined based on the surface areas exposed as discussed in the U.S. Nuclear Regulatory Commission (NRC) test plan (NRC, 2005) and the experimentally determined corrosion rates. The comparison of corrosion amounts indicates that corrosion amount for Nukon® low-density fiber insulation is two to three orders of magnitude higher in borated alkaline containment water compared to carbon steel, galvanized steel, and copper. The amount of corrosion products associated with these metals, except aluminum, can be neglected in simulations. Based on the dissolution rate for Nukon® low-density fiber insulation at 60 °C [140 °F], an average 7- μm [0.28-mil] diameter Nukon® low-density fiber would leach in approximately 180 hours.

Furthermore, the leached contribution from Nukon® low-density fiber insulation is approximately 10,000 times more than that for concrete walls. In this study, concrete particulates were assumed to be released instantly.

Based on the measured corrosion rates, estimated exposed surface area, and exposure time, the thermodynamic simulations indicate that formation of dominant solid phases is controlled by the presence of Nukon® low-density fiber insulation, aluminum, and concrete. The predicted dominant solid phases consisted of potentially amorphous silicate phases such as sodium aluminum silicate ($\text{NaAlSi}_3\text{O}_8$), calcium magnesium silicate [$\text{Ca}_2\text{Mg}_5\text{Si}_8\text{O}_{22}(\text{OH})_2$], calcium silicate (CaSiO_3), and silica (SiO_2). Although some of these constituents decreased proportionally with increasing time, the solid $\text{NaAlSi}_3\text{O}_8$ phase continued to be the dominant solid phase at all times. The formation of actual solid phases may be different depending on the reaction kinetics. The formation of $\text{NaAlSi}_3\text{O}_8$ coupled with the presence of alkaline solutions could lead to gel formation.

This study provides, based on thermodynamic simulations, a description of the expected evolution of soluble species in borated alkaline containment water at 60 °C [140 °F]. Both silicon- and calcium-bearing soluble phases were predicted in borated alkaline containment water. The dominant silicon-bearing soluble phases were SiO_2 (aqueous), $\text{H}_3\text{SiO}_4^{-1}$, and NaHSiO_3 , and the dominant calcium-bearing soluble phase was $\text{CaH}_2\text{BO}_3^{+1}$. Furthermore, the aqueous concentrations of boron and sodium increased with time.

Comparison of the calculations using measured corrosion rates with the calculations presented in Appendix C using literature data in literature indicates formation of similar dominant solid phases with the exception of iron silicates such as $\text{Fe}_3\text{Si}_2\text{O}_5(\text{OH})_4$ and $\text{Ca}_3\text{Fe}_2\text{Si}_3\text{O}_{12}$. The absence of iron-bearing silicate phases in calculations using measured corrosion rates was attributed to extremely low corrosion rate measured for carbon steel at pH 10 compared to the corrosion rate assumed in Appendix C calculations.

Thermodynamic simulations indicate that in alkaline simulated containment water at pH 10 there is no significant difference in corrosion product formation as high-temperature and pressure conditions during the initial stages of a LOCA event approach steady-state atmospheric pressure conditions. These results support the conclusion reached in Appendix C that there is no need for a pressurized test loop. The increases in silicon and calcium concentrations, along with the increases in boron and sodium concentrations, in aqueous phase as a function of time could be used to estimate and monitor ongoing corrosion in the system. This report provides insight to and is useful in understanding the evolution of solution chemistry and the formation of solid phases in integrated chemical effects tests at the University of New Mexico.

A comparison of constituents in pH = 7 and pH = 10 containment solution is provided in Table 1.

It should be noted that input for the simulations excludes organics to model formation of complexes due to organic binder retained in fiber insulation after heat treatment. While simulations examine complex interactions between metals and inorganic materials such as fiber insulation and aluminum, the inputs are based on the dissolution rates of individual components. Experimental studies to examine interactions between debris components were not conducted. If leaching of fiber insulation or concrete is restricted due to a formation of a coating on the surface, simulation results will be significantly different. For example, the

Characteristic	pH = 7 (Trisodium Phosphate Moderator)	pH = 10 (Sodium Hydroxide Moderator)
Dominant Solid Phases	Ca ₅ (OH)(PO ₄) ₃ and NaAlSi ₃ O ₈ with Fe ₃ (PO ₄) ₂ ·8H ₂ O {60 °C [140 °F]}, Fe ₃ O ₄ , and Fe ₃ Si ₂ O ₅ (OH) ₄ {150 °C [302 °F]}	NaAlSi ₃ O ₈ and Ca ₂ Mg ₅ Si ₈ O ₂₂ (OH) ₂ with Ca ₃ Fe ₂ Si ₃ O ₁₂ {60 °C [140 °F]} and Fe ₃ Si ₄ O ₁₀ (OH) ₄ {150 °C [302 °F]}
Temperature Dependencies	Redistribution of iron and zinc phases	Redistribution of iron phases
Sensitivity—Aluminum	Increasing aluminum leads to increasing Al(OH) ₃ {60 °C [140 °F]} and AlO(OH) {130 °C [266 °F]}	Increasing aluminum leads to increasing Al(OH) ₃ {60 °C [140 °F]} and increases NaAlSi ₃ O ₈ {130 °C [266 °F]}
Sensitivity—Carbon Steel	Increasing iron leads to increasing Fe ₃ (PO ₄) ₂ ·8H ₂ O {60 °C [140 °F]}, Fe ₃ O ₄ , and Fe ₃ Si ₂ O ₅ (OH) ₄ {130 °C [266 °F]}	Increasing iron leads to increasing Fe ₃ Si ₂ O ₅ (OH) ₄ {60 °C [140 °F]} and Ca ₃ Fe ₂ Si ₃ O ₁₂ {130 °C [266 °F]}
Sensitivity—Zinc	Increasing zinc leads to increasing Zn ₃ (OH)(PO ₄) ₃ ·2H ₂ O {60 °C [140 °F]}, Zn ₃ (OH)(PO ₄) ₃ ·2H ₂ O, and ZnO·Fe ₂ O ₃ {130 °C [266 °F]}	Increasing zinc leads to increasing ZnO·Fe ₂ O ₃ and Zn ₂ SiO ₄
Sensitivity—Copper	No corrosion, no influence	No corrosion, no influence
Sensitivity—Concrete	Increasing concrete leads to increasing Ca ₅ (OH)(PO ₄) ₃ and SiO ₂	Increasing concrete leads to increasing CaSiO ₃
Sensitivity—Fiber Insulation	Increasing fiber insulations leads to increasing NaAlSi ₃ O ₈	Increasing fiber insulations leads to increasing NaAlSi ₃ O ₈ and Ca ₂ Mg ₅ Si ₈ O ₂₂ (OH) ₂
Long-Term Trends (time)	Major solid constituents: Ca ₅ (OH)(PO ₄) ₃ , NaAlSi ₃ O ₈ , Ca ₂ Mg ₅ Si ₈ O ₂₂ (OH) ₂ , Fe ₃ Si ₄ O ₁₀ (OH) ₄ , SiO ₂ , and Zn ₂ SiO ₄	Major solid constituents: NaAlSi ₃ O ₈ , Ca ₂ Mg ₅ Si ₈ O ₂₂ (OH) ₂ , Ca ₃ Fe ₂ Si ₃ O ₁₂ , CaSiO ₃ , and Zn ₂ SiO ₄

Pourbaix diagram, shown in Figure 4-7, for aluminum in a pH 10 alkaline borated water at 60 °C [140 °F] indicates that at a pH 10 or higher aluminum is predominantly present as a soluble $\text{Al}(\text{OH})_4^-$ complex. Results are in contrast to simulations in the presence of dissolution products (silicate phases) from fiber insulation and concrete where aluminum is predominantly present in a solid phase such as $\text{NaAlSi}_3\text{O}_8$ (Table 4-6). The Pourbaix diagram, shown in Figure 4-8, for aluminum in a pH 10 alkaline borated water containing silica at 60 °C [140 °F] indicates that the $\text{NaAlSi}_3\text{O}_8$ solid phase is dominant up to a pH of 12.

ACKNOWLEDGMENTS

This report was prepared to document work performed by the Center for Nuclear Waste Regulatory Analyses (CNWRA) for the U.S. Nuclear Regulatory Commission (NRC) under Contract No. NRC-DR-04-04-087. The activities reported here were performed on behalf of the NRC Office of Nuclear Regulatory Research, Division of Engineering Technology. This report is an independent product of CNWRA and does not necessarily reflect the views or regulatory position of NRC.

Authors gratefully acknowledge the helpful discussions and reviews by the NRC staff.

The authors gratefully acknowledge the technical review of D. Dunn, editorial reviews by C. Cudd and J. Pryor, and the programmatic review of B. Sagar. Appreciation is due J. Gonzalez for assistance in preparing this report.

QUALITY OF DATA: Sources of data are referenced in each chapter. CNWRA-generated data contained in this report meet quality assurance requirements described in the CNWRA Quality Assurance Manual. Data from other sources, however, are freely used. The respective sources of non-CNWRA data should be consulted for determining levels of quality assurance. Experimental data have been recorded in CNWRA scientific notebook number 676.

ANALYSES AND CODES: StreamAnalyzer[®] Version 1.2 (OLI Systems, Inc., 2002a) and Environmental Simulation Program[®] Version 6.6 (OLI Systems, Inc., 2002b) were used for the thermodynamic simulations. These codes are controlled according to the requirements of CNWRA Technical operating procedure (CNWRA, 2003). Detailed calculations can be found in scientific notebook number 652E. Software validation specific to borated water is included in Appendix C.

References

CNWRA. "Development and Control of Scientific and Engineering Software." Technical Operating Procedure (TOP)-018. Rev. 8, Change 2. San Antonio, Texas: CNWRA. 2003.

OLI Systems, Inc. "StreamAnalyzer[®] Version 1.2." Morris Plains, New Jersey: OLI Systems, Inc. 2002a.

———. "Environmental Simulation Program[®] Version 6.6." Morris Plains, New Jersey: OLI Systems, Inc. 2002b.

1 INTRODUCTION

On March 29, 1979, the activation of the emergency core cooling system at the Three-Mile Island nuclear reactor resulting from the pressure-operated relief valve being stuck in the open position caused a release of 2,158 m³ [570,000 gal] of water, including 712 m³ [188,000 gal] of Susquehanna River water, into the reactor building basement. Then, 153 days after this loss-of-coolant-accident (LOCA) event, a green gelatinous precipitate material was observed on the floors and walls of the containment building (Johns, et al., 2003). The July 28, 1992, LOCA at Barseback-2 nuclear power plant led to emergency core cooling system failure as a result of plugging of the sump pump (Hermannson and Erixon, 1997). Consequently, the U.S. Nuclear Regulatory Commission (NRC) examined the strainer performance of United States boiling water reactors. The NRC required boiling water reactor licensees to install suction strainers with larger surface areas. For pressurized water reactors (PWRs), NRC issued Generic Safety Issue (GSI)-191, (NRC, 2003).

A LOCA event results in rapid changes in the time-temperature-pressure-chemistry-pH conditions in the containment environment of nuclear reactors. Changes in the coolant chemistry are further complicated because of the interactions of the materials present in the vicinity of a postulated LOCA pipe break. Typical materials in these areas include fiber insulation, concrete, paints, carbon steel, galvanized steel, scaffolding, and insulation jackets. Some of this debris could chemically react and eventually accumulate on the recirculation-sump screens or strainers and challenge the emergency core cooling system and containment spray system pumps. Table 1-1 shows the sources of various debris material and associated corrosion products. These complex interactions require a large number of experiments to obtain sufficient data to analyze the potential impact on a sump blockage caused by chemical precipitation.

Table 1-1. Sources of Debris on the Sump Screen and Strainers	
Sources	Corrosion/Erosion Products
Scaffold/Insulation Jackets	Aluminum, zinc
Insulation Fibers	Silicon, aluminum, calcium, magnesium, boron, alkalis
Heat exchangers, fan coolers, instrument-air lines	Copper
Steel	Iron, nickel, sulfur
Galvanized Steel	Zinc, iron
Concrete	Calcium, silicon, aluminum
Cooling Water	Boron, lithium, sodium
River Water	Organics
pH adjusters	Trisodium phosphate, hydrochloric acid, sodium hydroxide

In a previous study (Appendix C), thermodynamic simulations were used to identify critical variables from a large number of components present during and subsequent to a LOCA event in the containment system. Computational thermodynamics simulation calculations were conducted using Environmental Simulation Program[®] Version 6.6 (OLI Systems, Inc., 2002a) and StreamAnalyzer[®] Version 1.2 (OLI Systems, Inc., 2002b). In the study, chemical speciation of plausible reaction products in sump water after a representative LOCA event was modeled to (i) determine the need for a pressurized test loop and (ii) assess whether gelatinous products could form in the typical time-temperature-pressure-chemistry-pH regime following a LOCA event. The corrosion rates were based on conservative values between pH 7 and pH 10 in borated water, selected from the values published in the literature. The sensitivity analysis was conducted over a wide range of amounts of each component to evaluate the effects of temperature on speciation because the temperature-dependent data were not available in most cases. The study indicated a strong influence of pH and temperature on the formation of the dominant solid phases in the simulated containment water. In alkaline solutions at pH 10, potentially amorphous silicates such as $\text{NaAlSi}_3\text{O}_8$, $\text{Ca}_3\text{Fe}_2\text{Si}_3\text{O}_{12}$, and $\text{Fe}_3\text{Si}_4\text{O}_{10}(\text{OH})_2$ were predicted as dominant corrosion products. The formation of gelatinous material in alkaline solutions at pH 10 was inferred from the solids observed in the thermodynamic calculations. Further simulations may be necessary to refine the predicted solid phase assemblages. Furthermore, the study provided input to parameters for the development and operation of a circulating water test loop at the University of New Mexico to study experimentally the chemical reactions from metal and insulation corrosion and to examine the formation of precipitation products including gelatinous products.

The primary objective of this study is to improve predictive capability of the simulation model by reducing uncertainties in the corrosion rate values. Therefore, this study focused on (i) determining leaching rate of Nukon[®] low-density fiber insulation and concrete in borated alkaline solution at pH 10 at 60, 90, and 110 °C [140, 194, and 230 °F]; (ii) determining leaching rate of Nukon[®] low-density fiberglass insulation and carbon steel at pH 7 in borated trisodium phosphate solution at 60, 90, and 110 °C [140, 194, and 230 °F]; (iii) determining corrosion rates for aluminum, copper, galvanized steel, and carbon steel in borated alkaline water at pH 10 at 60, 90, and 110 °C [140, 194, and 230 °F]; and (iv) thermodynamic modeling of the chemical speciation of plausible reaction products in coolant waters after a postulated LOCA event using experimentally determined corrosion rates.

This report provides insight to and is useful in understanding the evolution of solution chemistry and the formation of solid phases in integrated chemical effects tests at the University of New Mexico.

2 CORROSION RATES OF DEBRIS COMPONENTS

Table 1-1 lists the source of various debris material and associated chemical elements. Corrosion rates of debris components were measured at 60, 90, and 110 °C [140, 194, and 230 °F] in borated alkaline containment water at pH 10. A review of corrosion data from the literature on similar components is provided in Appendix C, Chapter 2. Corrosion measurements on carbon steel, concrete, and Nukon® low-density insulation fiber were also made in borated trisodium phosphate containment water at pH 7. Boron concentration was fixed at 0.259 M [2,800 ppm]. A pH of 10 was adjusted by the addition of sodium hydroxide, and a pH of 7 was adjusted by the addition of trisodium phosphate. Corrosion of galvanized steel, copper, aluminum, and carbon steel was measured using ASTM G59–97 (ASTM International, 2004a), and corrosion rates were calculated using ASTM G102–89 (ASTM International, 2004b). Experimental details are provided in Appendix A. Corrosion rates for Nukon® glass and concrete were determined using ASTM C1220–98 (ASTM International, 2002). Experimental details are provided in Appendix B.

2.1 Zinc

In a containment building, zinc is present in galvanized steel and zinc-based protective coatings. Zinc coatings are top-coated with a design basis accident-qualified epoxy or a modified phenolic-epoxy. These top-coated zinc paints do not readily participate in chemical reactions. However, a small fraction of noncoated zinc paints could release zinc into solution. The measured galvanized steel corrosion rates in a pH 10 borated alkaline containment water at 60, 90, and 110 °C [140, 194, and 230 °F] are shown in Table 2-1. The corrosion rate for galvanized steel increases with the increase in the temperature. The increase in the corrosion rate is much larger between 90 and 110 °C [194 and 230 °F] compared to the increase in the corrosion rate between 60 and 90 °C [140 and 194 °F]. The measured corrosion rates were higher compared to the Griess and Bacarella (1969) study. Griess and Bacarella (1969) measured the corrosion rates of galvanized steel and zinc metal in 0.278 M boric acid [3,000 ppm boron] with 0.15 M sodium hydroxide [3,450 ppm sodium] solution between 55 and 140 °C [131 and 284 °F]. Both galvanized steel and zinc metal showed negligible corrosion.

Table 2-1. Measured Corrosion Rates for Debris Components in Borated Alkaline Containment Water at pH 10*			
Debris Component	Corrosion Rate {g/m ² ·h [mil/yr]}		
	Temperature 60 °C [140 °F]	Temperature 90 °C [194 °F]	Temperature 110 °C [230 °F]
Galvanized Steel (Zinc)	3.57×10^{-2} [1.73]	4.05×10^{-2} [1.96]	2.34×10^{-1} [11.4]
Aluminum	0.986 [126]	1.89 [241]	2.20 [281]
Carbon Steel	1.35×10^{-2} [0.594]	2.95×10^{-2} [1.30]	8.21×10^{-2} [3.61]
Copper	4.78×10^{-3} [0.184]	5.19×10^{-2} [2.00]	9.91×10^{-2} [3.82]
Nukon® Insulation	4.86×10^{-2} [6.71]	2.32×10^{-1} [32.0]	4.53×10^{-1} [62.6]

*Note: Details are provided in Appendixes A and B.

The measured corrosion rates in this study, however, are similar to the lower end of the corrosion rates observed by Piippo, et al. (1997) at 90 °C [194 °F]. At 90 °C [194 °F], the zinc corrosion rate varied from 0.04 g/m²-h [1.9 mil/yr] in borated solution at a pH 9.2 to 0.163 g/m²-h [7.9 mil/yr] in aerated solution at a pH 8. In Appendix C, based on the literature review, a corrosion rate of 0.163 g/m²-h [7.9 mil/yr] was adopted to simulate speciation of zinc during a postulated LOCA event because this value provided a conservative estimate. The measured value at pH 10 is almost three times lower than the adopted value for simulations at 90 °C [194 °F] in Appendix C. Simulations presented in Chapter 4 provide a realistic value for galvanized steel speciation while simulations presented in Appendix C provide an upper bound for chemical speciation during a postulated LOCA event in a PWR.

2.2 Aluminum

In a containment building, aluminum is present in scaffolding. Additional aluminum may come from fiber insulation and concrete in oxide form. The measured corrosion rates in pH 10 borated alkaline containment water at 60, 90, and 110 °C [140, 194, and 230 °F] are shown in Table 2-1. The corrosion rate for aluminum increases with the increase in the temperature. The increase in the corrosion rate is much larger between 90 and 110 °C [194 and 230 °F] compared to the increase in the corrosion rate between 60 and 90 °C [140 and 194 °F]. Aluminum shows the highest corrosion rate among galvanized steel, copper, and carbon steel. The corrosion rate of aluminum at 60 °C [140 °F] is one order of magnitude higher compared to carbon steel and galvanized steel and at least two orders of magnitude higher compared to copper. The measured corrosion rate for aluminum is higher compared to the corrosion rates measured by Griess and Bacarella (1969) for several aluminum alloys in 0.278 M boric acid [3,000 ppm boron] with 0.15 M [3,450 ppm sodium] sodium hydroxide solution between 55 and 140 °C [131 and 284 °F]. For aluminum alloys at 55 °C [131 °F], submerged corrosion rates ranged from 0.35 to 0.61 g/m²-h [45 to 78 mil/yr]. At 100 °C [212 °F], however, the measured corrosion rates by Griess and Bacarella (1969) for submerged samples ranged from 14.0 to 18.0 g/m²-h [1,800 to 2,300 mil/yr] and were significantly higher compared to the rates measured in this study at 110 °C [230 °F]. At 90 °C [194 °F], Piippo, et al. (1997) measured corrosion rates of 0.012 g/m²-h [1.5 mil/yr] in aerated solution at a pH 10 and 1.45 g/m²-h [186 mil/yr] in borated water. The corrosion rate observed in this study for aluminum in borated water at pH 10 is similar to the Piippo, et al. (1997) data. In Appendix C, based on the literature review, a corrosion rate of 1.45 g/m²-h [186 mil/yr] was adopted to simulate speciation of aluminum because this value provided a conservative estimate. The measured value at pH 10 used in simulations presented in Chapter 4 is similar to the adopted value for simulations at 90 °C [194 °F] in Appendix C. Simulations presented in Appendix C provide a reasonable assessment of aluminum speciation during a postulated LOCA event in a PWR.

2.3 Carbon Steel

Carbon steel is present as a structural steel in the containment building. Most of this carbon steel is protected by design basis accident-qualified coatings or is encased in insulation. The surface area of unprotected carbon steel is small. The measured corrosion rates in a pH 10 borated alkaline containment water at 60, 90, and 110 °C [140, 194, and 230 °F] are shown in Table 2-1. The corrosion rate for carbon steel increases with the increase in the temperature. At pH 10, the corrosion rate of the carbon steel was lower than the corrosion rate of galvanized steel (zinc). Carbon steel corrosion rate was also measured at 60, 90, and 110 °C [140, 194, and 230 °F] in a borated trisodium phosphate solution at pH 7. The measured corrosion rates

are shown in Table 2-2. The corrosion rate at pH 7 was higher compared to the corrosion rate at pH 10. The decrease in the corrosion rates at the higher temperature could be partly attributed to the fact that at pH 10, carbon steel behaves like a passive metal. In addition, the measured corrosion rate at pH 7 shows a decrease in the corrosion rate with an increase in temperature. The decrease in corrosion rate with temperature has been reported by Hall (1988) at 177 °C [350 °F]. Hall (1988) observed lower corrosion rates for SA-193 Grade B7 and SA-540 Grade B23 carbon steels at higher temperatures, and higher corrosion rates for SA-540 Grade B24 carbon steels at higher temperatures. This variability in corrosion is attributed to the availability of oxygen. The higher the temperature, the lower the dissolved concentration of oxygen in the solution. Griess and Bacarella (1969) measured the corrosion rates of A-108 and A-210 carbon steels in 0.15 M NaOH [3,450 ppm] sodium solution between 55 and 140 °C [131 and 284 °F] and showed a negligible attack on carbon steels in alkaline borated water regardless of the test conditions. Hall (1988) measured corrosion of SA-193 Grade B7, SA-540 Grade B23, and SA-540 Grade B24 carbon steels in borated water {0.092 M [1,000 ppm] boron} from 79 to 204 °C [175 to 400 °F]. At 79 °C [175 °F], a maximum corrosion rate of 19.0 g/m²·h [833 mil/yr] was observed for SA-193 B7 carbon steel. In Appendix C, based on the literature review, a corrosion rate of 19.0 g/m²·h [833 mil/yr] was adopted to simulate speciation of carbon steel because this value provided a conservative estimate. The measured values of corrosion rate used in simulations at pH 7 and pH 10 are several orders lower in magnitude than the corrosion rate value initially adopted for simulations at 90 °C [194 °F] in Appendix C. Simulations presented in Chapter 4 provide a realistic value for carbon steel speciation, while simulations presented in Appendix C provide an extremely conservative bound for carbon steel speciation during a postulated LOCA event in a PWR.

2.4 Copper

In a containment building, copper is present in fan coolers with small contributions from instrument air lines. The measured corrosion rates in pH 10 borated alkaline containment water at 60, 90, and 110 °C [140, 194, and 230 °F] are shown in Table 2-1. The corrosion rate for copper increases with the increase in the temperature. The increase in the corrosion rate was much larger between 90 and 110 °C [194 and 230 °F] compared to the increase in the corrosion rate between 60 °C and 90 °C [140 and 194 °F]. The measured corrosion rates were comparable to the Griess and Bacarella (1969) corrosion rate data. Griess and Bacarella (1969) measured the corrosion rate of copper in 0.15 M sodium hydroxide [3,450 ppm sodium] solution between 55 and 140 °C [131 and 284 °F]. For copper at 100 °C [212 °F], the average submerged corrosion rate was 0.013 g/m²·h [0.51 mil/yr], which is comparable to the corrosion rates measured in this study at 90 and 110 °C [194 and 230 °F]. In Appendix C,

Debris Component	Corrosion Rate {g/m ² ·h [mil/yr]}		
	Temperature 60 °C [140 °F]	Temperature 90 °C [194 °F]	Temperature 110 °C [230 °F]
Carbon Steel	1.27 × 10 ⁻¹ [5.59]	9.36 × 10 ⁻² [4.12]	2.14 × 10 ⁻² [0.944]
Nukon® Insulation	1.09 × 10 ⁻² [1.50]	7.5 × 10 ⁻² [10.4]	1.43 × 10 ⁻¹ [19.7]

based on the literature review, a corrosion rate of 0.03 g/m²·hr [1.2 mil/yr] to simulate speciation of copper during a postulated LOCA event was adopted because this value provided a conservative estimate. The measured value at pH 10 used in simulations presented in Chapter 4 is almost four times lower than the corrosion rate value adopted for simulations at 90 °C [194 °F] in Appendix C. Simulations presented in Appendix C provide an upper bound for chemical speciation during a postulated LOCA event in a PWR.

2.5 Concrete

Concrete contribution comes from the erosion of concrete surfaces caused by the impact of the water stream around the LOCA location. While a protective paint is applied to concrete surfaces in most plants, a small portion of the concrete is expected to be uncoated during the LOCA event. Table 2-3 shows the fraction of stone, cement, sand, and water present in a concrete mix. In determining the corrosion rate of concrete, it was assumed that the contribution from stones in concrete was negligible. Table 2-4 shows the amount of key components present in concrete. In Appendix C, based on the literature review, a dissolution rate of 0.13 g/m²·hr [14.7 mil/yr] was adopted to simulate cement speciation during a postulated LOCA event, because this value provided a conservative estimate and was modeled as dicalcium silicate. The corrosion rate of typical Portland cement was based on Jantzen (1984). Jantzen examined the release of calcium from cast cement, cold-pressed cement, warm-

Component	Amount kg [lb]	Fraction
Stone	30.6 [68]	0.45
Sand	19.8 [44]	0.29
Portland Cement	11.7 [26]	0.17
Water	5.29 [11.7]	0.08

*Holcim (US) Inc. "Material Certification Report—Hydraulic Cement, Portland Cement." Holly Hill, South Carolina: Holcim (US) Inc. 2004.

Major Components	Fraction (Cement Basis)	Fraction (Concrete Basis)
Calcium Oxide	0.63	0.109
Aluminum Oxide	0.05	0.009
Silicon Dioxide	0.21	0.036
Iron Oxide	0.04	0.006

*Holcim (US) Inc. "Material Certification Report—Hydraulic Cement, Portland Cement." Holly Hill, South Carolina: Holcim (US) Inc. 2004.

pressed cement (formed under elevated temperatures and pressures), and clinkered cement. Based on 28-day tests at 60 °C [140 °F], the average release of calcium ions into the solution was 0.13 g/m²·hr [14.7 mil/yr]. Table 2-5 shows measured release rates of oxides of calcium, aluminum, and silicon from concrete based on respective element release rates in Table B-2 in pH 10 borated alkaline containment water at 60, 90, and 110 °C [140, 194, and 230 °F]. Experimental details are provided in Appendix B. Because concrete is a heterogeneous mixture of cement, sand, and stones with different leaching rates, congruent release is not expected from its surfaces. In a 14-day leaching test conducted at 60, 90, and 110 °C [140, 194, and 230 °F] in a 0.236 M [2,550 ppm] boron solution at pH 10 indicated that the test solution saturates with leached products from concrete within 24 hours. The data shown in Table 2-5 were obtained by sampling the solution at four different times during the first 24 hours.

The measured leaching rate for concrete at pH 10 is almost an order of magnitude higher than the adopted value for simulations at 90 °C [194 °F] in Appendix C. The thermodynamic simulations presented in Appendix C could underestimate the formation of corrosion products from the leaching of concrete during a postulated LOCA event in a PWR. In simulations presented in Chapter 4, the measured value of concrete dissolution rate was used.

2.6 Fiber Insulation

Fiber insulation is widely used as pipe insulation in containment buildings with the amount of fiber insulation depending on the specific plant design. Nukon[®], an Owens-Corning brand, is installed in a large number of containment buildings. Tables 2-1 and 2-2 show the measured dissolution rates for Nukon[®] fiber insulation glass in pH 10 borated alkaline and pH 7 trisodium phosphate containment waters at 60, 90, and 110 °C [140, 194, and 230 °F].

Dissolution rates were measured on glass that is used for the manufacture of Nukon[®] fiber insulation. The corrosion rate for Nukon[®] low-density fiber insulation glass increases with the increase in the temperature and follows an Arrhenius relationship as shown in Figure 2-1. As expected, the measured dissolution rate in pH 10 solution is higher than the dissolution rate at pH 7 solution. The analyzed chemical composition of Nukon[®] insulation glass is shown in Table 2-6. Table 2-7 provides an estimate of the time required to leach a 7-µm [0.28-mil] plate using the dissolution rate shown in Table 2-1 for Nukon[®] insulation glass. At 60 °C [140 °F], 7 µm [0.28 mil] of thickness would leach completely in 180 hours. An average diameter of a

Table 2-5. Leaching Rate of Calcium Oxide, Aluminum Oxide, and Silicon Dioxide from Concrete in Borated Alkaline Containment Water at pH 10			
Concrete Component	Corrosion Rate [g/m²·h]		
	Temperature 60 °C [140 °F]	Temperature 90 °C [194 °F]	Temperature 110 °C [230 °F]
Calcium Oxide	1.02	1.65	3.08
Aluminum Oxide	5.7×10^{-2}	1.11×10^{-1}	1.68×10^{-1}
Silicon Dioxide	8.1×10^{-2}	2.36×10^{-1}	3.21×10^{-1}

Note: Details provided in Appendix B.

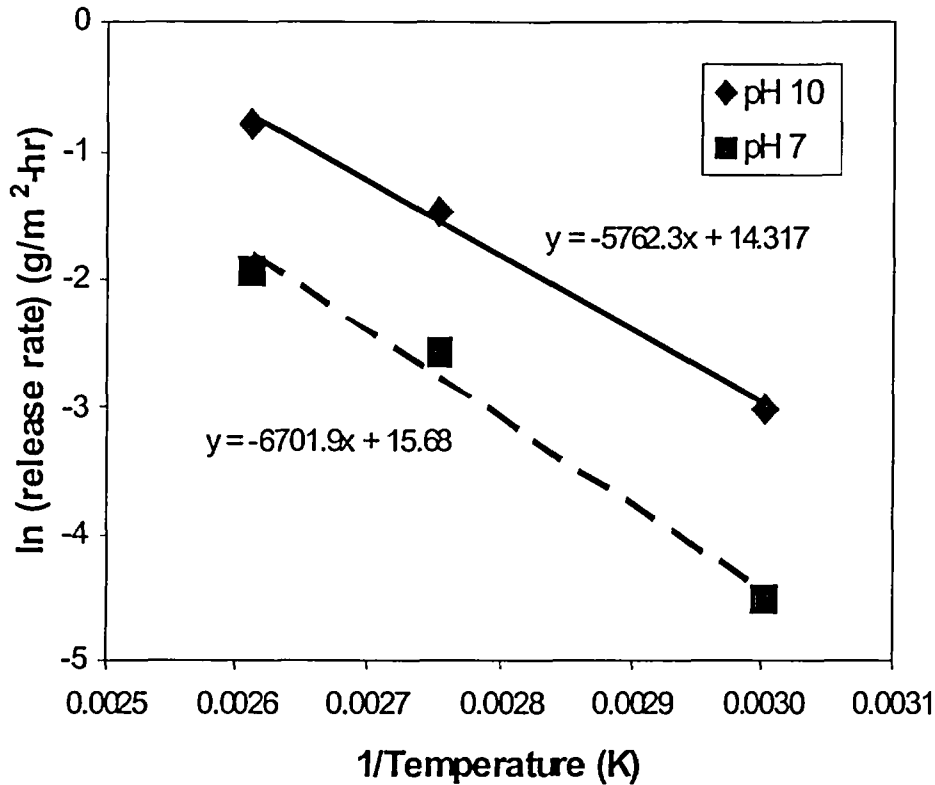


Figure 2-1. Relationship Between Release Rate and Temperature for Nukon® Low-Density Fiber Insulation Glass Between 60 and 110 °C [140 and 230 °F] at pH 7 and pH 10

Nukon® low-density fiber insulation is 7 µm [0.28 mil]. In simulations, presented in Chapter 4, the contributions from Nukon® low-density fiber insulation beyond 182 hours at 60 °C [140 °F] were fixed at the amount subjected to corrosion up to 182 hours. It should be noted, however, that a complete corrosion does not mean that insulation has disappeared. It merely reflects a change in chemical structure of the fiber. Most of the new solid phases formed in a fiber are expected to adhere to the surface of the fiber. With time, a small fraction of these phases could dislodge from the surface. A discussion on fiber insulation characteristics is provided in Appendix C, page 2-5. In Appendix C, based on the literature review, a corrosion rate of 0.025 g/m²-hr [1.2 mil/yr] is adopted to simulate speciation of Nukon® low-density fiber insulation during a postulated LOCA event because this value was expected to provide a conservative estimate. The measured corrosion rate value at pH 10, however, was almost an order of magnitude higher than the adopted value for simulations at 90 °C [194 °F] in Appendix C. The thermodynamic simulations presented in Appendix C could underestimate formation of corrosion products from the leaching of Nukon® low-density fiber insulation during a postulated LOCA event in a PWR. In simulations presented in Chapter 4, measured value of Nukon® dissolution rate was used.

Table 2-6. Analyzed Chemical Composition of Nukon[®] Fiber Insulation			
Component	Weight Percent	Molecular Weight	Mole Fraction
SiO ₂	63.7	60	0.651
Al ₂ O ₃	3.0	102	0.018
CaO	7.7	56	0.085
MgO	3.2	40	0.050
Na ₂ O	16.3	62	0.161
B ₂ O ₃	4.1	70	0.036

Table 2-7. Time Needed to Leach a 7-μm [0.28-mil]-Thick Nukon[®] Glass				
Temperature	Corrosion Rate [g/m²·h]	Density [kg/m³]	Rate μm/h [mil/h]	Time to Corrode 7 μm [hour]
60 °C [140 °F]	4.8×10^{-2}	2,500	1.92×10^{-2} [7.56×10^{-4}]	180
90 °C [194 °F]	2.41×10^{-2}	2,500	9.64×10^{-2} [3.80×10^{-3}]	38
110 °C [230 °F]	4.3×10^{-1}	2,500	1.72×10^{-1} [6.75×10^{-3}]	19

3 ESTIMATE OF DEBRIS COMPONENTS

Tables 1-1 and 2-1 list the sources of various elements present in debris components and their corrosion rates, respectively. The amount of corrosion product (CP) for a given component at a given elapsed time (*t*) is estimated based on Eq. (3-1).

$$CP = ESA \times CR \times t \quad (3-1)$$

where

- CP — corrosion product
- ESA — exposed surface area per unit containment volume, m²/m³
- CR — corrosion rate, g/m²·h
- t* — elapsed time, h

Exposed surface area is defined in the NRC test plan (NRC, 2005) and is discussed in Appendix C, Chapter 2.

The estimates of debris amount, the exposed surface area for aluminum, copper, galvanized steel, carbon steel, concrete walls, and Nukon[®] low-density fiber insulation are the same as presented in Appendix C, Chapter 2. A change in methodology, however, was adopted for estimating release from concrete particulates. Concrete contribution comes from exposed concrete walls and concrete particulates. In the NRC test plan (NRC, 2005), the exposed surface area of concrete walls per unit containment volume was estimated at 0.15 m²/m³ [0.045 ft²/ft³] and the total amount of concrete particulates was estimated at 22.43 g/m³ [0.0014 lbm/ft³]. Because the specific surface area of particulates is not known, this report conservatively assumes that oxides from cement and sand present in the concrete particulates were instantly released. Table 3-1 provides an estimate of oxides of calcium, aluminum, iron, and silicon released instantly from concrete particulates. The estimates shown in Table 3-1 are a product of the fraction of the component present in the concrete as shown in Table 2-5 and the amount of the concrete particulates per cubic meter. Tables 3-2 and 3-3 show the amounts of the debris components used as an input to conduct chemical speciation simulations to study the effect of temperature and to evaluate changes in the precipitation of solid and aqueous phases at 60 °C [140 °F] up to 360 hours. It should be noted that the contribution from concrete

Table 3-1. Estimate of Release from Concrete Particulates	
Components	Amount per L g [mol]
Calcium Oxide	2.42 × 10 ⁻³ [4.33 × 10 ⁻⁵]
Aluminum Oxide	2.00 × 10 ⁻⁴ [1.96 × 10 ⁻⁶]
Silicon Dioxide	8.01 × 10 ⁻⁴ [1.33 × 10 ⁻⁵]
Iron Oxide	1.44 × 10 ⁻⁵ [9.00 × 10 ⁻⁸]
Silicon Dioxide (Sand)	6.45 × 10 ⁻³ [1.07 × 10 ⁻⁴]

Table 3-2. Estimation of Debris Dissolution in pH 10 Borated Alkaline Containment Water Using Eq. (3-1)*			
Component	Amount Released g/L [mol/L]		
	After 30 minutes at 110 °C [230 °F]	After 30 minutes at 90 °C [194 °F]	After 30 minutes at 60 °C [140 °F]
Zinc from Galvanized Steel	1.5×10^{-4} [2.3×10^{-6}]	2.7×10^{-5} [4.1×10^{-7}]	2.4×10^{-5} [3.6×10^{-7}]
Aluminum	6.3×10^{-4} [2.3×10^{-5}]	5.4×10^{-4} [2.0×10^{-5}]	2.8×10^{-4} [1.0×10^{-5}]
Carbon Steel	7.0×10^{-6} [1.3×10^{-7}]	2.5×10^{-6} [4.5×10^{-8}]	1.1×10^{-6} [2.1×10^{-8}]
Copper	2.4×10^{-4} [3.8×10^{-6}]	1.3×10^{-5} [2.0×10^{-7}]	1.2×10^{-5} [1.8×10^{-7}]
Nukon®	1.5×10^{-1} [2.6×10^{-3}]	7.9×10^{-2} [1.3×10^{-3}]	1.6×10^{-2} [2.7×10^{-4}]
SiO ₂	9.9×10^{-2} [2.6×10^{-3}]	5.1×10^{-2} [8.5×10^{-4}]	1.1×10^{-2} [1.8×10^{-4}]
Al ₂ O ₃	4.7×10^{-3} [4.6×10^{-5}]	2.4×10^{-3} [2.4×10^{-5}]	5.0×10^{-4} [4.9×10^{-6}]
CaO	1.2×10^{-2} [2.2×10^{-4}]	6.2×10^{-3} [1.1×10^{-5}]	1.3×10^{-3} [2.3×10^{-5}]
MgO	5.1×10^{-3} [1.3×10^{-4}]	2.6×10^{-3} [6.5×10^{-4}]	5.4×10^{-4} [1.4×10^{-5}]
Na ₂ O	2.6×10^{-2} [4.1×10^{-4}]	1.3×10^{-2} [2.1×10^{-4}]	2.7×10^{-3} [4.4×10^{-5}]
B ₂ O ₃	6.4×10^{-3} [9.2×10^{-5}]	3.3×10^{-3} [4.7×10^{-5}]	6.9×10^{-4} [9.9×10^{-6}]
Concrete (particulates)			
SiO ₂	7.3×10^{-3} [1.2×10^{-4}]	7.3×10^{-3} [1.2×10^{-4}]	7.3×10^{-3} [1.2×10^{-4}]
Al ₂ O ₃	2.0×10^{-4} [2.0×10^{-6}]	2.0×10^{-4} [2.0×10^{-6}]	2.0×10^{-4} [2.0×10^{-6}]
CaO	2.4×10^{-3} [4.3×10^{-5}]	2.4×10^{-3} [4.3×10^{-5}]	2.4×10^{-3} [4.3×10^{-5}]
Concrete			
SiO ₂	8.0×10^{-6} [1.3×10^{-7}]	5.9×10^{-6} [9.8×10^{-8}]	2.0×10^{-6} [3.4×10^{-8}]
Al ₂ O ₃	4.2×10^{-6} [4.1×10^{-8}]	2.8×10^{-6} [2.7×10^{-8}]	1.4×10^{-6} [1.4×10^{-8}]
CaO	7.7×10^{-5} [1.4×10^{-6}]	4.1×10^{-5} [7.4×10^{-7}]	2.6×10^{-5} [4.6×10^{-7}]

*Note: Corrosion rates and estimated surface area are provided in Chapter 2 and Appendixes A, B, and C.

walls is negligible compared to the contribution from the concrete particulates. Furthermore, the amounts of calcium oxide, aluminum oxide, and silicon dioxide from concrete walls are negligible compared to the amounts released from Nukon® low-density fiber insulation. This lower contribution is attributed to the fact that the exposed surface area for per unit containment volume Nukon® low-density fiber insulation {678 m²/m³ [207 ft²/ft³]} is 10,000 times the surface area for exposed concrete walls {0.05 m²/m³ [0.15 ft²/ft³]}. After 148 hours at 60 °C [140 °F], the contribution of concrete particulates becomes negligible compared to the contribution from Nukon® low-density fiber insulation. The review of input values also indicates that the contributions from Nukon® low-density fiber insulation, aluminum, and concrete particulates dominate the concentration of input values.

Table 3-3. Estimation of Debris Dissolution in pH 10 Borated Alkaline Containment Water at 60 °C [140 °F] Using Eq. (3-1)*				
Component	Amount Released g/L [mol/L]			
	After 4 Hours	After 72 Hours	After 148 Hours	After 360 Hours
Zinc from Galvanized Steel	1.9×10^{-4} [2.9×10^{-6}]	3.4×10^{-3} [5.2×10^{-5}]	6.9×10^{-3} [1.1×10^{-4}]	1.7×10^{-2} [2.6×10^{-4}]
Aluminum	2.2×10^{-3} [8.3×10^{-5}]	4.0×10^{-2} [1.5×10^{-3}]	8.3×10^{-2} [3.1×10^{-3}]	2.0×10^{-1} [7.5×10^{-3}]
Carbon Steel	9.1×10^{-6} [1.7×10^{-7}]	1.7×10^{-4} [3.0×10^{-6}]	3.4×10^{-4} [6.1×10^{-6}]	8.2×10^{-4} [1.5×10^{-5}]
Copper	9.4×10^{-5} [1.5×10^{-6}]	1.7×10^{-3} [2.7×10^{-5}]	3.5×10^{-3} [5.5×10^{-5}]	8.4×10^{-3} [1.3×10^{-4}]
Nukon	1.3×10^{-1} [2.2×10^{-3}]	2.4×10^{-1} [4.0×10^{-2}]	4.9 [8.1×10^{-2}]	6.0 [1.0×10^{-1}]
SiO ₂	8.6×10^{-2} [1.4×10^{-3}]	1.5×10^0 [2.6×10^{-2}]	3.2×10^0 [5.2×10^{-2}]	3.9×10^0 [6.5×10^{-2}]
Al ₂ O ₃	4.0×10^{-3} [3.9×10^{-5}]	7.2×10^{-2} [7.1×10^{-4}]	1.5×10^{-1} [1.5×10^{-3}]	1.8×10^{-1} [1.8×10^{-3}]
CaO	1.0×10^{-2} [1.9×10^{-4}]	1.9×10^{-1} [3.3×10^{-3}]	3.8×10^{-1} [6.9×10^{-3}]	4.7×10^{-1} [8.4×10^{-3}]
MgO	4.4×10^{-3} [1.1×10^{-4}]	7.8×10^{-2} [2.0×10^{-3}]	1.6×10^{-1} [4.0×10^{-3}]	2.0×10^{-1} [4.9×10^{-3}]
Na ₂ O	2.2×10^{-2} [3.5×10^{-4}]	3.9×10^{-1} [6.4×10^{-3}]	8.1×10^{-1} [1.3×10^{-2}]	1.0×10^0 [1.6×10^{-2}]
B ₂ O ₃	5.5×10^{-3} [7.9×10^{-5}]	9.9×10^{-2} [1.4×10^{-3}]	2.0×10^{-1} [2.9×10^{-3}]	2.5×10^{-1} [3.6×10^{-3}]
Concrete (Particulates)				
SiO ₂	7.3×10^{-3} [1.2×10^{-4}]	7.3×10^{-3} [1.2×10^{-4}]	7.3×10^{-3} [1.2×10^{-4}]	7.3×10^{-3} [1.2×10^{-4}]
Al ₂ O ₃	2.0×10^{-4} [2.0×10^{-6}]	2.0×10^{-4} [2.0×10^{-6}]	2.0×10^{-4} [2.0×10^{-6}]	2.0×10^{-4} [2.0×10^{-6}]
CaO	2.4×10^{-3} [4.3×10^{-5}]	2.4×10^{-3} [4.3×10^{-5}]	2.4×10^{-3} [4.3×10^{-5}]	2.4×10^{-3} [4.3×10^{-5}]
Concrete				
SiO ₂	1.6×10^{-5} [2.7×10^{-7}]	2.9×10^{-4} [4.9×10^{-5}]	6.0×10^{-4} [1.0×10^{-5}]	1.5×10^{-3} [2.4×10^{-5}]
Al ₂ O ₃	1.1×10^{-5} [1.1×10^{-7}]	2.1×10^{-4} [2.0×10^{-6}]	4.2×10^{-4} [4.1×10^{-6}]	1.0×10^{-3} [1.0×10^{-5}]
CaO	2.0×10^{-4} [3.6×10^{-6}]	3.7×10^{-3} [6.6×10^{-5}]	7.5×10^{-3} [1.4×10^{-4}]	1.8×10^{-2} [3.3×10^{-4}]

*Note: Corrosion rates and estimated surface area are provided in Chapter 2 and Appendixes A, B, and C.

4 ANALYSIS OF CORROSION PRODUCTS IN ALKALINE CONTAINMENT WATER USING THERMODYNAMIC SIMULATIONS

The simulations presented in this chapter are focused on the thermodynamic modeling of the chemical speciation of plausible reaction products in coolant waters after a postulated LOCA event using experimentally determined corrosion rates. Speciation simulations were conducted (i) to study the effect of temperature, and (ii) to evaluate changes in the precipitation of solid and aqueous phases at 60 °C [140 °F] up to 360 hours. The results are compared to the simulations conducted in Appendix C, Chapter 3. Simulations are limited to the speciation in pH 10 borated alkaline containment water. Dissolved gases such as O₂ and CO₂ were not included in the input stream for the thermodynamic calculations. Because a majority of the multivalence elements are already in the highest valence state, a minimal effect of dissolved oxygen on the valence state of elements is expected. Furthermore, the atmospheric CO₂ is not expected to significantly change the pH of the solution, because the pH of the system is dominated by the presence of high concentrations of NaOH and H₃BO₃. The simulations at pH 7 were not conducted because corrosion rates of debris components, except carbon steel, are expected to be similar or lower than the corrosion rates at pH 10. For example, Nukon[®] low-density fiber insulation glass shows a lower magnitude corrosion rate at pH 7 compared to the corrosion rate at pH 10 (Chapter 2).

Simulations were made using a thermodynamic simulator developed by OLI Systems, Inc. (2002a,b) for evaluating aqueous chemical processes in industrial and environmental applications. The OLI Systems, Inc. data bank contains proprietary coefficients for predicting thermodynamic, transport, and physical properties for 80 elements of the periodic table and their associated aqueous inorganic species, as well as more than 5,000 organic species. The thermodynamic framework used by the OLI Systems, Inc. (2002a,b) code predicts behavior of multicomponent aqueous systems including aqueous liquid, vapor, organic liquid, and multiple solid phases for the general ranges of 0 to 30 molal, -50 to 300 °C [-58 to 572 °F], and 0–150 MPa [0–1,480 atm]. The software was validated (Appendix C) to examine the likelihood of formation and physical characteristics of any solid corrosion product that might be produced from the environment surrounding a postulated LOCA event.

4.1 Effect of Temperature

Simulations were conducted using input values shown in Table 3-2 at pH 10. The formation of solid phases as a function of temperature was examined at 110 °C [230 °F] at 304 kPa [3 atm], and 90 and 60 °C [194 and 140 °F] at 101 kPa [1 atm]. A pH 10 borated alkaline containment solution was obtained by adding 0.23 M sodium hydroxide [5,300 ppm sodium] and 0.259 M [2,800 ppm] boron as boric acid.

Table 4-1 shows the calculated pH and redox potential at different temperatures and pressures in borated alkaline containment water. At 60 °C [140 °F], the pH in an alkaline borated containment water was 10. A slight decrease in pH was observed with the increase in the temperature and pressure. Similarly, redox potential at 60 °C [140 °F] was -0.58 V versus the standard hydrogen electrode (V_{SHE}), and changed to -0.62 V versus V_{SHE} at 110 °C [230 °F]. These data are similar to simulation results cited in Appendix C, Table 3-1.

Table 4-1. pH and Redox Potential [Eh (V _{SHE})] of Borated Alkaline Containment Water with 0.259 M [2,800 ppm B] and 0.23 M [5,300 ppm Na] NaOH			
Test Conditions	pH	pH Neutral	Eh (V _{SHE})
60 °C [140 °F] at 101 kPa [1 atm]	10.0	6.1	-0.58
90 °C [194 °F] at 101 kPa [1 atm]	9.7	5.8	-0.60
110 °C [230 °F] at 304 kPa [3 atm]	9.6	5.2	-0.62

Figures 4-1 and 4-2 show the predicted amount of solid phases formed and their relative mol percent in a borated alkaline containment water, respectively. The mol percent distribution data are also summarized in Table 4-2. At 60 °C [140 °F] at 101 kPa [1 atm] in borated alkaline containment water, the calculated potentially amorphous solid phase was dominated by sodium aluminum silicate (NaAlSi₃O₈) with approximately 9-percent contribution from calcium magnesium silicate [Ca₂Mg₅Si₈O₂₂(OH)₂]. As the temperature increased to 110 °C [240 °F], 304 kPa [3 atm] pressure, the concentration of NaAlSi₃O₈ decreased to approximately 80 percent, while the concentration of Ca₂Mg₅Si₈O₂₂(OH)₂ increased to 17 percent. Irrespective of temperature and pressure, almost 100 percent of the solid phases formed at pH 10 were silicates. Smaller quantities, as shown in Table 4-2, of calcium iron silicate (Ca₃Fe₂Si₃O₁₂), zinc-iron oxide (ZnO·Fe₂O₃), and zinc silicate (Zn₂SiO₄) were observed. Simulation results indicate no phase change for copper. Most of the copper added as copper metal in the simulation remained as copper metal. Corrosion of metals was dominated by aluminum. The calculations are based on the solid phases in the OLI database. The presence of calcium, magnesium, aluminum, iron, and silicon in the solid phases are confirmed by energy dispersive spectroscopy (Appendix B, Figure B-6). The formation of actual solid phases may be different depending on the reaction kinetics.

Table 4-3 shows the predicted percentage of each element distributed in potential solid phases. Both magnesium and aluminum were fully incorporated in potentially amorphous solid phases. Silicon-bearing phases were observed in both soluble and insoluble phases in borated alkaline silicates. Approximately 30 percent of silicon was distributed within solid phases. The dominant silicon-bearing soluble phases were SiO₂ (aqueous), H₃SiO₄⁻¹, and NaHSiO₃. At 110 °C [230 °F], 304 kPa [3 atm] 19 percent of calcium was present in calcium-bearing solid phases, while at 60 °C [140 °F] 8 percent of calcium was present in calcium-bearing solid phases. The dominant calcium-bearing soluble phase was CaH₂BO₃⁺¹.

The speciation of corrosion products based on corrosion rates from literature is presented in Appendix C. Review of the simulation data presented in Appendix C, Figure 3-1, indicates NaAlSi₃O₈ was a dominant potentially amorphous solid phase in borated alkaline containment water with contributions from iron silicate [Fe₃Si₂O₅(OH)₄], Ca₃Fe₂Si₃O₁₂, and Ca₂Mg₅Si₈O₂₂(OH)₂. The absence of iron-bearing silicate phases, in the data presented in Figure 4-1 and Table 4-2, may be attributed to extremely low corrosion rates measured for carbon steel in pH 10 borated alkaline containment water. The formation of iron-bearing solid silicate phases was replaced by calcium magnesium silicate. With the exception of iron-bearing silicate phases observed in simulations presented in Appendix C, the observed speciation of solid phases was similar. The solid phases were dominated by the formation of silicates. The

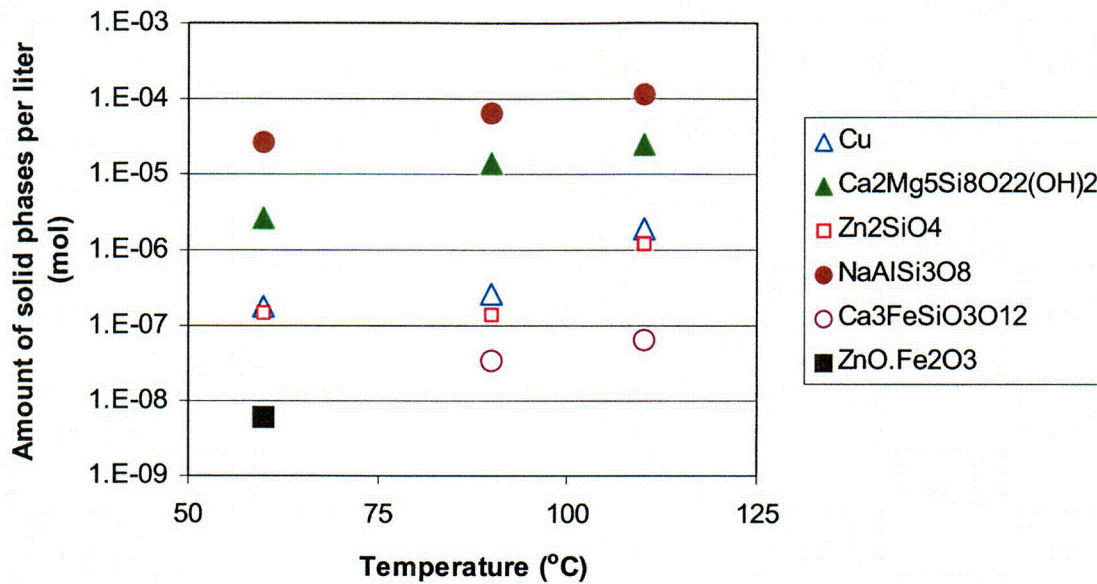


Figure 4-1. Calculated Amount, in mol, of Predicted Potentially Amorphous Solid Phases Formed As a Function of Temperature in 0.259 M [2,800 ppm] Boron in Borated Alkaline Containment Solution at pH 10 (Note: °F = 1.8 × °C + 32)

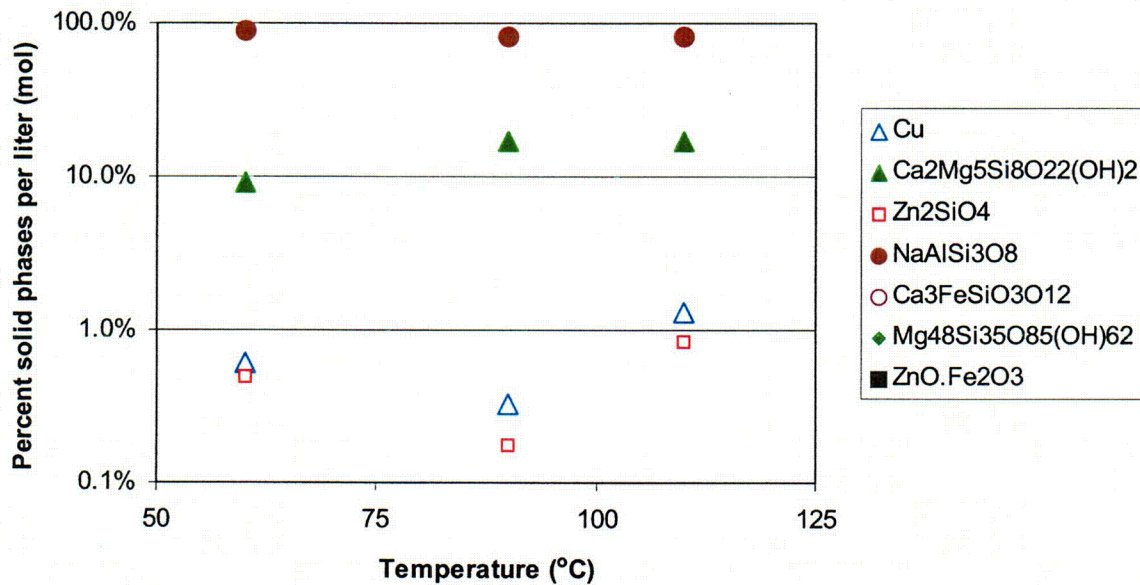


Figure 4-2. Calculated Percent Predicted Solid Phases Formed As a Function of Temperature in 0.259 M [2,800 ppm] Boron in Borated Alkaline Containment Solution at pH 10 (Note: °F = 1.8 × °C + 32)

Temperature and Pressure	NaAlSi ₃ O ₈ (Percent)	Ca ₂ Mg ₅ Si ₈ O ₂₂ (OH) ₂ (Percent)	Ca ₃ Fe ₂ Si ₃ O ₁₂ (Percent)	ZnO·Fe ₂ O ₃ (Percent)	Zn ₂ SiO ₄ (Percent)
110 °C [240 °F], 304 kPa [3 atm]	79.7	16.8	0.04	—	0.66
90 °C [194 °F], 101 kPa [1 atm]	84.2	15.6	0.02	—	0.09
60 °C [140 °F], 101 kPa [1 atm]	90.2	8.7	—	0.03	0.36

Temperature and Pressure	Major Contributors				Minor Contributors	
	Magnesium (Percent)	Aluminum (Percent)	Silicon (Percent)	Calcium (Percent)	Zinc (Percent)	Iron (Percent)
110 °C [230 °F], 304 kPa [3 atm]	100	100	32	19	81	98
90 °C [194 °F], 101 kPa [1 atm]	100	100	32	17	39	87
60 °C [140 °F], 101 kPa [1 atm]	100	100	35	8	63	75

contributions to the solid phases from zinc and iron are less than one mol percent compared to Nukon® low-density fiber insulation, concrete, and aluminum.

These results support the conclusion reached in Appendix C that there is no need for a pressurized test loop based on minimal changes observed in the speciation between 60 °C [140 °F] at 101 kPa [1 atm] and 110 °C [230 °F] at 304 kPa [3 atm].

4.2 Evolution of Solid and Aqueous Phases at 60 °C [140 °F]

Table 3-3 summarizes the expected increase in the amount of debris components with time at 60 °C [140 °F]. The amounts of debris were calculated for 0.5, 4, 32, 72, 148, 240, and 360 hours. For Nukon® low-density fiber insulation, it was estimated that the fiber would leach in 180 hours at 60 °C [140 °F]. Total amount from Nukon® low-density fiber insulation for time periods greater than 180 hours was, therefore, fixed at the 180-hour release amount.

In the simulations conducted for time periods beyond 32 hours at 60 °C [140 °F], the debris components carbon steel and copper were removed from the simulation input. The simulations failed to reach convergence because of extremely low concentrations of copper and carbon steel compared to the concentrations of Nukon® low-density fiber insulation, aluminum, and concrete. The simulation results indicate that the total mol percent of solid phases formed from carbon steel corrosion was less than 0.1 percent. Copper was thermodynamically stable and showed no corrosion. Table 4-4 shows simulation results with and without iron and copper for a 32-hour simulation at 60 °C [140 °F]. Results indicate no influence of removal of iron and copper on the dominant solid phases.

Table 4-4. Calculated Amount of Solid Phase Per Liter of Solution at pH 10, 60 °C [140 °F], at 32 Hours		
Potentially Amorphous Phase	32-Hour Input (mol)	32-Hour Input without Iron and Copper (mol)
NaAlSi ₃ O ₈	1.29 × 10 ⁻³	1.29 × 10 ⁻³
Ca ₂ Mg ₅ Si ₈ O ₂₂ (OH) ₂	1.76 × 10 ⁻⁴	1.72 × 10 ⁻⁴
CaSiO ₃	8.26 × 10 ⁻⁴	8.28 × 10 ⁻⁴
Zn ₂ SiO ₄	1.14 × 10 ⁻⁵	1.14 × 10 ⁻⁵
Ca ₃ Fe ₂ Si ₃ O ₁₂	6.60 × 10 ⁻⁷	—
Copper	1.18 × 10 ⁻⁵	—

Table 4-5 shows the calculated pH and redox potential at different temperatures and pressures in borated water with 0.259 M [2,800 ppm] boron and 0.23 M sodium hydroxide [5,300 ppm sodium]. At 60 °C [140 °F], the pH in the borated alkaline containment water with 0.259 M [2,800 ppm] boron was approximately 10. The pH remained near 10 for the time period ranging from 0.5 to 360 hours. The redox potential at 60 °C [140 °F] was approximately -0.61 V_{SHE} at 0.5 hour and changed slightly to -0.64 V_{SHE}. No significant changes were observed in either pH or redox conditions.

Figures 4-3 and 4-4 show the amount of potentially amorphous solid phases formed and their relative mol percent distribution in borated alkaline containment water, respectively, as a function of time at 60 °C [140 °F]. The mol percent distribution data is also summarized in Table 4-6. Simulation results show that the amount of solid phases observed at 60 °C [140 °F], pH 10 increases with time. Results also indicate that at 0.5 hour, dominant potentially amorphous solid phases consist of 89 mol percent NaAlSi₃O₈ and 10 mol percent Ca₂Mg₅Si₈O₂₂(OH)₂. The formation of calcium silicate (CaSiO₃) initiates at 32 hours and silica (SiO₂) at 72 hours. While the amount of calculated solid phases continues to increase, and NaAlSi₃O₈ continues to be a dominant solid phase with time (Figure 4-3), the formations of CaSiO₃ and SiO₂ result in redistribution of solid phases (Figure 4-4). Beyond 72 hours, dominant potentially amorphous solid phases consist of NaAlSi₃O₈, CaSiO₃, and SiO₂ with a smaller quantity of Ca₂Mg₅Si₈O₂₂(OH)₂. Decrease in SiO₂ mol percent and increase in NaAlSi₃O₈ mol percent after 148 hours are attributed to the fact that combination from the Nukon® low-density fiber insulation remains fixed beyond 180 hours while aluminum metal continues to increase with time. The contribution from concrete walls remains insignificant. Irrespective of time, at 60 °C [140 °F], the formation of solid phases is dominated by the formation by silicates and silica.

Table 4-7 shows the calculated percentage of each element incorporated in dominant solid phases. Both magnesium and aluminum were fully incorporated in solid phases. The concentrations of the other two major components of the debris, calcium and silicon, continue to increase in the solid phase with time. It should be noted that while the concentrations of silicon and calcium in solid phases continue to increase with time (Table 4-7), the total amounts of debris components that dissolve also continue to increase with time (Figure 4-3).

Time (Hour)	pH	Eh (V_{SHE})
0.5	9.96	-0.58
4	9.96	-0.61
32	9.95	-0.63
72	9.93	-0.63
148	10.0	-0.63
240	10.0	-0.64
360	10.0	-0.63

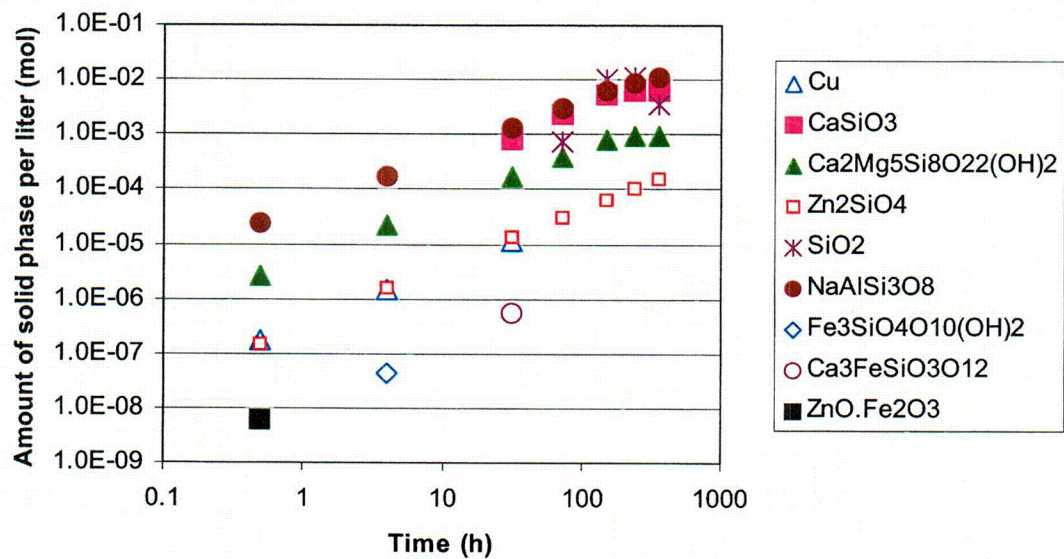


Figure 4-3. Calculated Amount, in Mol, of Predicted Solid Phases Formed As a Function of Time, in Hours, in 0.259 M [2,800 ppm] Borated Alkaline Containment Water at 60 °C [140 °F]

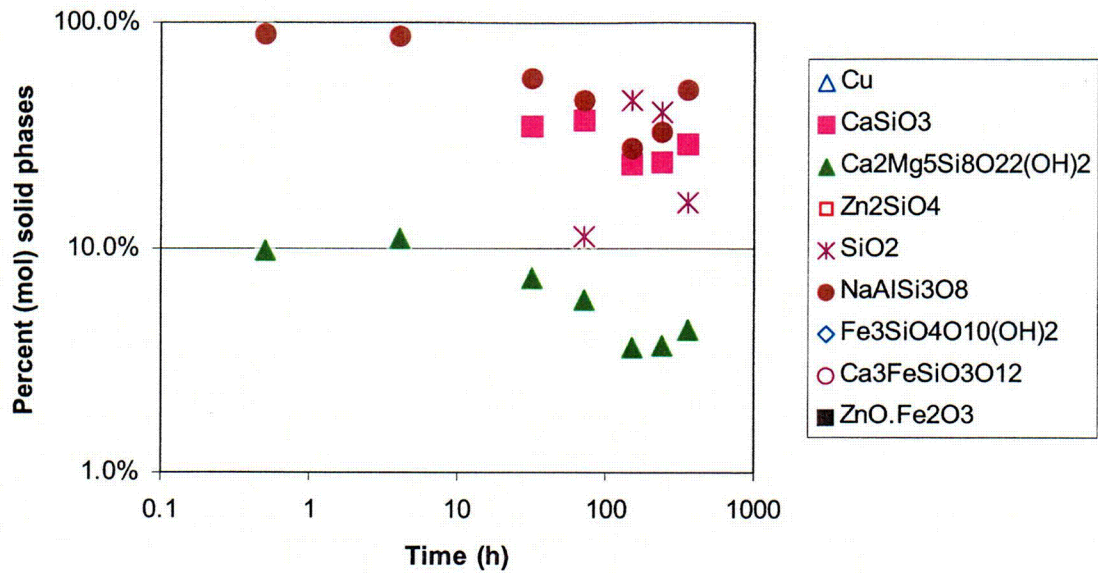


Figure 4-4. Calculated Percent Predicted Solid Phases Formed As a Function of Time in 0.259 M [2,800 ppm] Boron in Borated Alkaline Containment Water at pH 10 at 60 °C [140 °F]

Table 4-6. Percent of Potentially Amorphous Solid Phases at 60 °C [140 °F], 101 kPa [1 atm], pH 10					
Time (h)	NaAlSi₃O₈ (Percent)	Ca₂Mg₅Si₈O₂₂(OH)₂ (Percent)	CaSiO₃ (Percent)	SiO₂ (Percent)	Zn₂SiO₄ (Percent)
0.5	90.2	8.7	0	0	0.36
4	87.0	11.3	0	0	0.74
32	55.6	7.4	35.6	0	0.49
72	44.4	5.9	37.0	12.3	0.39
148	26.0	3.5	22.7	47.8	0.23
240	32.0	3.7	24.3	40.0	0.32
360	48.4	4.3	29.0	17.6	0.56

Time (Hour)	Major Contributors				Minor Contributors	
	Magnesium (Percent)	Aluminum (Percent)	Silicon (Percent)	Calcium (Percent)	Zinc (Percent)	Iron (Percent)
0.5	100	100	35	8	63	75
4	100	100	44	19	98	96
32	100	100	53	76	100	100
72	100	100	59	94	100	NA*
148	100	100	76	98	100	NA
240	100	100	79	98	100	NA
360	100	100	80	98	100	NA

*NA—not applicable.

The speciations of corrosion products based on corrosion rates from literature at 60 °C [140 °F] are presented in Appendix C. The dominant potentially amorphous solid phases formed in the borated containment water at pH 10 after 360 hours were SiO₂, CaSiO₃, NaAlSi₃O₈, Ca₂Mg₅Si₈O₂₂(OH)₂, Ca₃Fe₂Si₃O₁₂, and a minor quantity of Zn₂SiO₄. Comparison of data presented in Appendix C, Figure 3-2, indicates formation of similar phases in a 360-hour simulation at 60 °C [140 °F] with the exception of the iron phases. As indicated in Section 4.1, the absence of iron bearing silicate phases is attributed to the extremely low corrosion rate for carbon steel determined in this study. The formation of iron-bearing solid silicate phases was replaced by calcium magnesium silicate.

Both silicon- and calcium-bearing soluble phases were also observed in the borated containment water at pH 10. At 0.5 hour, approximately 68 mol percent of silicon and 92 mol percent calcium were distributed within various soluble silicates. Figures 4-5 and 4-6 show the concentrations of sodium and boron and concentrations of silicon and calcium, respectively, in soluble phases as a function of time at 60 °C [140 °F]. The dominant silicon-bearing soluble phases were SiO₂ (aqueous), H₃SiO₄⁻¹, and NaHSiO₃. The dominant calcium-bearing soluble phase was CaH₂BO₃⁺¹. It should be noted that while the concentrations of silicon and calcium in solid phases continue to increase with time (Table 4-7), the total amount of debris components also continues to increase with time (Figure 4-3). A net increase in the amount of debris components results in an increase in the soluble concentration of the elements shown in Figures 4-5 and 4-6. Results also indicate that the boron and sodium concentrations increase with time. Silicon, calcium, sodium, and boron are released from Nukon® low-density fiber insulation. Contributions for silicon and calcium could also come from concrete.

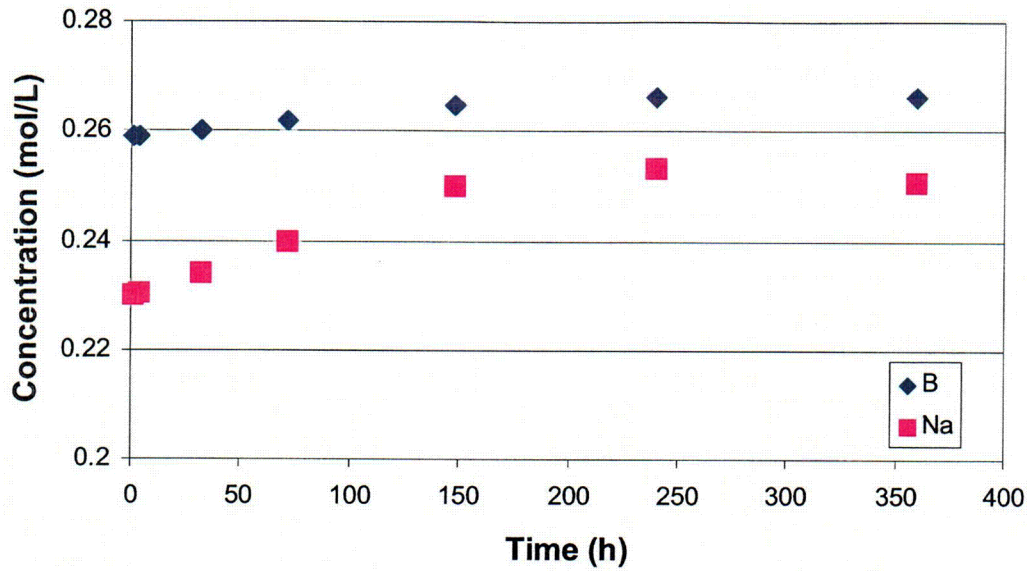


Figure 4-5. Calculated Sodium and Boron Concentrations, in mol/L, in Aqueous Phase As a Function of Time in 0.259 M [2,800 ppm] Borated Alkaline Containment Water in pH 10 at 60 °C [140 °F]

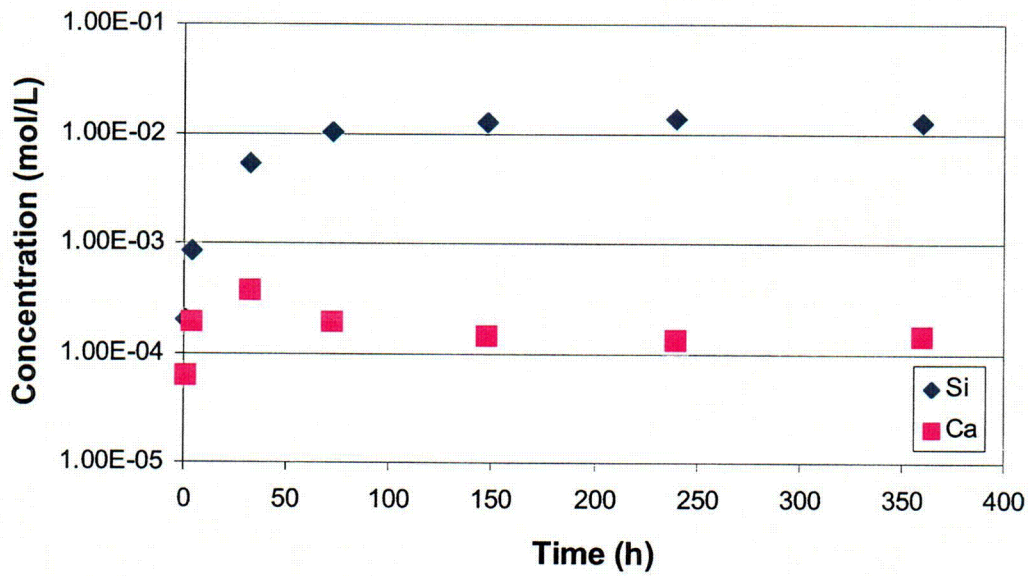


Figure 4-6. Calculated Calcium and Silicon Concentrations, mol/L, in Aqueous Phase As a Function of Time in 0.259 M [2,800 ppm] Borated Alkaline Containment Water in pH 10 at 60 °C [140 °F]

COF

The increase in silicon and calcium concentrations as a function of time, along with the increased boron and sodium concentrations, could be used to estimate and monitor ongoing corrosion in the system.

It should be noted that input for the simulations excludes organics to model the formation of complexes due to organic binder retained in fiber insulation after heat treatment. While simulations examine complex interactions between metals and inorganic materials such as fiber insulation and aluminum, the inputs are based on the corrosion or leaching rates of individual components. Experimental studies to examine interactions between debris components were not conducted. If leaching of fiber insulation or concrete is restricted due to a formation of a coating on the surface, simulations will result in significantly different results. For example, the Pourbaix diagram (Figure 4-7) for aluminum in a pH 10 alkaline borated water at 60 °C [140 °F] indicates that at a pH 10 or higher aluminum is predominantly present as a soluble $\text{Al}(\text{OH})_4^-$ complex. Results are in contrast to simulations in the presence of dissolution products from fiber insulation and concrete where aluminum is predominantly present in a solid phase as $\text{NaAlSi}_3\text{O}_8$ (Table 4-6). The Pourbaix diagram (Figure 4-8) for aluminum in a pH 10 alkaline borated water containing silica at 60 °C [140 °F] indicates that the $\text{NaAlSi}_3\text{O}_8$ solid phase is dominant up to a pH of 12.

The comparison of the results using measured corrosion rates with the results presented in Appendix C using literature data indicates formation of similar dominant solid phases with the exception of iron silicates such as $\text{Fe}_3\text{Si}_2\text{O}_5(\text{OH})_4$ and $\text{Ca}_3\text{Fe}_2\text{Si}_3\text{O}_{12}$. The absence of iron-bearing silicate phases in calculations using measured corrosion rates was attributed to an extremely low corrosion rate measured for carbon steel at pH 10 compared to the corrosion rate assumed in Appendix C calculations.

Higher measured dissolution rates for Nukon[®] fiber insulation and concrete result in higher concentration of solid phases. Solid phases, however, are similar in composition. It should be noted that despite a higher measured dissolution rate for concrete, Appendix C calculations are overly conservative, because the Appendix C analyses assumed concrete particulates to contribute at the same rate without an end-point at which particulates would be considered completely dissolved. In this analysis, because of the lack of a good estimate on the particulate surface area, the entire inventory of concrete particulates {22.43 g/m³ [0.0014 lbm/ft³]} was assumed to go through dissolution instantly. Despite this conservative assumption, the contribution from concrete particulates was significantly lower than the contributions from Nukon[®] fiber insulation.

This report provides insight to and is useful in understanding the evolution of solution chemistry and the formation of solid phases in integrated chemical effects tests at the University of New Mexico.

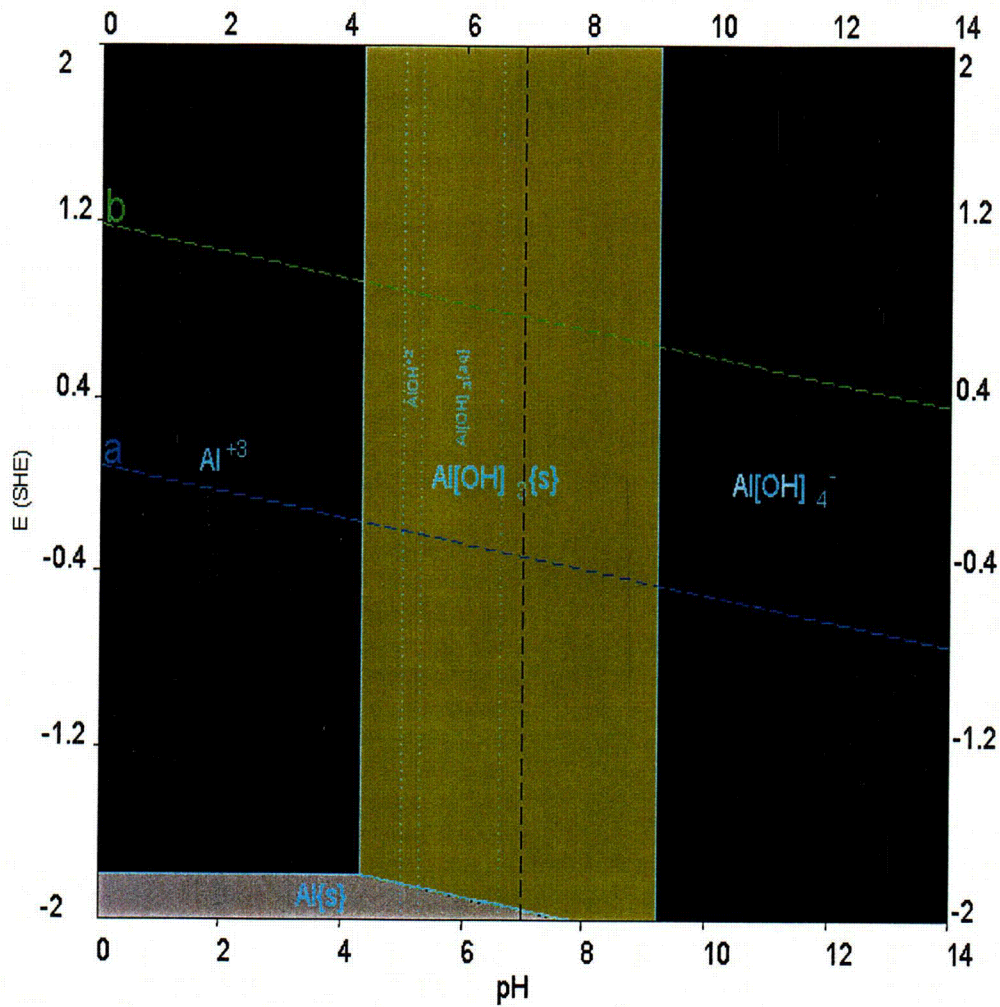


Figure 4-7. Pourbaix Diagram for Aluminum in a pH 10 Borated Alkaline Solution at 60 °C [140 °F]

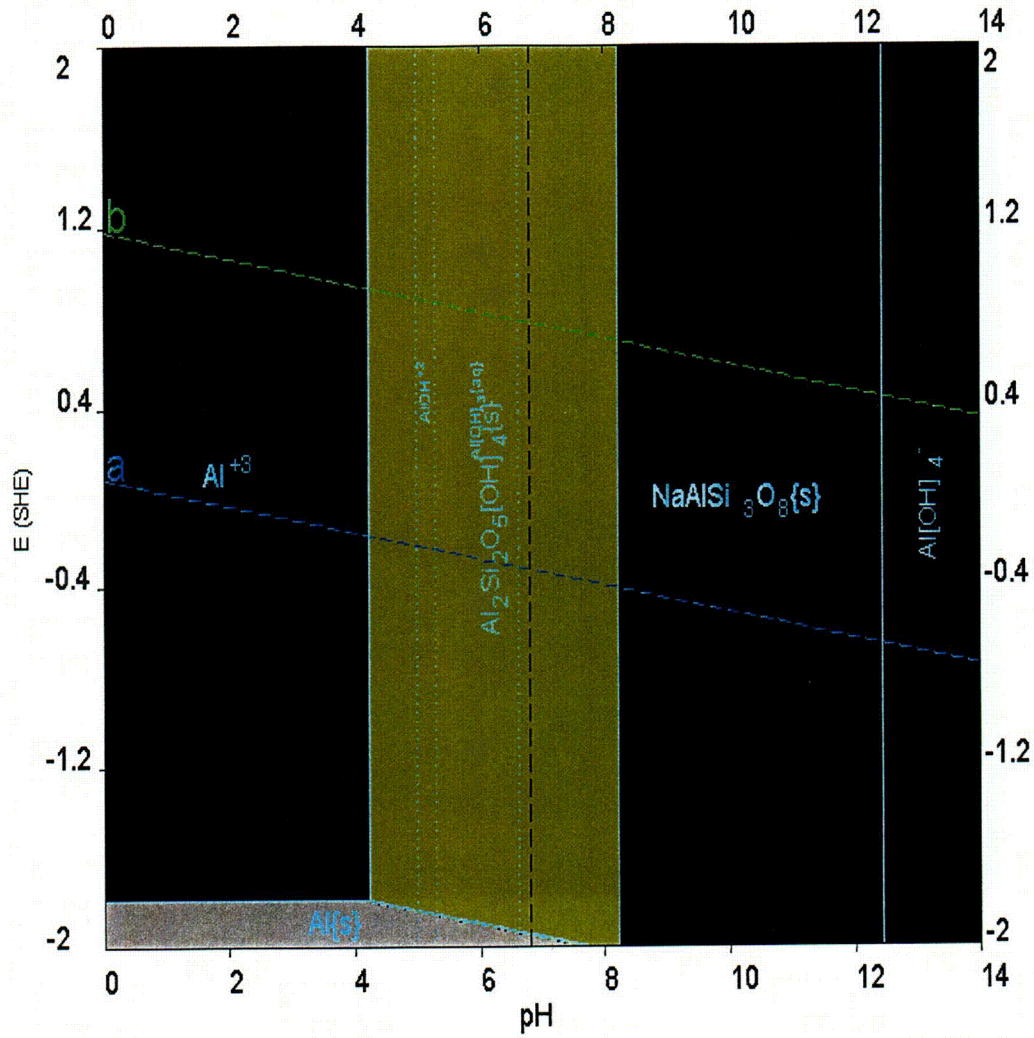


Figure 4-8. Pourbaix Diagram for Aluminum in a pH 10 Borated Alkaline Water Containing Silica at 60 °C [140 °F]

5 SUMMARY

Corrosions of galvanized steel, copper, aluminum, and carbon steel were measured using ASTM G59–97 (ASTM International, 2004a), and corrosion rates were calculated using ASTM G102–89 (ASTM International, 2004b) at 60, 90, and 110 °C [140, 194, and 230 °F] in borated {0.259 M [2,800 ppm] B} alkaline containment water at pH 10. Results indicate the following:

- Except for the corrosion rate of carbon steel, the corrosion rates of aluminum, copper, and galvanized steel increase with increase in temperature.
- The measured corrosion rates for aluminum, galvanized steel, and copper were lower than the corrosion rate values assumed in Appendix C, Chapter 2.
- A significant difference was observed between the measured carbon steel corrosion rate and the value assumed in Appendix C, Chapter 2. Carbon steel at pH 10 in borated alkaline containment water showed a passive behavior with a low corrosion rate. The measured corrosion rate in pH 7 borated trisodium phosphate containment water was approximately an order of magnitude higher than the corrosion rate in pH 10 borated alkaline containment water.

The dissolution rate for Nukon[®] glass was determined using ASTM C1220–98 (ASTM International, 2002) at 60, 90, and 110 °C [140, 194, and 230 °F] in borated {0.259 M [2,800 ppm] B} alkaline containment water at pH 10 and in borated {0.259 M [2,800 ppm] B} containment water at pH 7. A pH 10 was adjusted by the addition of sodium hydroxide and a pH 7 was adjusted by the addition of trisodium phosphate. Results indicate the following:

- The corrosion rate data showed a strong dependence on temperature. The corrosion rate increased with the increase in the temperature.
- The corrosion rate was higher than the value assumed in Appendix C, Chapter 2. The Nukon[®] low-density fiber insulation corrosion rate at pH 7 was lower compared to the corrosion rate at pH 10.

The dissolution rate for concrete was also determined using ASTM C1220–98 (ASTM International, 2002). Results indicate the following:

- The corrosion rate data showed a strong dependence on temperature. The corrosion rate increased with the increase in the temperature.
- The measured corrosion rate for concrete was higher than the value assumed in Appendix C, Chapter 2.

The thermodynamic simulations documented in this report were made using a thermodynamic simulator developed by OLI Systems, Inc. (2002b) for evaluating aqueous chemical processes in industrial and environmental applications. Computational thermodynamic simulation calculations were conducted using StreamAnalyzer[®] Version 1.2 (2002a). Key chemical components involved in speciation simulation were copper, carbon steel, galvanized steel, aluminum, Nukon[®] low-density fiber insulation, and concrete. The amount of corroded product

was determined based on the surface areas exposed as discussed in the NRC test plan, (NRC, 2005), and the experimentally determined corrosion rates. Thermodynamic simulations were conducted at 60, 90, and 110 °C [140, 194, and 230 °F]. At 90 and 110 °C [194 and 230 °F], simulations were based on corrosion of components for 30 minutes. At 60 °C [140 °F], simulations were based on corrosion of components from 30 minutes to 360 hours. The results of the corrosion rate measurements and estimate of corrosion amounts indicate the following:

- The comparison of corrosion amounts indicate that Nukon® low-density fiber insulation is two to three orders of magnitude higher compared to corrosion products from carbon steel, galvanized steel, and copper. Corrosion amounts associated with these metals, can be neglected in simulations.
- Based on the corrosion rate for Nukon® low-density fiber insulation at 60 °C [140 °F], an average 7-µm [0.28-mil]-diameter Nukon® low-density fiber would corrode in approximately 182 hours.
- The contributions of calcium, aluminum, and sulfur from Nukon® low-density fiber insulation are approximately 10,000 times more than the contribution from concrete walls. In this study, concrete particulates were assumed to be released instantly.

Analysis of the simulation data at 60, 90, and 110 °C [140, 194, and 230 °F] for 30 minutes in borated alkaline containment water at pH 10 indicates the following:

- The formation of potentially amorphous solid phases was predicted to be dominated by silicates. Sodium aluminum silicate ($\text{NaAlSi}_3\text{O}_8$) and calcium magnesium silicate [$\text{Ca}_2\text{Mg}_5\text{Si}_8\text{O}_{22}(\text{OH})_2$] constituted approximately 99 percent of the solid phases.
- Smaller quantities of calcium iron silicate ($\text{Ca}_3\text{Fe}_2\text{Si}_3\text{O}_{12}$), zinc-iron oxide ($\text{ZnO}\cdot\text{Fe}_2\text{O}_3$), and zinc silicate (Zn_2SiO_4) were observed. Simulation results indicate no phase change for copper. Contributions from metals were dominated by aluminum.
- A comparison with the simulation data presented in Appendix C, Figure 3-1, indicates the formation of similar dominant potentially amorphous solid phases with the exception of iron silicates such as $\text{Fe}_3\text{Si}_2\text{O}_5(\text{OH})_4$ and $\text{Ca}_3\text{Fe}_2\text{Si}_3\text{O}_{12}$. The absence of iron-bearing silicate phases was attributed to the fact that the measured carbon steel corrosion rate at pH 10 was extremely low compared to the corrosion rate assumed in Appendix C. In both cases, the solid phases were dominated by the formation of silicates. These results support the conclusion reached in Appendix C that there is no need for a pressurized test loop.

Analysis of simulation data at 60 °C [230 °F] from 30 minutes to 360 hours in borated alkaline containment water at pH 10 indicates the following:

- At 0.5 hour, dominant solid phases consisted of 90 mol percent $\text{NaAlSi}_3\text{O}_8$ and 9 mol percent $\text{Ca}_2\text{Mg}_5\text{Si}_8\text{O}_{22}(\text{OH})_2$. The formation of calcium silicate (CaSiO_3) initiated at 32 hours and silica (SiO_2) at 72 hours. $\text{NaAlSi}_3\text{O}_8$ continued to be a dominant potentially amorphous solid phase as a function of time. The formation of CaSiO_3 and SiO_2 resulted in redistribution of solid phases. Beyond 72 hours, dominant solid phases consist of $\text{NaAlSi}_3\text{O}_8$, CaSiO_3 and SiO_2 with a smaller quantity of $\text{Ca}_2\text{Mg}_5\text{Si}_8\text{O}_{22}(\text{OH})_2$. Irrespective of time at 60 °C [140 °F], the formation of solid phases is dominated by silicates and silica.

- A comparison of data presented in Appendix C indicates formation of similar phases in a 360-hour simulation at 60 °C [140 °F] with the exception of iron phases.
- Both silicon- and calcium-bearing soluble phases were observed in borated alkaline containment water. Dominant silicon-bearing soluble phases were SiO_2 (aqueous), $\text{H}_3\text{SiO}_4^{-1}$, and NaHSiO_3 , and dominant calcium-bearing soluble phase was $\text{CaH}_2\text{BO}_3^{+1}$. Furthermore, concentrations of boron and sodium in the solution increased with time.
- The increases in silicon and calcium concentrations, along with the increase in the boron and sodium concentrations, in the aqueous phase as a function of time could be used to estimate and monitor ongoing corrosion in the system.

Simulations provide insight to and is useful in understanding the evolution of solution chemistry and the formation of solid phases in integrated chemical effects tests at the University of New Mexico. The simulation results can be used to corroborate the evolution of solution chemistry and the formation of solid phases on the surfaces of the corroding components observed. It should be noted that while simulations were based on the measured corrosion rates, input for the simulation excludes organics to model formation of complexes due to organic binder retained in fiber insulation after heat treatment. While simulations examine complex interactions between metals and inorganic materials such as fiber insulation and aluminum, the inputs are based on the corrosion or leaching rates of individual components. Experimental studies to examine interactions between debris components were not conducted.

6 CONCLUSIONS

Based on the measured corrosion rates, estimated exposed surface area, and exposure time, the thermodynamic simulations indicate that formation of dominant solid phases is controlled by the presence of Nukon[®] low-density fiber insulation, aluminum, and concrete. The dominant potentially amorphous solid phases consisted of silicate phases such as $\text{NaAlSi}_3\text{O}_8$, $\text{Ca}_2\text{Mg}_5\text{Si}_8\text{O}_{22}(\text{OH})_2$, CaSiO_3 , and SiO_2 . Although some of these constituents decreased proportionally with increasing time, the solid $\text{NaAlSi}_3\text{O}_8$ phase continued to be a dominant solid phase as a function of time. The calculations are based on the solid phases in the OLI database. The formation of actual solid phases may be different depending on the reaction kinetics. The formation of $\text{NaAlSi}_3\text{O}_8$ coupled with the presence of alkaline solutions could lead to gel formation, resulting in clogging of the containment area sump pump suction strainers. Thermodynamic simulations confirm that no significant differences in corrosion product formation are expected in alkaline simulated containment water at pH 10 as the high-temperature and pressure conditions during the initial stages of a LOCA event approach steady-state conditions.

This study also provides, based on thermodynamic simulations, an evolution of soluble species in borated alkaline containment water at 60 °C [140 °F]. Both silicon- and calcium-bearing soluble phases were observed in borated alkaline containment water. The dominant silicon-bearing soluble phases were SiO_2 (aqueous), $\text{H}_3\text{SiO}_4^{-1}$, and NaHSiO_3 , and the dominant calcium-bearing soluble phase was $\text{CaH}_2\text{BO}_3^{+1}$. Furthermore, the concentrations of boron and sodium increased with time. The increase in silicon and calcium concentrations, along with the increase in boron and sodium concentrations, in aqueous phase as a function of time could be used to estimate and monitor ongoing corrosion in the system.

Simulations provide insights to and is useful in understanding the evolution of solution chemistry and the formation of solid phases in integrated chemical effects tests at the University of New Mexico.

It should be noted that while simulations were based on measured corrosion rates, input for the simulation excludes organics to model formation of complexes due to organic binder retained in fiber insulation after heat treatment. While simulations examines complex interactions between metals and inorganic materials such as fiber insulation and aluminum, the inputs are based on the corrosion or leaching rates of individual components. Experimental studies to examine interactions between debris components were not conducted.

7 REFERENCES

- ASTM International. "Metals Test Methods and Analytical Procedures." *ASTM G59-97 (Reapproved 2003): Standard Test Method for Conducting Potentiodynamic Polarization Resistance Measurement. Volume 3.02: Wear and Erosion—Metal Corrosion*. Published on CD ROM. West Conshohocken, Pennsylvania: ASTM International. 2004a.
- . "Metals Test Methods and Analytical Procedures." *ASTM G102-89 (1999): Standard Practice for Calculation of Corrosion Rates and Related Information from Electrochemical Measurements. Volume 3.02: Wear and Erosion—Metal Corrosion*. Published on CD ROM. West Conshohocken, Pennsylvania: ASTM International. 2004b.
- . "Nuclear, Solar, and Geothermal Energy." *ASTM C1220-98: Standard Test Method for Static Leaching of Monolithic Waste Forms for the Disposal of Radioactive Waste. Volume 12.01: Nuclear Energy (I)*. Published on CD ROM. West Conshohocken, Pennsylvania: ASTM International. 2002.
- Griess, J.C. and A.L. Bacarella. "Design Consideration of Reactor Containment Spray Systems—Part III: The Corrosion of Materials in Spray Solutions." ORNL-TM-2412, Part III. Oak Ridge, Tennessee: Oak Ridge National Laboratory. 1969.
- Hall, J.F. "Corrosion of Low Alloy Steel Fastener Materials Exposed to Borated Water." Proceedings of the Third International Symposium on Environmental Degradation of Materials in Nuclear Power Systems—Water Reactors. G.J. Theus and J.R. Weeks, eds. La Grange Park, Illinois: American Nuclear Society. pp. 711-722. 1988.
- Hermannson, H.P. and S. Erixon. "Chemical Environment for Strainers at Loss of Coolant Conditions in a PWR." SKI Report 98:12. Stockholm, Sweden: Swedish Nuclear Power Inspectorate. 1997.
- Jantzen, C.M. "Radioactive Waste-Portland Cement Systems II: Leaching Characteristics." *Journal of American Ceramic Society*. Vol. 67, No. 10. pp. 674-678. 1984.
- Johns, R.C., B.C. Letellier, K.J. Howe, and A.K. Ghosh. "Small-Scale Experiments: Effects of Chemical Reactions on Debris-Bed Head Loss." LA-UR-03-6415. Los Alamos, New Mexico: Los Alamos National Laboratory. 2003.
- NRC. "Test Plan: Characterization of Chemical and Corrosion Effects Potentially Occurring During a Pressurized Water Reactor LOCA." Rev. 12b. ML050450478. Washington, DC: NRC. 2005. <www.nrc.gov/reading-rm/adams.html>
- . NUREG/CR-6808, "Knowledge Base for the Effect of Debris on Pressurized Water Reactor Emergency Core Cooling Sump Performance." Washington, DC: NRC. February 2003.
- OLI Systems, Inc. "StreamAnalyzer[®] Version 1.2." Morris Plains, New Jersey: OLI Systems, Inc. 2002a.

_____. "Environmental Simulation® Program Version 6.6." Morris Plains, New Jersey: OLI Systems, Inc. 2002b.

Piippo, J., T. Laitinen, and P. Sirkai. "Corrosion Behavior of Zinc and Aluminum in Simulated Nuclear Accident Environments." STUK-YTO-TR 123. Helsinki, Finland: Finnish Center for Radiation and Nuclear Safety. 1997.

APPENDIX A

APPENDIX A

CORROSION RATE MEASUREMENT METHODS FOR METALS

The corrosion rates for aluminum, copper, zinc on galvanized steel surface, and carbon steel samples were determined in borated alkaline water at pH 10 at 60, 90, and 110 °C [140, 194, and 230 °F]. The corrosion rate for carbon steel was also determined in a borated trisodium phosphate solution at pH 7 at 60, 90, and 110 °C [140, 194, and 230 °F]. Borated alkaline containment water contained 0.259 M [2,800 ppm] boron, and the pH was adjusted by the addition of NaOH. Borated containment water {0.259 M [2,800 ppm] boron} at pH 7 was obtained by the addition of Na₃PO₄. The following two electrochemical methods were used for corrosion measurements:

- Polarization resistance method in accordance with ASTM G59–97 (ASTM International, 2004a), Standard Test Method for Conducting Potentiodynamic Polarization Resistance Measurements
- Alternate current impedance method according to ASTM G106–89 (ASTM International, 2004b), Standard Practice for Verification of Algorithm and Equipment for Electrochemical Impedance Measurements

The corrosion rates were calculated in accordance with ASTM G102–89 (ASTM International, 2004c), Standard Practice for Calculation of Corrosion Rates and Related Information from Electrochemical Measurements.

In practice, the corrosion rate measurements using electrochemical methods are determined in deaerated solution to avoid interference of the oxygen reduction reaction, especially for a passive system in which the passive current density is low. Because the measured or net current is the sum of the anodic current contributed from metal corrosion and the cathodic current contributed from oxygen reduction, the net current can be substantially reduced or even become cathodic when the dissolved oxygen concentration is large. For an active system in which the anodic current is high, the relative error caused by oxygen reduction is low.

A.1 Basis of the Electrochemical Methods

A.1.1 Polarization Resistance Method

The polarization resistance method is an electrochemical method that determines the amount of current density, I , obtained by polarizing the metal or alloy test specimen a few millivolts, E , from the corrosion potential, E_{corr} .

The polarization resistance, R_p , of the corroding test specimen is defined as the slope of the E versus I curve at the E_{corr} , and the resistance is related to the corrosion current density, I_{corr} , through Eq. (A-1)

$$R_p = \left. \frac{dE}{dI} \right|_{E_{\text{corr}}, \frac{dE}{dt} \rightarrow 0} = \frac{\beta_a \beta_c}{2.303 (\beta_a + \beta_c) I_{\text{corr}}} \quad (\text{A-1})$$

where

β_a and β_c — anodic and cathodic Tafel slopes in units of V/decade of current
 dE/dt — potential scan rate

After I_{corr} is obtained, the corrosion rate, CR , based on Faraday's law, is calculated according to Eq. (A-2)

$$CR = K \frac{I_{\text{corr}} EW}{\rho} \quad (\text{A-2})$$

where

K — constant with values depending on the units of other parameters in the equation
 EW — equivalent weight of the corroding metal or alloy test specimen
 ρ — density of the test specimen

In this method, the potential scan is performed within a few millivolts of the corrosion potential to avoid perturbing the system too much, which can alter the kinetics of the corrosion process and change the surface oxide film for passive metals. To avoid capacitive charging, the scan rate is sufficiently slow. A scan rate of 0.001 mV/s is usually used for passive metals, but a faster scan rate can be used for active metals.

A.1.2 Basis of Electrochemical Impedance Spectroscopy and Anodic Passive Current Density Methods

In principle, the electrochemical impedance spectroscopy and anodic polarization methods are also useful in the determination of the corrosion rate.

The electrochemical impedance spectra are usually obtained by applying a small amplitude potential (or current) perturbation to the working electrode at varying frequencies and subsequently measuring the resulting current (or potential). By scanning a wide range of frequencies, the polarization resistance of the metal can be determined by fitting the spectra to an equivalent electrical circuit model. After R_p is obtained, the corrosion rate can be calculated using Eqs. (A-1) and (A-2) as described previously. However, the data obtained by fitting to an equivalent circuit must be treated with caution, because there are no unique equivalent circuit and set of parameter values that describe the spectra. More details on this technique can be found in the literature (Scully, 1995; Cottis and Turgoos, 1999; Bard and Faulkner, 2001).

The corrosion current in Eq. (A-2) also can be estimated from the steady-state anodic current density measured in deaerated solution by polarizing the potential away from the corrosion potential.

A.2 Experimental

A.2.1 Metal Samples Preparation

The test specimens with dimensions of approximately 25 mm [1 in] (length), 25 mm [1 in] (width), and the thickness of the as-received material were cut from the as-received plates. The thickness of the as-received plates is 1.59 mm [0.0625 in]. Before measurement, the aluminum, copper, and carbon steel specimens were polished on successive grades of silicon carbide papers (320, 400, and 600 grit) and cleaned in deionized water and in acetone. The galvanized steel was cleaned only in deionized water and acetone without polishing, and all edges of the specimens were coated with microstop¹ to avoid exposure of steel to solution.

A.2.2 Electrochemical Cell

The measurements were conducted in a three-electrode electrochemical cell in N₂-deaerated solutions. The three electrodes consist of a test specimen (or working electrode), a reference electrode, and a counter electrode.

The measurements at 60 and 90 °C [140 and 194 °F] were conducted in 250-mL [0.067-gal] glass cells with Teflon lids. For tests at 60 and 90 °C [140 and 194 °F], an Alloy 825 wire, which was thermally sealed in glass tubing with an outer diameter of 9.52 mm [0.375 in], was connected to the specimen for electrical conduction. Test cells were fitted with a water-cooled condenser to minimize solution loss at elevated temperatures. A saturated calomel electrode was used as a reference electrode, and it was connected to the solution through a water-cooled Luggin probe with a porous silica tip to maintain the reference electrode at room temperature. A platinum flag was used as the counter electrode.

At 110 °C [230 °F], a stainless steel autoclave lined with Teflon was used as the test cell. The solution was deaerated with N₂ at least 1 hour before setting the temperature to 100 °C [212 °F]. The test specimen was held in solution using an Alloy 22 specimen holder, which was connected to an Alloy 22 rod shrunk in Teflon for electrical conduction. The specimen holder and the contact area between the Alloy 22 rod, specimen holder, and specimen were wrapped with Teflon tape to avoid contact with solution. A custom tungsten–tungsten oxide electrode was used as the reference electrode. Platinum was also used as the counter electrode in this test cell. The potentials of the tungsten–tungsten oxide in the same pH 10 solution used in the tests were measured at 25, 60, and 90 °C [77, 140, and 194 °F] to be -0.293, -0.443, and -0.536 V against a saturated calomel electrode maintained at room temperature. At 110 °C [230 °F], the potential was estimated to be -0.623 V_{SCE} by extrapolating to that temperature. At pH 7, the potential was calculated to be -0.445 V_{SCE} according to the Nernst equation for tungsten–tungsten oxide electrode and the potential in a pH 10 solution. Accordingly, all the applied potentials at 110 °C [230 °F] were adjusted against saturated calomel electrode, which is 0.241 V against standard hydrogen electrode at 25 °C [77 °F].

¹Stop-off lacquer. Tolber Chemical, Hope, Arkansas 71801.

A.2.3 Polarization Resistance and Cyclic Potentiodynamic Polarization

Polarization resistance measurements were conducted by measuring the current density while scanning the potential of the test specimens in the anodic direction for the range -10 to +10 mV or -20 to +10 mV, with respect to the corrosion potential. The scan rate used was 0.01 mV/s. The specimens were immersed in solution for 1 hour prior to the start of the tests. The value of the polarization resistance, R_p , was obtained by fitting a straight line to the data in the range of -5 to +5 mV with respect to the corrosion potential. The corrosion current density was calculated using Eq. (A-3)

$$i_{\text{corr}} = \frac{0.12}{2 \times 2.303 R_p} \quad (\text{A-3})$$

which was derived from Eq. (A-1), assuming values of 0.120 V/decade for the anodic and cathodic Tafel slopes, β_a and β_c (Shoesmith, 1987).

After this small linear polarization, potentiodynamic polarization was performed on the same electrode. The potential was scanned from 100 mV below the open circuit potential toward the more noble direction at a scan rate of 0.167 mV/s to 900 mV with respect to the reference electrode. Subsequently, the scanning was reversed until the potential reached -600 mV with respect to the reference electrode.

The potential and the resulting current were monitored using a computer-controlled potentiostat (Multichannel Solartron 1480).

A.2.4 Electrochemical Impedance Spectroscopy

The impedance measurements were conducted at the open-circuit potential with an alternate amplitude of ± 10 mV during the frequency range from 20 kHz to 1 mHz with 10 points per decade (Scully, 1995). The acquisition time per impedance spectrum is near 1.5 hours.

A.3 Results

A.3.1 Corrosion Rates from Polarization

Figures A-1, A-2, A-3, and A-4 show the potential versus current density plots for all four metals at 60, 90, and 110 °C [140, 194, and 230 °F] in a borated {0.259 M [2,800 ppm] boron} alkaline containment water at pH 10. From Figures A-1 and A-3, the polarization resistances for aluminum and copper were determined by linear fit to the data near the corrosion potential. For carbon steel and zinc, there was significant scatter in the polarization data (not shown here) during the range from -10 to 10 mV with respect to the corrosion potential. The scatter may be caused by the interference of electrical noise and the agitation of N₂ gas. Alternatively, the passive current densities from the potentiodynamic polarization curves shown in Figures A-2 and A-4 were used to determine the corrosion current. The data points chosen were indicated in the curves as a, b, and c. To be conservative, as indicated in point c, the larger current density in Figure A-2 was chosen as the corrosion current for carbon steel at 110 °C [230 °F]. Equations (A-2) and (A-3) were used to calculate the corrosion rates, which are summarized in

Table A-1. Measured Corrosion Rates for Aluminum, Carbon Steel, Copper, and Galvanized Steel (Zinc) in Borated Deaerated Alkaline Water at pH 10			
Metals	Corrosion Rate [g/m²·h (mil/yr)]		
	Temperature 60 °C [140 °F]	Temperature 90 °C [194 °F]	Temperature 110 °C [230 °F]
<u>Aluminum</u> Density 2.70 g/cm ³ Equivalent weight 9.66 g/mol	0.986 [126]	1.89 [241]	2.20 [281]
<u>Carbon Steel</u> Density 7.84 g/cm ³ Equivalent weight 27.9 g/mol	1.35×10^{-2} [0.594]	2.95×10^{-2} [1.30]	8.21×10^{-2} [3.61]
<u>Copper</u> Density 8.96 g/cm ³ Equivalent weight 63.5 g/mol	4.78×10^{-3} [0.184]	5.19×10^{-2} [2.00]	9.91×10^{-2} [3.82]
<u>Galvanized Steel (Zinc)</u> Density 7.13 g/cm ³ Equivalent weight 32.7 g/mol	3.57×10^{-2} [1.73]	4.05×10^{-2} [1.96]	2.34×10^{-1} [11.4]
Measured Corrosion Rates for Carbon Steel in Borated Water at pH 7			
Carbon Steel	1.27×10^{-1} [5.59]	9.36×10^{-2} [4.12]	2.14×10^{-2} [0.944]

Table A-1. The density and the equivalent weight for each metal used in the calculation also are included in Table A-1.

A similar method was used to determine the corrosion rate for carbon steel at 60, 90, and 110 °C [140, 194, and 230 °F] in a borated containment water {0.259 M [2,800 ppm] boron, and 0.17 M Na₃PO₄} at pH 7. The potential versus current density is plotted in Figure A-5. It is unclear what caused the significant open circuit potential increase by approximately 500 mV as the temperature increased from 90 to 110 °C [194 to 230 °F]. Similar results were obtained as the test at 110 °C [230 °F] was repeated. The most possible reason is attributed to oxide film property change as temperature increased to 110 °C [230 °F]. The polarization resistance was determined by linear fit to experimental data. The calculated corrosion rates are included in Table A-1 for comparison.

In a pH 7 solution, the corrosion rate of carbon steel is lower than the rate in pH 10 solution, which is consistent with that observed from the Pourbaix diagram (Macdonald and Cragnolino, 1989). The slightly alkaline solution is beneficial for carbon steel to maintain its passivity.

A.3.2 Comparison of Polarization in Aerated and Deaerated Solution

Figure A-6 shows a comparison of the potentiodynamic polarization curves for all four metals at 60 °C [140 °F] in air aerated and nitrogen deaerated borated {0.236 M [2,550 ppm] boron}

alkaline containment water at pH 10. This solution had approximately 9-percent lower boron concentration, attributed to the presence of moisture in boric acid. However, the lower boron concentration is not expected to change the comparison between aerated and deaerated solutions. Except for aluminum, the addition of oxygen increased the corrosion potentials by approximately 500 mV for carbon steel, copper, and zinc. This increase is expected because oxygen is a stronger oxidant than water. However, the polarization curves in aerated and deaerated solutions had a similar shape. The passive current densities for aluminum, carbon steel, and copper in aerated solutions, as shown in Figure A-6, were similar or slightly lower than the passive current densities in the deaerated solution. Table A-2 lists the calculated corrosion rate values in aerated and deaerated solutions. To keep consistency with data values in Table A-1, the corrosion rates for carbon steel and zinc were calculated from the potentiodynamic polarization curves (Figure A-6), whereas the corrosion rates for aluminum and copper were determined by linear fit to the data near the corrosion potential (not shown here). For zinc, the corrosion rate measured in aerated solution is slightly higher than the corrosion measured in the deaerated solution.

In summary, these metals have similar behavior in aerated and deaerated solutions at 60 °C [140 °F]. The corrosion rates measured in deaerated solution are representative for that measured in aerated solution.

A.3.3 Electrochemical Impedance Spectroscopy

Figures A-7, A-8, A-9, and A-10 are the impedance spectra for all four metals at 60, 90, and 110 °C [140, 194, and 230 °F] in a {0.236 M [2,550 ppm] boron} borated alkaline containment water at pH 10. The simplest model for a corroding metal consists of a solution resistance, R_s , a polarization resistance, R_p , and a double-layer capacitance, C_d , in parallel (Schueller and Taylor, 1993). The impedance spectra obtained for the four metals in Figures A-7, A-8, A-9, and A-10 indicate that the behavior of the four metals cannot be described simply by using the simple circuit. The presence of two time constants in aluminum, the high passivity of carbon steel, the diffusion process in copper and zinc, and the signal noise in the low-frequency region resulted in significant uncertainty in the estimation of R_p and the metal corrosion rates. The spectra for copper, carbon steel, and zinc were fitted with this simple circuit by excluding some

Table A-2. Comparison of Measured Corrosion Rates for Aluminum, Carbon Steel, Copper, and Galvanized Steel (Zinc) in Aerated and Deaerated pH 10 Alkaline Water at 60 °C [140 °F]		
Metals	Corrosion Rate [g/m ² ·h (mil/yr)]	
	Nitrogen Deaerated	Air Aerated
Aluminum	1.01 [128]	4.59 × 10 ⁻¹ [58.7]
Carbon Steel	1.15 × 10 ⁻² [0.508]	9.88 × 10 ⁻³ [0.435]
Copper	4.64 × 10 ⁻³ [0.179]	NA*
Zinc	4.21 × 10 ⁻² [2.04]	6.69 × 10 ⁻² [3.24]

*Not applicable—data are too noisy to fit, but the corrosion rate is small.

noisy data points in the low-frequency range, whereas the spectra for aluminum were fitted with a two-time constants circuit model. Table A-3 summarizes the corrosion rates determined by preliminarily fitting the spectra to the simple circuit. There are discrepancies from that measured using the direct current polarization method, Table A-1. The main reason is because of the high uncertainty in fitting the impedance spectra to the equivalent circuit.

Table A-3. Measured Corrosion Rates from Impedance Spectra for Aluminum, Carbon Steel, Copper, and Galvanized Steel (Zinc) in Deaerated Borated Alkaline Water at pH 10			
Metals	Corrosion Rate [g/m²·h (mil/yr)]		
	Temperature 60 °C [140 °F]	Temperature 90 °C [194 °F]	Temperature 110 °C [230 °F]
Aluminum	1.22 [157]	3.50 [448]	7.04 [901]
Carbon Steel	Extremely high uncertainty in fitting caused by high passivity	1.60 × 10 ⁻³ [7.04 × 10 ⁻²]	3.47 × 10 ⁻³ [1.53 × 10 ⁻¹]
Copper	1.93 × 10 ⁻² [0.742]	4.48 × 10 ⁻² [1.72]	8.68 × 10 ⁻² [3.35]
Zinc	3.42 × 10 ⁻² [1.66]	3.76 × 10 ⁻² [1.82]	2.85 × 10 ⁻² [1.38]

A.4 References

ASTM International. "Metals Test Methods and Analytical Procedures." *ASTM G59-97 (Reapproved 2003): Standard Test Method for Conducting Potentiodynamic Polarization Resistance Measurements. Volume 3.02: Wear and Erosion—Metal Corrosion.* Published on CD ROM. West Conshohocken, Pennsylvania: ASTM International. 2004a.

———. "Metals Test Methods and Analytical Procedures." *ASTM G106-89 (1999): Standard Practice for Verification of Algorithm and Equipment for Electrochemical Impedance Measurements. Volume 3.02: Wear and Erosion—Metal Corrosion.* Published on CD ROM. West Conshohocken, Pennsylvania: ASTM International. 2004b.

———. "Metals Test Methods and Analytical Procedures." *ASTM G102-89 (1999): Standard Practice for Calculation of Corrosion Rates and Related Information from Electrochemical Measurements. Volume 3.02: Wear and Erosion—Metal Corrosion.* Published on CD ROM. West Conshohocken, Pennsylvania: ASTM International. 2004c.

Bard, A.J. and L.R. Faulkner, eds. *Electrochemical Methods, Fundamentals and Applications.* 2nd Edition. New York City, New York: John Wiley & Sons, Inc. pp. 368-416. 2001.

Cottis, R. and S. Turgoos. *Electrochemical Impedance and Noise.* Houston, Texas: NACE International. 1999.

Macdonald, D.D. and G.A. Cragnolino. "Corrosion of Steam Cycle Materials." *The ASME Handbook on Water Technology for Thermal Power Systems*. P. Cohen, ed. New York City, New York: ASME. pp. 659–1,031. 1989.

Schueller, G.R.T. and S.R. Taylor. "Equivalent Circuit Modeling of Aluminum/Polymer Laminates Using Electrochemical Impedance Spectroscopy." *ASTM STP-1188: Electrochemical Impedance-Analysis and Interpretation*. J.R. Scully, D.C. Silverman, and M.W. Kendig, eds. Philadelphia, Pennsylvania: ASTM International. pp. 328–343. 1993.

Scully, J.R. *Electrochemical Corrosion Tests and Standards: Application and Interpretation*. R. Boboian, ed. Philadelphia, Pennsylvania: ASTM International. pp. 75–90. 1995.

Shoesmith, D.W. "Kinetics of Aqueous Corrosion." *Metals Handbook*. 9th Edition. Vol. 13. Metals Park, Ohio: ASM International. pp. 29–36. 1987.

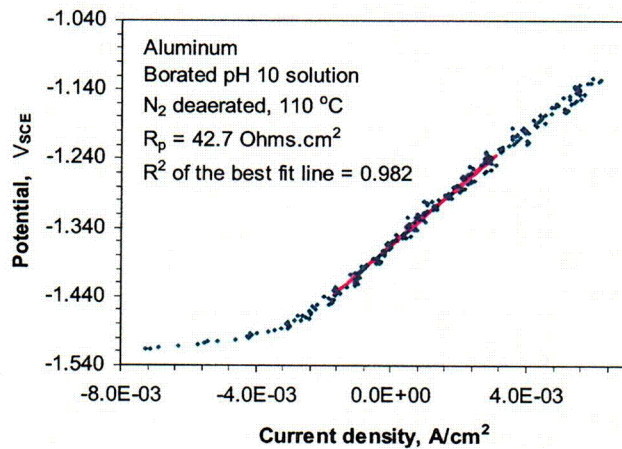
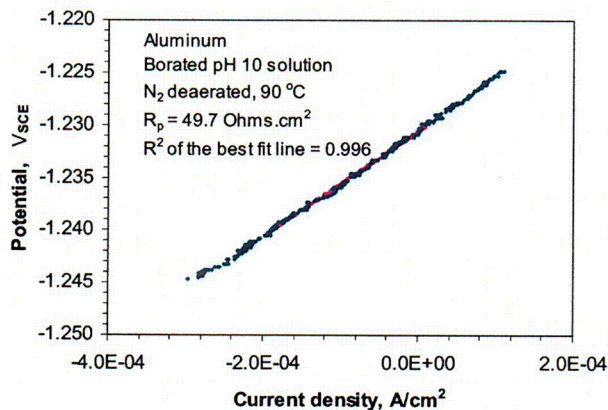
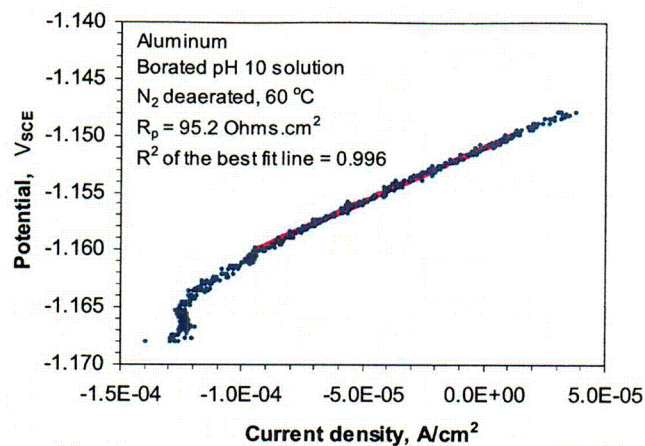


Figure A-1. Polarization Resistance Determined from Potential Versus Current Density for Aluminum in Deaerated pH 10 Sodium Hydroxide with 0.259 M [2,800 ppm] Boron at 60, 90, and 110 ° C [140, 194, and 230 ° F] Obtained Using a Scan Rate of 0.01 mV/s. Only Points within 5 mV or Less of the Corrosion Potential Were Used to Determine Polarization Resistance.

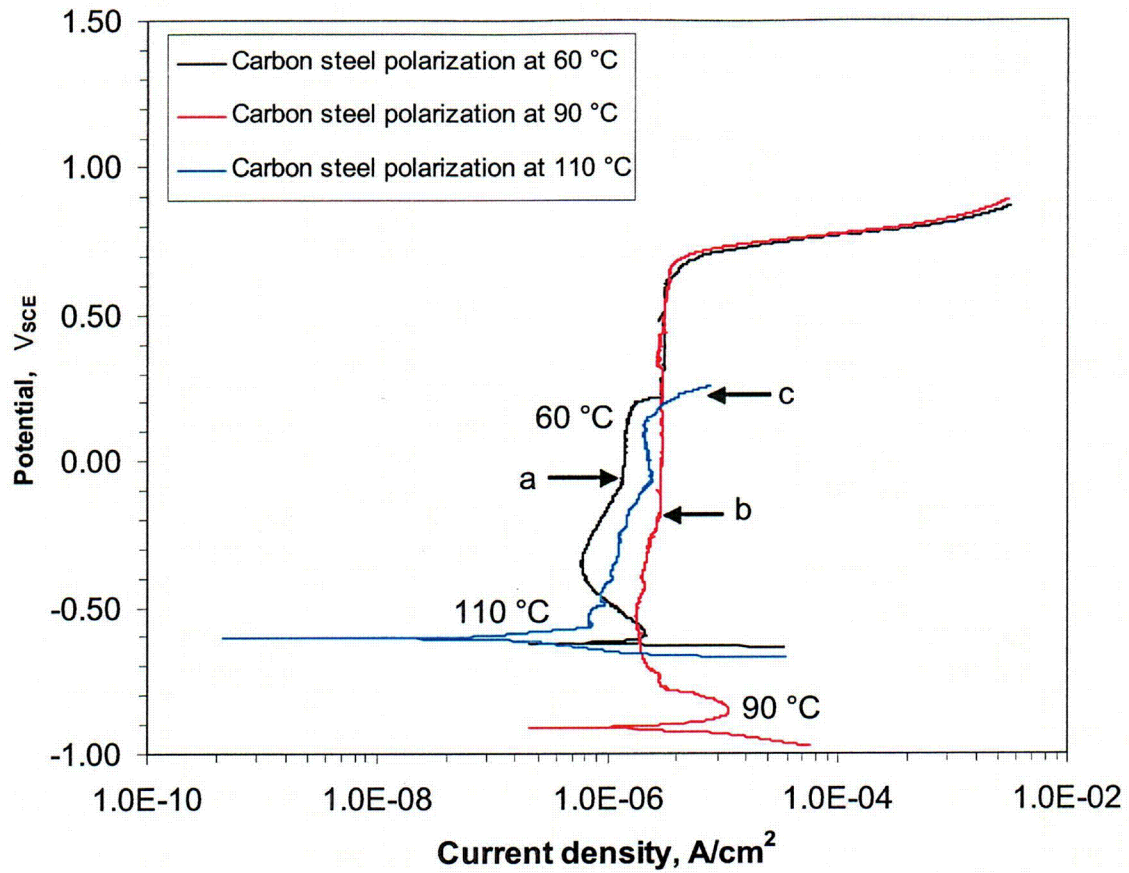


Figure A-2. Potentiodynamic Polarization Curves for Carbon Steel in Deaerated pH 10 Sodium Hydroxide with 0.259 M [2,800 ppm] Boron at 60, 90, and 110 °C [140, 194, and 230 °F] Obtained Using a Scan Rate of 0.167 mV/s. The Current Density Values at Three Data Points, a, b and c, As Indicated in the Curves Were Chosen for Calculating Corrosion Rates.

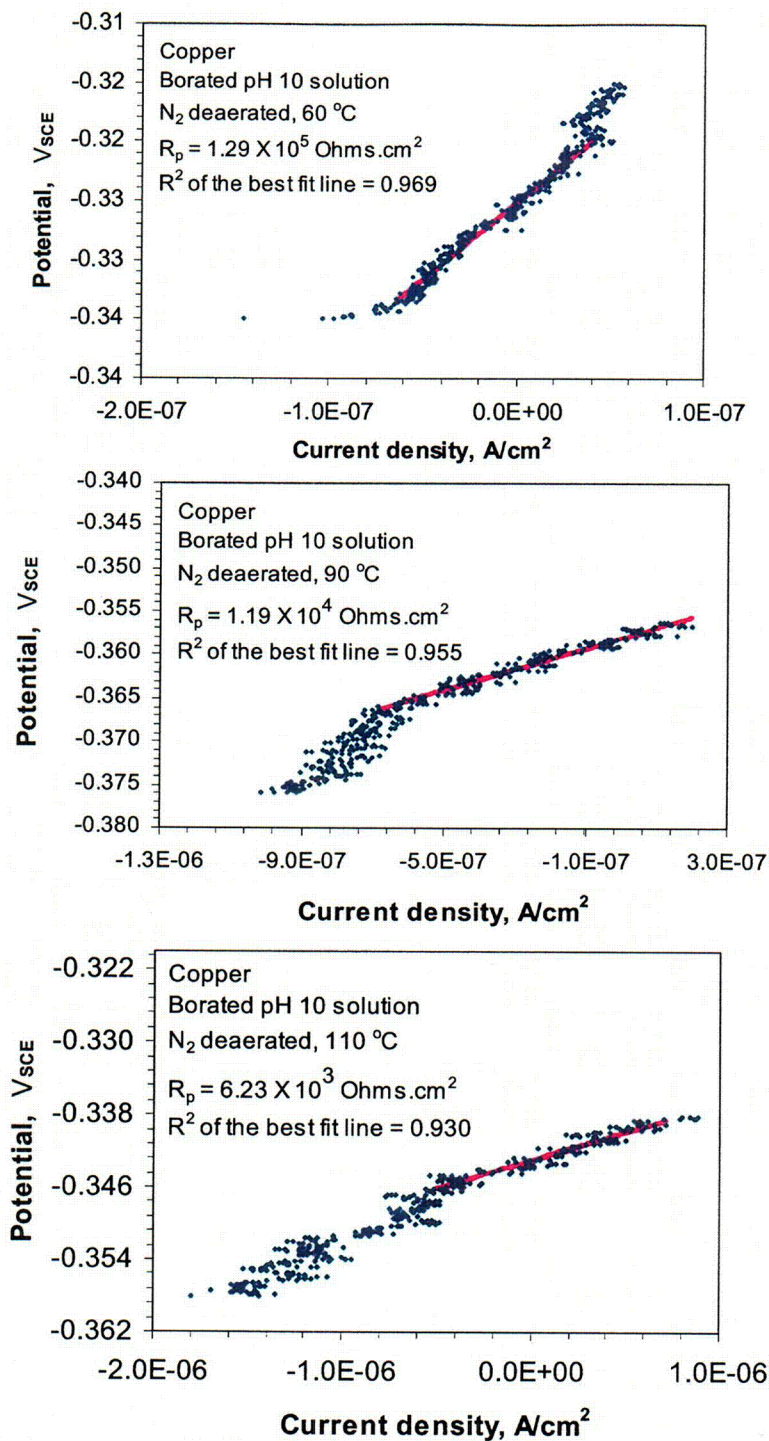


Figure A-3. Polarization Resistance Determined from Potential Versus Current Density for Copper in Deaerated pH 10 Sodium Hydroxide with 2,800 ppm Boron at 60, 90, and 110 °C [140, 194, and 230 °F] Obtained Using a Scan Rate of 0.01 mV/s. Only Points within 5 mV or Less of the Corrosion Potential Were Used to Determine Polarization Resistance.

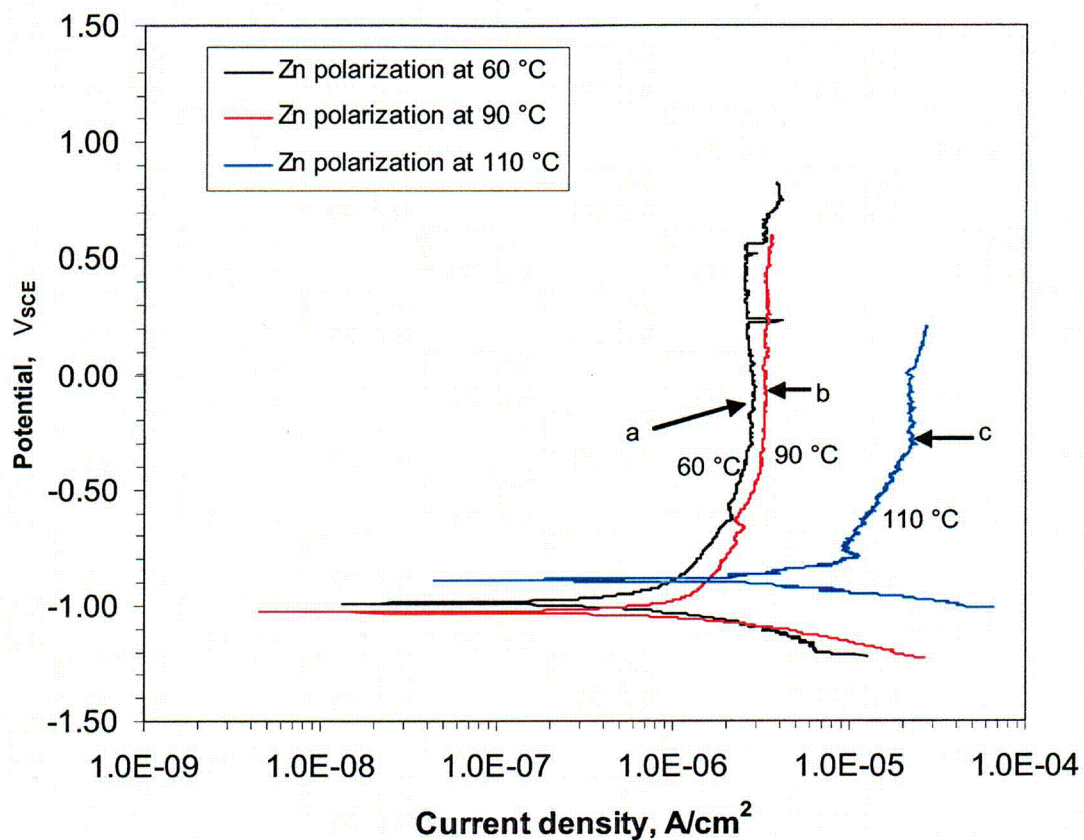


Figure A-4. Potentiodynamic Polarization Curves for Galvanized Steel (Zinc) in Deaerated pH 10 Sodium Hydroxide with 0.259 M [2,800 ppm] Boron at 60, 90, and 110 °C [140, 194, and 230 °F] Obtained Using a Scan Rate of 0.167 mV/s. The Current Density Values at Three Data Points, a, b and c, As Indicated in the Curves Were Chosen for Calculating Corrosion Rates. The Dips and Recoveries in the Curves Could Be Attributed to Temperature Fluctuations During Measurements.

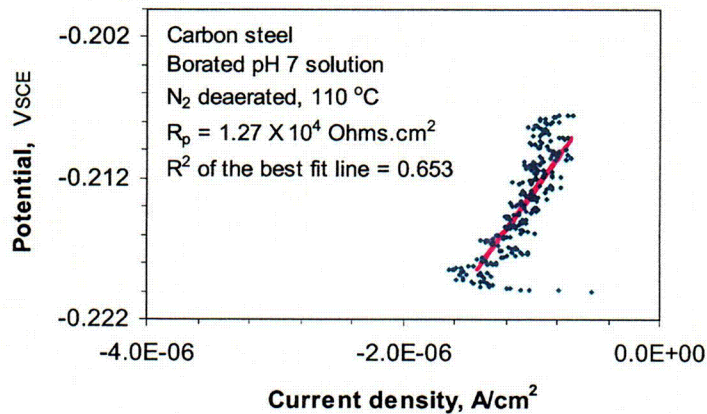
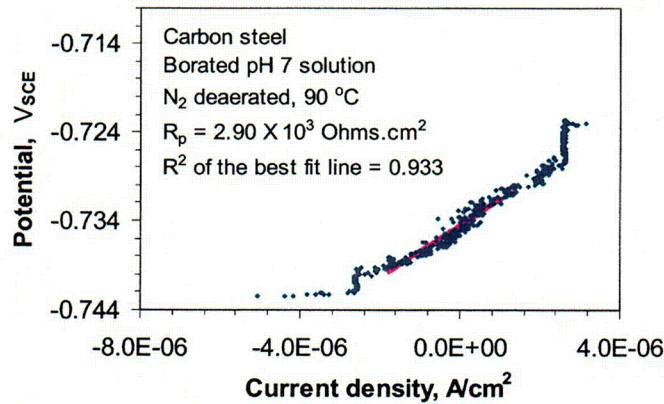
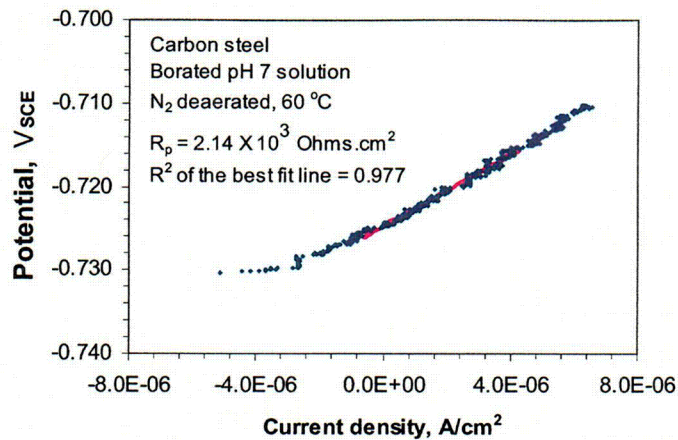


Figure A-5. Polarization Resistance Determined from Potential Versus Current Density for Carbon Steel in Deaerated pH 7 Trisodium Phosphate Solution with 0.259 M [2,800 ppm] Boron at 60, 90, and 110 °C [140, 194, and 230 °F] Obtained Using a Scan Rate of 0.01 mV/s. Only Points within 5 mV of the Corrosion Potential Were Used to Determine Polarization Resistance.

c/1

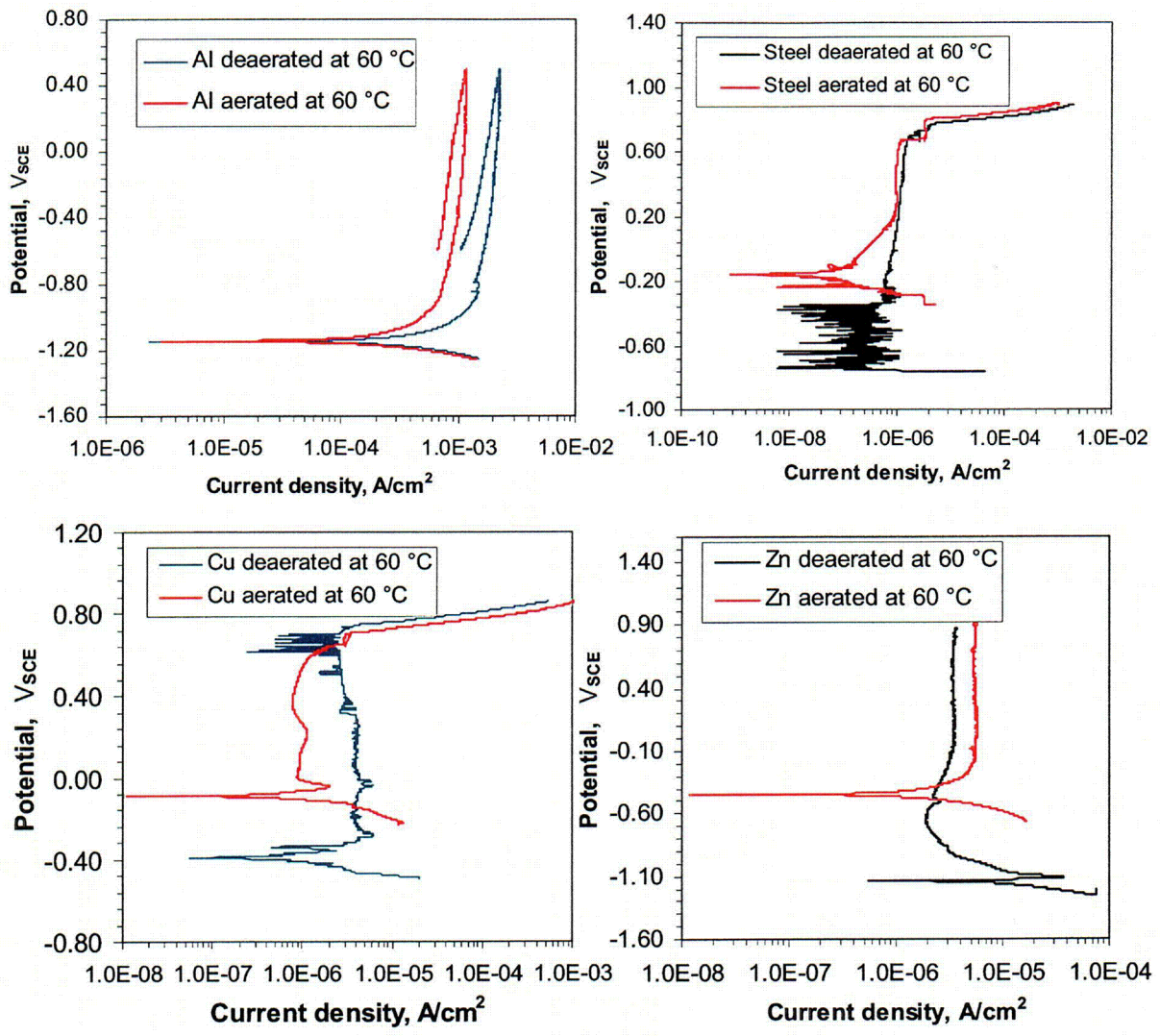


Figure A-6. Potentiodynamic Polarization Curves for Aluminum, Carbon Steel, Copper, and Zinc in Aerated and Nitrogen Deaerated pH 10 Sodium Hydroxide Solution with 0.236 M [2,550 ppm] Boron at 60 °C [140 °F]

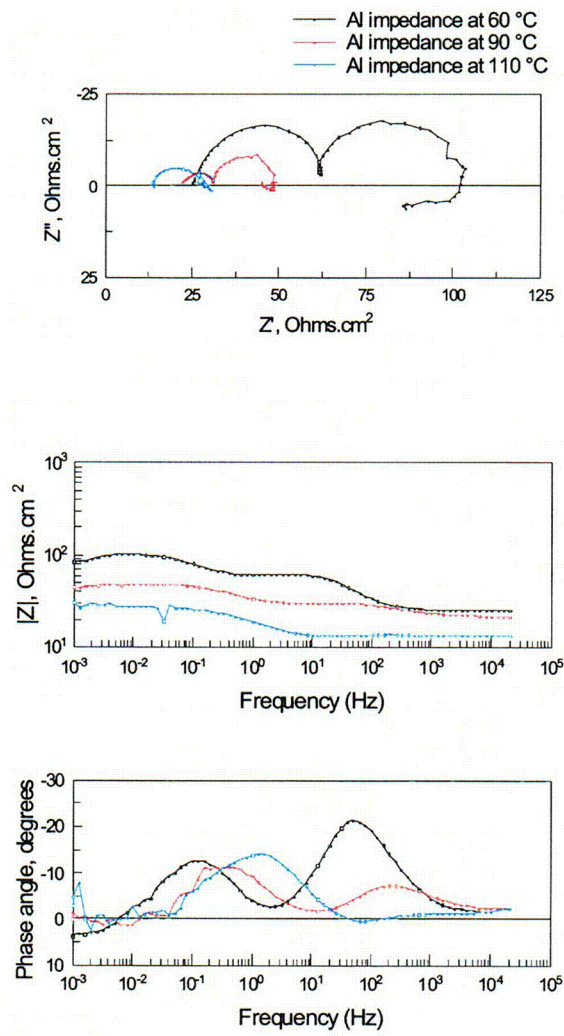


Figure A-7. Electrochemical Impedance Spectra Recorded from Potential Versus Current Density for Aluminum in Deaerated pH 10 Sodium Hydroxide with 0.236 M [2,550 ppm] Boron at 60, 90, and 110 °C [140, 194, and 230 °F]. The Spectra Indicate That the Polarization Resistance Decreases with the Increasing Temperature. Two Time Constants Equivalent Circuit Was Used to Fit the Spectra.

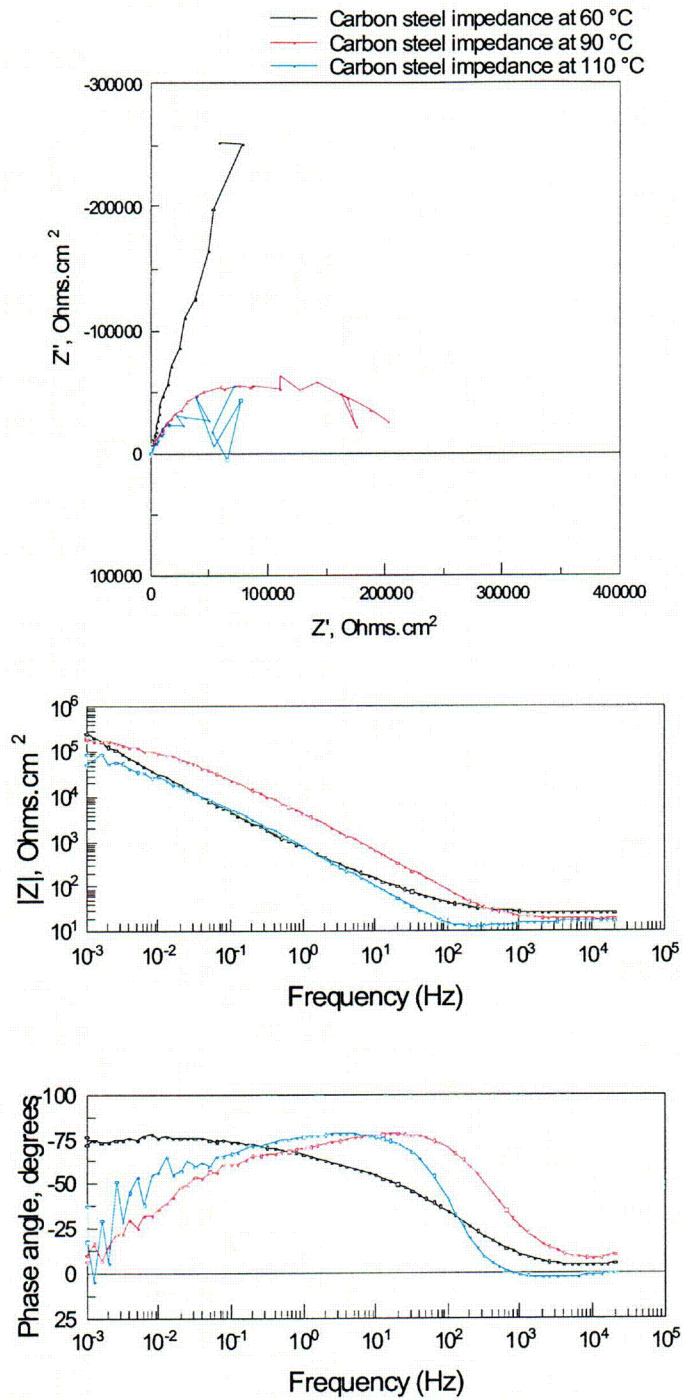


Figure A-8. Electrochemical Impedance Spectra Recorded from Potential Versus Current Density for Carbon Steel in Deaerated pH 10 Sodium Hydroxide with 0.236 M [2,550 ppm] Boron at 60, 90, and 110 °C [140, 194, and 230 °F]. The Spectra Suggest That Carbon Steel Retains High Passivity at 60 °C [140 °F].

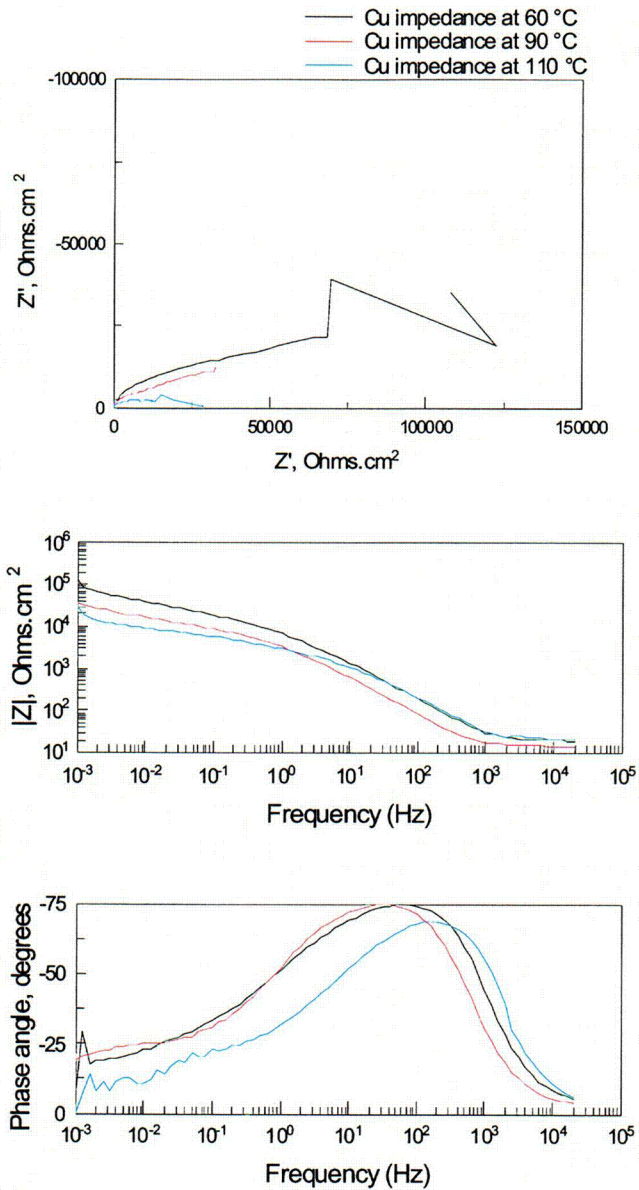


Figure A-9. Electrochemical Impedance Spectra Recorded from Potential Versus Current Density for Copper in Deaerated pH 10 Sodium Hydroxide with 0.236 M [2,550 ppm] Boron at 60, 90, and 110 °C [140, 194, and 230 °F]. The Spectra Show a Diffusion Process in the Low-Frequency Region.

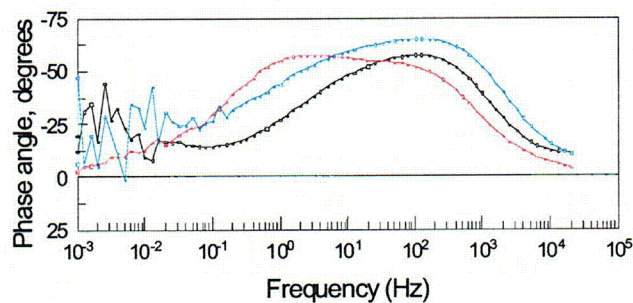
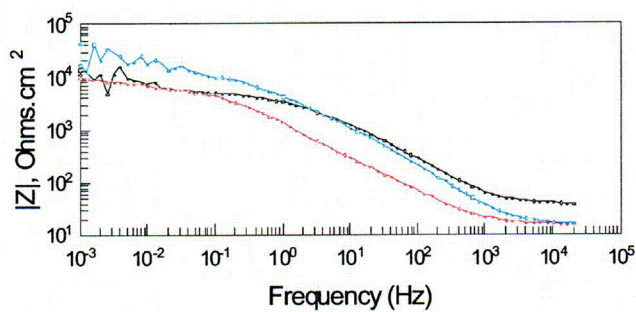
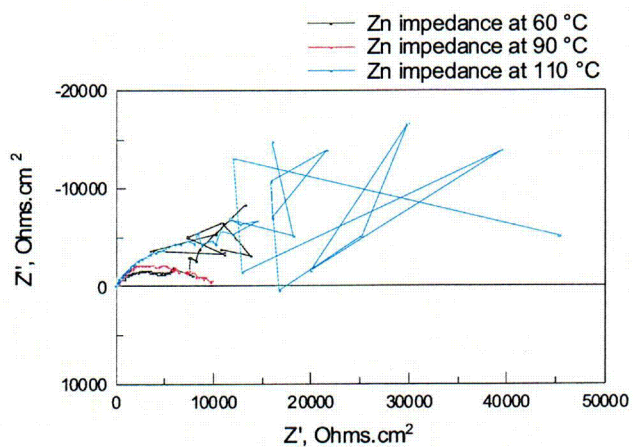


Figure A-10. Electrochemical Impedance Spectra Recorded from Potential Versus Current Density for Zinc in Deaerated pH 10 Sodium Hydroxide with 0.236 M [2,550 ppm] Boron at 60, 90, and 110 °C [140, 194, and 230 °F]. The Data in the Low-Frequency Region Are Noisy.

APPENDIX B

APPENDIX B CORROSION RATE MEASUREMENTS FOR FIBER INSULATION GLASS AND CONCRETE

The corrosion rates were determined in borated containment waters (pH 7 and 10) containing 0.259 M [2,800 ppm B] as H_3BO_3 addition at 60, 90, and 110 °C [140, 194, and 230 °F]. The pH 7 borated solution was obtained by adjusting the solution pH using trisodium phosphate in the form of $\text{Na}_3\text{PO}_4 \cdot 12\text{H}_2\text{O}$, whereas the pH 10 solution was adjusted by the addition of NaOH. The corrosion rates for fiber insulation glass were measured in both pH 7 and 10 borated containment waters. Only the pH 10 borated containment water was used for concrete corrosion rate measurements.

B.1 Experimental Methods

Bulk glass samples, provided by Owens Corning® for producing Nukon® low-density fiber insulation, were used in this study. These glass samples are referred hereafter as Nukon® glass. The composition of the Nukon® glass analyzed by inductively coupled plasma atomic emission spectrometry, as listed in Table 2-6 of this report, is similar to the composition of the low-density fiber insulation (Appendix C, Table 2-7) installed in a large number of containment buildings. A concrete block, cast with a cement/sand/aggregate ratio of 1:1.7:2.6 (by weight) and a water/cement ratio of 0.45:1 (by weight), was provided by the Electric Power Research Institute. The cement is mainly composed of 52 percent $3\text{CaO} \cdot \text{SiO}_2$, 20 percent $2\text{CaO} \cdot \text{SiO}_2$, 7 percent $3\text{CaO} \cdot \text{Al}_2\text{O}_3$, and 11 percent $4\text{CaO} \cdot \text{Al}_2\text{O}_3 \cdot \text{Fe}_2\text{O}_3$. The oxide composition of the cement is provided in Table 2-4 of this report. Figure B-1 shows the as-received Nukon® glass and concrete block samples.

The corrosion rates for Nukon® glass and concrete were determined using the static leaching method provided in ASTM Standard C-1220 (ASTM International, 2002). This method provides determination of corrosion rates without the influence of feedback effects from corrosion products. Static leaching tests for Nukon® glass and concrete were conducted in 60-ml [2.0 oz] polytetrafluoroethylene vessels using monolithic specimens. The representative Nukon® glass and concrete test specimens are displayed in Figure B-2. The test vessels were cleaned and checked for pH and fluoride release to meet the requirements specified in the test method. In all tests, a monolithic test specimen was placed in a 50-mL [1.7-oz] test solution with a geometric surface area of the specimen-to-solution volume ratio of approximately 10.0 m^{-1} . Test vessels were placed in ovens held at various temperatures and withdrawn at time intervals of 1, 3, 5, 7, and 14 days. In addition, one blank control test that did not contain a test sample in solution was carried out for 14 days for each solution-temperature combination. At the end of each test period, the vessels were removed from the ovens and allowed to cool. A small portion of the leachate was used to measure pH using a standard glass electrode and a calibrated pH meter. The leachate was then filtered with a $0.45\text{-}\mu\text{m}$ [0.018-mil] syringe filter for cation analysis using inductively coupled plasma atomic emission spectrometry.

The aforementioned leaching tests for concrete indicate that the leachate attains saturation within 1 day. Additional concrete leaching tests were conducted under low surface area-to-volume ratio conditions. In these tests, a small specimen was placed in a 125-mL [4.23-oz] test solution, resulting in a surface area of the specimen-to-solution volume ratio of

approximately 1.2 m^{-1} . The tests were performed at 60, 90, and 110 °C [140, 194, and 230 °F] for 1, 4, 8, and 24 hours.

For Nukon® glass release, the normalized elemental mass release, NR_i , based on the leached component i from the sample, was calculated using Eq. (B-1)

$$NR_i = \frac{(C_i - B_i) \times V}{F_i \times SA} \quad (\text{B-1})$$

where

- NR_i — normalized elemental mass release, in units of g/m^2
- C_i — concentration of element i in solution, in units of g/m^3
- B_i — concentration of element i in the blank solution, in units of g/m^3
- F_i — mass fraction of element i in the unleached specimen (dimensionless)
- V — volume of solution in test vessel, in units of m^3
- SA — surface area of test specimen, in units of m^2

The leaching rates were determined from the slopes of the normalized elemental mass release versus time plots.

In practice, normalization of elemental mass release using the mass fraction factor is not applicable for heterogeneous materials with different release rates for various components, such as concrete. The elemental mass release from concrete was calculated from the leaching solution concentration divided by the surface area-to-volume ratio. The leaching rates for various elements for concrete were determined from the slopes of the elemental mass release versus time curves.

B.2 Leaching Results

B.2.1 Nukon® Glass

The normalized release from Nukon® glass as a function of time at temperatures of 60, 90, and 110 °C [140, 194, and 230 °F], based on the matrix dissolution of silicon, is shown in Figure B-3 for the tests in borated containment water at pH 7 and in Figure B-4 for the pH 10 borated containment water. As evident in Figures B-3 and B-4, the silicon release from the Nukon® glass increases with increasing time, but it deviates from a linear trend for longer times. This nonlinear behavior was observed for the 110 °C [230 °F] tests in the pH 7 borated containment water and also for all tests in the pH borated containment water as a result of the extended diffusion path. The slope of the best-fit line between normalized release and time provides the leaching rate. Linear fit was obtained by using the linear portion of the curve as shown in Figures B-3 and B-4. The calculated leaching rates are given in Table B-1. It is apparent that leaching rate increases with increasing temperature in both solutions. Solution pH also has a strong influence on the leaching of Nukon® glass. At 110 °C [230 °F], a factor of 2.2 increase in leaching rate was measured in the borated containment water at pH 10, compared to the borated containment water at pH 7. This factor increases to 4.8 at a temperature of 60 °C [140 °F]. High leaching of Nukon® glass at alkaline pH is attributed to dissolution of the glass network. Because glass leaching is a thermally activated process, activation energy can be regressed from the experimental data by plotting in leaching rate versus $1/T$ as shown in

Table B-1. Measured Corrosion Rate for Nukon® Glass		
Temperature	Borated Containment Water at pH 7 (g/m ² ·h) [mil/yr]	Borated Containment Water at pH 10 (g/m ² ·h) [mil/yr]
60 °C [140 °F]	1.09 × 10 ⁻² [1.50]	4.86 × 10 ⁻² [6.71]
90 °C [194 °F]	7.56 × 10 ⁻² [10.4]	2.32 × 10 ⁻¹ [32.0]
110 °C [230 °F]	1.43 × 10 ⁻¹ [19.7]	4.53 × 10 ⁻¹ [62.6]

Figures B-3 and B-4. The activation energy values for Nukon® glass in the borated containment waters at pH 7 and 10 are 76.4 and 55.8 kJ/mol [18.2 and 13.3 kcal/mol], respectively. These values are consistent with the reported activation energies for dissolution of different glasses at various pH levels in the range of 54–84 kJ/mol [13–20 kcal/mol] (Perera, et al., 1991; Perera and Doremus, 1991).

The leached Nukon® glass samples were characterized to determine their morphology and chemical composition using optical microscopy and energy-dispersive x-ray spectroscopy. Figure B-5 shows changes in the surface conditions of the Nukon® glass after leaching for 1 day and 7 days in the pH 10 borated containment water. It is noted in Figure B-5 that while numerous small pits were observed on the glass surface immersed for one day, enhanced dissolution occurred in the sample tested for 7 days. This progressive leaching process is in agreement with the measured leaching solution concentrations. The chemical composition analysis from the near-surface regions of the corresponding glass conditions indicates the glass surface composition remained essentially unchanged after leaching in the borated containment water at pH 10. This result suggests that the extent of the leached glass surface is limited. In addition, as shown in Figure B-6, a white deposit rich in calcium and phosphorous was observed on the glass sample after leaching in the pH 7 borated containment water containing trisodium phosphate. The presence of the surface deposit which decreases the exposed surface area, may result in reduction in glass release. The significance of the deposit needs further evaluation.

To correlate the leaching behavior between bulk glass and fiber, the surfaces of the Nukon® fiberglass insulation, before and after leaching in the pH 10 borated containment water for 7 days, were examined by scanning electron microscopy. As shown in Figure B-7, although the surface of the starting fiberglass was smooth and clean, the leaching process caused severe damage to the fiberglass. Even though different modes of chemical attack as a result of leaching were observed, the leaching rates for the bulk Nukon® glass and the Nukon® low-density fiber insulation are expected to be similar because both materials have almost the identical composition (see Figure B-8), and glass composition is the primary determinant of glass dissolution.

B.2.2 Concrete

Figure B-9 shows the elemental release for aluminum, calcium, and silicon as a function of time for the concrete sample in the pH 10 borated containment water at various temperatures. As shown in Figure B-9, dissolution of calcium ions from the cement component was found to

predominate in concrete release for all temperatures. Many experiments have shown preferential leaching of calcium in the dissolution of cements as discussed by Harris, et al. (2002). The leaching results are consistent with the observed change in surface condition of the leached concrete sample, as displayed in Figure B-10. The concrete surface before leaching is shown in Figure B-1. The leaching rates from linear fits between elemental release and time for various elements and temperatures are provided in Table B-2. As temperature increases, the leaching rate for each element was observed to increase. It is apparent that corrosion of the concrete is dominated by the release of calcium. An activation energy of 22.6 kJ/mol [5.4 kcal/mol] can be obtained for the concrete material in the borated containment water at pH 10.

Table B-2. Measured Corrosion Rate for Various Elements for Concrete in Borated Containment Water at pH 10			
Element	60 °C [140 °F] (g/m ² ·h)	90 °C [194 °F] (g/m ² ·h)	110 °C [230 °F] (g/m ² ·h)
Aluminum	2.95×10^{-2}	5.93×10^{-2}	8.94×10^{-2}
Calcium	7.29×10^{-1}	1.18	2.20
Silicon	3.79×10^{-2}	1.12×10^{-1}	1.54×10^{-1}

B.3 References

ASTM International. "Nuclear, Solar, and Geothermal Energy." *ASTM C1220-98: Standard Test Method for Static Leaching of Monolithic Waste Forms for the Disposal of Radioactive Waste. Volume 12.01: Nuclear Energy (I)*. Published on CD ROM. West Conshohocken, Pennsylvania: ASTM International. 2002.

Harris, A.W., M.C. Manning, W.M. Tearle, and C.J. Tweed. "Testing of Models of the Dissolution of Cements—Leaching of Synthetic CSH Gels." *Cement and Concrete Research*. Vol. 32. pp. 731–746. 2002.

Perera, G. and R.H. Doremus. "Dissolution Rates of Commercial Soda-Lime and Pyrex Borosilicate Glasses: Influence of Solution pH." *Journal of American Ceramic Society*. Vol. 74. pp. 1,554–1,558. 1991.

Perera, G., R.H. Doremus, and W. Lanford. "Dissolution Rates of Silicate Glasses in Water at pH 7." *Journal of American Ceramic Society*. Vol. 74. pp. 1,269–1,274. 1991.

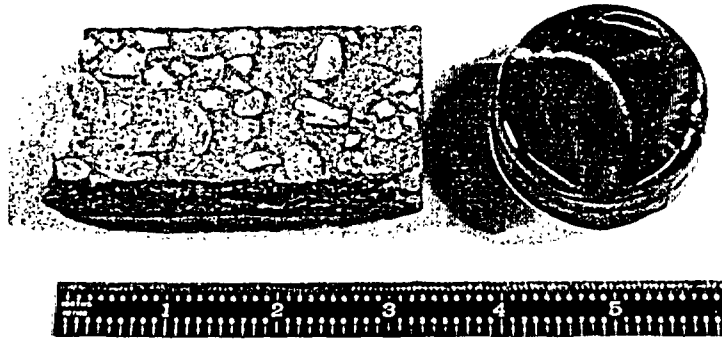


Figure B-1. Photograph Showing the As-Received Concrete Block (Left) and Nukon® Glass (Right) Samples. Scale in Inches.

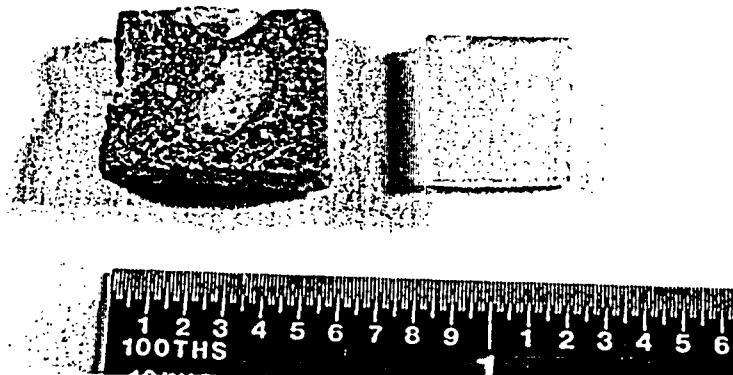


Figure B-2. Photograph Showing the Representative Nukon® Glass (Right) and Concrete (Left) Test Samples. Scale in Inches.

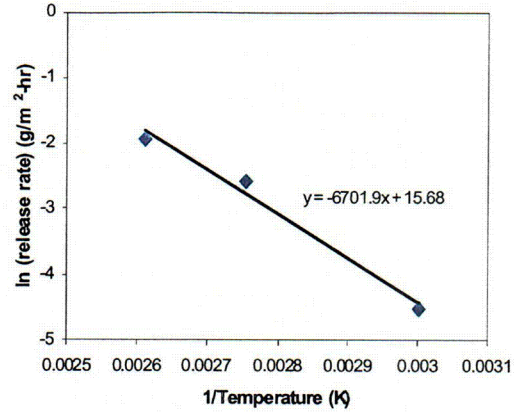
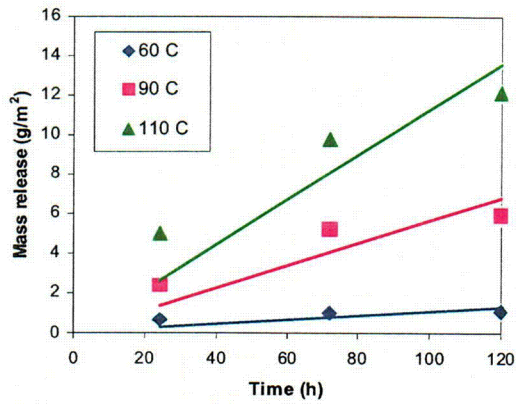


Figure B-3. Nukon® Glass Release Based on the Normalized Release for Silicon Versus Time (Left) and Linear Regression of Normalized Release Rate Versus Temperature (Right) in Borated Containment Water at pH 7

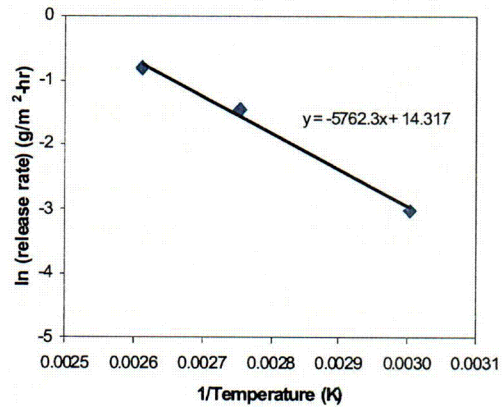
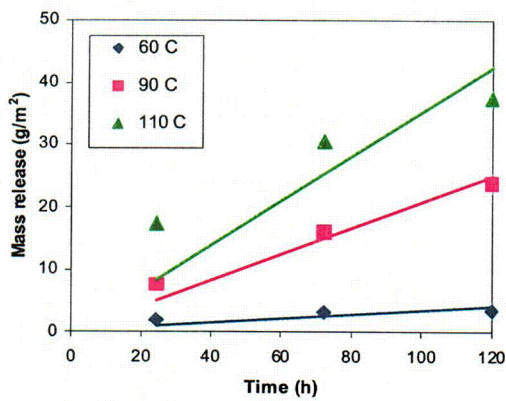


Figure B-4. Nukon® Glass Release Based on the Normalized Release for Silicon Versus Time (Left) and Linear Regression of Normalized Release Rate Versus Temperature (Right) in Borated Containment Water at pH 10

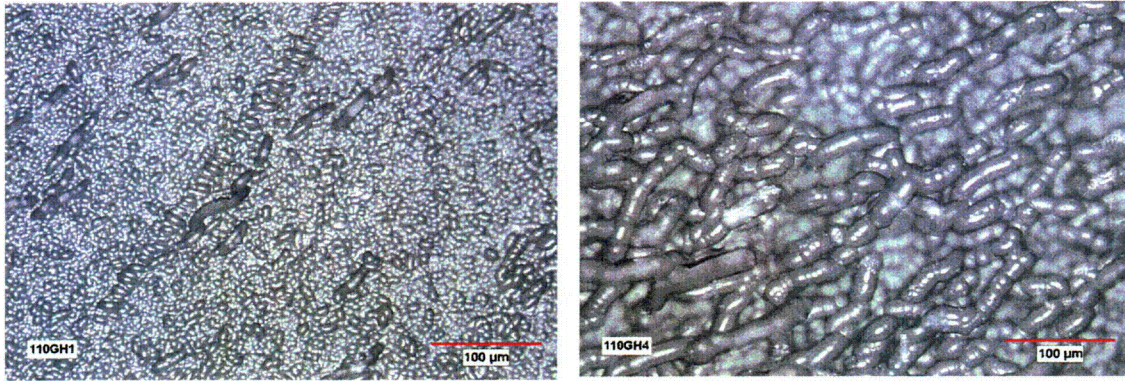


Figure B-5. Optical Microscopic Photographs Showing Changes in the Surface Conditions of the Nukon® Glass After Leaching in Borated Containment Water at pH 10 at 110 °C [230 °F] for 1 Day (Left) and 7 Days (Right)

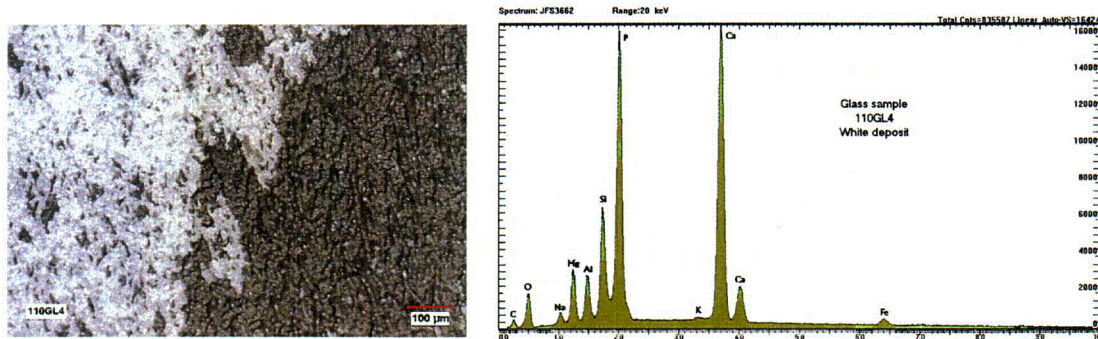


Figure B-6. Optical Microscopic Photograph Showing Surface Deposit on the Nukon® Glass After Leaching in the pH 7 Borated Containment Water Containing Trisodium Phosphate at 110 °C [230 °F] (Left) and the Energy-Dispersive X-Ray Spectrum on the Deposit (Right)

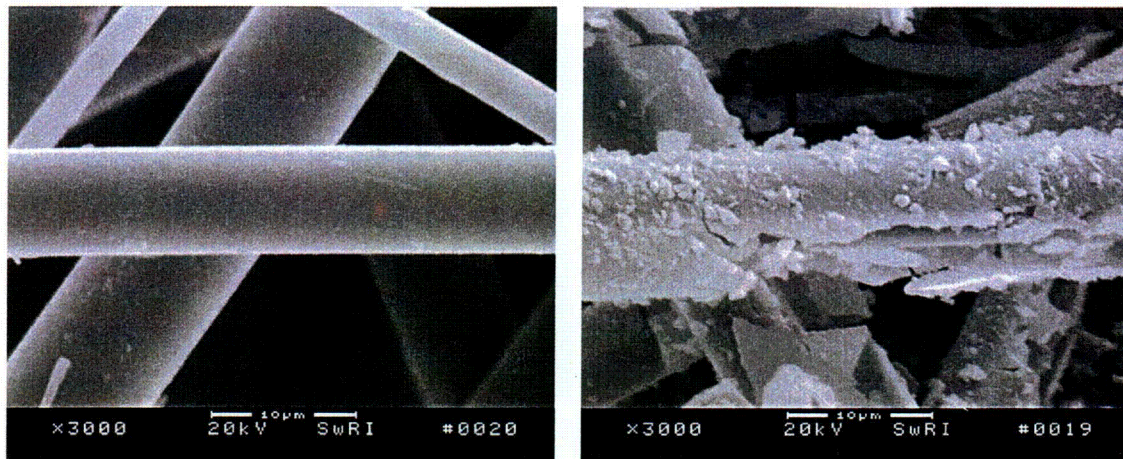


Figure B-7. Scanning Electron Micrographs of Nukon® Fiberglass Before Leaching (Left) and After Leaching in the pH 10 Borated Containment Water at 110 °C [230 °F] for 7 Days (Right)

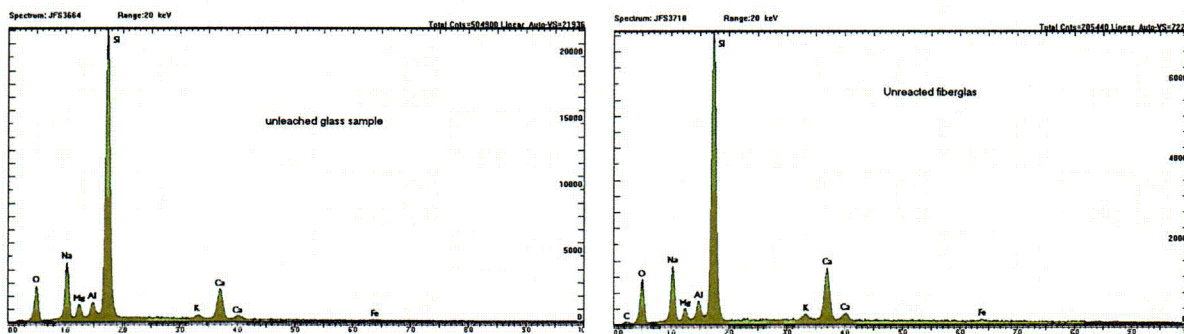


Figure B-8. Energy-Dispersive X-Ray Spectra on the Pristine Nukon® Glass (Left) and Fiberglass (Right)

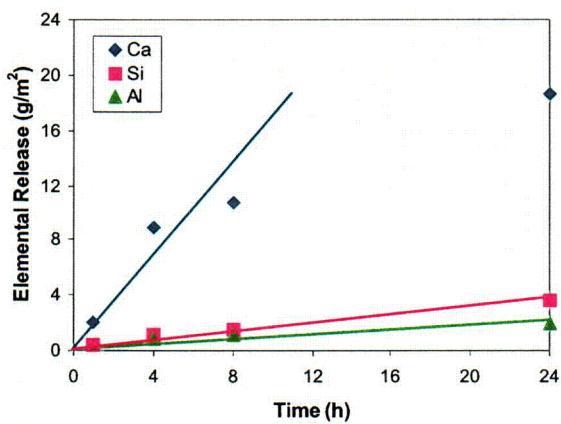
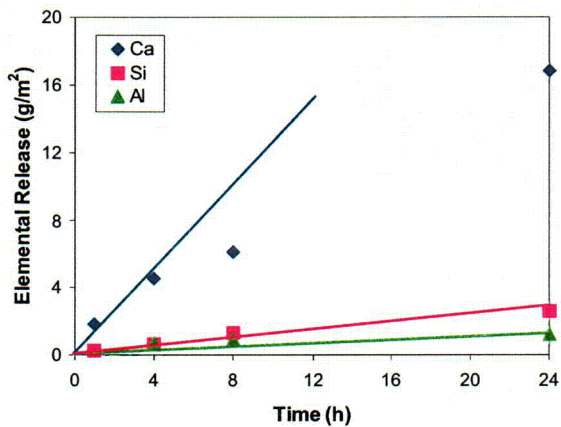
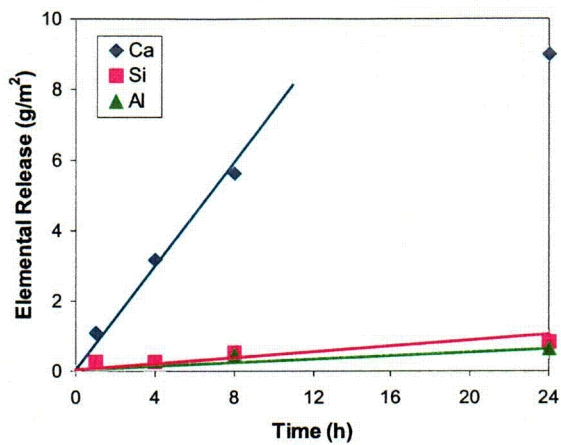


Figure B-9. Concrete Release Based on the Elemental Release Versus Time in the pH 10 Borated Containment Water at 60 °C [140 °F] (Top), 90 °C [194 °F] (Middle), and 110 °C [230 °F] (Bottom)

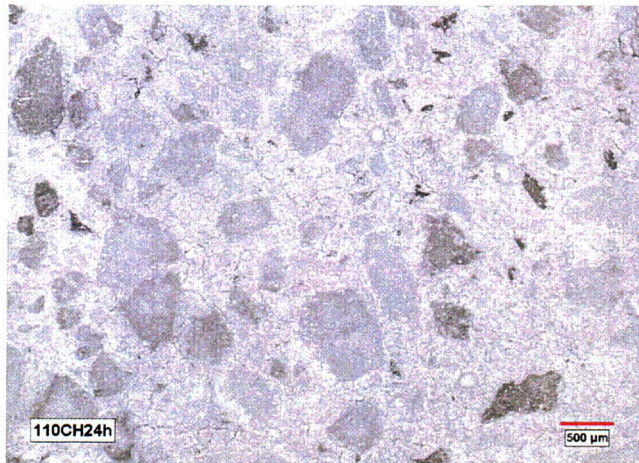


Figure B-10. Optical Microscopic Photograph Showing Change in the Surface Condition of the Concrete Sample After Leaching in the pH 10 Borated Containment Water at 110 °C [230 °F] for 24 Hours

APPENDIX C

Appendix C includes a report that provides a summary of plausible reaction products in coolant waters after a post LOCA event. Thermodynamic simulations were used to identify critical variables from a large number of components present during and subsequent to a LOCA event in the containment system. In this study, chemical speciation of plausible reaction products in sump water after a post LOCA event was modeled to (i) determine the need for a pressurized test loop and (ii) assess whether gelatinous products could form in the typical time-temperature-pressure-chemistry-pH regime following a LOCA event. The corrosion rates were based on conservative values between pH 7 and pH 10 in borated water, selected from the values published in the literature. The study provided input to parameters for the development and operation of a circulating water test loop at the University of New Mexico to study experimentally the chemical reactions from metal and insulation corrosion and to examine the formation of precipitation products including gelatinous products. This report was prepared to document work performed by the Center for Nuclear Waste Regulatory Analyses (CNWRA) for the U.S. Nuclear Regulatory Commission (NRC) under Contract No. NRC-DR-04-04-070.

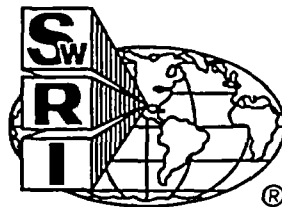
CWNRA 2004-07
Revision 1

CHEMICAL SPECIATION, USING THERMODYNAMIC MODELING, DURING A REPRESENTATIVE LOSS-OF-COOLANT ACCIDENT EVENT

Prepared for

**U.S. Nuclear Regulatory Commission
Contract NRC-DR-04-04-070**

**Center for Nuclear Waste Regulatory Analyses
San Antonio, Texas**



**CHEMICAL SPECIATION, USING THERMODYNAMIC
MODELING, DURING A REPRESENTATIVE
LOSS-OF-COOLANT ACCIDENT EVENT**

Prepared for

**U.S. Nuclear Regulatory Commission
Contract NRC-DR-04-04-070**

Prepared by

**V. Jain
L. Yang
K. Chiang**

**Center for Nuclear Waste Regulatory Analyses
San Antonio, Texas**

July 2004

CONTENTS

Section	Page
FIGURES	v
TABLES	vii
ACKNOWLEDGMENTS	ix
EXECUTIVE SUMMARY	xi
1 INTRODUCTION	1-1
2 CORROSION OF DEBRIS COMPONENTS	2-1
2.1 Zinc	2-1
2.2 Aluminum	2-3
2.3 Carbon Steel	2-5
2.4 Copper	2-6
2.5 Concrete	2-7
2.6 Fiber Insulation	2-8
3 FORMATION OF SOLID PHASES DUE TO CORROSION OF COMPONENTS IN ALKALINE CONTAINMENT WATER	3-1
3.1 Sensitivity Analyses	3-7
3.1.1 Behavior of Zinc Metal in the Simulated Containment Water	3-7
3.1.2 Behavior of Aluminum Metal in Simulated Containment Water	3-9
3.1.3 Behavior of Carbon Steel in Simulated Containment Water	3-10
3.1.4 Behavior of Concrete in Simulated Containment Water	3-10
3.1.5 Behavior of Fiber Insulation in Simulated Containment Water	3-13
4 FORMATION OF SOLID PHASES DUE TO CORROSION OF COMPONENTS IN Na ₃ PO ₄ CONTAINMENT WATER	4-1
4.1 Sensitivity Analyses	4-4
4.1.1 Behavior of Zinc Metal in the Simulated Containment Water	4-5
4.1.2 Behavior of Aluminum Metal in Simulated Containment Water	4-5
4.1.3 Behavior of Carbon Steel in Simulated Containment Water	4-8
4.1.4 Behavior of Concrete in Simulated Containment Water	4-8
4.1.5 Behavior of Fiber Insulation in Simulated Containment Water	4-10
5 EVALUATION OF A NEED TO CONDUCT EXPERIMENTS AT HIGH TEMPERATURE AND PRESSURE SYSTEM	5-1
5.1 Need to Conduct Experiments at High Temperature and Pressure System in an Alkaline Simulated Containment Water	5-1
5.2 Need to Conduct Experimental Analysis in a High-Temperature High-Pressure System in Simulated Containment Water Containing Trisodium Phosphate	5-3

CONTENTS (continued)

Section	Page
6 EVALUATION OF POTENTIAL FOR GEL FORMATION	6-1
7 SUMMARY AND CONCLUSIONS	7-1
7.1 Conclusions	7-2
8 FUTURE WORK	8-1
9 REFERENCES	9-1
APPENDIX A SOFTWARE VALIDATION AND SIMULATION METHODS	A-1
APPENDIX B TYPICAL OLI SIMULATION OUTPUT	B-1

FIGURES

Figure		Page
2-1	Surface Area Versus Diameter for Various Graphite Powders and Tokamak Dusts	2-9
3-1	Concentration, in mol/L, of Dominant Solid Phases As a Function of Temperature and Pressure in 0.26 M [2,800 ppm] Boron in an Alkaline Simulated Containment Water at pH 10	3-3
3-2	Concentration, in mol/L, of Dominant Solid Phases at 150 °C [302 °F], 507 kPa [5 atm] for 0.5 Hour at 60 °C [140 °F] for 15 Days in [2,800 ppm] Boron Alkaline Simulated Containment Water at pH 10	3-5
3-3	Dominant Solid Phases at 60 °C [140 °F], 101 kPa [1 atm] As a Function of pH	3-6
3-4	Dominant Solid Phases at 130 °C [266 °F], 304 kPa [3 atm] As a Function of pH	3-6
3-5	Dominant Solid Phases at 60 °C [140 °F], 101 kPa [1 atm] As a Function of Zinc in Simulated Containment Water at pH 10	3-8
3-6	Dominant Solid Phases at 130 °C [266 °F], 101 kPa [1 atm] As a Function of Zinc in Simulated Containment Water at pH 10	3-8
3-7	Dominant Solid Phases at 60 °C [140 °F], 101 kPa [1 atm] As a Function of Aluminum Metal in Simulated Containment Water at pH 10	3-11
3-8	Dominant Solid Phases at 130 °C [266 °F], 304 kPa [3 atm] As a Function of Aluminum Metal in Simulated Containment Water at pH 10	3-11
3-9	Dominant Solid Phases at 60 °C [140 °F], 101 kPa [1 atm] As a Function of Iron in Simulated Containment Water at pH 10	3-12
3-10	Dominant Solid Phases at 130 °C [266 °F], 304 kPa [3 atm] As a Function of Iron in Simulated Containment Water at pH 10	3-12
3-11	Dominant Solid Phases at 60 °C [140 °F], 101 kPa [1 atm] As a Function of Ca ₂ SiO ₄ in Simulated Containment Water at pH 10	3-14
3-12	Dominant Solid Phases at 130 °C [266 °F], 304 kPa [3 atm] As a Function of Ca ₂ SiO ₄ in Simulated Containment Water at pH 10	3-14
3-13	Dominant Solid Phases at 60 °C [140 °F], 101 kPa [1 atm] at Different Fiber Insulation Concentrations in Simulated Containment Water at pH 10	3-15
3-14	Dominant Solid Phases at 130 °C [266 °F], 304 kPa [3 atm] at Different Fiber Insulation Concentrations in Simulated Containment Water at pH 10	3-15
4-1	Concentration, in mol/L, of Dominant Solid Phases As a Function of Temperature and Pressure in 0.26 M [2,800 ppm] Boron in Na ₃ PO ₄ Simulated Containment Water at pH 7	4-2
4-2	Concentration, in mol/L, of Dominant Solid Phases at 150 °C [302 °F], 507 kPa [5 atm] for 0.5 Hour at 60 °C [140 °F] for 15 Days in a 0.26 M [2,800 ppm] Boron, Na ₃ PO ₄ Simulated Containment Water at pH 7	4-4
4-3	Dominant Solid Phases at 60 °C [140 °F], 101 kPa [1 atm] As a Function of Zinc in Simulated Containment Water at pH 7	4-6
4-4	Dominant Solid Phases at 130 °C [266 °F], 304 kPa [3 atm] As a Function of Zinc in Simulated Containment Water at pH 7	4-6

FIGURES (continued)

Figure		Page
4-5	Dominant Solid Phases at 60 °C [140 °F], 101 kPa [1 atm] As a Function of Aluminum in Simulated Containment Water at pH 7	4-7
4-6	Dominant Solid Phases at 130 °C [266 °F], 304 kPa [3 atm] As a Function of Aluminum Concentration in Simulated Containment Water at pH 7	4-7
4-7	Dominant Solid Phases at 60 °C [140 °F], 101 kPa [1 atm] As a Function of Iron Concentration in Simulated Containment Water at pH 7	4-9
4-8	Dominant Solid Phases at 130 °C [266 °F], 304 kPa [3 atm] As a Function of Iron Concentration in Simulated Containment Water at pH 7	4-9
4-9	Dominant Solid Phases at 60 °C [140 °F], 101 kPa [1 atm] As a Function of Ca ₂ SiO ₄ in Simulated Containment Water at pH 7	4-11
4-10	Dominant Solid Phases at 130 °C [266 °F], 304 kPa [3 atm] As a Function of Ca ₂ SiO ₄ in Simulated Containment Water at pH 7	4-11
4-11	Dominant Solid Phases at 60 °C [140 °F], 101 kPa [1 atm] at Different Fiber Insulation Concentrations in Simulated Containment Water Containing Na ₃ PO ₄ ...	4-12
4-12	Dominant Solid Phases at 130 °C [266 °F], 101 kPa [1 atm] at Different Fiber Insulation Concentrations in Simulated Containment Water Containing Na ₃ PO ₄ ...	4-13
6-1	Silicon and Aluminum Tetrahedra Units	6-2
6-2	A Basic Alkali Aluminosilicate Structural Unit	6-2
6-3	A Polymeric Poly(Sialate-Siloxo) Unit	6-2
6-4	A Polymeric Poly(Sialate-Disiloxo) Unit	6-2

TABLES

Table	Page
1-1	Sources of Debris on the Sump Screen and Strainers 1-2
1-2	Solids from Bottom Containment Water 1-3
2-1	Summary of Corrosion Rate Data for Zinc and Galvanized Zinc 2-2
2-2	Estimation of Zinc in Simulated Containment Water 2-3
2-3	Summary of Corrosion Rate Data for Aluminum 2-4
2-4	Estimation of Aluminum in Simulated Containment Water 2-5
2-5	Summary of Corrosion Rate Data for Carbon Steel 2-6
2-6	Estimation of Carbon Steel in Simulated Containment Water 2-7
2-7	Summary of Corrosion Rate Data for Copper 2-7
2-8	Estimation of Copper in Simulated Containment Water 2-8
2-9	Estimation of Concrete (Non-Particulate) in Simulated Containment Water 2-9
2-10	Estimation of Concrete (Particulate) in Simulated Containment Water 2-10
2-11	Chemical Composition of Nukon® Fiber Insulation 2-10
2-12	Estimation of Fiber Insulation in Simulated Containment Water 2-11
2-13	Estimation of Fiber Glass in the Nukon® Insulation in Simulated Containment Water 2-11
3-1	Input Values Per Liter of Solution for Simulations 3-1
3-2	pH and Redox Potential [Eh (V_{SHE})] of Simulated Containment Water 3-2
3-3	Percent Element Distribution in Solid Phases at pH 10 3-3
3-4	Percent Solid Phases at pH 10 3-4
4-1	pH and Redox Potential [Eh (V_{SHE})] of Simulated Containment Water 4-1
4-2	Percent Element Distribution in Solid Phase at pH 7 4-2
4-3	Percent Solid Phases at pH 7 4-3
7-1	Comparison of Constituents in pH = 7 and pH = 10 Containment Solutions 7-5

ACKNOWLEDGMENTS

This report was prepared to document work performed by the Center for Nuclear Waste Regulatory Analyses (CNWRA) for the U.S. Nuclear Regulatory Commission (NRC) under Contract No. NRC-DR-04-04-070. The activities reported here were performed on behalf of the NRC Office of Nuclear Regulatory Research, Division of Engineering Technology. This report is an independent product of CNWRA and does not necessarily reflect the views or regulatory position of NRC.

The authors gratefully acknowledge the technical reviews of Y.-M. Pan and D. Dunn, editorial reviews by P. Mackin and J. Pryor, and the programmatic review of B. Sagar. Appreciation is due J. Gonzalez for assistance in preparing this report.

QUALITY OF DATA: Sources of data are referenced in each chapter. CNWRA-generated data contained in this report meet quality assurance requirements described in the CNWRA Quality Assurance Manual. Data from other sources, however, are freely used. The respective sources of non-CNWRA data should be consulted for determining levels of quality assurance. Experimental data have been recorded in CNWRA scientific notebook number 642.

ANALYSES AND CODES: StreamAnalyzer Version 1.2[®] (2002a) and Environmental Simulation Program (ESP) Version 6.6[®] (OLI Systems, Inc., 2002b) were used for the thermodynamic simulations. These codes are controlled according to the requirements of CNWRA Technical Operating Procedure (CNWRA, 2003). Detailed calculations can be found in scientific notebook numbers 652E and 572.

References

CNWRA. "Development and Control of Scientific and Engineering Software." Technical Operating Procedure—TOP-018. Rev. 8, Change 2. San Antonio, Texas: CNWRA. 2003.

OLI Systems, Inc. "StreamAnalyzer Version 1.2." Morris Plains, New Jersey: OLI Systems, Inc. 2002a.

———. "Environmental Simulation Program Version 6.6." Morris Plains, New Jersey: OLI Systems, Inc. 2002b.

EXECUTIVE SUMMARY

A loss-of-coolant accident (LOCA) event results in rapid changes in the time-temperature-pressure-chemistry-pH conditions in the containment environment of nuclear reactors. Changes in the coolant chemistry are further complicated because of the interactions of the materials present inside the containment. These complex interactions require a large number of experiments to obtain sufficient data to analyze the potential impact on a sump screen blockage caused by chemical precipitation. Thermodynamic simulations, using thermodynamic simulation software allow the identification of critical variables and their ranges from a large number of constituents present, during, and following a LOCA event in the containment system. This study modeled chemical speciation of plausible reaction products in containment water after a representative LOCA event to (i) determine the need for a pressurized test loop, (ii) assess whether gelatinous products could form in the typical time-temperature-pressure-chemistry-pH regime following a LOCA event, and (iii) validate OLI Systems, Inc. software (OLI Systems, Inc., 2002a,b) for speciation in borated waters.

Computational thermodynamics simulation calculations were conducted using Environmental Simulation Program (ESP) Version 6.6[®] (OLI Systems, Inc., 2002a) and StreamAnalyzer Version 1.2[®] (OLI Systems, Inc., 2002b).

Key components in chemical speciation simulation were copper, carbon steel, zinc, aluminum, fiber insulation, and concrete in 0.26 M [2,800 ppm] boron solution. The surface areas exposed during a LOCA event for these components were provided by the U.S. Nuclear Regulatory Commission, and corrosion rates for these components from literature data were used to estimate amounts of corrosion.

The influence of pressure, temperature, and pH on chemical speciation was studied by speciating a fixed amount of each component based on its corrosion rate. These amounts were speciated at 150 °C [302 °F] at 507 kPa [5 atm], 130 °C [266 °F] at 304 kPa [3 atm], and 90 °C [194 °F] and 60 °C [140 °F] at 101 kPa [1 atm]. The formation of solid phases as a function of temperature and pressure was examined at pH 10 and 7. A pH of 10 was obtained by the addition of 0.23 mol/L sodium hydroxide [5,300 ppm sodium], and a pH of 7 was obtained by the addition of 8.4×10^{-3} mol/L Na_3PO_4 [630 ppm sodium]. The corrosion rate was selected based on conservative values obtained between pH 7 and 10 in borated water. The temperature-dependent data were not available in most cases. Therefore, the sensitivity analysis was conducted over a wide range of amounts of each component to evaluate the effect of temperature on speciation. Furthermore, uncertainties exist in the estimation of the surface area for concrete particulates. The NRC Test Plan, Revision 12b (NRC, 2005), provides the amount of concrete particulates per unit volume but the information on the size and size distribution is not available to estimate exposed surface area. While relevant data could improve prediction of solid phases, the simulations presented in this study demonstrate the potential of solid phase corrosion products covering a wide range of components present in a containment system.

In alkaline solutions silicates are major corrosion products. A strong influence of pH and temperature was observed in the formation of the dominant solid phases in the simulated containment water. A review of the simulation data and the associated sensitivity analysis in alkaline simulated containment water at pH 10 indicates $\text{NaAlSi}_3\text{O}_8$, $\text{Ca}_3\text{Fe}_2\text{Si}_3\text{O}_{12}$, and $\text{Fe}_3\text{Si}_2\text{O}_5(\text{OH})_4$ are dominant solid phases that contribute to more than 90 percent of the solid

phases formed between 150 °C [302 °F], 507 kPa [5 atm], and 60 °C [140 °F], 101 kPa [1 atm]. Despite iron phase changes, most of the iron remained a solid. Based on the simulations, it can be inferred that minimal changes in the solid phase formation are expected as high temperature and pressure conditions during the initial stages of a LOCA event approach steady-state conditions. Therefore, testing under high temperature and pressure conditions is not necessary.

A review of the simulation data and the associated sensitivity analyses in Na₃PO₄ simulated containment water at pH 7 indicates significant differences in the solid phase formation in Na₃PO₄ simulated containment water at pH 10. At pH 7, Ca₅(OH)(PO₄)₃ was the dominant solid phase, containing approximately 100 percent of calcium; while at pH 10, calcium was approximately 1 percent insoluble at 60 °C (140 °F). Irrespective of temperature and pressure, more than 90 percent of the solids precipitated as Ca₅(OH)(PO₄)₃ and NaAlSi₃O₈. Both iron and zinc showed a decrease in solid phase concentration with a decrease in temperature and pressure. The contribution of zinc was below 2 percent and iron below 9 percent compared to the total solid phases. Based on these simulations, it can be inferred that minimal changes in solid phase formation are expected as high temperature and pressure conditions during the initial stages of a LOCA event approach steady-state conditions.

A review of the literature about geopolymers and glass indicates that, in alkaline solutions, aluminosilicate unit can react with an alkali silicate unit to form polysialate (-Si-O-Al-O-), poly(sialate-siloxo) (-Si-O-Al-O-Si-O-), or poly(sialate-disiloxo) (-O-Si-O-Al-O-Si-O-Si-O-) polymers. These polysialates condense as gels similar to organic polymers at temperatures below 100 °C [212 °F]. Gel formation, a precursor to polymerization, occurs in an alkaline solution when silicon, aluminum, and alkali ions are present. Gelling, however, requires an alkaline pH. Therefore, gel is likely to form in alkaline simulated containment water.

OLI Systems, Inc. software was validated by comparing simulation results with data on borated water published in the literature and with results of solubility type experiments using borated water containing CaCO₃ or ZnCO₃ in the temperature range of 25°C [77°F] to 130°C [266°F]. Data showed a good agreement between published literature and OLI Systems, Inc. simulation. Except for ZnCO₃ at 130°C [266°F], the experimentally measured solubility data agreed with the OLI Systems, Inc. simulation results for the dominant solid or soluble phases, including aqueous H₃BO₃, aqueous NaOH, and solid CaCO₃ or solid ZnCO₃. A large variation was observed for soluble phases of zinc and calcium and was attributed to the variation and uncertainty in published data used in OLI Systems, Inc. software database.

Suggestions for future work include deriving a better understanding of corrosion rates.

REFERENCES

NRC. "Test Plan: Characterization of Chemical and Corrosion Effects Potentially Occurring During a Pressurized Water Reactor LOCA." Rev. 12b. ML050450478. Washington, DC: NRC. 2004.

OLI Systems, Inc. "Environmental Simulation Program Version 6.6." Morris Plains, New Jersey: OLI Systems, Inc. 2002a.

———. "StreamAnalyzer Version 1.2." Morris Plains, New Jersey: OLI Systems, Inc. 2002b.

1 INTRODUCTION

On March 29, 1979, the activation of the emergency core cooling system (ECCS) at the Three-Mile Island nuclear reactor resulting from the pressure-operated relief valve being stuck in the open position led to a release of 2,158 m³ [570,000 gal] of water, including 712 m³ [188,000 gal], of Susquehanna River water, into the reactor building basement. One-hundred fifty-three days after this loss-of-coolant-accident event (LOCA), a green gelatinous precipitate material was observed on the floors and walls of the containment building. The July 28, 1992, LOCA at Barseback-2 nuclear power plant led to ECCS failure due to plugging of the sump pump. Consequently, the U.S. Nuclear Regulatory Commission (NRC) examined the strainer performance of U.S. boiling water reactors. The NRC required boiling water reactor licensees to install suction strainers with larger surface areas and, for pressurized water reactors, NRC issued Generic Safety Issue (GSI)-191, Assessment of Debris Accumulation on Pressurized Water Reactor Sump Performance.

During a potential LOCA event within the containment of a light-water reactor, materials in the vicinity of a pipe break could dislodge, react chemically, and be transported to the containment floor. Typical materials in these areas include fiber insulation, concrete, paints, galvanized steel, scaffolding, and insulation jackets. Some of this debris could eventually accumulate on the recirculation-sump screens or strainers and challenge the ECCS and containment spray system pumps. Table 1-1 shows the sources of various debris material and associated corrosion products.

Using laboratory tests, Johns, et al. (2003) studied the conditions that could lead to formation of a gelatinous material similar to that observed on the Three Mile Island nuclear reactor floor and walls. This study, however, did not examine elements such as copper, nickel, magnesium, sulfur, and chromium that were found in the gelatinous phase. Table 1-2 shows the composition of the solids found at the bottom of the containment building at the Three-Mile Island nuclear reactor. The high copper content is speculated to originate from the river water. Copper concentration in the Susquehanna River water, however, is three to five orders of magnitude lower than the concentration found in the containment system. Uncertainties associated with the corrosion rates of materials shown in Table 1-1 and the composition of solids found in the containment building shown in Table 1-2 make it difficult to define the origin of the gelatinous material.

The primary objective of this project is to thermodynamically model the chemical speciation of plausible reaction products in coolant waters after a representative LOCA event to (i) determine if an experimental pressurized loop test is needed to evaluate precipitation behavior during initial LOCA conditions (Chapter 5); (ii) assess whether gelatinous products could form in the typical time-temperature-pressure-chemistry-pH regime following a LOCA event (Chapter 6); and (iii) validate OLI Systems, Inc. software (OLI Systems, Inc, 2002a,b) for speciation in borated waters (Appendix A). The formation of gelatinous material is inferred from the solids observed in the thermodynamic calculations.

This study also provides input to parameters for the development and operation of a circulating water test loop. The test loop is being constructed at the University of New Mexico to study experimentally chemical reactions from metal corrosion and insulation leaching, and examine the formation of precipitation products including gelatinous products.

Table 1-1. Sources of Debris on the Sump Screen and Strainers	
Sources	Corrosion/Erosion Products
Scaffold/insulation jackets	Aluminum, zinc
Insulation fibers	Silicon, aluminum, calcium, magnesium, boron, alkalis
Steel	Iron, nickel, sulfur
Galvanized steel	Zinc, iron
Concrete	Calcium, silicon
Cooling water	Boron, lithium
River water	Organics
pH adjusters	Trisodium phosphate, hydrochloric acid, sodium hydroxide
Heat exchangers, fan coolers, instrument-air lines	Copper

Table 1-2. Solids from Bottom Containment Water— Three Mile Island (Parts Per Million on Total Volume of Bottom Sample)*	
Silver	8.0
Aluminum	8.0
Boron	3.0
Calcium	2.0
Cadmium	< 0.5
Cobalt	< 0.1
Chromium	2.0
Cesium	< 0.5
Copper	54.0
Iron	10.0
Iodine	0.7
Indium	0.3
Potassium	1.0
Lithium	< 0.3
Magnesium	7.0
Manganese	1.0
Molybdenum	< 1.0
Sodium	< 1.0
Nickel	10.0
Phosphorus	0.4
Rubidium	< 0.3
Sulfur	5.0
Strontium	< 0.2
Tellurium	< 0.2
Titanium	0.5
Zinc	2.0
Uranium	0.106
Plutonium	0.00016
*NRC RFP No. RS-RES-04-070	

2 CORROSION OF DEBRIS COMPONENTS

Table 1-1 lists source of various debris material and associated corrosion products. In this section, corrosion rates and their expected corrosion product accumulations are estimated based on the surface area exposed as defined in the NRC Test Plan, Revision 12b: Characterization of Chemical and Corrosion Effects Potentially Occurring During a Pressurized Water Reactor LOCA (NRC, 2005).

2.1 Zinc

In a containment building, zinc is present in galvanized steel and zinc based protective coatings. Zinc coatings are top coated with a design basis accident qualified epoxy or a modified phenolic-epoxy. These top-coated zinc paints do not readily participate in chemical reactions. However, a small fraction of noncoated zinc paints could release zinc into solution.

Griess and Bacarella (1969), Niyogi, et al. (1982), Piippo, et al. (1997), and Johns, et al. (2003) have examined the corrosion rate of zinc. Griess and Bacarella (1969) measured corrosion rate of galvanized steel and zinc metal in 0.28 M [3,000 ppm] boron with 0.15 M sodium hydroxide [3,450 ppm sodium] solution between 55 and 140 °C [131 and 284 °F]. Both galvanized steel and zinc metal showed negligible corrosion. Some samples showed a slight weight gain with many small blisters of zinc oxide. Griess and Bacarella (1969) concluded, based on these observations, that corrosion damage to a galvanized surface is insignificant. Piippo, et al. (1997) examined zinc corrosion from 50 to 170 °C [122 and 388 °F] in environments ranging from reducing (nitrogen) to oxidizing (air), and in borated (pH 9.2) solutions. The highest corrosion rate for zinc was 11.27 g/m²·h [545 mil/yr] at 170 °C [338 °F]. At 90 °C [194 °F], zinc corrosion rate varied from 0.04 g/m²·h [1.9 mil/yr] in borated solution at a pH of 9.2 to 0.163 g/m²·h [7.9 mil/yr] in aerated solution at pH 8. A higher than one order of magnitude increase in zinc corrosion rate was observed in borated solution when the temperature was increased from 90 to 110 °C [194 to 230 °F]. Niyogi, et al. (1982) estimated a zinc corrosion rate of 0.23 g/m²·h [11.4 mil/yr] at 91 °C [196 °F] using an empirical corrosion rate relationship. Recently, Johns, et al. (2003), using the weight loss method, examined corrosion rate of zinc in 0.033-M boric acid [360-ppm boron] and 2.0 × 10⁻⁴ M lithium hydroxide [1.4 ppm lithium] solution. Tests were conducted between 22 and 80 °C [72 and 176 °F] at a pH of 7 or 9. The pH was adjusted by the addition of sodium hydroxide or hydrochloric acid. A maximum weight loss was obtained at room temperature for an immersed sample indicating a corrosion rate of 0.012 g/m²·h [0.58 mil/yr]. This rate could result in reprecipitation of soluble phases on the surface of zinc to compromise measurements so that the sample would exhibit weight gain rather than weight loss. The measured zinc corrosion rates could have been compromised by using glass bottles that could leach silica and alkalis at higher temperatures. Table 2-1 provides a summary of corrosion rate data for zinc and galvanized steel.

Using a maximum immersed surface area and a minimum volume of available containment water {~1,893 m³ [~500,000 gal]}, zinc surface to containment volume ratio is estimated as 26.2 m²/m³ [8.0 ft²/ft³] for galvanized steel (see Table 2-2). Because the immersed fraction for galvanized zinc is estimated as 0.05, the total immersed surface area-to-containment volume reduces to 1.31 m²/m³ [0.4 ft²/ft³]. The non-top coated zinc paint is neglected in the simulations.

Table 2-1. Summary of Corrosion Rate Data for Zinc and Galvanized Zinc			
Reference	Solution	Temperature	Corrosion Rate
Griess & Bacarella (1969)	0.28 M [3,000 ppm] boron + 0.15 M sodium hydroxide [3,450 ppm sodium]	55 to 140 °C [131 to 284 °F]	Negligible
Niyogi, et al. (1982)	Not described	91 °C [196 °F]	0.23 g/m ² ·h [11.4 mil/yr]
Pippo, et al. (1997)	pH = 8.0 & 9.2 borated solutions	50 to 170 °C [122 to 388 °F]	0.04 g/m ² ·h [1.9 mil/yr] at pH = 9.2 in borated solution and 0.163 g/m ² ·h [7.9 mil/yr] in aerated solution at 90 °C [194 °F]; an order of magnitude increase in rates at 110 °C; and 11.27 g/m ² ·h [545 mil/yr] at 170 °C [338 °F]
Johns, et al. (2003)	0.033 M [360 ppm] boron + 2.0 × 10 ⁻⁴ M [1.4 ppm] lithium	22 to 80 °C [72 to 176 °F]	0.012 g/m ² ·h [0.58 mil/yr]
References			
Griess, J.C. and A.L. Bacarella. "Design Consideration of Reactor Containment Spray Systems —Part III: The Corrosion of Materials in Spray Solutions." ORNL-TM-2412, Part III. Oak Ridge, Tennessee: Oak Ridge National Laboratory. 1969.			
Niyogi, K.K., R.R. Lunt, and J.S. Mackenzie. NUREG/CP-0038, "Corrosion of Aluminum and Zinc in Containment Following a LOCA and Potential for Precipitation of Corrosion Products in the Sump." Proceedings of the Second International Conference on the Impact of Hydrogen on Water Reactor Safety, Albuquerque, New Mexico, October 3-7, 1982. Rockville, Maryland: NRC. pp. 410-423. October 1982.			
Piippo, J., T. Laitinen, and P. Sirkai. "Corrosion Behavior of Zinc and Aluminum in Simulated Nuclear Accident Environments." STUK-YTO-TR 123. Helsinki, Finland: Finnish Center for Radiation and Nuclear Safety. 1997.			
Johns, R.C., B.C. Letellier, K.J. Howe, and A.K. Ghosh. "Small-Scale Experiments: Effects of Chemical Reactions on Debris-Bed Head Loss." LA-UR-03-6415. Los Alamos, New Mexico: Los Alamos National Laboratory. 2003.			

Surface Area/Volume m ² /m ³ [ft ² /ft ³]	Immersed Fraction	Immersed Surface Area/Volume m ² /m ³ [ft ² /ft ³]	Corrosion Rate g/m ² ·h [mil/yr]	Time (hour)	Amount Released Per Liter g [mol]
26.2 [8.0]	0.05	1.31 [0.4]	0.163 [7.9]	1/2	1.1 × 10 ⁻⁴ [1.6 × 10 ⁻⁶]

In this study, a zinc corrosion rate of 0.163 g/m²·h [7.9 mil/yr] at 90 °C [194 °F] in aerated solution at pH 8 was used for basecase simulation, because this value provided a conservative estimate. The basecase simulations were conducted at 60 and 90 °C [140 and 194 °F] at 101 kPa [1 atm], 130 °C [266 °F] at 304 kPa [3 atm] pressure, and 150 °C [302 °F] at 507 kPa [5 atm] pressure. The effect of temperature and corrosion rate on the formation of solid phases was evaluated by conducting sensitivity analysis at 60 °C [140 °F], 101 kPa [1 atm]; and 130 °C [266 °F], 304 kPa [3 atm]. Table 2-2 shows the amount of zinc released in grams and in mole per liter of simulated containment solution, in 0.5 hour using a corrosion rate of 0.163 g/m²·h [7.9 mil/yr]. Based on temperature-time profiles for postulated LOCA event, 30 minutes represents maximum time containment solution remains above 90 °C [194 °F].

2.2 Aluminum

In a containment building, aluminum may be present in scaffolding. Additional aluminum may come from fiber insulation in oxide form.

Piippo, et al. (1997), Griess and Bacarella (1969), and Niyogi, et al. (1982) have examined the corrosion rate of aluminum. Griess and Bacarella (1969) measured corrosion rates of several aluminum alloys in 0.20 M [3,000 ppm] boron with 0.15 M sodium hydroxide [3,450 ppm sodium] solution between 55 and 140 °C [131 and 284 °F]. The corrosion rate for sprayed samples was higher than for submerged samples. For aluminum alloys at 55 °C [131 °F], spray corrosion rates ranged from 1.0 to 1.5 g/m²·h [130 to 190 mil/yr], and submerged corrosion rates ranged from 0.35 to 0.61 g/m²·h [45 to 78 mil/yr]. At 100 °C [212 °F], spray corrosion rates ranged from 9.4 to 33.4 g/m²·h [1,200 to 4,300 mil/yr], and submerged corrosion rates ranged from 14.0 to 18.0 g/m²·h [1,800 to 2,300 mil/yr]. The aluminum alloys 1100, 3003, and 6061 corroded at very high rates, with sprayed samples showing higher attack than submerged samples. While the submerged samples showed uniform corrosion, extensive pitting was observed in samples subjected to spray. Niyogi, et al. (1982) estimated an aluminum corrosion rate of 23.9 g/m²·h [3060 mil/yr] at 90 °C [194 °F] using an empirical relationship. However, Niyogi, et al. (1982) suggested a long-term aluminum corrosion rate of 1.6 g/m²·h [200 mil/yr]. Piippo, et al. (1997) examined aluminum corrosion from 50 to 130 °C [122 to 266 °F] in environments ranging from reducing (nitrogen) to oxidizing (air), and in buffered borated solution at a pH of 9.2. Aluminum in buffered borated water showed the highest corrosion rate. At 90 °C [194 °F], Piippo, et al. (1997) measured corrosion rates of 0.012 g/m²·h [1.5 mil/yr] in aerated solution at pH 10 and 1.45 g/m²·h [186 mil/yr] in borated water. Corrosion rates measured for immersed samples by Griess and Bacarella (1969) are a factor of 10 higher than these measured by Piippo, et al. (1997). Table 2-3 provides a summary of corrosion rate data for aluminum.

Table 2-3. Summary of Corrosion Rate Data for Aluminum			
Reference	Solution	Temperature	Corrosion Rate
Griess & Bacarella (1969)	0.28 M [3,000 ppm] boron + 0.15 M sodium hydroxide [3,450 ppm sodium]	55 to 140 °C [131 to 284 °F]	At 55 °C [131 °F], spray corrosion rates ranged from 1.0 to 1.5 g/m ² ·h [130 to 190 mil/yr], and submerged corrosion rates ranged from 0.35 to 0.61 g/m ² ·h [45 to 78 mil/yr]. At 100 °C [212 °F], spray corrosion rates ranged from 9.4 to 33.4 g/m ² ·h [1,200 to 4,300 mil/yr], and submerged corrosion rates ranged from 14.0 to 18.0 g/m ² ·h [1,800 to 2,300 mil/yr].
Nyogi, et al. (1982)	Not described	90 °C [194 °F]	23.9 g/m ² ·h [3060 mil/yr]
Pippo, et al. (1997)	pH = 9.2 borated solutions, pH = 10 aerated solution	50 to 130 °C [122 to 266 °F]	At 90 °C [194 °F], corrosion rates were 0.012 g/m ² ·h [1.5 mil/yr] in aerated solution at pH 10 and 1.45 g/m ² ·h [186 mil/yr] in borated water.
References			
Griess, J.C. and A.L. Bacarella. "Design Consideration of Reactor Containment Spray Systems —Part III: The Corrosion of Materials in Spray Solutions." ORNL-TM-2412, Part III. Oak Ridge, Tennessee: Oak Ridge National Laboratory. 1969.			
Niyogi, K.K., R.R. Lunt, and J.S. Mackenzie. NUREG/CP-0038, "Corrosion of Aluminum and Zinc in Containment Following a LOCA and Potential for Precipitation of Corrosion Products in the Sump." Proceedings of the Second International Conference on the Impact of Hydrogen on Water Reactor Safety, Albuquerque, New Mexico, October 3-7, 1982. Rockville, Maryland: NRC. pp. 410-423. October 1982.			
Piippo, J., T. Laitinen, and P. Sirkai. "Corrosion Behavior of Zinc and Aluminum in Simulated Nuclear Accident Environments." STUK-YTO-TR 123. Helsinki, Finland: Finnish Center for Radiation and Nuclear Safety. 1997.			

Using a maximum immersed surface area and a minimum volume of available containment water, an aluminum metal surface area-to-volume ratio is estimated as 11.5 m²/m³ [3.5 ft²/ft³] as shown in Table 2-4. Because the immersed fraction for aluminum is 0.05, the total immersed surface area-to-containment volume reduces to 0.57 m²/m³ [0.17 ft²/ft³].

Basecase simulations for aluminum were conducted using a corrosion rate of 1.45 g/m²·h [186 mil/yr] at 90 °C [194 °F] (Piippo, et al., 1997). The effects of temperature and corrosion rate on the formation of solid phases was evaluated by conducting sensitivity analysis at 60 °C [140 °F], 101 kPa [1 atm]; and 130 °C [266 °F], 304 kPa [3 atm]. Table 2-4 also shows the amount of aluminum released in grams and in mole per liter of simulated containment solution in 0.5 hour using a corrosion rate of 1.45 g/m²·h [186 mil/yr].

Surface Area/Volume m ² /m ³ [ft ² /ft ³]	Immersed Fraction	Immersed Surface Area/Volume m ² /m ³ [ft ² /ft ³]	Corrosion Rate g/m ² ·h [mil/yr]	Time (hour)	Amount Released Per Liter g [mol]
11.5 [3.5]	0.34	0.57 [0.17]	1.45 [186]	1/2	4.2 × 10 ⁻⁴ [1.5 × 10 ⁻⁵]

2.3 Carbon Steel

Carbon steel is present as structural steel in the containment building. However, most of the carbon steel is protected by design basis accident qualified coatings or is encased in insulation. Estimates are that the unprotected carbon steel surface area is small.

Griess and Bacarella (1969) and Hall (1988) have examined the corrosion rate of carbon steels in borated water. Griess and Bacarella (1969) measured the corrosion rate of A-108 and A-210 carbon steels in 0.15 M sodium hydroxide [3,450 ppm sodium] solution between 55 and 140 °C [131 and 284 °F]. The corrosion rate for sprayed samples was higher than for submerged samples. Results showed a negligible attack on carbon steels in alkaline borated water regardless of the test conditions. Hall (1988) measured corrosion of SA-193 Grade B7, SA-540 Grade B23, and SA-540 Grade B24 carbon steels {0.092 M [1,000 ppm] boron} borated water from 79 to 204 °C [175 to 400 °F]. At 79 °C [175 °F], a maximum corrosion rate of 19.0 g/m²·h [833 mil/yr], and an average corrosion rate of 14.6 g/m²·h [639 mil/yr], was observed for SA-193 B7 carbon steel. Average corrosion rates at 79 °C [175 °F] for SA-540 Grade B23 and SA-540 Grade B24 were 16.7 g/m²·h [731 mil/yr] and 6.0 g/m²·h [265 mil/yr], respectively. At 177 °C [350 °F], average corrosion rates for SA-193 Grade B7, SA-540 Grade B23, and SA-540 Grade B24 carbon steels were 4.3 g/m²·h [190 mil/yr], 14.8 g/m²·h [650 mil/yr], and 11.3 g/m²·h [495 mil/yr], respectively. Table 2-5 provides a summary of corrosion rate data for carbon steel.

The corrosion rates at 177 °C [350 °F] were lower for SA-193 Grade B7, and SA-540 Grade B23 at higher temperatures while for SA-540 Grade B24 the corrosion rate was higher at higher temperatures. Therefore, based from the work of Hall (1988) and Griess and Bacarella (1969), in alkaline solutions, carbon steel behaves as a passive material.

Using a maximum immersed surface area and a minimum volume of available water, a carbon steel surface area-to-volume ratio is estimated as 0.49 m²/m³ [0.15 ft²/ft³] as shown in Table 2-6. Because the immersed fraction for carbon steel is 0.34, the total immersed surface area-to-containment volume reduces to 0.17 m²/m³ [0.05 ft²/ft³].

Basecase simulations for carbon steel were conducted using a corrosion rate of 19.0 g/m²·h [833 mil/yr] at 90 °C [194 °F]. The effect of the temperature and corrosion rate on the formation of solid phases was evaluated by conducting sensitivity analysis at 60 °C [140 °F], 101 kPa [1 atm]; and 130 °C [266 °F], 304 kPa [3 atm]. Table 2-6 also shows the amount of carbon steel released in grams and in mole per liter of simulated containment solution in 0.5 hour using a corrosion rate of 19.0 g/m²·h [833 mil/yr].

Table 2-5. Summary of Corrosion Rate Data for Carbon Steel			
Reference	Solution	Temperature	Corrosion Rate
Griess & Bacarella (1969)	0.28 M [3,000 ppm] boron + 0.15 M sodium hydroxide [3,450 ppm sodium]	55 to 140 °C [131 to 284 °F]	Negligible
Hall (1988)	0.092 M [1,000-ppm] boron	79 to 204 °C [175 to 400 °F]	At 79 °C [175 °F], a maximum corrosion rate of 19.0 g/m ² ·h [833 mil/yr], and an average corrosion rate of 14.6 g/m ² ·h [639 mil/yr], for SA-193 B7 carbon steel. Average corrosion rates at 79 °C [175 °F] for SA-540 Grade B23 and SA-540 Grade B24 were 16.7 g/m ² ·h [731 mil/yr] and 6.0 g/m ² ·h [265 mil/yr]. At 177 °C [350 °F], average corrosion rates for SA-193 Grade B7, SA-540 Grade B23, and SA-540 Grade B24 carbon steels were 4.3 g/m ² ·h [190 mil/yr], 14.8 g/m ² ·h [650 mil/yr], and 11.3 g/m ² ·h [495 mil/yr].
References			
Griess, J.C. and A.L. Bacarella. "Design Consideration of Reactor Containment Spray Systems —Part III: The Corrosion of Materials in Spray Solutions." ORNL-TM-2412, Part III. Oak Ridge, Tennessee: Oak Ridge National Laboratory. 1969.			
Hall, J.F. "Corrosion of Low Alloy Steel Fastener Materials Exposed to Borated Water." Proceedings of the Third International Symposium on Environmental Degradation of Materials in Nuclear Power Systems—Water Reactors. G.J. Theus and J.R. Weeks, eds. La Grange Park, Illinois: American Nuclear Society. pp. 711–722. 1988.			

2.4 Copper

In a containment building, copper is present in fan coolers with small contributions from instrument air lines.

Griess and Bacarella (1969) examined the corrosion rate of copper and copper alloys in borated water. Griess and Bacarella (1969) also measured the corrosion rate of copper in 0.15 M sodium hydroxide [3,450-ppm sodium] solution between 55 and 140 °C [131 and 284 °F]. The corrosion rates for sprayed samples were higher than for submerged samples. For copper at

Surface Area/Volume m ² /m ³ [ft ² /ft ³]	Immersed Fraction	Immersed Surface Area/Volume m ² /m ³ [ft ² /ft ³]	Corrosion Rate g/m ² ·h [mil/yr]	Time (hour)	Amount Released Per Liter g [mol]
0.49 [0.15]	0.05	0.17 [0.05]	19.0 [833]	1/2	1.6 × 10 ⁻⁴ [2.8 × 10 ⁻⁵]

Reference	Solution	Temperature	Corrosion Rate
Griess & Bacarella (1969)*	0.28 M [3,000 ppm] boron + 0.15 M sodium hydroxide [3,450 ppm sodium]	55 to 140 °C [131 to 284 °F]	At 100 °C [212 °F], the average spray corrosion rate was 0.043 g/m ² ·h [1.7 mil/yr], and the average submerged corrosion rate was 0.013 g/m ² ·h [0.51 mil/yr].
*Griess, J.C. and A.L. Bacarella. "Design Consideration of Reactor Containment Spray Systems —Part III: The Corrosion of Materials in Spray Solutions." ORNL-TM-2412, Part III. Oak Ridge, Tennessee: Oak Ridge National Laboratory. 1969.			

100 °C [212 °F], the average spray corrosion rate was 0.043 g/m²·h [1.7 mil/yr], and the average submerged corrosion rate was 0.013 g/m²·h [0.51 mil/yr]. Table 2-7 provides a summary of corrosion rate data for copper.

Using a maximum immersed surface area and a minimum volume of available containment water, a copper surface area-to-volume ratio is estimated as 19.7 m²/m³ [6.0 ft²/ft³] as shown in Table 2-8. Since the immersed fraction for copper is 0.25, the total immersed surface area-to-containment volume reduces to 4.9 m²/m³ [1.5 ft²/ft³].

Basecase simulations were conducted using a corrosion rate of 0.03 g/m²·hr [1.2 mil/yr] at 90 °C [194 °F]. The effect of the temperature and corrosion rate on the formation of solid phases was evaluated by conducting sensitivity analysis at 60 °C [140 °F], 101 kPa [1 atm]; and 130 °C [266 °F], 304 kPa [3 atm]. Table 2-8 also shows the amount of copper released in grams and mole per liter of simulated containment solution, in 0.5 hour using a corrosion rate of 0.03 g/m²·hr [1.2 mil/yr].

2.5 Concrete

Concrete contribution comes from the erosion of concrete surfaces due to the impact of the water stream around the LOCA location. While a protective paint is applied to concrete surfaces, a small portion of the concrete is expected to be uncoated during the LOCA event. Using a maximum immersed surface area and a minimum volume of available containment water, a concrete surface area-to-containment volume ratio is estimated as 0.15 m²/m³

Surface Area/Volume m ² /m ³ [ft ² /ft ³]	Immersed Fraction	Immersed Surface Area/Volume m ² /m ³ [ft ² /ft ³]	Corrosion Rate g/m ² ·h [mil/yr]	Time (hour)	Amount Released Per Liter g [mol]
19.7 [6.0]	0.25	4.9 [1.5]	0.03 [1.2]	1/2	7.6 × 10 ⁻⁵ [1.2 × 10 ⁻⁶]

[0.045 ft²/ft³] as shown in Table 2-9. Since the immersed fraction for concrete is 0.34, the total immersed surface area-to-volume reduces to 0.05 m²/m³ [0.015 ft²/ft³]. The total amount of concrete particulate is estimated as 22.25 g/m³ [0.0014 lbm/ft³]. Carmack, et al. (1998) determined the dust particle size and surface area associated with graphite powders and compared it with Tokamaks (General Atomics DIII-D, MIT's Alcator CMOD, and Princeton's TFTR) dusts as shown in Figure 2-1. For 10–15-μm [0.39–0.59-mil]-diameter graphite particles, the specific surface area was approximately 15 m²/g [7.3 × 10⁴ ft²/lbm]. This specific surface area was used to estimate the amount of concrete particulate as shown in Table 2-10.

Concrete or cement is a mixture of tricalcium silicate, dicalcium silicate, and tricalcium aluminate. To simplify the simulation, cement was represented by dicalcium silicate. The corrosion rate of typical Portland cement was based on Jantzen (1984). Jantzen (1984) examined the release of calcium from cast cement, cold-pressed cement, warm-pressed cement, formed under elevated temperatures and pressures, and clinkered cement. Based on 28-day tests at 60 °C [140 °F], the average release of calcium ions into the solution was 0.13 g/m²·hr [14.7 mil/yr]. Tables 2-9 and 2-10 indicate that the contributions from concrete floors and walls are negligible compared to the contribution from concrete particulates. Therefore, only concrete particulates were included in the simulation.

Basecase simulations were conducted using a dissolution rate of 0.13 g/m²·h [14.7 mil/yr]. The effect of temperature and dissolution rate on the formation of solid phases was evaluated by conducting sensitivity analysis at 60 °C [140 °F], 101 kPa [1 atm]; and 130 °C [266 °F], 304 kPa [3 atm]. Tables 2-9 and 2-10 also show the amount of concrete dissolved in grams and moles per liter of simulated containment solution in 0.5 hour using a dissolution rate of 0.13 g/m²·h [14.7 mil/yr].

2.6 Fiber Insulation

Fiber insulation is primarily made of glass fiber wool. The diameter of glass fiber wool ranges from 3 to 10 μm [0.12 to 0.39 mil] with a mean diameter of 7.0 μm [0.28 mil]. Binders of as much as 25-percent weight are added to hold the insulation together. Typically, these binders are phenol formaldehyde resin based. The binders are applied immediately after fiberization. These binders accumulate as droplets, which upon curing at an elevated temperature, flatten on the fiber surface. During curing, phenol formaldehyde converts to an insoluble polymer. Most of the fiber wool compositions are not designed for aggressive acid or alkaline conditions. A significant difference in fiber insulation dissolution rates is not expected among different fiber insulation brands because most of the manufacturers use a similar glass composition. An average Nukon® fiber insulation composition is shown in Table 2-11. A surface area to volume ratio of fiber glass in the fiber insulation is approximately 4.33 × 10⁵ m²/m³ [1.32 × 10⁵ ft²/ft³].

Surface Area/Volume m ² /m ³ [ft ² /ft ³]	Immersed Fraction	Immersed Surface Area/Volume m ² /m ³ [ft ² /ft ³]	Corrosion Rate g/m ² ·h [mil/yr]	Time (hour)	Amount Released per Liter g [mol]
0.15 [0.045]	0.34	0.05 [0.015]	0.13 [14.7]	1/2	3.3 × 10 ⁻⁶ [1.9 × 10 ⁻⁸]

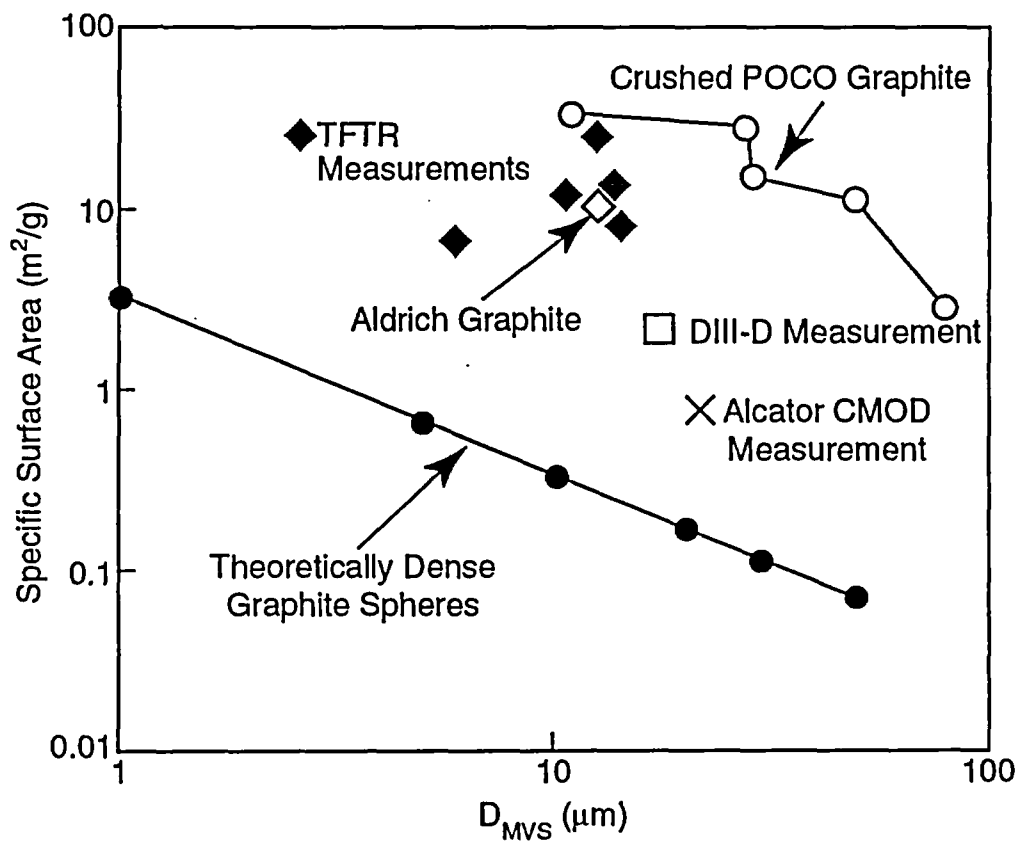


Figure 2-1. Surface Area Versus Diameter for Various Graphite Powders and Tokamak Dusts (Carmack, et al., 1998)

Amount/Volume g/m ³ [lbm/ft ³]	Specific Surface Area m ² /g [ft ² /lbm]	Immersed Surface Area/Volume m ² /m ³ [ft ² /ft ³]	Corrosion Rate g/m ² ·hr [mil/yr]	Time (hour)	Amount Released Per Liter g [mol]
22.25 [0.0014]	15 [7.3 × 10 ⁴]	333 [101]	0.13 [14.7]	1/2	1.0 × 10 ⁻² [1.3 × 10 ⁻⁴]

Component	Weight Percent	Molecular Weight	Mole Fraction
SiO ₂	62.5	60	0.637
Al ₂ O ₃	3.6	102	0.022
CaO	8.2	56	0.090
MgO	3.45	40	0.053
Na ₂ O	15.8	62	0.156
B ₂ O ₃	5.0	70	0.044

Fiber insulation is widely used as pipe insulation in containment buildings. The amount of fiber insulation depends on the specific plant design. Nukon®, an Owens-Corning brand, is installed in a large number of containment buildings.

Using a maximum immersed volume of fiber insulation and a minimum volume of available containment water and assuming an immersed Nukon fiber fraction of 0.75, the ratio of the surface area of glass fibers in Nukon insulation to the volume of containment water is estimated at $7.8 \times 10^2 \text{ m}^2/\text{m}^3$ [$2.4 \times 10^2 \text{ ft}^2/\text{ft}^3$] as shown in Table 2-12.

Most of the dissolution studies about fiber insulation materials used simulated lung solution for toxicity studies. Corrosion, however, is an important parameter for the disposal of radioactive waste in glass, and a large volume of literature is devoted to the subject. Because the fiber insulation and typical nuclear waste glasses have similar compositions (in fact, fiber insulation glasses have better chemical durability than nuclear waste glasses because of the higher concentration of silica), a corrosion rate of 0.025 g/m²·h [3.4 mil/yr], determined by Pan, et al. (2003) for surrogate nuclear waste glasses at 90 °C [194 °F], is used in the simulations. Assuming the density of glass is 2,500 kg/m³ [157 lbm/ft³], an average corrosion rate can be expressed as 0.24 μm/day [3.4 mil/yr]. For a radius of 3.5 μm [0.14 mil], fiber would dissolve in approximately 14.6 days. The glass corrosion rate, however, would decrease with time because of the formation of secondary layers on the surface of the glass. The corrosion rate used in the simulations represents a conservative estimate for fiber insulation corrosion. Basecase simulations were conducted using a fiber insulation dissolution rate of 0.025 g/m²·h [3.4 mil/yr] at 90 °C [194 °F]. The effect of temperature and corrosion rate on the formation of

Table 2-12. Estimation of Fiber Insulation in Simulated Containment Water	
Parameter	Value
Volume of Nukon [®] /Volume of Water, m ³ /m ³ [ft ³ /ft ³]	0.137 [0.137]
Immersed Fraction	0.75
Immersed Volume of Nukon [®] /Volume of Water, m ³ /m ³ [ft ³ /ft ³]	0.103 [0.103]
Density of Nukon [®] , kg/m ³ [lbf/ft ³]	38.1 [2.4]
Weight of Nukon [®] /Volume of Water, kg/m ³ [lbf/ft ³]	3.9 [0.25]
Density of Fiber Glass, kg/m ³ [lbf/ft ³]	2,500 [157]
Surface Area/Volume Ratio of Glass Fiber, m ² /m ³ [ft ² /ft ³]	4.3 × 10 ⁵ [1.3 × 10 ⁵]
Surface Area of Fiber Glass/Volume of Water, m ² /m ³ [ft ² /ft ³]	678 [207]
Corrosion Rate, g/m ² ·h [mil/yr]	0.025 [3.4]
Time, hour	1/2
Amount of Glass Fiber in Insulation, g/l [mol/l]	8.5 × 10 ⁻³ [1.4 × 10 ⁻⁴]

Table 2-13. Estimation of Fiber Glass in the Nukon [®] Insulation in Simulated Containment Water	
Component	Amount Per Liter of Solution (mol)
SiO ₂	9.0 × 10 ⁻⁵
Al ₂ O ₃	3.0 × 10 ⁻⁶
CaO	1.3 × 10 ⁻⁵
MgO	7.4 × 10 ⁻⁶
Na ₂ O	2.2 × 10 ⁻⁵
B ₂ O ₃	6.2 × 10 ⁻⁶

solid phases was evaluated by conducting a sensitivity analysis at 60 °C [140 °F], 101 kPa [1 atm]; and 130 °C [266 °F], 304 kPa [3 atm]. Table 2-13 shows the amount of fiber insulation released in grams and moles per liter of simulated containment solution in 0.5 hour using a corrosion rate of 0.025 g/m²·h [3.4 mil/yr].

3 FORMATION OF SOLID PHASES DUE TO CORROSION OF COMPONENTS IN ALKALINE CONTAINMENT WATER

This chapter uses the software validated in Appendix A to examine the potential and nature of any solid corrosion products that might form in the environment surrounding a LOCA event.

Simulations presented in this chapter assumed a pressure of 507 kPa [5 atm] and 150 °C [302 °F] as the peak temperature of the containment water immediately following a LOCA event. The influence of pressure, temperature, and pH on chemical speciation was studied by speciating a fixed amount of each component based on its corrosion rate. Speciation simulations were conducted at 150 °C [302 °F] at 507 kPa [5 atm], 130 °C [266 °F] at 304 kPa [3 atm], and 90 °C [194 °F] and 60 °C [140 °F] at 101 kPa [1 atm]. The amount of each component was estimated based on the corrosion rate at 90 °C [194 °F] for 0.5 hour. Given the significant uncertainties in corrosion rates in borated water as a function of temperature and to provide a comparative assessment on the effects of temperature and pressure, a fixed amount of each component was used as input for simulations. Input values for the simulations are shown in Table 3-1. The basis for selecting these values was discussed in Chapter 2. Simulations were conducted at pH 10, and the formation of solid phases as a function of temperature and pressure was examined. Appendix B shows a typical simulation output. A pH of 10 was obtained by adding 0.23 mol/L [5,300 ppm Na] NaOH. The precipitation of phases during the 15-day operation for the containment system at 60 °C [140 °F] was estimated by multiplying the hourly corrosion amount of each component by 720. Additional 0.24 M H₃BO₃

Table 3-1. Input Values Per Liter of Solution for Simulations

Component	Corrosion Rate g/m ² ·h [mil/yr]	Amount Released/ Liter in 0.5 Hour g [mol]
Nukon® Fiber	0.025 [3.4]	8.5 × 10 ⁻³ [1.4 × 10 ⁻⁴]
SiO ₂	—	5.4 × 10 ⁻³ [9.0 × 10 ⁻⁵]
Al ₂ O ₃	—	3.1 × 10 ⁻⁴ [3.0 × 10 ⁻⁶]
MgO	—	3.0 × 10 ⁻⁴ [7.4 × 10 ⁻⁶]
Na ₂ O	—	1.4 × 10 ⁻³ [2.2 × 10 ⁻⁵]
B ₂ O ₃	—	4.3 × 10 ⁻⁴ [6.2 × 10 ⁻⁶]
CaO	—	7.1 × 10 ⁻⁴ [7.3 × 10 ⁻⁵]
Concrete (Ca ₂ SiO ₄)	0.13 [14.7]	1.0 × 10 ⁻² [1.3 × 10 ⁻⁴]
Aluminum metal	1.45 [186]	4.2 × 10 ⁻⁴ [1.5 × 10 ⁻⁵]
Zinc metal	0.163 [7.9]	1.1 × 10 ⁻⁴ [1.6 × 10 ⁻⁶]
Iron metal	19.0 [833]	1.6 × 10 ⁻⁴ [2.8 × 10 ⁻⁵]
Copper metal	0.03 [1.2]	7.6 × 10 ⁻⁵ [1.2 × 10 ⁻⁶]
B(OH) ₃	N/A	16.1 [0.26]
NaOH	N/A	9.2 [0.23]

was needed to maintain pH at 10. An increase in pH was observed as the concentration of corrosion components increased in the simulation. This increase in pH was attributed to the hydrolysis reactions associated with the fiber insulation. Corrosion rates of the components at 90 °C [194 °F] were used in the simulations to estimate the amount of each component. Use of such rates leads to conservative assessment of long-term corrosion because corrosion rates of components are expected to be lower at 60 °C [140 °F] which is expected to be the temperature of the containment water during steady-state operations.

Table 3-2 shows the calculated pH and redox potential at different temperatures and pressures in borated water with 0.26-M [2,800-ppm] boron and 0.23-M [5,300-ppm Na] NaOH. At 60 °C (140 °F), pH in alkaline borated water with 0.26-M [2,800-ppm] boron was 10. A slight decrease in pH was observed with the increase in the temperature and pressure. Similarly, redox potential at 60 °C [140 °F] was approximately -0.6 V versus the standard hydrogen electrode (V_{SHE}).

Test Conditions	pH	Eh (V_{SHE})
60 °C [140 °F] at 101 kPa [1 atm]	10.0	-0.60
90 °C [194 °F] at 101 kPa [1 atm]	9.7	-0.62
130 °C [266 °F] at 304 kPa [3 atm]	9.5	-0.64
150 °C [302 °F] at 507 kPa [5 atm]	9.4	-0.65

Figure 3-1 shows the concentrations of solid phases at pH 10. The dominating solid phases in the simulated containment water were sodium aluminum silicate ($NaAlSi_3O_8$), calcium iron silicate ($Ca_3Fe_2Si_3O_{12}$), iron silicate [$Fe_3Si_2O_5(OH)_4$], and Fe_3O_4 . In addition, calcium magnesium silicate [$Ca_2Mg_5Si_8O_{22}(OH)_2$], $ZnO \cdot Fe_2O_3$, and copper were observed in smaller quantities.

Table 3-3 shows the solid phase percentage for each element present in the simulated containment water. Table 3-4 provides a percent distribution of solid phases for compounds at different temperatures and pressures. Table 3-4 demonstrates that, even though silicon was not present as SiO_2 solid phase, more than 90 percent of the solid phases observed at pH 10 are silicates. Simulation results indicate no phase change for copper. Most of the copper added as copper metal in the simulation remained as copper metal. The concentration of $Ca_2Mg_5Si_8O_{22}(OH)_2$ did not change from 150 °C [302 °F], 507 kPa [5 atm] to 60 °C [140 °F], 101 kPa [1 atm], and 100 percent of the magnesium was incorporated in the solid phase. Zinc was present as $ZnO \cdot Fe_2O_3$, and the solid phase concentration increased with decrease in temperature. At 60 °C [140 °F], 101 kPa [1 atm], 100 percent of zinc was present as $ZnO \cdot Fe_2O_3$, while at 150 °C [302 °F], 507 kPa [5 atm], zinc was completely soluble as $Zn(OH)_3^{-1}$ phase. Aluminum was present in $NaAlSi_3O_8$ phase and the solid phase concentration increased with decrease in temperature. At 60 °C [140 °F], 101 kPa [1 atm], 100 percent of aluminum was present as $NaAlSi_3O_8$, while at 150 °C [302 °F], 507 kPa [5 atm], aluminum was completely soluble as $Al(OH)_4^{-1}$ phase. Iron metal was associated with the formation of several solid phases. The concentration of $Ca_3Fe_2Si_3O_{12}$ decreased with decrease in temperature. At 90 °C

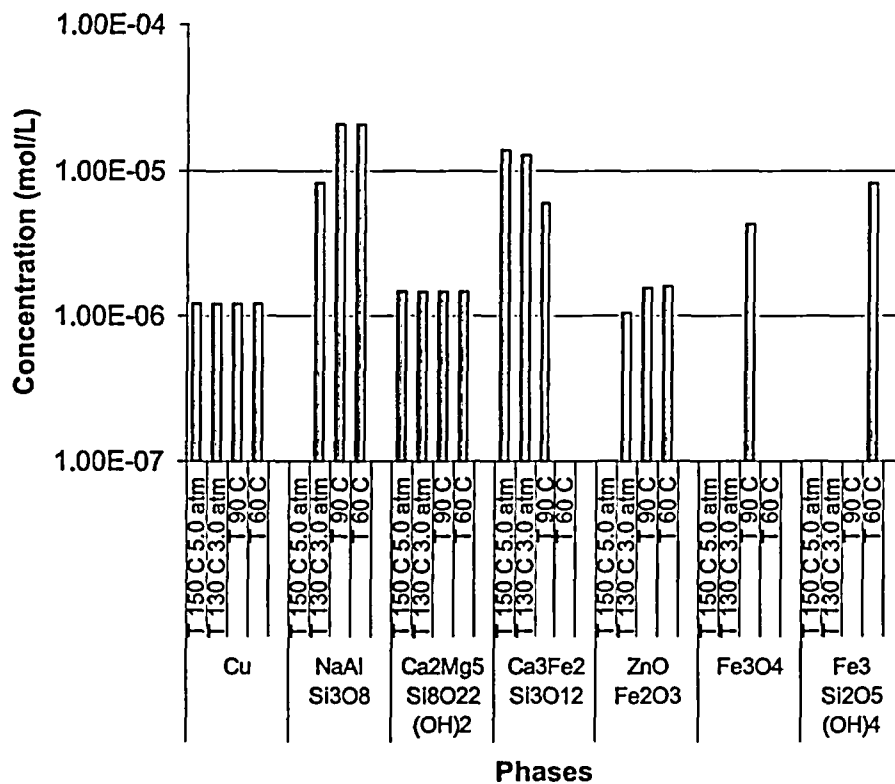


Figure 3-1. Concentration, in mol/L, of Dominant Solid Phases As a Function of Temperature and Pressure in 0.26 M [2,800 ppm] Boron in an Alkaline Simulated Containment Water at pH 10

Temperature and Pressure	Magnesium (Percent)	Iron (Percent)	Aluminum (Percent)	Zinc (Percent)	Silicon (Percent)	Calcium (Percent)
150 °C [302 °F], 507 kPa [5 atm]	100	100	0	0	25	17
130 °C [266 °F], 304 kPa [3 atm]	100	100	39	66	35	16
90 °C [194 °F], 101 kPa [1 atm]	100	100	100	98	43	8
60 °C [140 °F], 101 kPa [1 atm]	100	100	100	98	42	1

Temperature and Pressure	NaAlSi ₃ O ₈ (Percent)	Ca ₂ Mg ₅ Si ₈ O ₂₂ (OH) ₂ (Percent)	Fe ₃ Si ₂ O ₅ (OH) ₄ (Percent)	Ca ₃ Fe ₂ Si ₃ O ₁₂ (Percent)	ZnO·Fe ₂ O ₃ (Percent)	Fe ₃ O ₄ (Percent)
150 °C [302 °F], 507 kPa [5 atm]	0	10	—	90	0	—
130 °C [266 °F], 304 kPa [3 atm]	35	6	—	54	4	—
90 °C [194 °F], 101 kPa [1 atm]	61	4	—	17	5	12
60 °C [140 °F], 101 kPa [1 atm]	65	5	26	—	5	—

[194 °F], iron was present as Ca₃Fe₂Si₃O₁₂, ZnO·Fe₂O₃, and Fe₃O₄. At 60 °C [140 °F], iron was present as Fe₃Si₂O₅(OH)₄ and ZnO·Fe₂O₃. Even though new iron bearing phases were formed as the temperature decreased from 150 °C [302 °F], 507 kPa [5 atm] to 60 °C [140 °F], 100 percent of the iron remained in solid phase.

Table 3-3 shows the percent of distribution for elements at different temperatures and pressures. The Ca₃Fe₂Si₃O₁₂ solid phase concentration decreased from 1.4 × 10⁻⁵ to 0 mol/L when the temperature dropped from 150 °C [302 °F], 507 kPa [5 atm] to 60 °C [140 °F], indicating retrograde solubility of calcium with temperature as shown in Figure 3-1. As calcium dissolves, the solid phase of Fe₃O₄ changes at 90 °C [194 °F] to Fe₃Si₄O₁₀(OH)₂ at 60 °C [140 °F], 101 kPa [1 atm]. Both soluble and insoluble silicon bearing phases were observed in the simulated containment water. At 150 °C [302 °F], 507 kPa [5 atm], 25 percent of silicon was distributed within various solid silicates, while at 60 °C [140 °F], 42 percent of silicon bearing phases were distributed in solid phases. The dominant silicon bearing soluble phases were SiO₂ (aqueous), H₃SiO₃⁻¹, and NaHSiO₃. The increase in silicon bearing solid phases is attributed to the formation of NaAlSi₃O₈. Only 17 percent of calcium was present in calcium bearing solid phases at 150 °C [302 °F], 507 kPa [5 atm], while 1 percent of calcium was present in calcium bearing solid phases at 60 °C [140 °F].

A major difference observed at 130 °C [266 °F], 304 kPa [3 atm] and 60 °C [140 °F] was a redistribution of iron phases. However, despite redistribution, 100 percent of the iron remained in the solid form. Results also indicate that the solubility of ZnO·Fe₂O₃ and NaAlSi₃O₈ decreased with a decrease in temperature and pressure, resulting in a higher concentration of solids at lower temperatures. As corrosion proceeds, concentration of corroded species increases with time.

Figure 3-2 compares the observed solid phases at pH 10 after 15 days of corrosion at 60 °C [140 °F] with solid phases observed at 130 °C [266 °F], 304 kPa [3 atm] in 0.5 hour. Additional 0.24 M H₃BO₃ was needed to maintain pH at 10. An increase in pH was observed as the concentration of corrosion components increased in the simulation. This increase in pH was attributed to hydrolysis reactions associated with the fiber insulation.

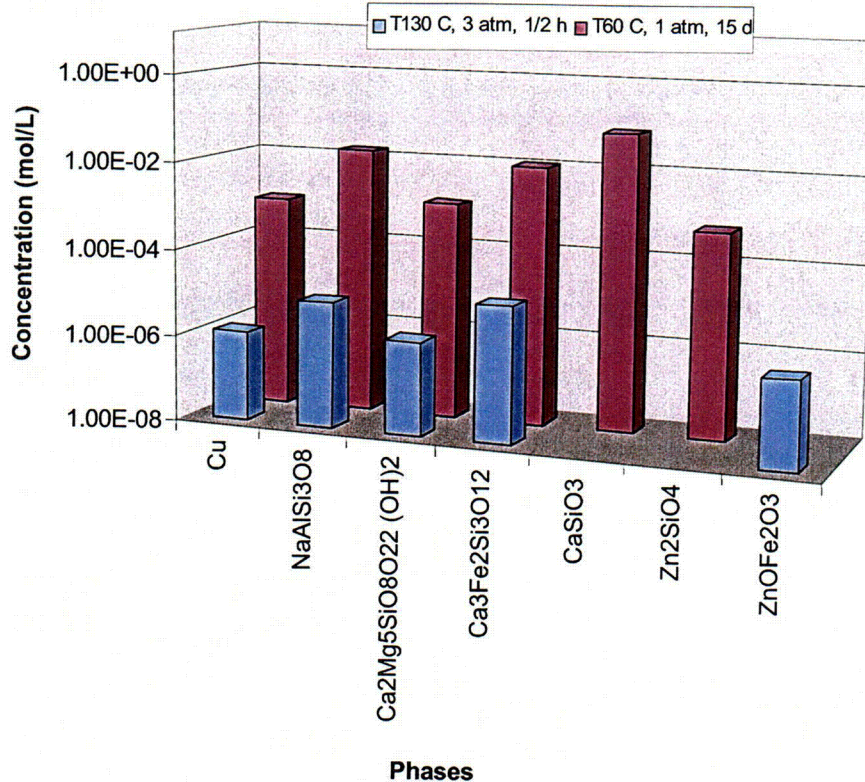


Figure 3-2. Concentration, in mol/L, of Dominant Solid Phases at 150 °C [302 °F], 507 kPa [5 atm] for 0.5 Hour at 60 °C [140 °F] for 15 Days in a 0.26-M [2,800-ppm] Boron Alkaline Simulated Containment Water at pH 10

The dominant solid phases formed in the simulated containment water at pH 10 after 15 days were SiO₂, CaSiO₃, NaAlSi₃O₈, Ca₂Mg₅Si₈O₂₂(OH)₂, Ca₃Fe₂Si₃O₁₂, and a minor quantity of Zn₂SiO₄. Simulation results show that the concentrations of solid phases observed at 60 °C [140 °F], pH 10 were much larger than those observed at 130 °C [266 °F], 304 kPa [3 atm] in 0.5 hour. With the exception of ZnO·Fe₂O₃ observed at 130 °C [266 °F], 304 kPa [3 atm], solid phases formed at pH 10 at 130 °C [266 °F], 304 kPa [3 atm] in a 15-day simulation were similar to the high temperature and high pressure phase results in the simulations. In addition, CaSiO₃ solid phase was also observed at 60 °C [140 °F]. The simulations indicate that with the exception of ZnO·Fe₂O₃, similar solid phases are formed in the first 0.5 hour of the LOCA event at 150 °C [302 °F], 507 kPa [5 atm] as those from a 15-day or longer simulation test at 60 °C [140 °F].

Figures 3-3 and 3-4 indicate there are major differences in the formation of dominant silicate solid phases at 60 °C [140 °F] and 130 °C [266 °F], 304 kPa [3 atm] as a function of pH. Figure 3-3 shows the speciation of the dominant solid phases as a function of pH in the alkaline range between pH 7 and 11 at 60 °C [140 °F]. The pH of the solution was adjusted by the addition of NaOH. At 60 °C [140 °F], at pH 7, the dominant solid phases were NaAlSi₃O₈ and Fe₃Si₂O₅(OH)₄, while at pH 10, the dominant solid phases were NaAlSi₃O₈ and Fe₃O₄. At pH

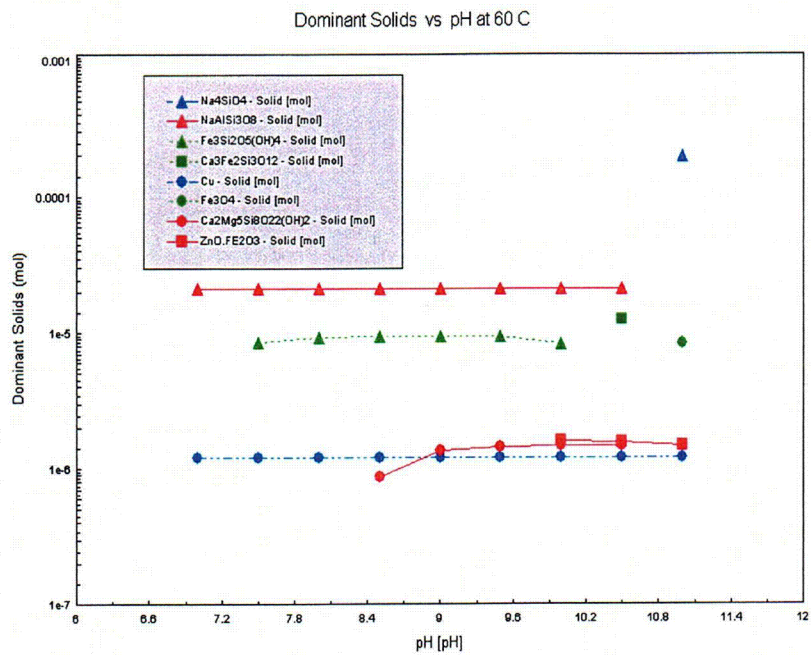


Figure 3-3. Dominant Solid Phases at 60 °C [140 °F], 101 kPa [1 atm] As a Function of pH

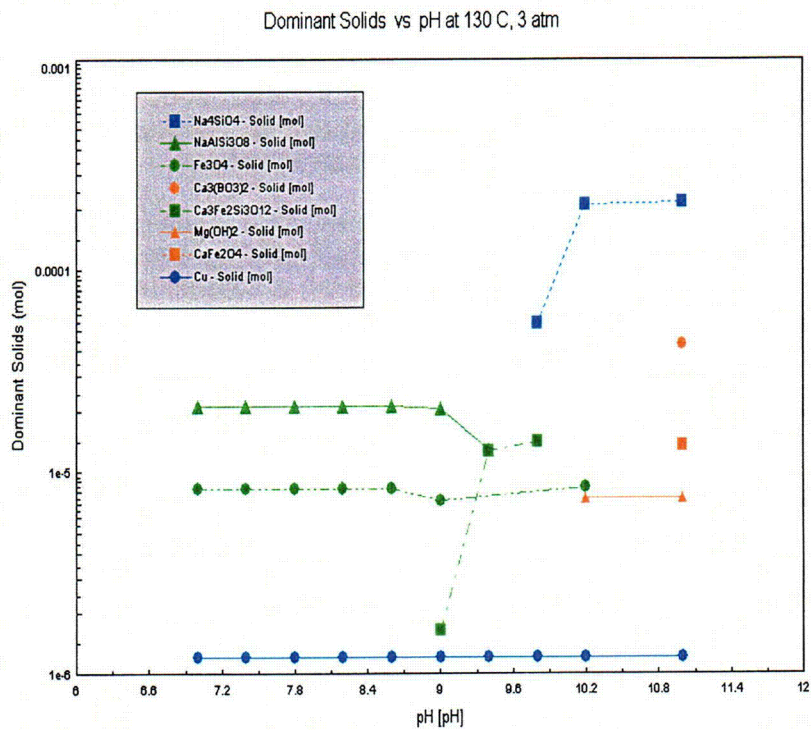


Figure 3-4. Dominant Solid Phases at 130 °C [266 °F], 304 kPa [3 atm] As a Function of pH

exceeding 11, Na_4SiO_4 was a dominant solid phase and its concentration exceeded the concentration of other solid phases by an order of magnitude.

Figure 3-4 shows the speciation of the solid phases as a function of pH at 130 °C [266 °F], 304 kPa [3 atm] pressure. At 130 °C [266 °F], 304 kPa [3 atm] and pH 7, the dominant solid phases were $\text{NaAlSi}_3\text{O}_8$ and Fe_3O_4 , while at pH exceeding 10, the dominant solid phase was Na_4SiO_4 . The concentration of this phase exceeded the concentration of other solid phases by an order of magnitude. At pH 9, Fe_3O_4 transformed to $\text{Ca}_3\text{Fe}_2\text{Si}_3\text{O}_{12}$.

The formation of iron phases depends on temperature, pressure, and pH. However, irrespective of the solid phase formed, 100 percent of the iron was associated with solid phases. At 60 °C [140 °F], as the pH increased, the iron phase transformed from $\text{Fe}_3\text{Si}_2\text{O}_5(\text{OH})_4$ at pH 7, to Fe_3O_4 at pH 10, and to $\text{Ca}_3\text{Fe}_2\text{Si}_3\text{O}_{12}$ at pH 10.6. At 130 °C [266 °F], 304 kPa [3 atm], the iron phase transformed from Fe_3O_4 at pH 7, to $\text{Ca}_3\text{Fe}_2\text{Si}_3\text{O}_{12}$ at pH 9, and to CaFe_2O_4 at pH 11. The differences in iron phases are attributed to the availability of silicon. In an alkaline environment, the solubility of silica increases with increase in pH and temperature. Since silicates are major corrosion products, pH and temperature have strong influence on the formation of the dominant solid phases in simulated containment water.

Even though iron phase changes are clearly evident from these simulations, the solubility of iron in containment solutions remained close to zero.

3.1 Sensitivity Analyses

The simulations are based on corrosion rates at 90 °C [194 °F]. As discussed in Chapter 2, corrosion rates could vary significantly with temperature. To gain confidence in the results, a series of simulations was conducted while varying the amount of each component and analyzing any effects on the formation of solid phases.

3.1.1 Behavior of Zinc Metal in the Simulated Containment Water

The effect of zinc corrosion rate on the formation of solid phases was evaluated by conducting sensitivity analyses at 60 °C [140 °F] and 130 °C [266 °F], 304 kPa [3 atm]. The amount of zinc in the simulated containment solution is directly related to its corrosion rate for a fixed interval of time. The zinc concentration in the basecase simulation was 2×10^{-6} mol/L. In the sensitivity analysis, the zinc concentration was varied between 1×10^{-8} and 1×10^{-4} mol/L. Figures 3-5 and 3-6 show the influence of zinc additions on the formation of solid phases and soluble $\text{Zn}(\text{OH})_3^{-1}$ phase in the simulated containment water at pH 10, 60 °C [140 °F] and 130 °C [266 °F], and 304 kPa [3 atm]. These data show that at 60 °C [140 °F], zinc was predominantly present as a solid $\text{ZnO}\cdot\text{Fe}_2\text{O}_3$ phase. However at 130 °C [266 °F], the difference in concentration between solid $\text{ZnO}\cdot\text{Fe}_2\text{O}_3$ and soluble $\text{Zn}(\text{OH})_3^{-1}$ was smaller than the difference at 60 °C [140 °F], while it is predominantly present as a soluble $\text{Zn}(\text{OH})_3^{-1}$ phase at concentrations below 3×10^{-8} mol/L at 60 °C [140 °F] and 1×10^{-6} mol/L at 130 °C [266 °F], 304 kPa [3 atm]. Zinc is predominantly present as a mixture of solid Zn_2SiO_4 and $\text{ZnO}\cdot\text{Fe}_2\text{O}_3$ phases at concentrations higher than 3×10^{-5} mol/L at 60 °C [140 °F] and 130 °C [266 °F], 304 kPa [3 atm]. The formation of Zn_2SiO_4 occurs by a reduction in $\text{Fe}_3\text{Si}_2\text{O}_5(\text{OH})_4$ concentration at 60 °C [140 °F] and $\text{Ca}_3\text{Fe}_2\text{Si}_3\text{O}_{12}$ concentration at 130 °C [266 °F], 304 kPa [3 atm]. Again, the formation of $\text{Ca}_3\text{Fe}_2\text{Si}_3\text{O}_{12}$ at 130 °C [266 °F], 304 kPa [3 atm] and the

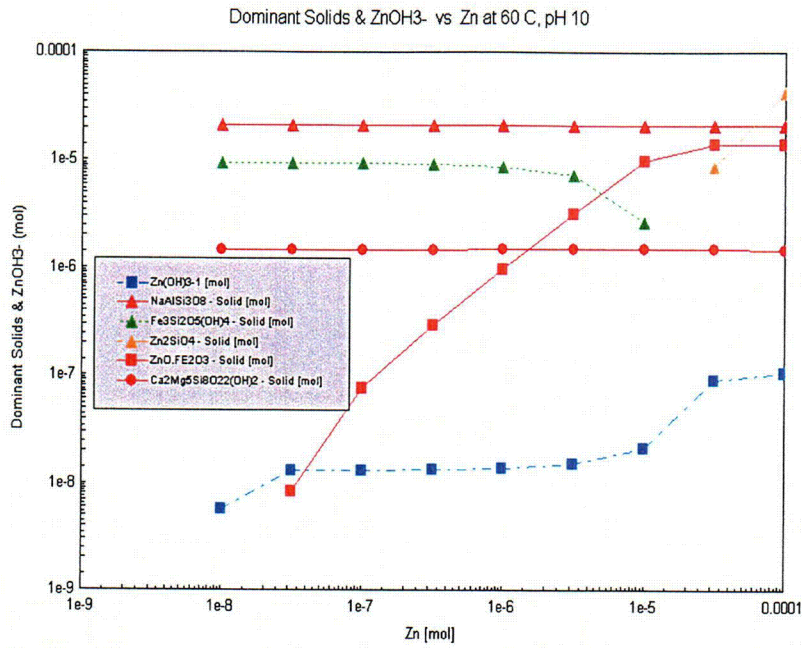


Figure 3-5. Dominant Solid Phases at 60 °C [140 °F], 101 kPa [1 atm] As a Function of Zinc in Simulated Containment Water at pH 10

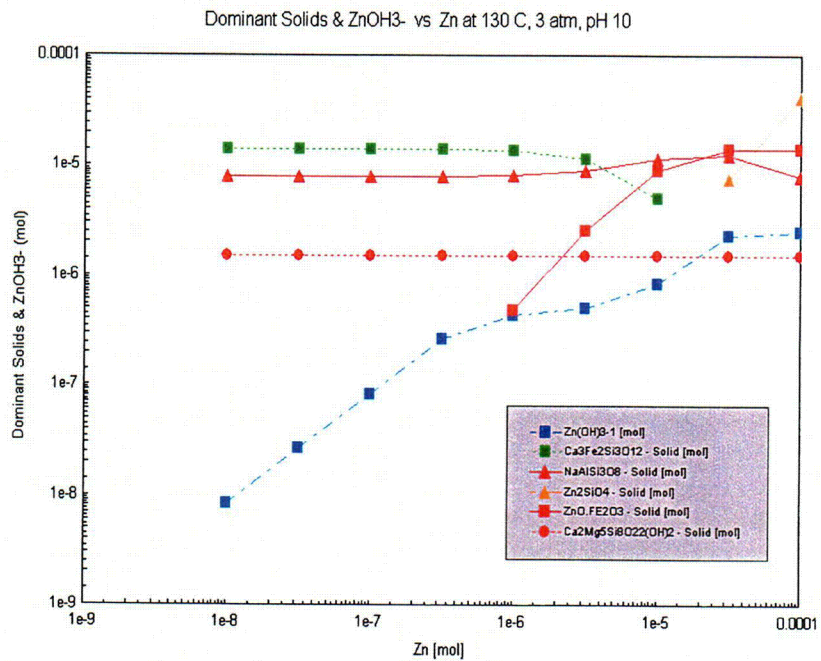


Figure 3-6. Dominant Solid Phases at 130 °C [266 °F], 101 kPa [1 atm] As a Function of Zinc in Simulated Containment Water at pH 10

formation of $\text{Fe}_3\text{Si}_4\text{O}_{10}(\text{OH})_2$ at 60 °C [140 °F] are attributed to the retrograde solubility of calcium in iron bearing minerals.

The influence of zinc was limited to interactions between solid phases associated with iron and zinc. Dominant solid phases such as $\text{NaAlSi}_3\text{O}_8$ and $\text{Ca}_2\text{Mg}_5\text{Si}_8\text{O}_{22}(\text{OH})_2$ are not influenced by the presence of zinc-containing phases in the simulated containment water. The soluble $\text{Zn}(\text{OH})_3^{1-}$ phase is present in the simulated containment water only at low concentrations of zinc. The formation of solid Zn_2SiO_4 is also consistent with a 15-day simulation test where solid Zn_2SiO_4 was a predominant solid species.

The increase in zinc concentration increases the concentrations of $\text{ZnO}\cdot\text{Fe}_2\text{O}_3$ and Zn_2SiO_4 by incorporating iron and silicon present in $\text{Fe}_3\text{Si}_2\text{O}_5(\text{OH})_4$ at 60 °C [140 °F] and $\text{Ca}_3\text{Fe}_2\text{Si}_3\text{O}_{12}$ at 130 °C [266 °F], 304 kPa [3 atm]. This exchange does not influence other solid phases that were formed in the simulated containment water after a LOCA event.

3.1.2 Behavior of Aluminum Metal in Simulated Containment Water

The source of aluminum is aluminum metal and fiber insulation. The effect of aluminum metal concentration on the formation of solid phases was evaluated by conducting a sensitivity analysis at 60 °C [140 °F] and 130 °C [266 °F], 304 kPa [3 atm]. The aluminum metal concentration in the basecase simulation was 1.5×10^{-5} mol/L. In the sensitivity analysis, the aluminum metal concentration was varied between 1×10^{-7} and 1×10^{-3} mol/L.

Figures 3-7 and 3-8 show the influence of aluminum metal additions on the formation of solid phases in the simulated containment water at 60 °C [140 °F] and 130 °C [266 °F], 304 kPa [3 atm] and pH 10. These data show that at 60 °C [140 °F], aluminum was predominantly present as a solid $\text{NaAlSi}_3\text{O}_8$ phase. However, at 130 °C [266 °F], 304 kPa [3 atm], aluminum was predominantly present as $\text{Al}(\text{OH})_4^{-1}$ soluble phase.

At 60 °C [140 °F], dominant solid phases were $\text{Fe}_3\text{Si}_2\text{O}_5(\text{OH})_4$ and $\text{NaAlSi}_3\text{O}_8$. The concentration of $\text{NaAlSi}_3\text{O}_8$ phase increased with increase in the aluminum concentration in the simulated containment water. However, for aluminum concentrations higher than 3×10^{-5} mol/L, formation of $\text{NaAlSi}_3\text{O}_8$ was followed by the transformation of $\text{Fe}_3\text{Si}_4\text{O}_{10}(\text{OH})_2$ to Fe_3O_4 and dissolution of $\text{Ca}_2\text{Mg}_5\text{Si}_8\text{O}_{22}(\text{OH})_2$ phase. In addition, when aluminum concentration exceeded 2×10^{-4} mol/L, $\text{Al}(\text{OH})_3$ was the dominant solid phase along with solid $\text{NaAlSi}_3\text{O}_8$ and soluble $\text{Al}(\text{OH})_4^{-1}$ phases.

At 130 °C [266 °F], 304 kPa [3 atm], dominant solid phases were $\text{Ca}_3\text{Fe}_2\text{Si}_3\text{O}_{12}$ and $\text{NaAlSi}_3\text{O}_8$. However, the majority of the aluminum was present as $\text{Al}(\text{OH})_4^{-1}$ soluble species at 130 °C [266 °F], 304 kPa [3 atm]. For aluminum concentration higher than 3×10^{-6} mol/L, the concentration of the $\text{NaAlSi}_3\text{O}_8$ phase increased with the increase in the aluminum concentration in the simulated containment water. In addition, for aluminum concentrations higher than 1×10^{-4} mol/L, the formation of $\text{NaAlSi}_3\text{O}_8$ was followed by the transformation of $\text{Ca}_3\text{Fe}_2\text{Si}_3\text{O}_{12}$ to Fe_3O_4 , and for aluminum concentrations higher than 3×10^{-5} mol/L, dissolution of $\text{Ca}_2\text{Mg}_5\text{Si}_8\text{O}_{22}(\text{OH})_2$ phase was observed. In addition, when aluminum concentration exceeded 2×10^{-4} mol/L, solid $\text{NaAlSi}_3\text{O}_8$ and Fe_3O_4 were the dominant solid phases. Again formation of $\text{Ca}_3\text{Fe}_2\text{Si}_3\text{O}_{12}$ at 130 °C [266 °F], 304 kPa [3 atm] and formation of $\text{Fe}_3\text{Si}_4\text{O}_{10}(\text{OH})_2$ at 60 °C [140 °F] are attributed to the retrograde solubility of calcium in iron bearing minerals.

Figures 3-7 and 3-8 demonstrate that the addition of aluminum metal increases the concentration of $\text{NaAlSi}_3\text{O}_8$ solid phase. However, the influence of aluminum metal was only observable when the concentration of aluminum metal was comparable to the aluminum concentration from the fiber insulation.

The increase in aluminum concentration increased the concentration of $\text{NaAlSi}_3\text{O}_8$ solid phase by incorporating silicon present in $\text{Fe}_3\text{Si}_2\text{O}_5(\text{OH})_4$ at 60 °C [140 °F] and in $\text{Ca}_3\text{Fe}_2\text{Si}_3\text{O}_{12}$ at 130 °C [266 °F], 304 kPa [3 atm]. In addition, for aluminum concentrations higher than 3×10^{-5} mol/L, dissolution of $\text{Ca}_2\text{Mg}_5\text{Si}_8\text{O}_{22}(\text{OH})_2$ phase was observed. In addition, formation of $\text{Al}(\text{OH})_3$ occurs for aluminum concentrations exceeding 2×10^{-4} mol/L at 60 °C [140 °F].

3.1.3 Behavior of Carbon Steel in Simulated Containment Water

The source of iron is carbon steel. The effect of iron metal concentration on the formation of solid phases was evaluated by conducting a sensitivity analysis at 60 °C [140 °F] and 130 °C [266 °F], 304 kPa [3 atm]. The iron concentration in the basecase simulation was 2.8×10^{-5} mol/L. In the sensitivity analysis, the iron concentration was varied between 1×10^{-7} and 1×10^{-3} mol/L. Figures 3-9 and 3-10 show the influence of iron additions on the formation of solid phases in the simulated containment water at a pH of approximately 10 at 60 °C [140 °F] and 130 °C [266 °F], 304 kPa [3 atm]. The data show that, irrespective of temperature and pressure, iron present in solid phases increased with an increase in iron concentration. However, the nature of iron bearing solid phases is different at different iron concentrations and temperatures.

At 60 °C [140 °F], the dominant solid phase was $\text{NaAlSi}_3\text{O}_8$. For iron concentrations below 1×10^{-5} mol/L, iron was predominantly present as $\text{ZnO} \cdot \text{Fe}_2\text{O}_3$, and above 1×10^{-5} mol/L, iron was predominantly present as $\text{Fe}_3\text{Si}_2\text{O}_5(\text{OH})_4$. Formation of Fe_3O_4 was observed at 1×10^{-3} mol/L. For iron concentrations higher than 1×10^{-4} mol/L, dissolution of $\text{Ca}_2\text{Mg}_5\text{Si}_8\text{O}_{22}(\text{OH})_2$ phase was observed.

At 130 °C [266 °F], 304 kPa [3 atm], the dominant solid phase was $\text{NaAlSi}_3\text{O}_8$. For iron concentrations below 1×10^{-6} mol/L iron was predominantly present as $\text{ZnO} \cdot \text{Fe}_2\text{O}_3$. Between 1×10^{-6} and 7×10^{-5} mol/L, iron was predominantly present as $\text{Ca}_3\text{Fe}_2\text{Si}_3\text{O}_{12}$; and above 7×10^{-5} mol/L, iron was predominantly present as Fe_3O_4 . The dissolution of $\text{Ca}_2\text{Mg}_5\text{Si}_8\text{O}_{22}(\text{OH})_2$ solid phase was not observed. For iron concentrations exceeding 5×10^{-6} mol/L, $\text{NaAlSi}_3\text{O}_8$ the solid phase was consumed by the formation of $\text{Ca}_3\text{Fe}_2\text{Si}_3\text{O}_{12}$.

Again, formation of $\text{Ca}_3\text{Fe}_2\text{Si}_3\text{O}_{12}$ at 130 °C [266 °F], 304 kPa [3 atm] and formation of $\text{Fe}_3\text{Si}_2\text{O}_5(\text{OH})_4$ at 60 °C [140 °F] are attributed to the retrograde solubility of calcium in iron bearing minerals. Despite these phase changes, all iron present was in the solid phase.

3.1.4 Behavior of Concrete in Simulated Containment Water

CaO and SiO_2 are the main contributors from concrete (assuming Ca_2SiO_4 is the primary concrete constituent). Both CaO and SiO_2 are also present in fiber insulation. The contribution of CaO from concrete is 1.3×10^{-4} mol/L, while the contribution of CaO from fiber insulation is 1.3×10^{-5} mol/L. The calcium contribution from concrete is about 10 times larger than that from fiber insulation. The effect of concrete concentration on the formation of solid phases was evaluated by conducting a sensitivity analysis at 60 °C [140 °F] and 130 °C [266 °F], 304 kPa

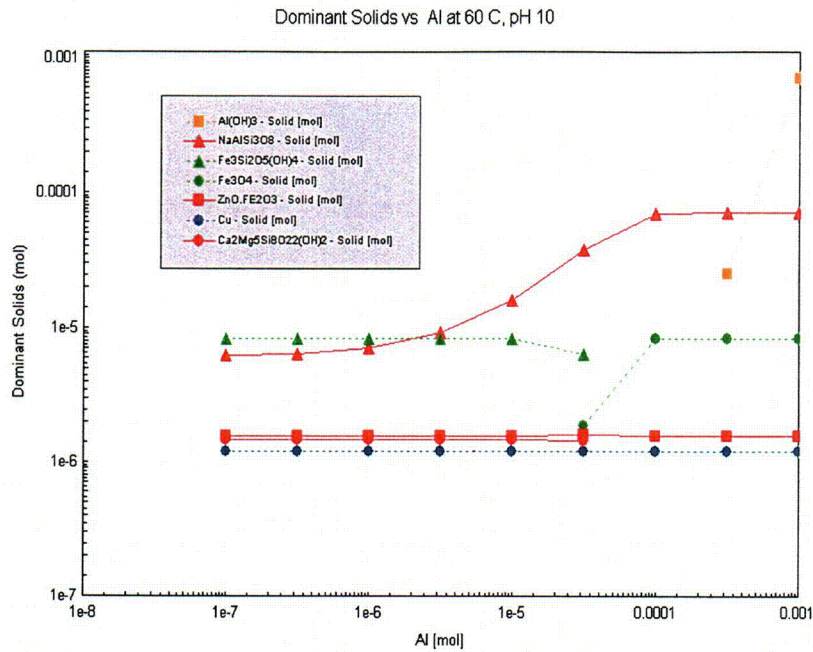


Figure 3-7. Dominant Solid Phases at 60 °C [140 °F], 101 kPa [1 atm] As a Function of Aluminum Metal in Simulated Containment Water at pH 10

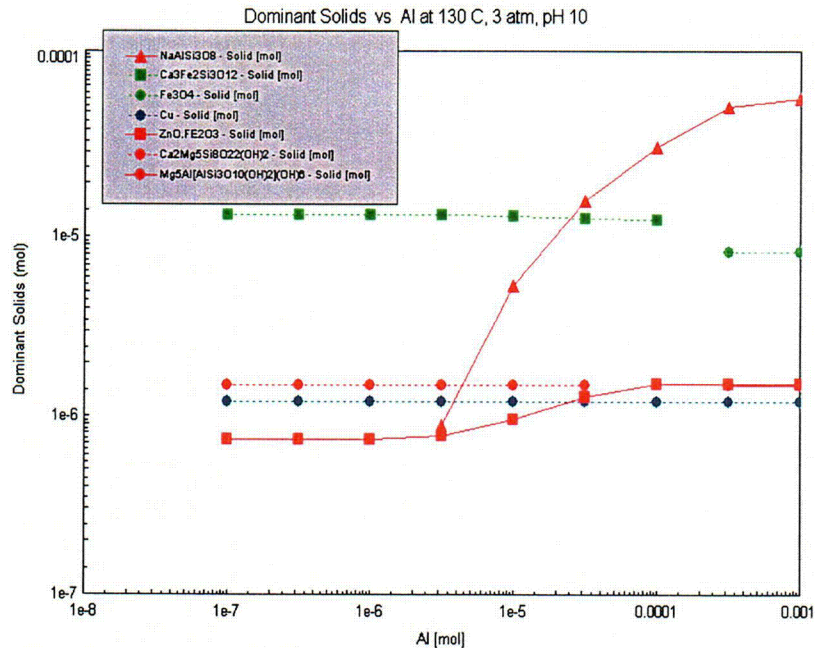


Figure 3-8. Dominant Solid Phases at 130 °C [266 °F], 304 kPa [3 atm] As a Function of Aluminum Metal in the Simulated Containment Water at pH 10

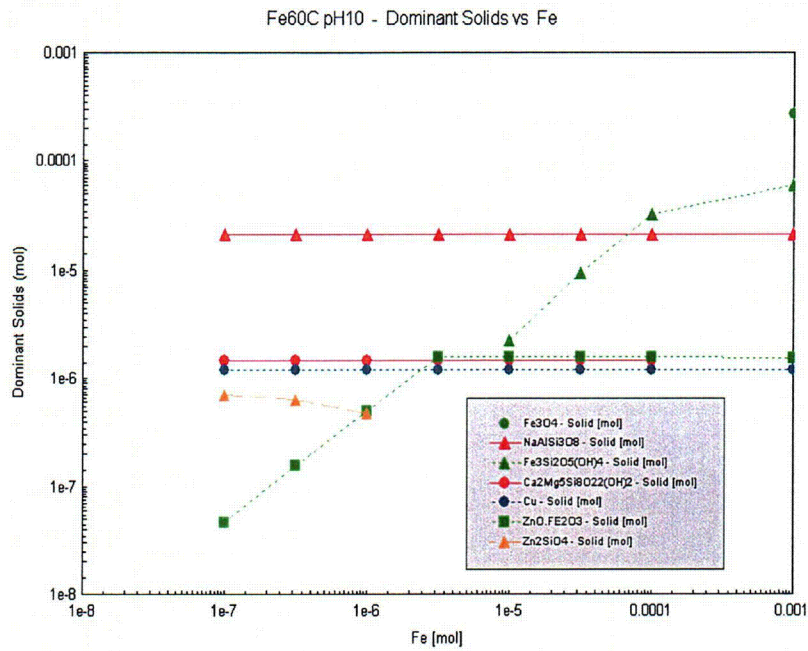


Figure 3-9. Dominant Solid Phases at 60 °C [140 °F], 101 kPa [1 atm] As a Function of Iron in Simulated Containment Water at pH 10

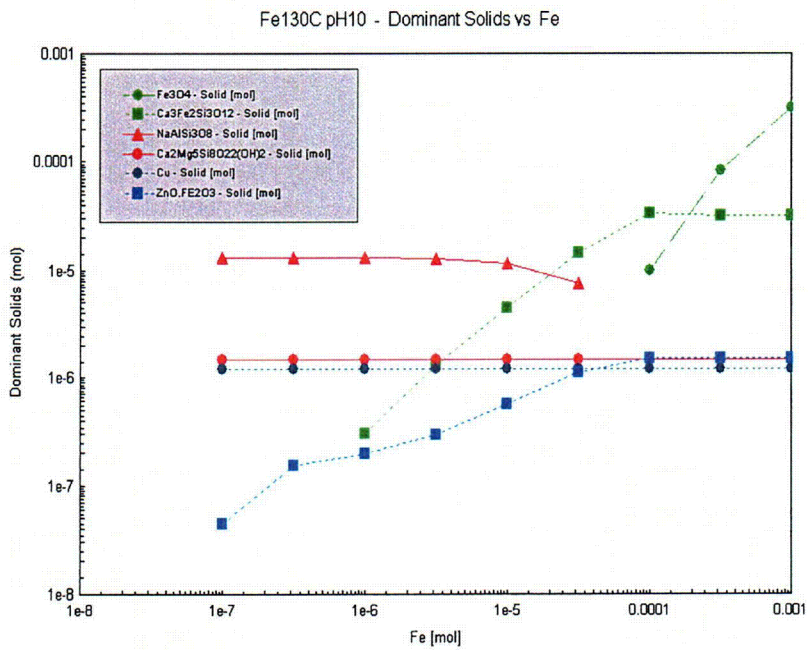


Figure 3-10. Dominant Solid Phases at 130 °C [266 °F], 304 kPa [3 atm] As a Function of Iron in Simulated Containment Water at pH 10

[3 atm]. The sensitivity analysis was conducted by varying the amount of Ca_2SiO_4 in the simulated containment water. The concrete concentration in the basecase simulation was 1.3×10^{-4} mol/L. In the sensitivity analysis, the Ca_2SiO_4 concentration was varied between 1×10^{-6} and 1×10^{-2} mol/L. The CaO and SiO_2 contributions from fiber insulation were fixed while conducting the sensitivity analysis. Figures 3-11 and 3-12 show the influence of Ca_2SiO_4 additions on the formation of solid phases in the simulated containment water at pH 10 at 60 °C [140 °F] and 130 °C [266 °F], 304 kPa [3 atm].

At 60 °C [140 °F], the dominant solid phase was $\text{NaAlSi}_3\text{O}_8$. For Ca_2SiO_4 concentrations below 3×10^{-5} mol/L, iron was predominantly present as Fe_3O_4 . Between 3×10^{-5} mol/L and 3×10^{-4} mol/L Ca_2SiO_4 concentration, iron was present as $\text{Fe}_3\text{Si}_4\text{O}_{10}(\text{OH})_2$. Above 3×10^{-4} mol/L Ca_2SiO_4 concentration, iron was predominantly present as $\text{Ca}_3\text{Fe}_2\text{Si}_3\text{O}_{12}$. As the concentration of calcium and silicon increases, the iron phase changes from oxide iron silicate to calcium iron silicate. For Ca_2SiO_4 concentrations exceeding 1×10^{-3} mol/L higher, CaSiO_3 was the dominant solid phase. Other solid phases were in insignificant concentrations. CaSiO_3 was also the dominant phase observed in a 15-day simulation.

At 130 °C [266 °F], 304 kPa [3 atm], the iron bearing phase was the dominant solid phase. The $\text{NaAlSi}_3\text{O}_8$ solid phase was observed between 1×10^{-4} and 3×10^{-3} mol/L Ca_2SiO_4 concentration. Aluminum is fairly soluble at 130 °C [266 °F], 304 kPa [3 atm]. For Ca_2SiO_4 concentration below 3×10^{-5} mol/L, iron was predominantly present as Fe_3O_4 and above 3×10^{-4} mol/L Ca_2SiO_4 concentration, iron was predominantly present as $\text{Ca}_3\text{Fe}_2\text{Si}_3\text{O}_{12}$. For Ca_2SiO_4 concentrations exceeding 1×10^{-3} mol/L higher, CaSiO_3 was the dominant solid phase. Other solid phases were in insignificant concentration. In addition, for Ca_2SiO_4 concentrations exceeding 3×10^{-3} mol/L, $\text{Ca}_2\text{B}_2\text{O}_5$ solid phase was also observed.

Based on thermodynamic simulations in the presence of Ca_2SiO_4 exceeding 1×10^{-3} mol/L, irrespective of the temperature and pressure, the concentration of CaSiO_3 increased with an increase of concrete concentration. The dominant solid phases below 1×10^{-3} mol/L Ca_2SiO_4 concentration were a series of iron bearing phases with almost all iron remaining in a solid phase along with $\text{NaAlSi}_3\text{O}_8$. At 60 °C [140 °F], $\text{NaAlSi}_3\text{O}_8$ was a dominant solid phase. At 130 °C [266 °F], 304 kPa [3 atm], aluminum is significantly soluble, and $\text{NaAlSi}_3\text{O}_8$ solid phase occurred in a narrow range of Ca_2SiO_4 concentration.

3.1.5 Behavior of Fiber Insulation in Simulated Containment Water

Insulation consists of several components as shown in Table 2-11. Both CaO and SiO_2 are also present in concrete. The effect of fiber insulation concentration on the formation of solid phases was evaluated by conducting a sensitivity analysis at 60 °C [140 °F] and 130 °C [266 °F], 304 kPa [3 atm]. In the sensitivity analysis, the insulation concentration was varied from 1×10^{-3} mol/L to 10 times the basecase fiber insulation concentration. The CaO and SiO_2 contributions from concrete were fixed while conducting the sensitivity analysis for fiber insulation.

Figures 3-13 and 3-14 show the influence of fiber insulation on the formation of dominant solid phases in the simulated containment water at a pH of 10 at 60 °C [140 °F] and 130 °C [266 °F], 304 kPa [3 atm]. At 60 °C [140 °F], 101 kPa [1 atm] in a 10 times the basecase concentration of fiber insulation in the simulated containment water, dominant solid phases were $\text{NaAlSi}_3\text{O}_8$, $\text{Ca}_2\text{Mg}_5\text{Si}_8\text{O}_{22}(\text{OH})_2$, $\text{Ca}_3\text{Fe}_2\text{Si}_3\text{O}_{12}$, and Zn_2SiO_4 . As the amount of silicon reduced on

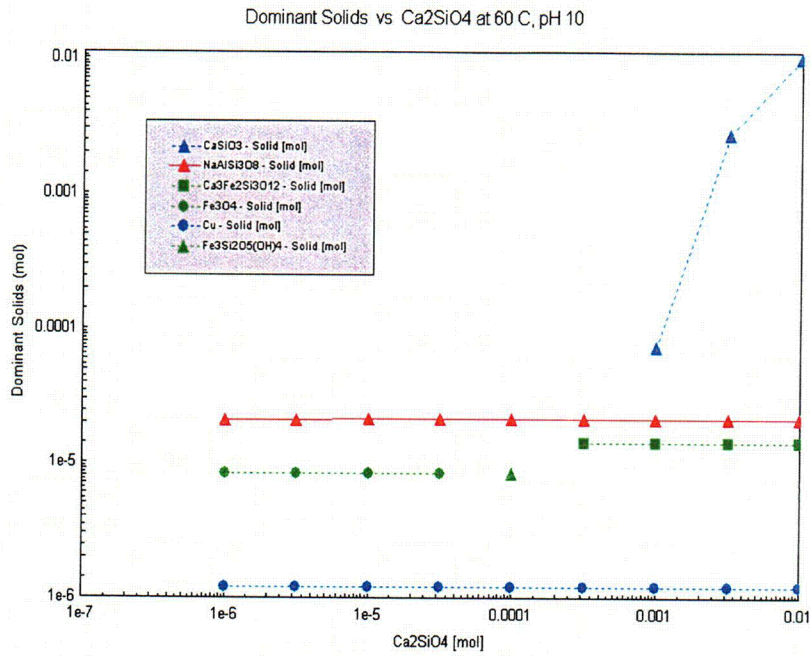


Figure 3-11. Dominant Solid Phases at 60 °C [140 °F], 101 kPa [1 atm] As a Function of Ca₂SiO₄ in Simulated Containment Water at pH 10

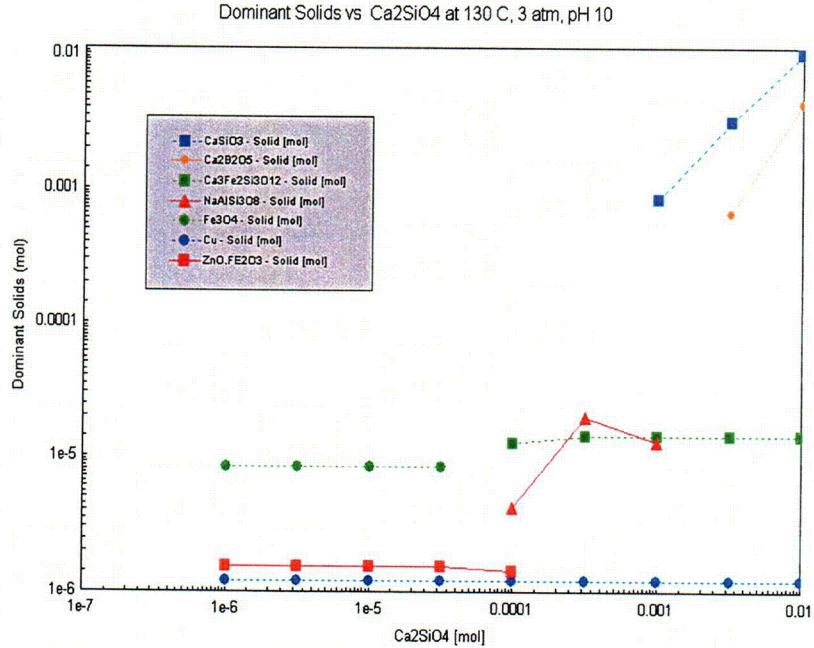


Figure 3-12. Dominant Solid Phases at 130 °C [266 °F], 304 kPa [3 atm] As a Function of Ca₂SiO₄ in Simulated Containment Water at pH 10

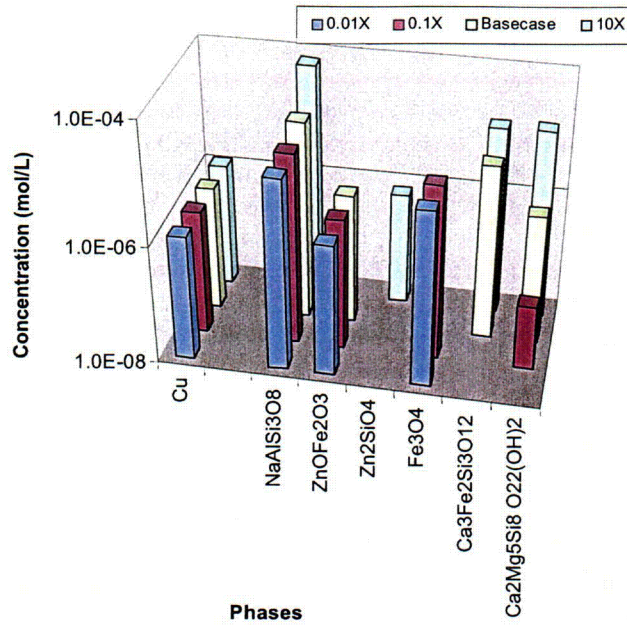


Figure 3-13. Dominant Solid Phases at 60 °C [140 °F], 101 kPa [1 atm] at Different Fiber Insulation Concentrations in Simulated Containment Water at pH 10

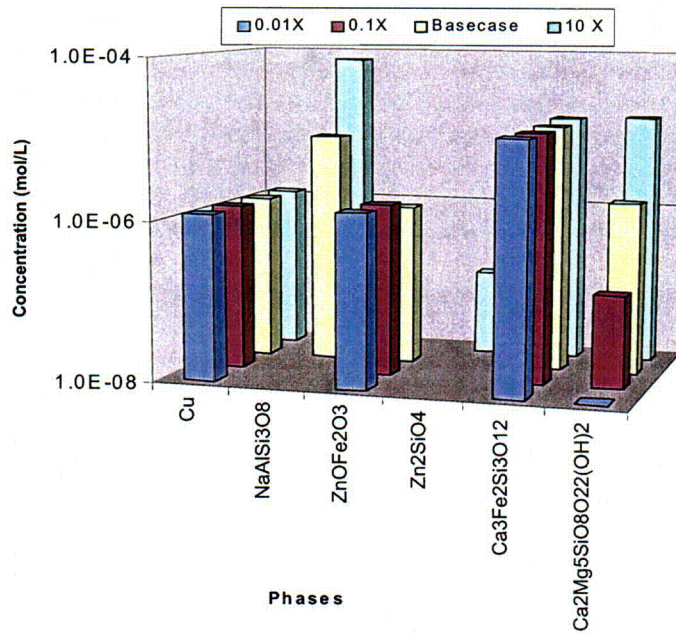


Figure 3-14. Dominant Solid Phases at 130 °C [266 °F], 304 kPa [3 atm] at Different Fiber Insulation Concentrations in Simulated Containment Water at pH 10

decreasing the concentration of insulation fiber, the silicate phases formed at 60 °C [140 °F], underwent transformation. As the 10 times the basecase concentration is reduced to basecase fiber insulation concentration, Zn_2SiO_4 changed to $ZnO \cdot Fe_2O_3$. At further reduction in fiber insulation concentration, $Ca_3Fe_2Si_3O_{12}$ converted to Fe_3O_4 . In addition, the concentration of $Ca_2Mg_5Si_8O_{22}(OH)_2$ continued to decrease as the concentration of fiber insulation was reduced. The formation of $Ca_2Mg_5Si_8O_{22}(OH)_2$ was limited by the amount of magnesium from the fiber insulation. At 1×10^{-3} times the basecase fiber insulation concentration, 100 percent of magnesium was soluble in the simulated containment water.

At 130 °C [266 °F], 304 kPa [3 atm], in a 10 times the basecase concentration of fiber insulation, dominant solid phases were the same as at 60 °C [140 °F]. Similar to the phase changes observed at 60 °C [140 °F], the silicate phases undergo transformation as the amount of silicon is reduced with decreasing concentration of insulation fiber. As 10 times the basecase concentration is reduced to the basecase fiber insulation concentration, Zn_2SiO_4 changed to $ZnO \cdot Fe_2O_3$. In addition, the concentration of $Ca_2Mg_5Si_8O_{22}(OH)_2$ continued to decrease as the concentration of fiber insulation was reduced. The formation of $Ca_2Mg_5Si_8O_{22}(OH)_2$ was limited by the amount of magnesium from the fiber insulation. At 1×10^{-3} times the basecase fiber insulation concentration, 100 percent of magnesium was soluble in the simulated containment water. However, no change in $Ca_3Fe_2Si_3O_{12}$ phase was observed in simulations at 130 °F [266 °F] and 304 kPa [3 atm].

Irrespective of the temperature and pressure, the formation of silicate phases continued even at 1/1000 of the basecase concentration but the number of phases and their concentration reduced as the concentration of fiber insulation reduced. At 60 °C [140 °F], iron phase distribution underwent a significant change. At lower fiber concentration, iron was predominantly present as Fe_3O_4 . However, as the concentration increases, iron combined with zinc to form $Ca_3Fe_2Si_3O_{12}$. At 130 °C [266 °F], 304 kPa [3 atm], iron was present exclusively as $Ca_3Fe_2Si_3O_{12}$.

This fiber insulation sensitivity analysis at pH 10 indicated no significant impact on the formation of solid phases over a wide fiber insulation concentration range in simulated containment water after a LOCA event.

4 FORMATION OF SOLID PHASES DUE TO CORROSION OF COMPONENTS IN Na₃PO₄ CONTAINMENT WATER

This chapter is similar to Chapter 3 but substitutes the chemical environment with Na₃PO₄ containment water, resulting in a pH ≈ 7.

Simulations presented in this chapter assume a pressure of 507 kPa [5 atm] and 150 °C [302 °F] as the peak temperature for the containment water immediately following a LOCA event. The influence of pressure, temperature, and pH was studied by speciating a fixed amount of each component based on its corrosion rate. Simulations were conducted at 150 °C [302 °F] at 507 kPa [5 atm], 130 °C [266 °F] at 304 kPa [3 atm], and 90 °C [194 °F] and 60 °C [140 °F] at 101 kPa [1 atm]. The amount of each component was estimated based on corrosion at 90 °C [194 °F] for 0.5 hour. Given the significant uncertainties in the corrosion rates in borated water as a function of temperature and to provide a comparative assessment of the effect of temperature and pressure, a fixed amount of components was used as an input for the simulations. Input values used in the simulations are shown in Table 3-1. The basis for selecting these values was discussed in Chapter 2. The boron concentration was fixed at 0.26 M [2,800 ppm]. Simulations were conducted at a pH of 7, and the formation of solid phases as a function of temperature and pressure was examined. A pH of 7 was obtained by the addition of 8.4×10^{-3} mol/L of Na₃PO₄. The precipitation of phases during a 15-day operation of the containment system at 60 °C [140 °F] was estimated by multiplying the hourly corrosion rate of each component by 720. An additional amount of 1.5 M H₃BO₃ was needed to maintain a pH 7. An increase in pH was observed as the concentration of corrosion components increased in the simulation. This increase in pH was attributed to the hydrolysis reactions associated with the fiber insulation. Corrosion rates of the components at 90 °C [194 °F] were used for simulation at different temperatures. These estimates lead to a conservative assessment of long-term corrosion. Corrosion rates of components are expected to be lower at 60 °C [140 °F] which is the likely temperature of the containment water during steady-state.

Table 4-1 shows the calculated pH and Eh at quantity of temperatures and pressures in borated water with 0.26-M [2,800-ppm] boron and 8.4×10^{-3} mol/L Na₃PO₄. At 60 °C [140 °F], pH in 8.4×10^{-3} mol/L of Na₃PO₄ borated water with 0.26-M [2,800-ppm] boron was 7. A slight decrease in pH was observed with the increase in the temperature and pressure. Similarly, redox potential at 60 °C [140 °F] was approximately -0.4 V versus the standard hydrogen electrode (V_{SHE}). Figure 4-1 shows the concentration of solid phases at a pH of 7. Table 4-2 provides a percent solid phase for each element present in the simulated containment water.

Test Conditions	pH	Eh (V _{SHE})
60 °C [140 °F] at 101 kPa [1 atm]	7.0	-0.40
90 °C [194 °F] at 101 kPa [1 atm]	7.0	-0.42
130 °C [266 °F] at 304 kPa [3 atm]	7.0	-0.44
150 °C [302 °F] at 507 kPa [5 atm]	7.0	-0.45

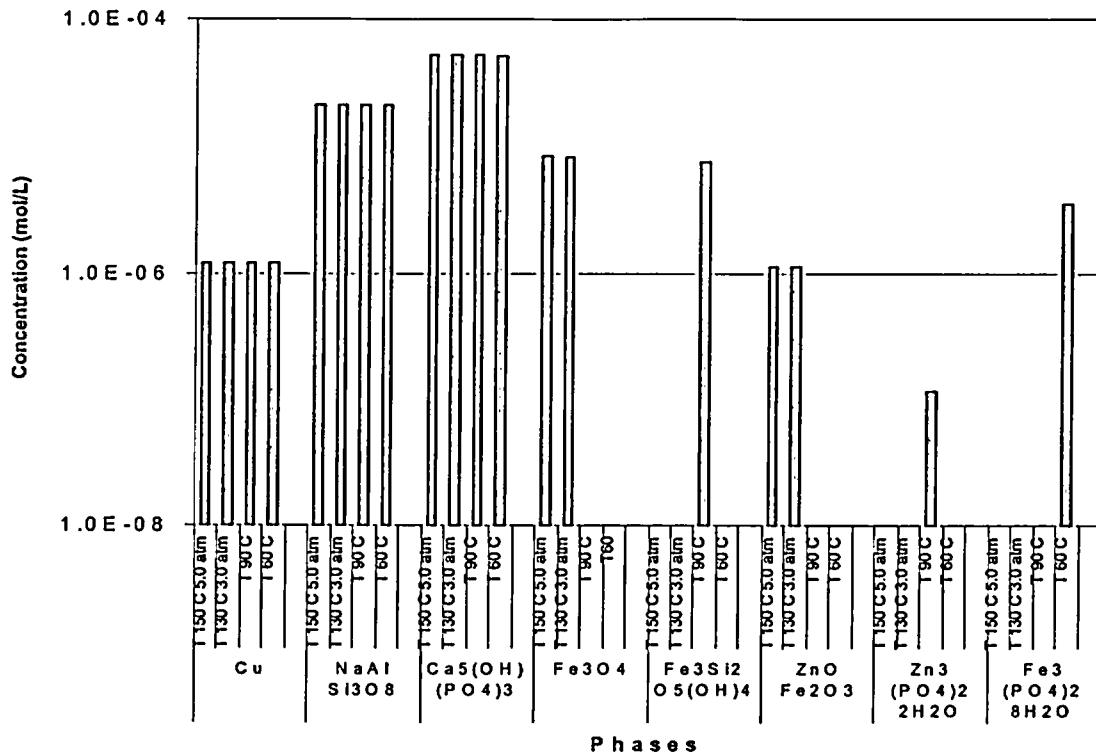


Figure 4-1. Concentration, in mol/L, of Dominant Solid Phases As a Function of Temperature and Pressure in 0.26-M [2,800-ppm] Boron in Na₃PO₄ Simulated Containment Water at pH 7

Temperature and Pressure	Magnesium (Percent)	Iron (Percent)	Aluminum (Percent)	Zinc (Percent)	Silicon (Percent)	Calcium (Percent)
150 °C [302 °F], 507 kPa [5 atm]	0	91	100	90	35	100
130 °C [266 °F], 304 kPa [3 atm]	0	96	100	72	29	99
90 °C [194 °F], 101 kPa [1 atm]	0	82	100	22	36	99
60 °C [140 °F], 101 kPa [1 atm]	0	38	100	0	29	96

Table 4-3 provides a percent distribution of solid phases for compounds observed at different temperatures and pressures. Table 4-3 shows that over 90 percent of the solids precipitated come from $\text{Ca}_5(\text{OH})(\text{PO}_4)_3$ and $\text{NaAlSi}_3\text{O}_8$ phases at pH 7. The contributions from other solid phases is around 10 percent. The other phases include $\text{Fe}_3\text{Si}_4\text{O}_{10}(\text{OH})_2$, $\text{Fe}_3(\text{PO}_4)_2 \cdot 8\text{H}_2\text{O}$, Fe_3O_4 , $\text{ZnO} \cdot \text{Fe}_2\text{O}_3$, and $\text{Zn}_3(\text{OH})(\text{PO}_4)_3 \cdot 2\text{H}_2\text{O}$. The contribution of zinc containing phases was less than 2 percent. The $\text{Ca}_5(\text{OH})(\text{PO}_4)_3$ solid phase concentration remained the same from 150 °C [302 °F], 507 kPa [5 atm] to 60 °C [140 °F], and contained almost 100 percent of the calcium present in the simulated containment water. There was no phase change observed for copper. Most of the copper added in the simulation remained as copper metal. Aluminum is present as aluminum metal and fiber insulation. All the aluminum was in $\text{NaAlSi}_3\text{O}_8$ and no change in concentration was observed in the simulation temperature range. A redistribution of iron phases similar to the iron behavior in pH 10 was observed. However, different phases were formed. At temperatures above 130 °C [266 °F], 304 kPa [3 atm], iron was present as Fe_3O_4 and $\text{ZnO} \cdot \text{Fe}_2\text{O}_3$. Greater than 90-percent of the iron was associated with these two solid phases. $\text{ZnO} \cdot \text{Fe}_2\text{O}_3$ phase contained 90-percent zinc at 150 °C [302 °F], 507 kPa [5 atm] and 72 percent zinc at 130 °C [266 °F], 304 kPa [3 atm]. At 90 °C [194 °F], 101 kPa [1 atm], zinc was present as $\text{Zn}_3(\text{OH})(\text{PO}_4)_3 \cdot 2\text{H}_2\text{O}$ which incorporated about 22-percent zinc, and iron was present as $\text{Fe}_3\text{Si}_4\text{O}_{10}(\text{OH})_2$ which incorporated 82-percent iron. At 60 °C [140 °F], 100 percent of zinc was present as a ZnHPO_4 soluble phase, while 38 percent of the iron was present as $\text{Fe}_3(\text{PO}_4)_2 \cdot 8\text{H}_2\text{O}$. Magnesium that was released from fiber insulation was 100-percent soluble. Between 150 °C [302 °F], 507 kPa [5 atm] and 60 °C [140 °F], 29 to 36-percent of the silicon was distributed within various solid silicates. No significant change in silicon distribution was observed.

Simulations indicated no significant changes in the precipitation of dominant solid phases resulting from silicon, aluminum, calcium, and magnesium as the temperature decreased from 150 to 60 °C [302 to 140 °F] and the pressure dropped from 5 to 101 kPa [1 atm]. Significant phase changes and redistribution of iron and zinc phases were observed as shown in Figure 4-1. In addition, the elemental concentration for both iron and zinc in solid phase reduced significantly as shown in Table 4-2. While reduction in the amount of solid phases at a lower temperature would assist in unclogging the sump pump, it is important to analyze the formation of phases during steady-state operations. As corrosion proceeds, the concentration of corroded species increases with time. Figure 4-2 compares the observed solid phases at

Temperature and Pressure	$\text{NaAlSi}_3\text{O}_8$ (Percent)	$\text{Ca}_5(\text{OH})(\text{PO}_4)_3$ (Percent)	$\text{Fe}_3\text{Si}_4\text{O}_{10}(\text{OH})_2$ (Percent)	$\text{Fe}_3(\text{PO}_4)_2 \cdot 8\text{H}_2\text{O}$ (Percent)	$\text{ZnO} \cdot \text{Fe}_2\text{O}_3$ (Percent)	Fe_3O_4 (Percent)
150 °C [302 °F], 507 kPa [5 atm]	25	63	—	—	2	10
130 °C [266 °F], 304 kPa [3 atm]	25	63	1	—	4	10
90 °C [194 °F], 101 kPa [1 atm]	26	64	9	—	—	—
60 °C [140 °F], 101 kPa [1 atm]	28	67	—	5	—	—

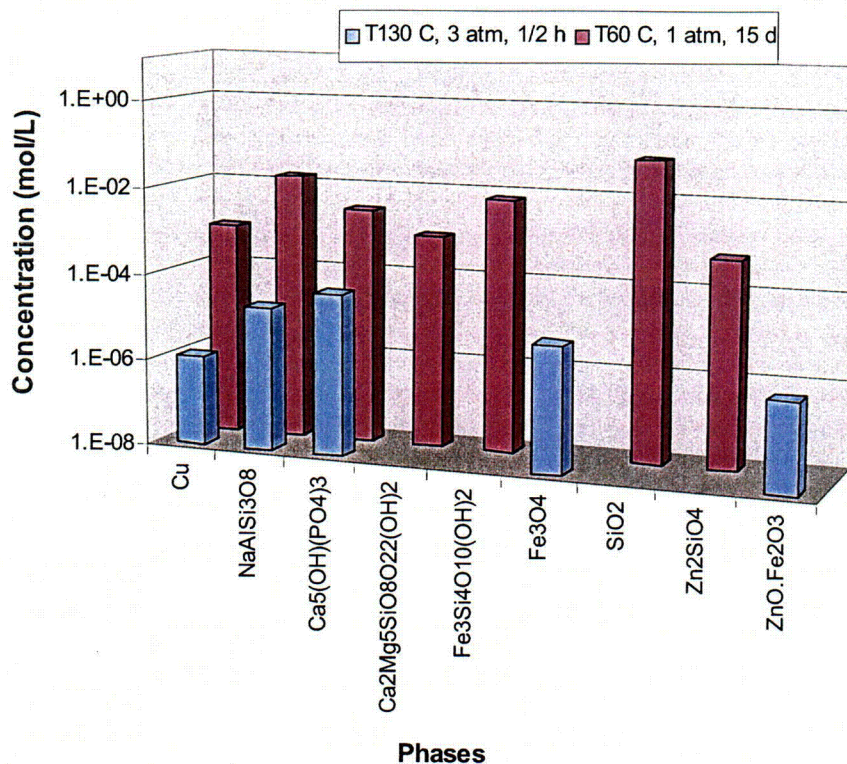


Figure 4-2. Concentration, in mol/L, of Dominant Solid Phases at 150 °C [302 °F], 507 kPa [5 atm] for 0.5 Hour at 60 °C [140 °F] for 15 Days in a 0.26 M [2,800 ppm] Boron, Na₃PO₄ Simulated Containment Water at pH 7

pH 7 after a 15-day corrosion test at 60 °C [140 °F] with 0.5 hour corrosion at 130 °C [266 °F], 304 kPa [3 atm]. The dominant solid phases formed at pH 7 after 15 days were Ca₅(OH)(PO₄)₃, NaAlSi₃O₈, Ca₂Mg₅Si₈O₂₂(OH)₂, Fe₃Si₄O₁₀(OH)₂, and SiO₂ with a minor quantity of Zn₂SiO₄ in the simulated containment water. While Ca₅(OH)(PO₄)₃ and NaAlSi₃O₈ concentrations were similar to the high-temperature high-pressure phases, CaSiO₃, Ca₂Mg₅Si₈O₂₂(OH)₂, Fe₃Si₄O₁₀(OH)₂, and Zn₂SiO₄ were not observed at high-temperature and pressure for pH 7 at 130 °C [266 °F], 304 kPa [3 atm].

This simulation indicates that solid phases formed in the first 0.5 hour of a LOCA event at 130 °C [266 °F], 304 kPa [3 atm] may not be found in a 15-day or longer simulation test at 60 °C [140 °F].

4.1 Sensitivity Analyses

The above simulations in Na₃PO₄ containment water at pH 7 are based on corrosion rates at 90 °C [194 °F]. As discussed in Chapter 2, corrosion rates could vary significantly with

temperature. To gain confidence in simulations, a series of simulations was conducted by varying the amount of each component and analyzing its influence on the formation of solid phases.

4.1.1 Behavior of Zinc Metal in the Simulated Containment Water

The effect of zinc corrosion rate on the formation of solid phases was evaluated by conducting a sensitivity analysis at 60 °C [140 °F] and 130 °C [266 °F], 304 kPa [3 atm]. The zinc concentration in the basecase simulation was 2×10^{-6} mol/L. In the sensitivity analysis the zinc concentration was varied between 1×10^{-8} and 1×10^{-4} mol/L. Figures 4-3 and 4-4 show the influence of zinc additions on the formation of solid phases in the simulated containment water at pH 7; 60 °C [140 °F]; and 130 °C [266 °F]; 304 kPa [3 atm]. Also shown in the figures are soluble Zn(OH)^{+1} and Zn^{+2} phases.

The data show that at 60 °C [140 °F], zinc was predominantly present as a soluble phase consisting of Zn(OH)^{+1} and Zn^{+2} below 2.5×10^{-6} mol/L concentration of zinc, while at 130 °C [266 °F], 304 kPa [3 atm] a zinc-based soluble phase was formed below 1×10^{-6} mol/L zinc concentration. At 60 °C [140 °F] and zinc concentration exceeding 2.5×10^{-6} mol/L, zinc was predominantly present as $\text{Zn}_3(\text{OH})(\text{PO}_4)_3 \cdot 2\text{H}_2\text{O}$ solid phase. At 60 °C [140 °F], dominant phases such as $\text{Ca}_5(\text{OH})(\text{PO}_4)_3$ and $\text{NaAlSi}_3\text{O}_8$, were not influenced by zinc additions as shown in Figure 4-3. However, at 130 °C [266 °F], 304 kPa [3 atm] and zinc concentrations exceeding 1×10^{-6} mol/L, zinc was present as $\text{ZnO} \cdot \text{Fe}_2\text{O}_3$ up to 2×10^{-5} mol/L and as $\text{Zn}_3(\text{OH})(\text{PO}_4)_3 \cdot 2\text{H}_2\text{O}$ at concentrations exceeding 2×10^{-5} mol/L. In addition, a reduction in Fe_3O_4 concentration was observed due to incorporation of iron in $\text{ZnO} \cdot \text{Fe}_2\text{O}_3$. At 130 °C [266 °F], 304 kPa [3 atm], dominant phases such as $\text{Ca}_5(\text{OH})(\text{PO}_4)_3$ and $\text{NaAlSi}_3\text{O}_8$, were not influenced by zinc additions as shown in Figure 4-4.

The influence of zinc was limited to interactions between solid phases associated with iron and zinc. Dominant solid phases such as $\text{NaAlSi}_3\text{O}_8$ and $\text{Ca}_5(\text{OH})(\text{PO}_4)_3$ were not influenced by the presence of zinc-containing phases in the simulated containment water. The formation of solid Zn_2SiO_4 occurred in a 15-day simulation test where solid Zn_2SiO_4 was a predominant solid species. The increase in zinc concentration increased the concentrations of $\text{Zn}_3(\text{OH})(\text{PO}_4)_3 \cdot 2\text{H}_2\text{O}$ at 60 °C [140 °F], and $\text{Zn}_3(\text{OH})(\text{PO}_4)_3 \cdot 2\text{H}_2\text{O}$ and $\text{ZnO} \cdot \text{Fe}_2\text{O}_3$ at 130 °C [266 °F], 304 kPa [3 atm].

4.1.2 Behavior of Aluminum Metal in Simulated Containment Water

The source for aluminum is aluminum metal and fiber insulation. The effect of aluminum metal concentration on the formation of solid phases was evaluated by conducting a sensitivity analysis at 60 °C [140 °F], and 130 °C [266 °F], 304 kPa [3 atm]. The aluminum concentration in the basecase simulation was 1.5×10^{-5} mol/L. In the sensitivity analysis, the aluminum concentration was varied between 1×10^{-7} and 1×10^{-3} mol/L. Figures 4-5 and 4-6 show the influence of aluminum additions on the formation of solid phases in the simulated containment water at pH 7 at 60 °C [140 °F] and 130 °C [266 °F], 304 kPa [3 atm]. These data show that in the simulated containment water at pH 7 at 60 °C [140 °F], aluminum was predominantly present as $\text{NaAlSi}_3\text{O}_8$. However, for aluminum concentrations exceeding 1.0×10^{-4} mol/L, formation of Al(OH)_3 occurred at 60 °C [140 °F], and AlO(OH) forms at 130 °C [266 °F], 304 kPa [3 atm]. However, in a 15-day simulation, aluminum was exclusively present as $\text{NaAlSi}_3\text{O}_8$. At both temperatures, $\text{Ca}_5(\text{OH})(\text{PO}_4)_3$ was an additional dominant solid phase. Other solid phases

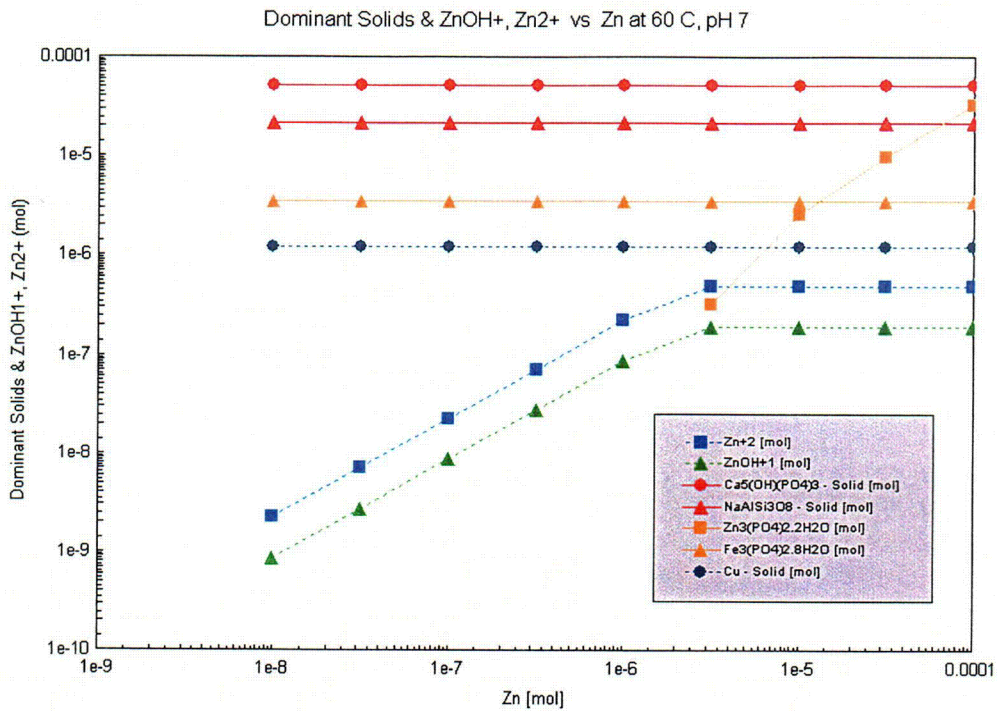


Figure 4-3. Dominant Solid Phases at 60 °C [140 °F], 101 kPa [1 atm] As a Function of Zinc in Simulated Containment Water at pH 7

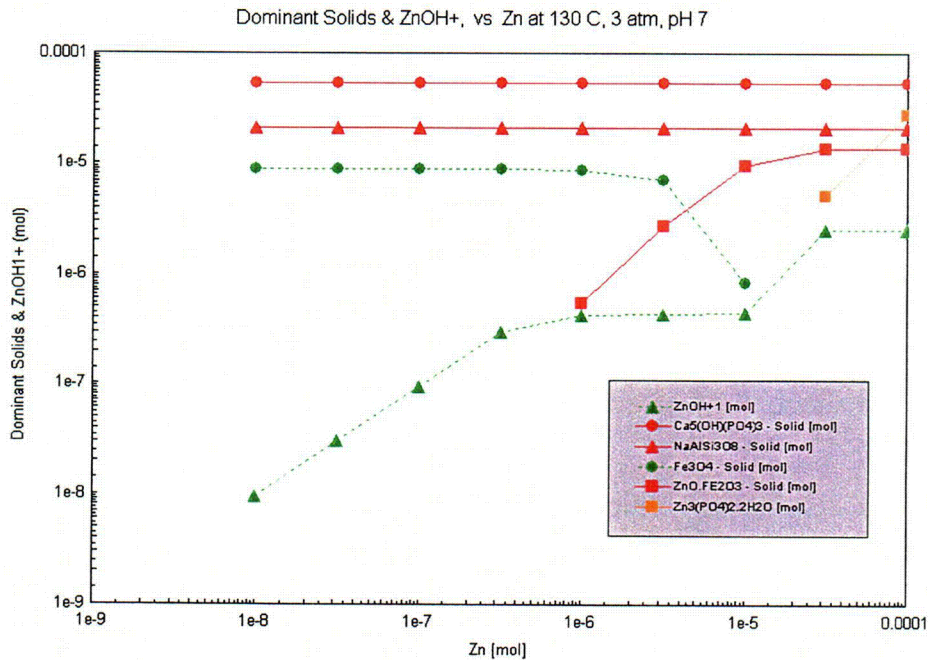


Figure 4-4. Dominant Solid Phases at 130 °C [266 °F], 304 kPa [3 atm] As a Function of Zinc in Simulated Containment Water at pH 7

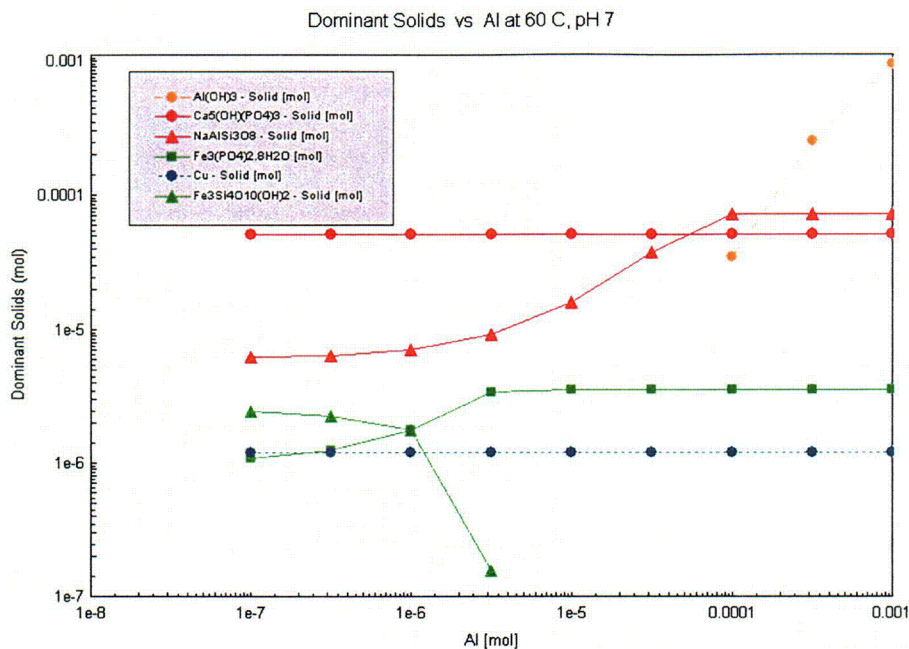


Figure 4-5. Dominant Solid Phases at 60 °C [140 °F], 101 kPa [1 atm] As a Function of Aluminum in Simulated Containment Water at pH 7

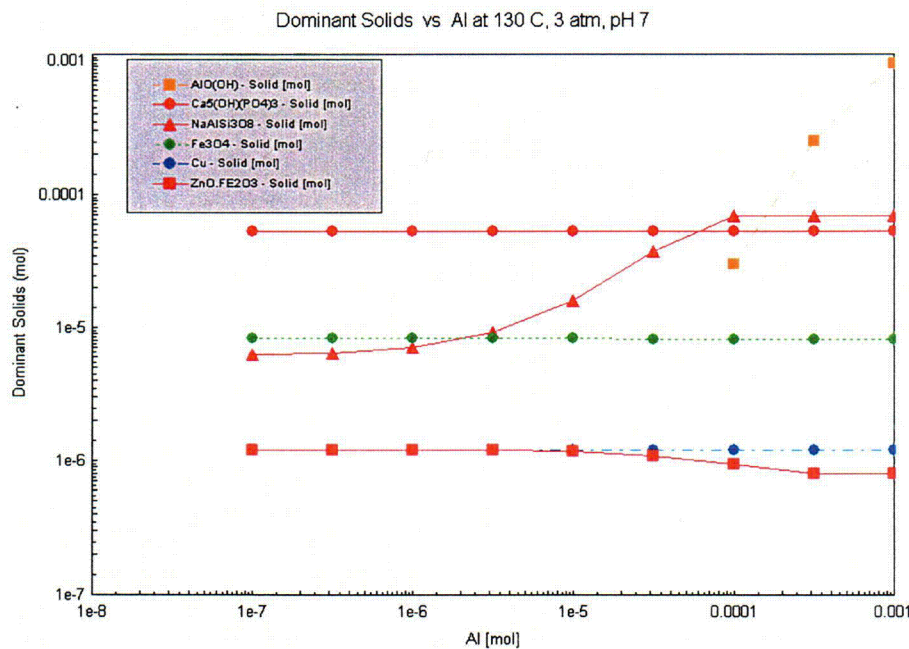


Figure 4-6. Dominant Solid Phases at 130 °C [266 °F], 304 kPa [3 atm] As a Function of Aluminum Concentration in Simulated Containment Water at pH 7

were at least an order of magnitude lower in concentration. Even though at 60 °C [140 °F], $\text{Fe}_3\text{Si}_4\text{O}_{10}(\text{OH})_2$ transformed to $\text{Fe}_3(\text{PO}_4)_2 \cdot 8\text{H}_2\text{O}$, the concentration of iron containing solid phase remained well below that of the dominant $\text{Ca}_5(\text{OH})(\text{PO}_4)_3$ phase.

The influence of aluminum was limited to increasing the concentration of $\text{NaAlSi}_3\text{O}_8$ and formation of $\text{Al}(\text{OH})_3$ that occurred at 60 °C [140 °F], and $\text{AlO}(\text{OH})$ at 130 °C [266 °F], 304 kPa [3 atm]. $\text{NaAlSi}_3\text{O}_8$ and $\text{Ca}_5(\text{OH})(\text{PO}_4)_3$ remained dominant solid phases. For aluminum concentrations exceeding 3.0×10^{-4} mol/L, the dominant phase was $\text{Al}(\text{OH})_3$ at 60 °C [140 °F], and $\text{AlO}(\text{OH})$ at 130 °C [266 °F], 304 kPa [3 atm]. However, in a 15-day simulation, aluminum was exclusively present as $\text{NaAlSi}_3\text{O}_8$.

4.1.3 Behavior of Carbon Steel in Simulated Containment Water

The contribution for iron comes from carbon steel. The effect of iron metal concentration on the formation of solid phases was evaluated by conducting sensitivity analysis at 60 °C [140 °F] and 130 °C [266 °F], 304 kPa [3 atm]. The iron concentration in the basecase simulation was 2.8×10^{-5} mol/L. In the sensitivity analysis, the iron concentration was varied between 1×10^{-7} and 1×10^{-3} mol/L. Figures 4-7 and 4-8 show the influence of iron additions on the formation of solid phases in the simulated containment water at a pH of 7 at 60 °C [140 °F] and 130 °C [266 °F], 304 kPa [3 atm].

The data show that at 60 °C [140 °F] and below 7×10^{-4} mol/L iron concentration, iron was predominantly present as a soluble Fe^{+2} phase, while at 130 °C [266 °F], 304 kPa [3 atm], an iron-based soluble phase was formed below 1×10^{-6} mol/L iron concentration. At 60 °C [140 °F] and iron concentration exceeding 7×10^{-4} mol/L, iron was predominantly present as $\text{Fe}_3(\text{PO}_4)_2 \cdot 8\text{H}_2\text{O}$ solid phase. At 60 °C [140 °F], dominant phases were $\text{Ca}_5(\text{OH})(\text{PO}_4)_3$ and $\text{NaAlSi}_3\text{O}_8$, and were not influenced by iron additions as shown in Figure 4-7. However, at 130 °C [266 °F], 304 kPa [3 atm] and iron concentrations exceeding 1×10^{-6} mol/L, iron was present as $\text{ZnO} \cdot \text{Fe}_2\text{O}_3$ up to 1×10^{-5} mol/L, and as Fe_3O_4 from 1×10^{-5} mol/L and in combination with $\text{Fe}_3\text{Si}_2\text{O}_5(\text{OH})_4$ for concentrations exceeding 3×10^{-4} mol/L iron. The contribution of iron phases below 3×10^{-5} mol/L iron concentration was insignificant compared to other dominant phases.

The influence of iron was limited to increasing the concentration of $\text{Fe}_3(\text{PO}_4)_2 \cdot 8\text{H}_2\text{O}$ at 60 °C [140 °F], and the concentration of Fe_3O_4 and $\text{Fe}_3\text{Si}_2\text{O}_5(\text{OH})_4$ at 130 °C [266 °F], 304 kPa [3 atm]. Iron had no influence on $\text{NaAlSi}_3\text{O}_8$ and $\text{Ca}_5(\text{OH})(\text{PO}_4)_3$ which were the dominant solid phases. The influence of iron was not expected below 3×10^{-4} mol/L concentration of iron.

4.1.4 Behavior of Concrete in Simulated Containment Water

CaO and SiO_2 are the main contributors from concrete (assuming Ca_2SiO_4 is the primary concrete constituent). Both CaO and SiO_2 are also present in fiber insulation. The contribution of CaO from concrete is 2×10^{-4} mol/L while the contribution of CaO from insulation is 8.3×10^{-4} mol/L. The effect of concrete concentration on the formation of solid phases was evaluated by conducting a sensitivity analysis at 60 °C [140 °F] and 130 °C [266 °F], 304 kPa [3 atm]. The analysis was conducted by varying the amount of Ca_2SiO_4 in the simulated containment solution. The concrete concentration in the basecase simulation was 1.3×10^{-4} mol/L. In the sensitivity analysis, the Ca_2SiO_4 concentration varied between 1×10^{-6}

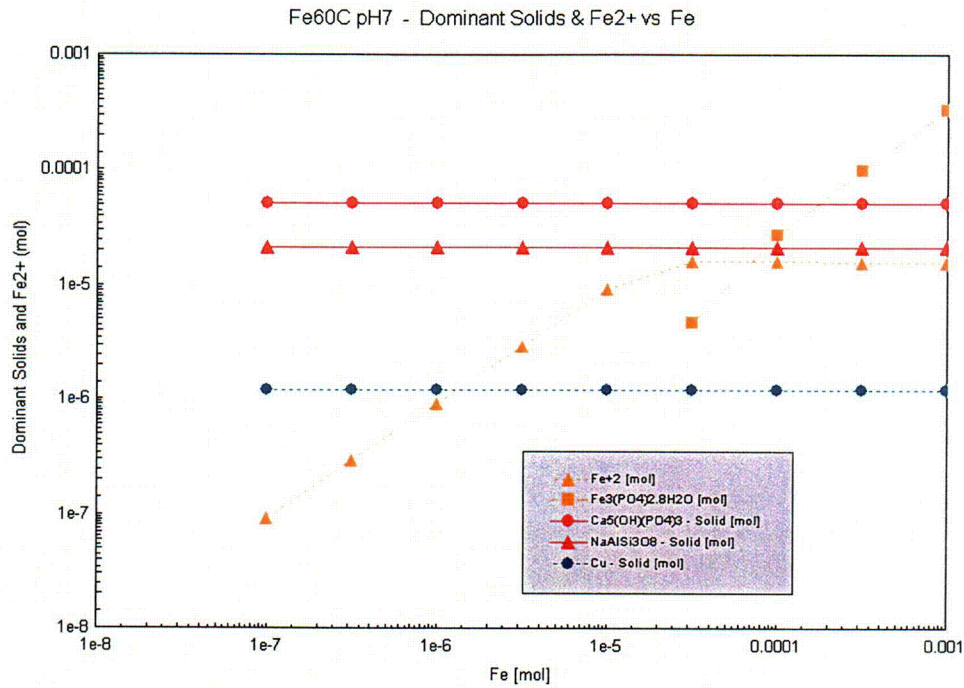


Figure 4-7. Dominant Solid Phases at 60 °C [140 °F], 101 kPa [1 atm] As a Function of Iron Concentration in the Simulated Containment Water at pH 7

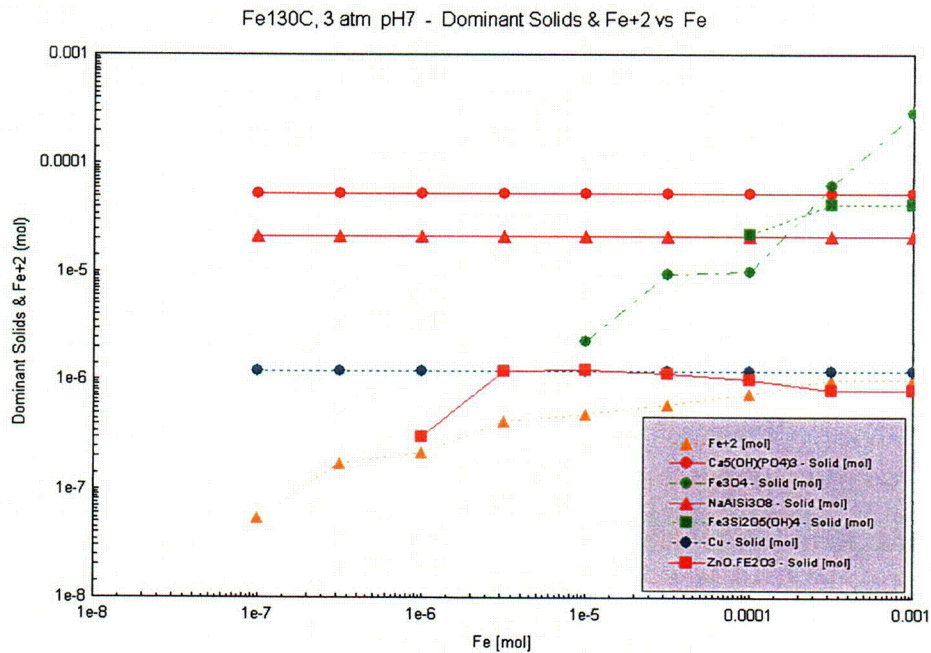


Figure 4-8. Dominant Solid Phases at 130 °C [266 °F], 304 kPa [3 atm] As a Function of Iron Concentration in Simulated Containment Water at pH 7

and 1×10^{-2} mol/L. The CaO and SiO₂ contributions from fiber insulation were fixed while conducting the sensitivity analysis for concrete.

Figures 4-9 and 4-10 show the influence of concrete additions on the formation of dominant phases in the simulated containment water at a pH of 7 at 60 °C [140 °F] and 130 °C [266 °F], 304 kPa [3 atm]. These data show that concrete was predominantly present as Ca₅(OH)(PO₄)₃, and its concentration increased with the concrete concentration. For concrete concentration exceeding 1×10^{-4} mol/L at 60 °C [140 °F] and 3×10^{-4} mol/L at 130 °C [266 °F], 304 kPa [3 atm], SiO₂ was observed as a dominant solid phase along with Ca₅(OH)(PO₄)₃. One other dominant solid phase included NaAlSi₃O₈ for which concentration did not change with temperature or pressure. A conversion of Fe₃(PO₄)₂·8H₂O to Fe₃Si₄O₁₀(OH)₂ at concrete concentration of 1×10^{-4} mol/L at 60 °C [140 °F]. At 130 °C [266 °F], 304 kPa [3 atm], Fe₃O₄ converted to Fe₃Si₄O₁₀(OH)₂ at about 1×10^{-4} mol/L and to Ca₃Fe₂Si₃O₁₂ at 1×10^{-3} mol/L. At 3.5×10^{-4} mol/L and 60 °C [140 °F] concentration of concrete, ZnO·Fe₂O₃ converted to solid Zn₂SiO₄. At 130 °C [266 °F], 304 kPa [3 atm], zinc was soluble below 3×10^{-3} mol/L concrete concentration. However, the concentration of zinc-based solid phases was insignificant compared to the dominant solid phases.

The influence of concrete was limited to increasing the concentration of Ca₅(OH)(PO₄)₃ at 60 °C [140 °F], and 130 °C [266 °F], 304 kPa [3 atm]. At concrete concentrations exceeding 1×10^{-3} mol/L, SiO₂ was observed as an additional dominating solid phase. While transformation of the zinc phase was insignificant, the transformation of iron phases could be important below 1×10^{-4} mol/L. Concrete concentration had no influence on NaAlSi₃O₈ which was the dominant solid phase.

4.1.5 Behavior of Fiber Insulation in Simulated Containment Water

Fiber insulation is contained in several components as shown in Table 2-7. Both CaO and SiO₂ are also present in concrete. The effect of fiber insulation concentration on the formation of solid phases was evaluated by conducting a sensitivity analysis at 60 °C [140 °F] and 130 °C [266 °F], 304 kPa [3 atm]. In the sensitivity analysis, the fiber insulation concentration was varied from 1×10^{-3} to 10 times the basecase concentration. The CaO and SiO₂ contributions from concrete were fixed while conducting the sensitivity analysis for fiber insulation.

Figures 4-11 and 4-12 show the influence of fiber insulation on the formation of dominant solid phases in the simulated containment water at pH of 7 at 60 °C [140 °F] and 130 °C [266 °F], 304 kPa [3 atm].

At 60 °C [140 °F], in a 10 times the basecase concentration of fiber insulation the dominant solid phases were Ca₅(OH)(PO₄)₃, NaAlSi₃O₈, and Fe₃Si₄O₁₀(OH)₂. Both Ca₅(OH)(PO₄)₃ and NaAlSi₃O₈ were present as dominant solid species for all concentrations evaluated. As the amount of silicon was reduced due to decreasing the concentration of insulation fiber, the Fe₃Si₄O₁₀(OH)₂ phase formed at 60 °C [140 °F] converted to Fe₃(PO₄)₂·8H₂O. In addition, the concentration of NaAlSi₃O₈ continued to decrease as the concentration of fiber insulation was reduced.

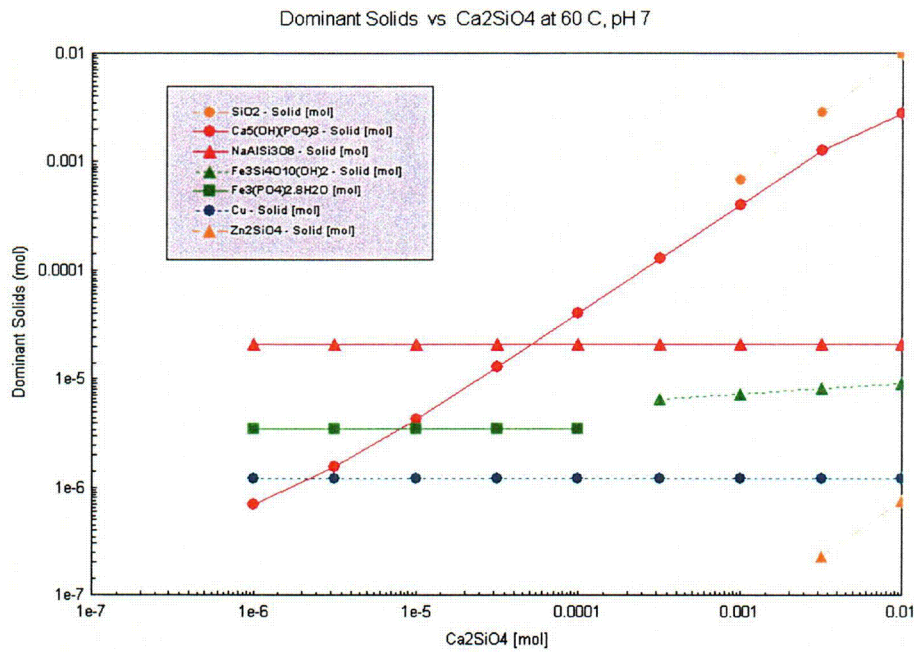


Figure 4-9. Dominant Solid Phases at 60 °C [140 °F], 101 kPa [1 atm] As a Function of Ca₂SiO₄ in Simulated Containment Water at pH 7

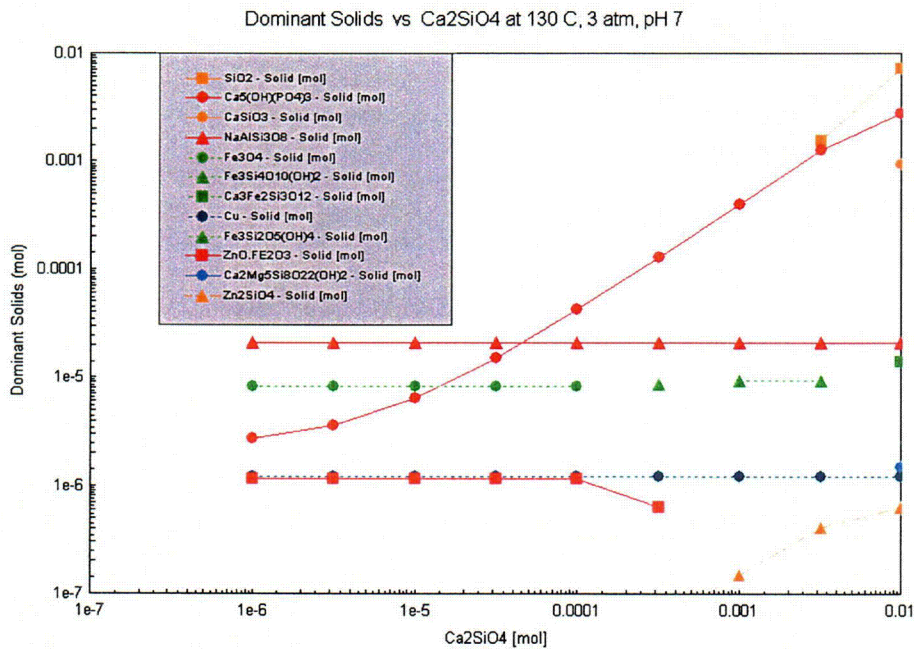


Figure 4-10. Dominant Solid Phases at 130 °C [266 °F], 304 kPa [3 atm] As a Function of Ca₂SiO₄ in Simulated Containment Water at pH 7

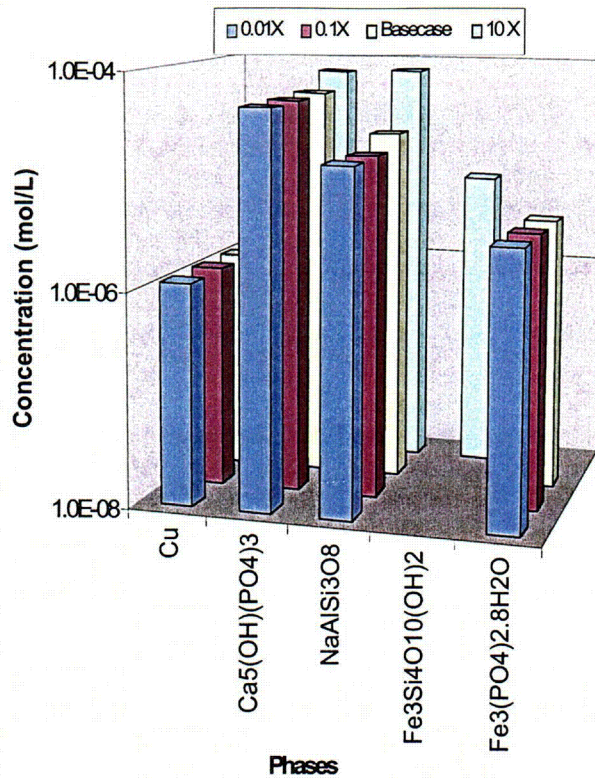


Figure 4-11. Dominant Solid Phases at 60 °C [140 °F], 101 kPa [1 atm] at Different Fiber Insulation Concentrations in Simulated Containment Water Containing Na_3PO_4

At 130 °C [266 °F], 304 kPa [3 atm], in a 10 times the basecase concentration of fiber insulation in the simulated containment water, dominant solid phases were the same as a 60 °C [140 °F]. As the amount of silicon was reduced due to decreasing the concentration of insulation fiber, the $\text{Fe}_3\text{Si}_4\text{O}_{10}(\text{OH})_2$ phase transformed to Fe_3O_4 and $\text{ZnO}\cdot\text{Fe}_2\text{O}_3$. In addition, the concentration of $\text{NaAlSi}_3\text{O}_8$ continues to decrease as the concentration of fiber insulation was reduced.

Except for iron phase redistribution, no significant changes were observed as fiber insulation corroded. The fiber insulation sensitivity analysis at pH 7 indicated no significant impact on the formation of solid phases over a wide fiber insulation concentration range in simulated containment water after a LOCA event.

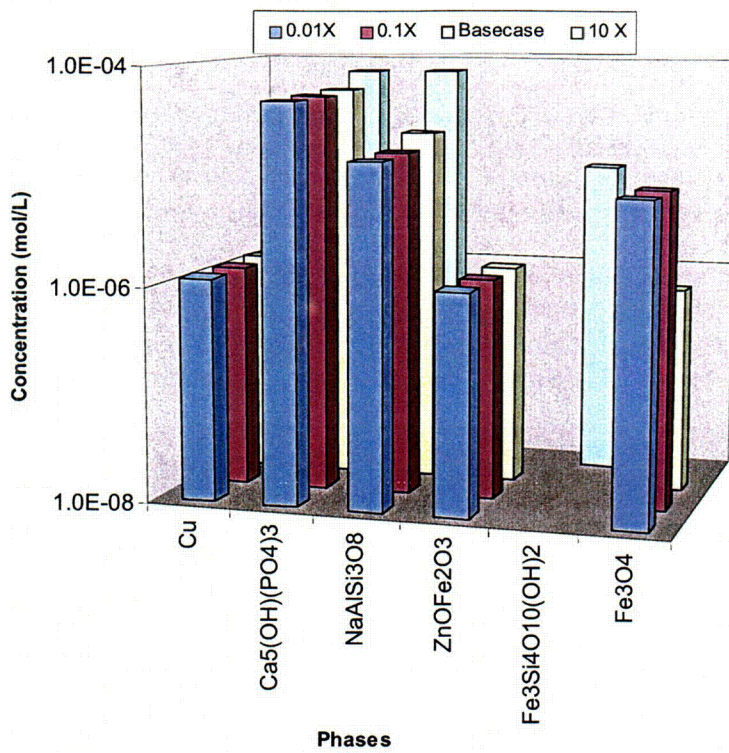


Figure 4-12. Dominant Solid Phases at 130 °C [266 °F], 101 kPa [1 atm] at Different Fiber Insulation Concentrations in Simulated Containment Water Containing Na₃PO₄

5 EVALUATION OF A NEED TO CONDUCT EXPERIMENTS AT HIGH TEMPERATURE AND PRESSURE SYSTEM

An evaluation of the need to conduct integrated chemical effects tests (planned at the University of New Mexico) at high temperature and pressure to simulate initial stages of a LOCA event has been performed. This requires an assessment of solid phases that exclusively occur either at high temperature and pressure or at steady-state operating conditions. In addition, the distribution of an element within solid and liquid phases at any given temperature and pressure is important. If 100 percent of an element is present in a solid phase but the composition of the solid phase changes, the effect on sump clogging could be minimal. However, if element solubility changes, the effect on sump clogging can be significant. The concentrations of solid phases through a range of temperatures and pressures are also important. Concentration of phases is a product of corrosion rate and time. Typically, the higher the temperature, the higher the corrosion rate. A higher corrosion rate at higher temperature can be simulated as corrosion at lower temperature but for longer times. For example, the corrosion in 0.5 hour at 130 °C [266 °F], 304 kPa [3 atm], is equivalent to corrosion for 50 hours at 60 °C [140 °F] if the corrosion rate is 100 times lower, or that for 500 hours at 60 °C [140 °F] if the corrosion rate is 1,000 times lower.

The simulations presented in this report (Chapters 3 and 4) are based on corrosion rate data from literature. The selection of corrosion rates was based on conservative values for pH between 7 and 10 in borated water. In some cases, (e.g., fiber insulation corrosion), no data were available for borated water. In these cases, a best estimate based on other closely related (e.g., nuclear waste glasses for fiber insulation) environment was used. Corrosion rates are highly dependent on temperature. However, temperature-dependent data were often not available. Therefore, sensitivity analysis was conducted over a wide range of amounts for each component to evaluate the effect of temperature change. Furthermore, uncertainties exist in estimation of the surface area for concrete particulates. The NRC Test Plan, Revision 12b (NRC, 2005), provides the amount of concrete particulates per unit volume, but the information on the size and size distribution is not available to estimate exposed surface area. While relevant data could improve prediction of solid phase formation more accurately, the simulations presented in this study provide a reasonable assessment of solid phase corrosion product formation covering a wide range of components present in a containment system.

5.1 Need to Conduct Experiments at High Temperature and Pressure System in an Alkaline Simulated Containment Water

A review of simulation data and associated sensitivity analysis (Chapter 3) for an alkaline simulated containment water at pH 10 indicates that

- (i) $\text{NaAlSi}_3\text{O}_8$, $\text{Ca}_3\text{Fe}_2\text{Si}_3\text{O}_{12}$, and $\text{Fe}_3\text{Si}_2\text{O}_5(\text{OH})_4$ were dominant solid phases that contributed to over 90 percent of the solid phases formed between at 150 °C [302 °F], 507 kPa [5 atm] and 60 °C [140 °F]. The $\text{Ca}_3\text{Fe}_2\text{Si}_3\text{O}_{12}$ solid phase was formed at 150 °C [302 °F], 507 kPa [5 atm] while $\text{Fe}_3\text{Si}_2\text{O}_5(\text{OH})_4$ was formed at 60 °C [140 °F] and is attributed to the retrograde solubility of calcium in iron bearing minerals. Despite these phase changes, all the iron was always present in the solid phase (Figure 3-1).

- (ii) Copper had no influence on the precipitation of solid phases. No corrosion of copper is expected (Figure 3-1).
- (iii) Zinc contribution was below 5 percent to the total solid phases. Zinc was dominantly present as $\text{ZnO}\cdot\text{Fe}_2\text{O}_3$ for which solubility decreased with the decrease in temperature (Table 3-4). At 60 °C [140 °F], 98 percent of zinc was present in solid phase (Table 3-3). Zinc was predominantly present as a mixture of solid Zn_2SiO_4 and $\text{ZnO}\cdot\text{Fe}_2\text{O}_3$ phases at concentrations higher than 3×10^{-5} mol/L at 60 °C [140 °F] and 130 °C [266 °F], 304 kPa [3 atm] or at 10 times the basecase concentration of fiber insulation (Figures 3-5 and 3-6).
- (iv) Aluminum metal has always associated with $\text{NaAlSi}_3\text{O}_8$ for which solubility decreased with decrease in temperature (Table 3-1). At 60 °C [140 °F], 100 percent of aluminum was present in the solid phase (Table 3-3). An increase in the aluminum concentration increased the concentration of $\text{NaAlSi}_3\text{O}_8$ solid phase. In addition, formation of $\text{Al}(\text{OH})_3$ occurred for aluminum concentrations exceeding 3×10^{-4} mol/L at 60 °C [140 °F]. The formation of $\text{Al}(\text{OH})_3$ was not observed at 130 °C [266 °F], 304 kPa [3 atm] (Figures 3-7 and 3-8).
- (v) Calcium-containing components showed higher solubility at lower temperatures. Concrete and fiber insulation were the key sources for calcium. At 130 °C [266 °F], 304 kPa [3 atm], 17 percent of calcium was associated with calcium-bearing solid phases, while at 60 °C [140 °F], only 1 percent was associated with calcium-bearing solid phases (Table 3-3). The calcium phases formed at higher temperatures tended to solubilize at lower temperatures, and thereby, could assist in unclogging pump strainers. Irrespective of the temperature and pressure, for Ca_2SiO_4 exceeding 1×10^{-3} mol/L, the concentration of CaSiO_3 increased with an increase in concrete concentration (Figures 3-11 and 3-12).
- (vi) The concentration of silicon in the solid phase increased with decrease in temperature. At 130 °C [266 °F], 304 kPa [3 atm], 25 percent of silicon was associated with solid silicate phases, while at 60 °C [140 °F], 42 percent of silicon was associated with solid silicate phases (Table 3-3). In a 15-day simulation at 60 °C [140 °F], all components (except copper) present in the simulated containment water were present as solid silicates (Figure 3-2). As silicon concentration was reduced, the concentration of silicate phases reduced also (Figures 3-13 and 3-14).
- (vii) At 60 °C [140 °F], for iron concentrations below 1×10^{-5} mol/L, iron was predominantly present as $\text{ZnO}\cdot\text{Fe}_2\text{O}_3$, and above 1×10^{-5} mol/L iron was predominantly present as $\text{Fe}_3\text{Si}_2\text{O}_5(\text{OH})_4$ (Figures 3-9 and 3-10). Formation of Fe_3O_4 was observed at 1×10^{-3} mol/L. At 130 °C [266 °F], 304 kPa [3 atm], for iron concentration below 1×10^{-6} mol/L iron was predominantly present as $\text{ZnO}\cdot\text{Fe}_2\text{O}_3$. Between 1×10^{-6} and 7×10^{-5} mol/L iron was predominantly present as $\text{Ca}_3\text{Fe}_2\text{Si}_3\text{O}_{12}$, and above 7×10^{-5} , iron was predominantly present as Fe_3O_4 . Again formation of $\text{Ca}_3\text{Fe}_2\text{Si}_3\text{O}_{12}$ at 130 °C [266 °F], 304 kPa [3 atm] and formation of $\text{Fe}_3\text{Si}_2\text{O}_5(\text{OH})_4$ at 60 °C [140 °F] are attributed to the retrograde solubility of calcium in iron-bearing minerals. Despite these phase changes, all iron was in the solid phase. At lower fiber insulation concentrations and pH 10, iron was predominantly present as Fe_3O_4 . As the concentration of fiber insulation increased, iron was present as $\text{Ca}_3\text{Fe}_2\text{Si}_3\text{O}_{12}$. In a 15-day simulation, iron was exclusively present as

$\text{Ca}_3\text{Fe}_2\text{Si}_3\text{O}_{12}$ (Figures 3-13 and 3-14). In all cases, most of the iron was associated with the solid phases (Figure 3-2).

These simulations indicated, irrespective of temperature and pressure, that silicates of iron and aluminum contribute 90 percent of the solid phases formed in an alkaline solution at pH 10. While the distribution and formation of these silicate phases could change based on temperature, pressure, or concentration, the total percentage of solid phases in simulated containment water remains around 90 percent. The contributions of other solid phases are less than 10 percent. Based on these simulations, we conclude that minimal changes are expected as the high-temperature and pressure conditions that exist during the initial stages of a LOCA event approach steady-state conditions.

5.2 Need to Conduct Experimental Analysis in a High-Temperature High-Pressure System in Simulated Containment Water Containing Trisodium Phosphate

A review of simulation data and associated sensitivity analysis (Chapter 4) for a trisodium phosphate simulated containment water at pH 7 indicates that

- (i) There were significant differences in solid phase formation in Na_3PO_4 containing simulated containment water at pH 7 compared to alkaline simulated containment water at pH 10. At pH 7, $\text{Ca}_5(\text{OH})(\text{PO}_4)_3$ was the dominant solid phase, containing almost 100 percent of the calcium, while at pH 10, calcium was approximately 1 percent soluble at 60 °C [140 °F]. A significantly higher quantity of solid phases was formed in solutions containing Na_3PO_4 compared to alkaline containment water (Figures 3-1 and 4-1).
- (ii) Irrespective of temperature and pressure, over 90 percent of the solids precipitated originate from $\text{Ca}_5(\text{OH})(\text{PO}_4)_3$ and $\text{NaAlSi}_3\text{O}_8$ at pH 7 (Table 4-3).
- (iii) $\text{Ca}_5(\text{OH})(\text{PO}_4)_3$ was the dominant solid phase and increased with an increase in concrete concentration. For concentration of concrete exceeding 3×10^{-4} mol/L, $\text{Ca}_5(\text{OH})(\text{PO}_4)_3$ coexisted with solid SiO_2 phase. The concentrations of these two phases far exceed contributions from other solid phases (Figures 4-7 and 4-8).
- (iv) Copper had no influence on the precipitation of solid phases (Figure 4-1).
- (v) Aluminum metal was always associated with $\text{NaAlSi}_3\text{O}_8$, and the concentration of $\text{NaAlSi}_3\text{O}_8$ increased with an increase in aluminum concentration. However, formation of $\text{Al}(\text{OH})_3$ and $\text{AlO}(\text{OH})$ was observed for aluminum concentrations exceeding 3×10^{-4} mol/L at 60 °C [140 °F] and 130 °C [266 °F], 304 kPa [3 atm], respectively (Figures 4-5 and 4-6). In a 15-day simulation, aluminum was present exclusively as $\text{NaAlSi}_3\text{O}_8$ (Figure 4-2).
- (vi) Both iron and zinc showed a decrease in solid phase concentration with decrease in temperature and pressure. The solid phase concentration of zinc reduced from 90 percent solid phase at 150 °C [302 °F] to a fully soluble phase at 60 °C [140 °F] (Table 4-1). The solid phase concentration of iron reduced from 91 percent at 150 °C [302 °F] to 38 percent at 60 °C [140 °F] (Table 4-1). However, this decrease in solid

phase concentration was accompanied by changes in the composition of the solid phase. At 150 °C [302 °F], 507 kPa [5 atm], and 130 °C [266 °F], 304 kPa [3 atm], iron and zinc were present as Fe_3O_4 and $\text{ZnO}\cdot\text{Fe}_2\text{O}_3$ (Table 4-2). However, at 90 °C [194 °F], zinc was present as $\text{Zn}_3(\text{PO}_4)_2\cdot 2\text{H}_2\text{O}$ and iron was present as $\text{Fe}_3\text{Si}_4\text{O}_{10}(\text{OH})_2$. When the temperature was reduced to 60 °C [140 °F], zinc was completely soluble, and iron was present as $\text{Fe}_3(\text{PO}_4)_2\cdot 8\text{H}_2\text{O}$. The formation of these phases was limited to interaction between zinc and iron. Dominant phases such as $\text{Ca}_5(\text{OH})(\text{PO}_4)_3$ and $\text{NaAlSi}_3\text{O}_8$ were not influenced by zinc and iron.

- (vii) As the amount of silicon was reduced due to a reduction in fiber insulation concentration, $\text{Fe}_3\text{Si}_4\text{O}_{10}(\text{OH})_2$ converted to $\text{Fe}_3(\text{PO}_4)_2\cdot 8\text{H}_2\text{O}$ at 130 °C [266 °F], 304 kPa [3 atm] as a mixture of Fe_3O_4 and $\text{ZnO}\cdot\text{Fe}_2\text{O}_3$. Other than reorganization of iron phases, no significant changes were observed (Figures 5-11 and 5-12).
- (viii) The dominant solid phases formed after 15 days were $\text{Ca}_5(\text{OH})(\text{PO}_4)_3$ and $\text{NaAlSi}_3\text{O}_8$, with minor quantities of $\text{Ca}_2\text{Mg}_5\text{Si}_8\text{O}_{22}(\text{OH})_2$, $\text{Fe}_3\text{Si}_4\text{O}_{10}(\text{OH})_2$, SiO_2 , and Zn_2SiO_4 (Figure 5-2). While $\text{Ca}_5(\text{OH})(\text{PO}_4)_3$ and $\text{NaAlSi}_3\text{O}_8$ were present at high-temperature, high-pressure phases, $\text{Fe}_3\text{Si}_4\text{O}_{10}(\text{OH})_2$, SiO_2 , $\text{Ca}_2\text{Mg}_5\text{Si}_8\text{O}_{22}(\text{OH})_2$, and Zn_2SiO_4 were not observed at high temperature and pressure at pH 7 at 130 °C [266 °F], 507 kPa [5 atm]. Conversion of Fe_3O_4 and $\text{ZnO}\cdot\text{Fe}_2\text{O}_3$ to $\text{Fe}_3\text{Si}_4\text{O}_{10}(\text{OH})_2$ and Zn_2SiO_4 was observed.

These simulations indicated that both iron and zinc have increased solubility as temperature was reduced from 150 °C [302 °F] to 60 °C [140 °F]. Irrespective of temperature and pressure, $\text{Ca}_5(\text{OH})(\text{PO}_4)_3$ and $\text{NaAlSi}_3\text{O}_8$ contribute over 90 percent of the solid phases formed in a Na_3PO_4 , pH 7 solution. The distribution of these two phases did not significantly change as a function of temperature and pressure. Based on these simulations, we conclude that minimal chemical changes are expected as the high-temperature and pressure conditions that exist during the initial stages of a LOCA event approach steady-state conditions. Therefore, the integrated chemical effects tests planned at the University of New Mexico can be performed at atmospheric pressure and 60 ° [140 °F]. There is no need for a pressurized test loop.

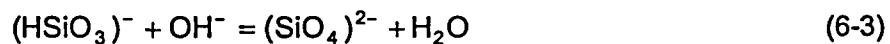
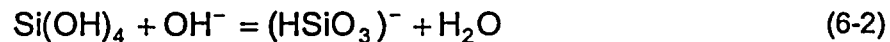
6 EVALUATION OF POTENTIAL FOR GEL FORMATION

This section provides an analysis of the potential for formation of a precipitate gel that could clog containment room pump straining after a LOCA event.

SiO₂ is marginally soluble in water as shown by Eq. (6-1).



However, in alkaline solutions, the reactions shown by Eqs. (6-2) and (6-3) occur.



The formation of silicate ions (SiO₄)²⁻ occurs at pH exceeding 10. A typical silicate tetrahedra structural unit is shown in Figure 6-1. A silica tetrahedra unit consists of a silicon atom surrounded by four oxygen atoms. In solutions containing NaOH, silicate ion reacts to form sodium trisilicate. This is commonly referred to as water glass and is widely used as an adhesive. Insoluble metal silicates, when precipitated from aqueous solution, are usually a gelatinous, amorphous mass. In dilute solutions, precipitation occurs at pH below which metal hydroxide would precipitate. Often, hydroxides are precipitated along with silica by mutual coagulation when a solution of polyvalent metal salt is mixed with a solution of soluble alkali metal silicate (Iler, 1955).

In the presence of aluminum ions, silicon ions are replaced in the tetrahedra structure as shown in Figure 6-1. The charge is balanced by a monovalent alkali ion or a divalent alkaline earth ion. The structural units shown in Figure 6-1 for silicon and aluminum combine to form alkali aluminosilicate or polysialate structural units as shown in Figure 6-2. The structure consists of SiO₄⁻⁴ and AlO₄⁻⁴ tetrahedras linked alternately by mutual sharing of oxygen atoms as shown in Figure 6-2. The charge is balanced by positive ions (M) such as alkalis (lithium, sodium, potassium, cesium) or alkaline earths (calcium, magnesium).

In alkaline solutions, the aluminosilicate unit can react with an alkali silicate unit to form polysialate (-Si-O-Al-O-), poly(sialate-siloxo) (-Si-O-Al-O-Si-O-), or poly(sialate-disiloxo) (-O-Si-O-Al-O-Si-O-Si-O-) polymers as shown in Figures 6-3 and 6-4. These polysialates condense to a gel similar to organic polymers at temperatures below 100 °C [212 °F].

This brief analysis indicates that gelling, a precursor to polymerization, could occur in alkaline solutions when silicon, aluminum, and alkali ions are present. Therefore, gel formation is likely in alkaline simulated containment water because gelling requires a higher pH.

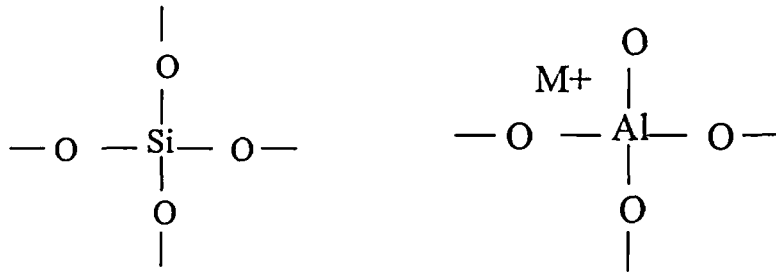


Figure 6-1. Silicon and Aluminum Tetrahedra Units

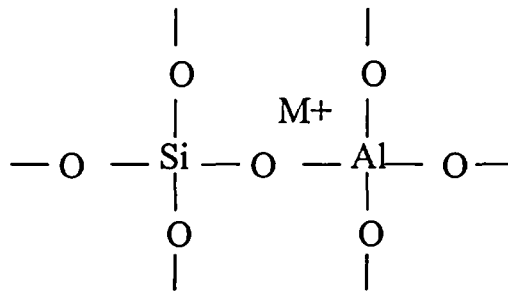


Figure 6-2. A Basic Alkali Aluminosilicate Structural Unit. This Is also Referred to As Polysialate (-Si-O-Al-O-) Unit.

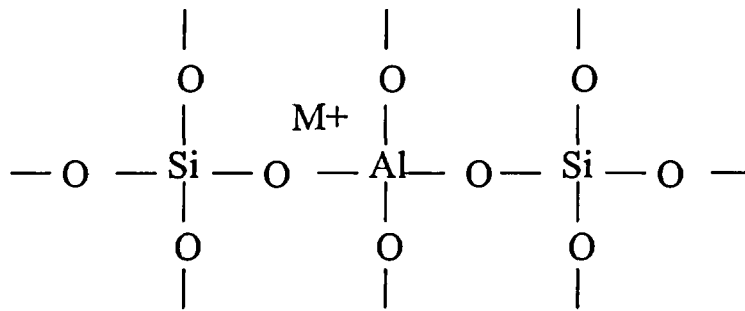


Figure 6-3. A Polymeric Poly(Sialate-Siloxo) Unit

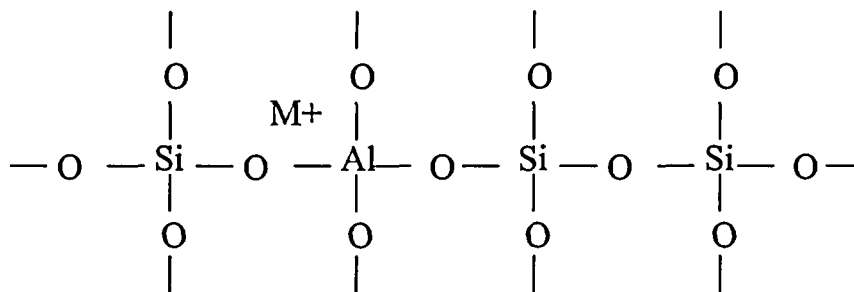


Figure 6-4. A Polymeric Poly(Sialate-Disiloxo) Unit

7 SUMMARY AND CONCLUSIONS

A LOCA event causes rapid changes in the time-temperature-pressure-chemistry-pH conditions in the containment environment. Changes in the coolant chemistry are further complicated because of the interactions among the materials typically present. These complex interactions will require extensive experimentation for an adequate analysis of the potential for sump blockage caused by chemical precipitation. Thermodynamic simulations allow identification of critical variables and their ranges considering the large number of components present in the containment system during and subsequent to a LOCA event. This study modeled chemical speciation of plausible chemical reaction products in containment water after a representative LOCA event using thermodynamic simulation software. This report: (i) concludes that there is no need for a pressurized test loop, (ii) assesses the formation of gelatinous products in the typical time-temperature-pressure-chemistry-pH regime following a LOCA event, and (iii) validates OLI Systems, Inc. software for speciation in borated waters.

The calculations documented in this report were made using a thermodynamic simulator developed by OLI Systems, Inc. for evaluating aqueous chemical processes in industrial and environmental applications. The simulations varied the amount of key components, pH moderators (i.e., sodium hydroxide versus trisodium phosphate), pH, temperature, and pressure to determine the need for a pressurized test loop for additional investigation. Computational thermodynamics simulation calculations were conducted using ESP Version 6.6[®] and StreamAnalyzer Version 1.2[®]. Key chemical components involved in speciation simulation were copper, carbon steel, zinc, aluminum, fiber insulation, and concrete in 0.26-M [2,800-ppm] boron solution. The surface areas exposed for these components during a LOCA event were provided by the U.S. Nuclear Regulatory Commission, and literature data on corrosion rate for these components were used to estimate amounts of corrosion. Given significant uncertainties in corrosion rates in borated water as a function of temperature, and to provide a comparative assessment of the effects of temperature and pressure, a fixed amount of each component was used as an input for simulations. The amount of each component was estimated based on the corrosion rate at 90 °C [194 °F] for 0.5 hour.

The influence of pressure, temperature, and pH on chemical speciation was studied by speciating a fixed amount of each component based on its corrosion rate. In each simulation, a fixed amount was speciated at 150 °C [302 °F] at 507 kPa [5 atm], 130 °C [266 °F] at 304 kPa [3 atm], and 90 °C [194 °F] and 60 °C [140 °F] at 101 kPa [1 atm]. The boron concentration was fixed at 0.26 M [2,800 ppm]. The formation of solid phases as a function of temperature and pressure was examined at pH values of 10 and 7. A pH of 10 was obtained by the addition of 0.23 mol/L [5,300 ppm Na] NaOH, and pH 7 was obtained by the addition of 8.4×10^{-3} mol/L of Na₃PO₄. The precipitation of phases during a 15-day operation of the containment system at 60 °C [140 °F] was estimated by multiplying the hourly corrosion rate of each component by 720. The pH was adjusted to account for an increase in pH due to the increase in the concentration of corrosion components. This increase in pH was attributed to hydrolysis reactions associated with fiber insulation. The estimate for the total amount of corrosion product was conservatively based on the corrosion rates of the components at 90 °C [194 °F]. Corrosion rates of components are expected to be lower at 60 °C [140 °F] the expected steady-state temperature.

The need to conduct experiments at high temperature and pressure to simulate initial stages of a LOCA event requires an assessment of solid phases that exclusively occur at high

temperature and pressure. In addition, distribution of elements in solid and liquid phases at any given temperature and pressure is important. If 100 percent of an element is present in a solid phase, but the composition of the solid phase changes, the effect on sump clogging should be minimal. On the other hand, if the element become soluble, the effect on sump clogging could be significant. However, the concentration of phases is a product of corrosion rate and time. Typically, the higher the temperature, the higher the corrosion rate. The effect of a higher corrosion rate at higher temperature can be simulated by corrosion at a lower temperature for longer times. For example, the corrosion amount in 0.5 hour at 130 °C [266 °F], 304 kPa [3 atm] will be equivalent to 50 hours at 60 °C [140 °F] if the corrosion rate is 100 times lower, or 500 hours at 60 °C [140 °F] if the corrosion rate is 1,000 times lower.

The simulations documented in this report are based on corrosion rate data from literature. The selected corrosion rates were conservative values between pH 7 and 10 in borated water. In some cases, for example fiber insulation corrosion, no data were available in borated water. In such cases, a best estimate based on other closely related systems was used. Corrosion rates are highly dependent on temperature, but temperature-dependent data were not available in most cases. Therefore, sensitivity analysis was conducted over a wide range to evaluate the effect of temperature. Furthermore, uncertainties exist in the estimation of the surface area for concrete particulates. The NRC Test Plan, Revision 12b (NRC, 2005), provides the amount of concrete particulates per unit volume, but the information on the size and size distribution is not available to estimate exposed surface area. While better data could improve prediction of solid phases, the simulations presented in this study reasonably assess the potential for solid phase corrosion product formation covering a wide range of concentrations for each component present in a containment system during a LOCA event.

7.1 Conclusions

Review of simulation data and associated sensitivity analyses in alkaline simulated containment water at pH 10 indicate the following.

- $\text{NaAlSi}_3\text{O}_8$, $\text{Ca}_3\text{Fe}_2\text{Si}_3\text{O}_{12}$ and $\text{Fe}_3\text{Si}_4\text{O}_{10}(\text{OH})_2$ were dominant solid phases that contributed to over 90 percent of the solid phases formed between 150 °C [302 °F], 507 kPa [5 atm] and 60 °C [140 °F].
- The $\text{Ca}_3\text{Fe}_2\text{Si}_3\text{O}_{12}$, solid phase was formed at 150 °C [302 °F], 507 kPa [5 atm], while $\text{Fe}_3\text{Si}_2\text{O}_5(\text{OH})_4$ was formed at 60 °C [140 °F]. This transformation was attributed to the retrograde solubility of calcium in iron bearing minerals. Despite these phase changes, all the iron was present in the solid phase.
- Copper had no influence on the precipitation of solid phases, and no corrosion of copper is expected.
- The contribution from zinc was insignificant compared to other solid phases and was limited to 5 percent to the total quantity of solid phases.
- Sensitivity analyses for aluminum indicated formation of $\text{Al}(\text{OH})_3$ for aluminum concentrations exceeding 2×10^{-4} mol/L at 60 °C [140 °F]. The formation of $\text{Al}(\text{OH})_3$ was not observed at 130 °C [266 °F], 304 kPa [3 atm].

- Sensitivity analyses for concrete indicated, irrespective of the temperature and pressure, for Ca_2SiO_4 exceeding 1×10^{-3} mol/L, the concentration of CaSiO_3 increased with an increase of concrete concentration.
- In a 15-day simulation at 60 °C [140 °F], all solid phases (except copper) present in the simulated containment water were solid silicates.
- As silicon concentration was reduced, the concentration of silicate phases reduced also. In an alkaline environment, the solubility of silica increased with an increase in pH and temperature. Since silicates were major corrosion products, a strong influence of pH and temperature was observed on the formation of the dominant solid phases in the simulated containment water. However, at pH 10, irrespective of the temperature, pressure, and concentration, silicates of aluminum and iron contribute 90 percent of the solid phases.

Based on these simulations, we conclude that no significant differences in corrosion product formation are expected in alkaline simulated containment water at pH 10 as the high-temperature and pressure conditions during the initial stages of a LOCA event approach steady-state conditions.

Review of simulation data and associated sensitivity analysis in a trisodium phosphate simulated containment water at pH 7 indicated that:

- There were significant differences in the solid phase formation in Na_3PO_4 containing simulated containment water at pH 7 from that in alkaline simulated containment water at pH 10.
- At pH 7, $\text{Ca}_5(\text{OH})(\text{PO}_4)_3$ was the dominant solid phase containing almost 100 percent of calcium, while at pH 10, calcium was approximately 1 percent insoluble at 60 °C [140 °F].
- A significantly larger quantity of solid phases were formed in a solution containing Na_3PO_4 compared to alkaline containment water. $\text{Ca}_5(\text{OH})(\text{PO}_4)_3$ and $\text{NaAlSi}_3\text{O}_8$ contributed to over 90 percent of the solid phases.
- Sensitivity analyses for concrete indicated increase in the $\text{Ca}_5(\text{OH})(\text{PO}_4)_3$ concentration with a increase in the concrete concentration. For concentrations of concrete exceeding 3×10^{-4} mol/L, $\text{Ca}_5(\text{OH})(\text{PO}_4)_3$ coexisted with solid SiO_2 phase. The concentrations of these two phases far exceeded contributions from other solid phases.
- Copper had no influence on the precipitation of solid phases.
- The sensitivity analyses for aluminum indicated an increase in the concentrations of $\text{NaAlSi}_3\text{O}_8$ with an increase in aluminum concentration. Formation of $\text{Al}(\text{OH})_3$ and $\text{AlO}(\text{OH})$ was observed for aluminum concentrations exceeding 3×10^{-4} mol/L at 60 °C [140 °F] and 130 °C [266 °F], 304 kPa [3 atm], respectively. In a 15-day simulation, aluminum was present exclusively as $\text{NaAlSi}_3\text{O}_8$.

- Both iron and zinc showed a decrease in solid phase concentration with decrease in temperature and pressure. The contribution of zinc was below 2 percent and that of iron is below 9 percent compared to the total solid phases. Other than a reorganization of iron phases, no significant changes were observed.
- The dominant solid phases formed after 15 days were $\text{Ca}_5(\text{OH})(\text{PO}_4)_3$ and $\text{NaAlSi}_3\text{O}_8$, with minor quantities of $\text{Ca}_2\text{Mg}_5\text{Si}_8\text{O}_{22}(\text{OH})_2$, $\text{Fe}_3\text{Si}_4\text{O}_{10}(\text{OH})_2$, SiO_2 , and Zn_2SiO_4 in the simulated containment water.

Based on the observations, we conclude that changes in solid phase formation for iron and zinc are expected as high temperature and pressure conditions during the initial stages of a LOCA event approach steady-state conditions. However, both iron and zinc showed increased solubility as temperature was reduced from 150 °C [302 °F] to 60 °C [140 °F]. Irrespective of temperature and pressure, $\text{Ca}_5(\text{OH})(\text{PO}_4)_3$ and $\text{NaAlSi}_3\text{O}_8$ contribute over 90 percent of the solid phases formed in a Na_3PO_4 , pH 7 solution. The distribution of these two phases did not significantly change as a function of temperature and pressure. A comparison of the constituents in pH = 7 and pH = 10 containment solutions is provided in Table 7-1.

In alkaline solutions, aluminosilicate units can react with alkali silicate units to form polysialate (-Si-O-Al-O-), poly(sialate-siloxo) (-Si-O-Al-O-Si-O-), or poly(sialate-disiloxo) (-O-Si-O-Al-O-Si-O-Si-O-) polymers. These polysialates condense as a gel similar to organic polymers at temperatures below 100 °C [212 °F]. Such polymers are widely used in the manufacture of geopolymers. Gel formation, a precursor to polymerization, could occur in alkaline solutions when silicon, aluminum, and alkali ions are present. Therefore, gel formation is likely in alkaline simulated containment water because gelling requires a high pH. This gel formation could result in clogging of containment area sump pump suction strainers.

Characteristic	pH = 7 (Trisodium Phosphate Moderator)	pH = 10 (Sodium Hydroxide Moderator)
Dominant Solid Phases	Ca ₅ (OH)(PO ₄) ₃ and NaAlSi ₃ O ₈ with Fe ₃ (PO ₄) ₂ ·8H ₂ O {60 °C [140 °F]}, and Fe ₃ O ₄ and Fe ₃ Si ₂ O ₅ (OH) ₄ {150 °C [302 °F]}	NaAlSi ₃ O ₈ and Ca ₂ Mg ₅ Si ₈ O ₂₂ (OH) ₂ , with Ca ₃ Fe ₂ Si ₃ O ₁₂ {60 °C [140 °F]} and Fe ₃ Si ₄ O ₁₀ (OH) ₄ {150 °C [302 °F]}
Temperature Dependencies	Redistribution of iron and zinc phases	Redistribution of iron phases
Sensitivity—Aluminum	Increasing aluminum leads to increasing Al(OH) ₃ {60 °C [140 °F]} and AlO(OH) {130 °C [266 °F]}	Increasing aluminum leads to increasing Al(OH) ₃ {60 °C [140 °F]} and increases NaAlSi ₃ O ₈ {130 °C [266 °F]}
Sensitivity—Carbon Steel	Increasing iron leads to increasing Fe ₃ (PO ₄) ₂ ·8H ₂ O {60 °C [140 °F]}, Fe ₃ O ₄ , and Fe ₃ Si ₂ O ₅ (OH) ₄ {130 °C [266 °F]}	Increasing iron leads to increasing Fe ₃ Si ₂ O ₅ (OH) ₄ {60 °C [140 °F]} and Ca ₃ Fe ₂ Si ₃ O ₁₂ {130 °C [266 °F]}
Sensitivity—Zinc	Increasing zinc leads to increasing Zn ₃ (OH)(PO ₄) ₃ ·2H ₂ O {60 °C [140 °F]}, Zn ₃ (OH)(PO ₄) ₃ ·2H ₂ O, and ZnO·Fe ₂ O ₃ {130 °C [266 °F]}	Increasing zinc leads to increasing ZnO·Fe ₂ O ₃ and Zn ₂ SiO ₄
Sensitivity—Copper	No corrosion, no influence	No corrosion, no influence
Sensitivity—Concrete	Increasing concrete leads to increasing Ca ₅ (OH)(PO ₄) ₃ and SiO ₂	Increasing concrete leads to increasing CaSiO ₃
Sensitivity—Fiber Insulation	Increasing fiber insulations leads to increasing NaAlSi ₃ O ₈	Increasing fiber insulations leads to increasing NaAlSi ₃ O ₈ and Ca ₂ Mg ₅ Si ₈ O ₂₂ (OH) ₂
Long-Term Trends (time)	Major solid constituents: Ca ₅ (OH)(PO ₄) ₃ , NaAlSi ₃ O ₈ , Ca ₂ Mg ₅ Si ₈ O ₂₂ (OH) ₂ , Fe ₃ Si ₄ O ₁₀ (OH) ₂ , SiO ₂ , and Zn ₂ SiO ₄	Major solid constituents: NaAlSi ₃ O ₈ , Ca ₂ Mg ₅ Si ₈ O ₂₂ (OH) ₂ , Ca ₃ Fe ₂ Si ₃ O ₁₂ , CaSiO ₃ , and Zn ₂ SiO ₄

8 FUTURE WORK

This report is based on corrosion rate data published in the open literature. However, in many cases, corrosion rate data are not relevant to expected containment water composition and pH. There are significant uncertainties in the corrosion rates in borated water as a function of temperature and pH. Laboratory experiments to determine corrosion rate of components in expected containment water environment would improve simulation results and provide more confidence for conclusions drawn from the simulations.

9 REFERENCES

- Carmack, W.J., G.R. Smolik, R.A. Anderl, R.J. Paweklo, and P.B. Hembree. "Takamak Dust Particle Size and Surface Area Measurement." Log. No. E014. Idaho Falls, Idaho. Idaho National Engineering and Environmental Laboratory. 1998.
- Griess, J.C. and A.L. Bacarella. "Design Consideration of Reactor Containment Spray Systems—Part III: The Corrosion of Materials in Spray Solutions." ORNL-TM-2412, Part III. Oak Ridge, Tennessee: Oak Ridge National Laboratory. 1969.
- Hall, J.F. "Corrosion of Low Alloy Steel Fastener Materials Exposed to Borated Water." Proceedings of the Third International Symposium on Environmental Degradation of Materials in Nuclear Power Systems—Water Reactors. G.J. Theus and J.R. Weeks, eds. La Grange Park, Illinois: American Nuclear Society. pp. 711–722. 1988.
- Iler, R.K. *The Colloid Chemistry of Silica and Silicates*. Ithaca, New York: Cornell University Press. 1955.
- Jantzen, C.M. "Radioactive Waste-Portland Cement Systems II: Leaching Characteristics." *Journal of American Ceramic Society*. Vol. 67, No. 10. pp. 674–678. 1984.
- Johns, R.C., B.C. Letellier, K.J. Howe, and A.K. Ghosh. "Small-Scale Experiments: Effects of Chemical Reactions on Debris-Bed Head Loss." LA-UR-03-6415. Los Alamos, New Mexico: Los Alamos National Laboratory. 2003.
- Niyogi, K.K., R.R. Lunt, and J.S. Mackenzie. NUREG/CP-0038, "Corrosion of Aluminum and Zinc in Containment Following a LOCA and Potential for Precipitation of Corrosion Products in the Sump." Proceedings of the Second International Conference on the Impact of Hydrogen on Water Reactor Safety, Albuquerque, New Mexico, October 3–7, 1982. Rockville, Maryland: NRC. pp. 410–423. October 1982.
- NRC. "Test Plan: Characterization of Chemical and Corrosion Effects Potentially Occurring During a Pressurized Water Reactor LOCA." Rev. 12b. ML050450478. Washington, DC: NRC. 2005.
- OLI Systems, Inc. "StreamAnalyzer Version 1.2." Morris Plains, New Jersey: OLI Systems, Inc. 2002a.
- . "Environmental Simulation Program Version 6.6." Morris Plains, New Jersey: OLI Systems, Inc. 2002b.
- Pan, Y.-M, V. Jain, and O. Pensado. "Degradation of High-Level Waste Glass Under Simulated Repository Conditions." *Journal of Non-Crystalline Solids*. Vol. 319. pp. 74–88. 2003.
- Piippo, J., T. Laitinen, and P. Sirkai. "Corrosion Behavior of Zinc and Aluminum in Simulated Nuclear Accident Environments." STUK-YTO-TR 123. Helsinki, Finland: Finnish Center for Radiation and Nuclear Safety. 1997.

APPENDIX A

SOFTWARE VALIDATION AND SIMULATION METHODS

A LOCA event involves rapid changes in the time-temperature-pressure-chemistry-pH conditions. Changes in the coolant chemistry are further complicated because of interactions among the materials present in the vicinity of the LOCA event (see Table 1-1). These potentially complex interactions necessitate a large number of experiments to obtain sufficient data to analyze the potential for sump blockage caused by chemical precipitation. Thermodynamic simulations allow identification of critical variables and their ranges from a large number of components present in the containment system during and subsequent to a LOCA event.

The calculations in this project were made using a thermodynamic simulator developed by OLI Systems, Inc. (OLI Systems, Inc., 2002a,b) for evaluating aqueous chemical processes in industrial and environmental applications. The OLI Systems, Inc. data bank contains proprietary coefficients for predicting thermodynamic, transport, and physical properties for 80 elements of the periodic table and their associated aqueous inorganic species, as well as more than 5,000 organic species. The thermodynamic framework used by the OLI Systems, Inc. code (OLI Systems, Inc., 2002a,b) predicts behavior of multicomponent aqueous systems including aqueous liquid, vapor, organic liquid, and multiple solid phases for the general ranges of 0 to 30 molal, -50 to 300 °C [-58 to 572 °F], and 0–150 MPa [0–1,480 atm].

The simulations conducted for this study varied the amounts of key components, pH moderators (i.e., sodium hydroxide versus trisodium phosphate), pH, temperature, and pressure to determine the need for a pressurized test loop to better characterize system response. Computational thermodynamics simulation calculations were conducted using Environmental Simulation Program (ESP) Version 6.6[®] and StreamAnalyzer Version 1.2[®] developed by OLI Systems, Inc. Following simulations and sensitivity analyses of key variables including corrosion products, species that have a potential for causing sump head loss were ranked.

A.1 OLI Systems Software Validation

A.1.1 OLI Simulation Packages

The ESP Version 6.6[®] and StreamAnalyzer Version 1.2[®] are two packages of the simulation software developed by OLI Systems, Inc. (2002a,b). ESP Version 6.6[®] is for evaluating the thermodynamic properties of a group of streams that are connected to various chemical reaction units in a chemical process in industrial and environmental applications. StreamAnalyzer Version 1.2[®] is designed to simulate the thermodynamic properties of a single stream. The two packages share the same thermodynamic frame work—OLI engine. StreamAnalyzer Version 6.6[®] is a more recent product and provides user-friendly graphical user-interaction interfaces. Because ESP Version 6.6[®] is based on earlier designs, it does not support the graphical user-interfaces.

ESP Version 6.6[®] and StreamAnalyzer Version 1.2[®] were validated for applications in the high-level waste project (Yang, 2003). However, the previous validation tests did not include the systems that are related to the primary coolant of the pressurized nuclear reactors.

Validation tests to verify if these OLI Systems, Inc. software packages can be used for the boron-containing solutions were conducted according to the contract requirements. This chapter documents the validation results for both ESP Version 6.6[®] and StreamAnalyzer Version 1.2[®] packages in the solutions containing boric acid and borates.

A.1.2 OLI Engine

The OLI Systems, Inc. engine has a large database of thermodynamic parameters and represents standard-state properties using the Helgeson, et al. (1981) equation-of-state and represents excess properties using the aqueous activity coefficient expressions developed by Bromley (1972) and Pitzer (1973, 1991).

For stream simulations, if the temperature, pressure, and composition are specified, ESP Version 6.6[®] and StreamAnalyzer Version 1.2[®] packages can calculate the following thermodynamic properties:

- Concentration of ionic species in liquid phase (speciation)
- Solid/liquid equilibrium
- Vapor/liquid equilibrium
- Vapor/liquid equilibrium
- Vapor/liquid/solid equilibrium (including deliquescence processes at a mutual deliquescence point)

For process simulations, if the input streams are fully defined, ESP Version 6.6[®] allows the calculations of the thermodynamic properties of all process streams if the operating parameters such as reaction temperature, pressure, and the fraction distilled for an evaporator are specified.

A.1.3 OLI Systems, Inc. ESP Version 6.6[®] Application Example

Figure A-1 shows an example evaporation process that was simulated using ESP Version 6.6[®] for a high-level waste stream. The input stream was a brine solution containing salts that can hydrolyze and produce acidic gases when heated. The calculation was started after the following parameters were specified:

- (i) Input stream temperature, pressure, and brine composition
- (ii) Operation mode of evaporator Unit A (dew point, for example), pressure for the dew point calculation, and the amount of the incoming stream to be evaporated (90 percent, for example)
- (iii) Operation mode of Evaporator Unit B (dew point, for example), pressure for the dew point calculation, and the amount of the incoming stream, L1, to be evaporated (90 percent, for example)
- (iv) Temperature of Condenser Unit C
- (v) Temperature of Condenser Unit D

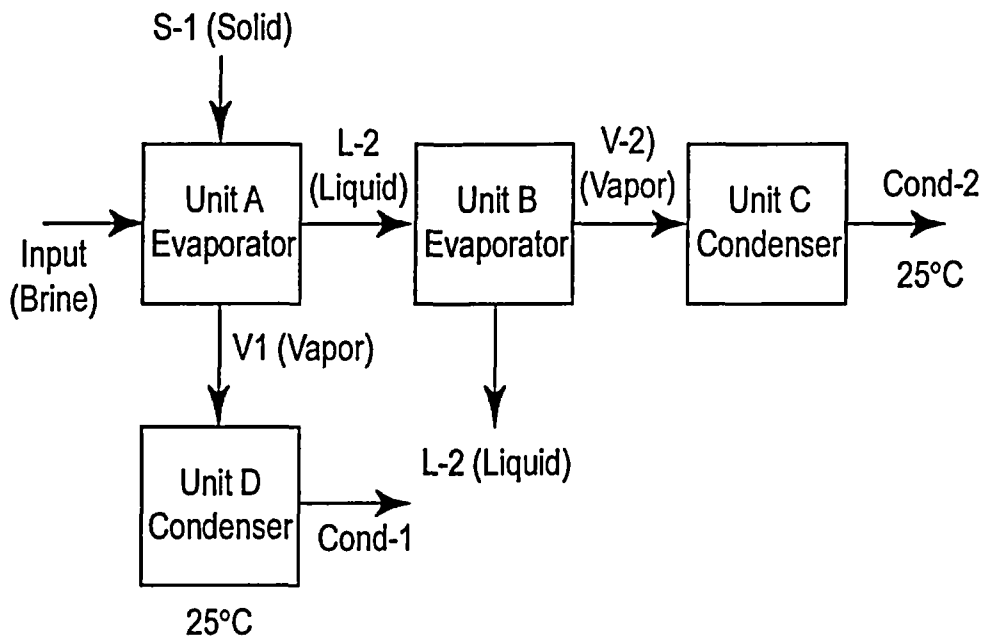


Figure A-1. Application Example of OLI Systems, Inc. ESP Version 6.6[®]; Simulation of Acid Production by Concentrated Brine in Staged Evaporation Processes (Note: °F = 1.8 × °C + 32).

After the calculation, the temperatures of the evaporators, the concentrations of the ionic species, and the pH in each stream of the process were available. The pH in the Cond-1 stream was the room temperature pH of the condensate collected after 90 percent of the incoming brine was evaporated, and the pH in the Cond-2 stream was the pH of the condensate collected upon further evaporation after 90 percent of the incoming brine had been evaporated, respectively. The former was called the cumulative pH, and the later was called the interval pH. Figure A-2 shows the calculated cumulative and interval pH values. Both the cumulative and the interval pH decreased with the increase in the degree of distillation. In addition, the interval pH was lower than the cumulative pH, which implies most of the acid was produced in the later stages of evaporation.

A.2 Validation Results

A.2.1 Test Case 1—Solubility of Boric Acid in Water

The test case described in this section includes the calculations of the total dissolved boron in a boric acid solution in the temperature range of 20 to 94 °C [68 to 201 °F] to obtain the solubility of boric acid. The calculation was conducted using a mixer reactor, which is a continuously stirred tank reactor. This calculation was to verify if the ESP Version 6.6[®] and StreamAnalyzer Version 1.2[®] software packages can be used to accurately predict the thermodynamic properties in a boron-containing solution at different temperature conditions.

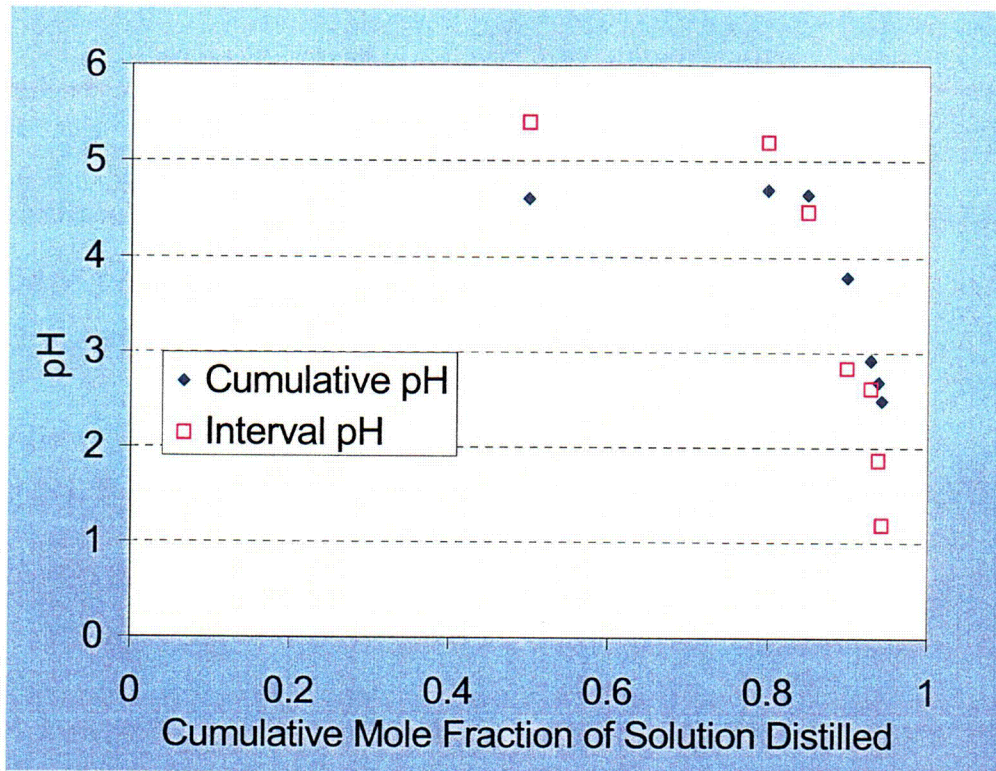


Figure A-2. Application Example of OLI Systems, Inc. ESP Version 6.6[®]; Simulation Results for Acid Production by a Concentrated Brine Solution in Staged Evaporation Processes

A.2.1.1 Test Input

Input temperatures were 20, 40, 60, 75, and 94 °C [68, 104, 140, 167, and 201 °F]. The input pressure was 101 kPa [1 atm].

A.2.1.2 Test Procedure

The test was run by specifying the calculation type as a constant pressure isotherm. The input stream contains 8 mol [494.5 g] of boric acid [B(OH)₃] and 55.508 mol [1 kg] of water.

A.2.1.3 Test Results

The calculations with ESP Version 6.6[®] provided the following parameters for each phase (aqueous, solid, and vapor) of the input and output streams:

- List of all chemical species and their quantities
- Temperature
- Pressure
- pH
- Total molar flow

- Total mass flow
- Total volume
- Enthalpy
- Density
- Vapor fraction
- Solid fraction
- Organic fraction
- Osmotic pressure
- Redox potential
- Electrical specific conductivity
- Electrical molar conductivity
- Absolute viscosity
- Relative viscosity
- Ionic strength

The calculations with StreamAnalyzer Version 1.2[®] provided the following parameters:

- List of all chemical species and their quantities
- Temperature
- Pressure
- pH
- Ionic strength
- Osmotic pressure
- Water H₂O activity
- Electrical specific conductivity
- Electrical molar conductivity
- Absolute viscosity
- Relative viscosity
- Density
- Enthalpy
- Total molar amount in aqueous phase
- Total molar amount in vapor phase
- Total molar amount in solid phase
- Total mass amount in aqueous phase
- Total mass amount in vapor phase
- Total mass amount in solid phase
- Total volume in aqueous phase
- Total volume in vapor phase
- List of species scaling tendencies
- List of species activity coefficients in liquid phase
- List of species equilibrium constants
- List of species ionic mobilities
- List of species self diffusivities

Partial lists of the parameters calculated with the ESP Version 6.6[®] and StreamAnalyzer 1.2[®] are provided in Tables A-1 and A-2. The comparisons of the calculated solubilities of boric acid in water with the experimental data obtained by Nies and Hulbert (1967) are also given in the corresponding tables, and plotted in Figure A-3. The deviations between the calculated

Table A-1. ESP Version 6.6[®] Speciation Results and Comparison of the Calculated Boric Acid Solubilities with the Experimental Values at Different Temperatures

Temperature °C [°F]	20 [68]		40 [104]		60 [140]		75 [167]		94 [201]	
Phase	Aqueous	Solid	Aqueous	Solid	Aqueous	Solid	Aqueous	Solid	Aqueous	Solid
pH	3.63	—	3.32	—	3.04	—	2.85	—	2.62	—
Flow Units	mol/hr	mol/hr	mol/hr	mol/hr	mol/hr	mol/hr	mol/hr	mol/hr	mol/hr	mol/hr
H ₂ O	55.51	—	55.51	—	55.51	—	55.51	—	55.51	—
B(OH) ₃	0.81	7.19	1.45	6.55	2.38	5.61	3.37	4.62	5.16	2.83
OH	3.0×10^{-11}	—	6.2×10^{-11}	—	1.1×10^{-10}	—	1.5×10^{-10}	—	1.9×10^{-10}	—
B ₃ O ₃ (OH) ₄ ⁻	2.3×10^{-4}	—	4.8×10^{-4}	—	9.2×10^{-4}	—	1.4×10^{-3}	—	2.5×10^{-3}	—
B ₄ O ₅ (OH) ₄	8.0×10^{-9}	—	6.3×10^{-9}	—	6.2×10^{-9}	—	6.9×10^{-9}	—	9.1×10^{-9}	—
B(OH) ₄ ⁻	1.8×10^{-6}	—	2.4×10^{-6}	—	2.9×10^{-6}	—	3.2×10^{-6}	—	3.5×10^{-6}	—
H ⁺	2.4×10^{-4}	—	4.9×10^{-4}	—	9.4×10^{-4}	—	1.5×10^{-3}	—	2.6×10^{-3}	—
B ₂ O(OH) ₅	2.0×10^{-6}	—	5.5×10^{-6}	—	1.2×10^{-5}	—	2.1×10^{-5}	—	3.7×10^{-5}	—
Total, g/hr	1,050.3	444.4	1,089.5	405.2	1,147.6	347.1	1,208.9	285.8	1,319.6	175.0
Volume, L/hr	1.03	—	1.07	—	1.11	—	1.16	—	1.25	—
Enthalpy, cal/hr	-4.0×10^6	-1.9×10^6	-4.1×10^6	-1.7×10^6	-4.4×10^6	-1.5×10^6	-4.6×10^6	-1.2×10^6	-5.0×10^6	-7.4×10^5
Density, g/L	1,016.48	—	1,022.64	—	1,030.60	—	1,038.65	—	1,053.20	—

A-6

Table A-1. ESP Version 6.6[®] Speciation Results and Comparison of the Calculated Boric Acid Solubilities with the Experimental Values at Different Temperatures (continued)

Temperature °C [°F]	20 [68]		40 [104]		60 [140]		75 [167]		94 [201]	
Phase	Aqueous	Solid	Aqueous	Solid	Aqueous	Solid	Aqueous	Solid	Aqueous	Solid
Solubilities of Boric Acid in Water										
Calc. B (M)	0.79	—	1.36	—	2.14	—	2.90	—	4.13	—
Exp. B (M)*	0.78	—	1.32	—	2.14	—	2.98	—	4.24	—
Deviation (%)	1.37	—	2.72	—	0.28	—	-2.73	—	-2.60	—
Input parameters: H ₂ O: 55.508 mol; B(OH) ₃ : 8 mol.										
*Nies, N.P. and R.W. Hulbert. "Solubility Isotherms in the System Sodium Oxide-Boric Oxide-Water." <i>Journal of Chemical Engineering Data</i> . Vol. 12, No. 3. pp. 303-313. 1967.										

Table A-2. StreamAnalyzer Version 1.2 [®] Speciation Results and Comparison of the Calculated Boric Acid Solubilities with the Experimental Values at Different Temperatures										
Temperature °C [°F]	20 [68]		40 [104]		60 [140]		75 [167]		94 [201]	
Phase	Aqueous	Solid	Aqueous	Solid	Aqueous	Solid	Aqueous	Solid	Aqueous	Solid
Unit	mol	—	mol	—	mol	—	mol	—	mol	—
H ₂ O	55.508	0	55.509	0	55.51	0	55.511	—	—	—
B(OH) ₃	0.81	7.19	1.45	6.55	2.38	5.61	3.37	—	—	—
B(OH) ₄ ⁻	1.82 × 10 ⁻⁶	0	2.4 × 10 ⁻⁶	0	2.93 × 10 ⁻⁶	0	3.24 × 10 ⁻⁶	—	—	—
B ₂ O(OH) ₅ ⁻	1.96 × 10 ⁻⁶	0	5.48 × 10 ⁻⁶	0	1.24 × 10 ⁻⁵	0	2.07 × 10 ⁻⁵	—	—	—
B ₃ O ₃ (OH) ₄	2.34 × 10 ⁻⁴	0	4.84 × 10 ⁻⁴	0	9.21 × 10 ⁻⁴	0	1.45 × 10 ⁻³	—	—	—
B ₄ O ₅ (OH) ₄	7.99 × 10 ⁻⁹	0	6.31 × 10 ⁻⁹	0	6.19 × 10 ⁻⁹	0	6.90 × 10 ⁻⁹	—	—	—
H ⁺	2.37 × 10 ⁻⁴	0	4.92 × 10 ⁻⁴	0	9.36 × 10 ⁻⁴	0	1.47 × 10 ⁻³	—	—	—
OH ⁻	3.01 × 10 ⁻¹¹	0	6.19 × 10 ⁻¹¹	0	1.08 × 10 ⁻¹⁰	0	1.48 × 10 ⁻¹⁰	—	—	—
Total Mole, mol	56.3	0	57.0	0	57.9	0	58.9	—	—	—
Total Volume, L	1.03	—	1.07	—	1.11	—	1.16	—	—	—
Total Mass, g	1,050.3	—	1,089.5	—	1,147.6	—	1,208.9	—	—	—
Density, g/L	1,016.5	—	1,022.7	—	1,030.6	—	1,038.7	—	—	—
Solubilities of Boric Acid in Water										
Calc. B, M	7.87	—	1.36	—	2.14	—	2.90	—	—	—
Exp. B ₂ O ₃ * (wt%)	2.66	—	4.50	—	7.22	—	10.00	—	14.00	—

Table A-2. StreamAnalyzer Version 1.2[®] Speciation Results and Comparison of the Calculated Boric Acid Solubilities with the Experimental Values at Different Temperatures (continued)

Temperature °C [°F]	20 [68]		40 [104]		60 [140]		75 [167]		94 [201]	
Phase	Aqueous	Solid	Aqueous	Solid	Aqueous	Solid	Aqueous	Solid	Aqueous	Solid
Exp. B, M	0.78	—	1.32	—	2.14	—	2.98	—	4.24	—
Deviation, %	1.38	—	2.74	—	0.29	—	-2.72	—	—	—

Input parameters: H₂O: 55.508 mol; B(OH)₃: 8 mol.

*Nies, N.P. and R.W. Hulbert. "Solubility Isotherms in the System Sodium Oxide-Boric Oxide-Water." *Journal of Chemical Engineering Data*. Vol. 12, No. 3. pp. 303-313. 1967.

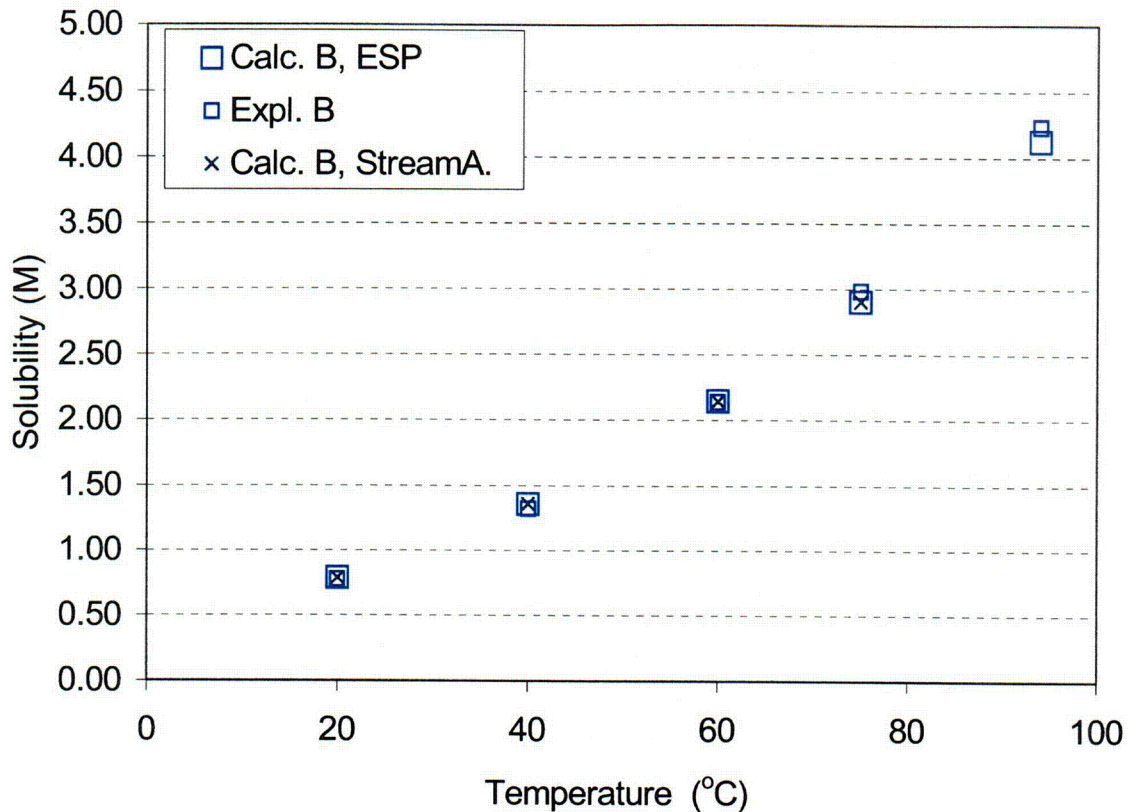


Figure A-3. Comparison of the Calculated Boric Acid Solubilities Using ESP Version 6.6[®] and StreamAnalyzer Version 1.2[®] with the Experimental Values at Different Temperatures (Note: °F = 1.8 × °C + 32).

solubilities and the experimentally obtained solubilities are within ±3 percent. Therefore, the calculated solubilities for boric acid in water are in good agreement with the experimentally measured solubilities by Nies and Hulbert (1967) in the temperature range between 20 and 94 °C [68 and 201 °F] for ESP Version 6.6[®] and between 20 and 75 °C [68 and 167 °F] for StreamAnalyzer Version 1.2[®]. The results from ESP Version 6.6[®] are essentially the same as those from StreamAnalyzer Version 1.2[®].

A.2.2 Test Case 2—Solubility of Borax in Water

This test case calculates the total dissolved boron and sodium in borax-water systems in the temperature range of 20 to 94 °C [68 to 201 °F]. The calculations were conducted using a mixer reactor (a continuously stirred tank reactor). The objective of this test was to verify if the ESP Version 6.6[®] and StreamAnalyzer Version 1.2[®] software packages can be used to adequately predict the thermodynamic properties in a boron- and sodium-containing solution at varying temperatures.

A.2.2.1 Test Input

Input temperatures were 20, 40, 60, 75, and 94 °C [68, 104, 140, 167, and 201.2 °F]. The input pressure was 101 kPa [1 atm].

A.2.2.2 Test Procedure

The test was run by specifying the calculation type as constant pressure isotherm. The input stream contains 2 mol [201.2g] of borax ($\text{Na}_2\text{B}_4\text{O}_7$) and 55.508 mol [1 kg] of water.

A.2.2.3 Test Results

Tables A-3 and A-4 present the speciation results calculated with ESP Version 6.6[®] and StreamAnalyzer Version 1.2[®], respectively. For the boric acid case, these tables list the temperature and pressure used in the calculation, the resulting ionic strength, and the calculated concentrations of ionic species, including boron- and sodium-containing species. Tables A-3 and A-4 also list the calculated total dissolved boron and sodium concentrations and show comparisons with the experimental data given by Nies and Hulbert (1967). The calculated solubility results in Tables A-3 and A-4 are also presented in Figure A-4. The deviations of the calculated results from the experimental data are within ± 3.5 percent for both ESP Version 6.6[®] and StreamAnalyzer Version 1.2[®] at temperatures between 20 and 40 °C [68 and 104 °F]. The deviations are within ± 10 percent in the temperature range from 60 to 94 °C [140 to 201 °F] for ESP Version 6.6[®] and from 60 to 75 °C [140 to 167 °F] for StreamAnalyzer Version 1.2[®]. The results from ESP Version 6.6[®] are consistent with those from StreamAnalyzer Version 1.2[®].

A.2.3 Test Case 3—Dissociation Constant of Boric Acid in a Concentrated Sodium Chloride Solution

The test cases described in this section calculate the speciation and dissociation of boric acid in a concentrated sodium chloride solution in the temperature range of 25 to 90 °C [77 to 194 °F] to obtain the dissociation equilibrium constant for boric acid in a brine solution. The calculation was conducted using a mixer reactor. This calculation was to verify if the ESP Version 6.6[®] software can be used to accurately predict the thermodynamic behavior of boron containing species in concentrated brine solutions at different temperatures. As StreamAnalyzer Version 1.2[®] shares the same OLI Systems, Inc. engine with ESP Version 6.6[®] and the two previous cases have shown that the results from ESP Version 6.6[®] are close to the results from StreamAnalyzer Version 1.2[®], no calculation was performed with StreamAnalyzer Version 1.2[®] for this test case.

A.2.3.1 Test Input

Input temperatures were 25, 40, 58, and 90 °C [77, 104, 136, and 194 °F]. The input pressure was 101 kPa [1 atm].

Table A-3. ESP Version 6.6[®] Speciation Results and Comparison of the Calculated Borax Solubilities with the Experimental Values at Different Temperatures

Temperature °C [°F]	20 [68]		40 [104]		60 [140]		75 [167]		94 [201]	
	Aqueous	Solid	Aqueous	Solid	Aqueous	Solid	Aqueous	Solid	Aqueous	Solid
pH	9.30	—	9.16	—	9.08	—	9.01	—	8.95	—
Flow Units	mol/hr	mol/hr	mol/hr	mol/hr	mol/hr	mol/hr	mol/hr	mol/hr	mol/hr	mol/hr
H ₂ O	36.09	—	36.97	—	48.44	—	48.70	—	49.58	—
B(OH) ₃	0.03	—	0.05	—	0.08	—	0.09	—	0.10	—
NaB(OH) ₄ ⁻	3.2 × 10 ⁻³	—	1.2 × 10 ⁻²	—	6.0 × 10 ⁻²	—	9.0 × 10 ⁻²	—	1.5	—
OH ⁻	1.2 × 10 ⁻⁵	—	4.1 × 10 ⁻⁵	—	1.5 × 10 ⁻⁴	—	2.8 × 10 ⁻⁴	—	5.6 × 10 ⁻⁴	—
B ₃ O ₃ (OH) ₄ ⁻	1.8 × 10 ⁻²	—	5.4 × 10 ⁻²	—	1.8	—	2.5	—	3.5	—
B ₄ O ₅ (OH) ₄ ⁻	5.3 × 10 ⁻²	—	1.3	—	5.4	—	6.9	—	1.2	—
B(OH) ₄ ⁻	4.3 × 10 ⁻²	—	8.8 × 10 ⁻²	—	2.0	—	2.5	—	3.0	—
H ⁺	4.8 × 10 ⁻¹⁰	—	7.5 × 10 ⁻¹⁰	—	1.4 × 10 ⁻⁹	—	1.6 × 10 ⁻⁹	—	2.0 × 10 ⁻⁹	—
Na ⁺	0.17	—	0.41	—	1.52	—	1.96	—	3.13	—
B ₂ O(OH) ₅ ⁻	0.00	—	0.01	—	0.05	—	0.09	—	0.16	—
Na ₂ B ₄ O ₇ ·10H ₂ O	—	1.91	—	1.79	—	—	—	—	—	—
Na ₂ B ₄ O ₇ ·4H ₂ O	—	—	—	—	—	1.21	—	0.97	—	0.36
Total, g/hr	672	730	721	682	1,072	331	1,136	266	1,304	99
Volume, L/hr	0.65	0.43	0.68	0.40	0.91	0.24	0.93	0.19	0.97	0.07

Table A-3. ESP Version 6.6 [®] Speciation Results and Comparison of the Calculated Borax Solubilities with the Experimental Values at Different Temperatures (continued)										
Temperature °C [°F]	20 [68]		40 [104]		60 [140]		75 [167]		94 [201]	
Enthalpy, cal/hr	-2.56 × 10 ⁶	-2.89 × 10 ⁶	-2.73 × 10 ⁶	-2.69 × 10 ⁶	-4.07 × 10 ⁶	-1.32 × 10 ⁶	-4.31 × 10 ⁶	-1.06 × 10 ⁶	-4.95 × 10 ⁶	-3.94 × 10 ⁶
Density, g/L	1,030	1,712	1,067	1,712	1,184	1,366	1,228	1,366	1,341	1,366
Solubilities in Borax in Water										
Calc. Na (M)	0.26	—	0.61	—	1.68	—	2.12	—	3.22	—
Calc. B (M)	0.52	—	1.22	—	3.37	—	4.25	—	6.41	—
Expl* Na (M)†	0.25	—	0.63	—	1.84	—	2.23	—	3.52	—
Expl B (M)†	0.51	—	1.26	—	3.70	—	4.47	—	7.08	—
Deviation, Na (%)	1.66	—	-2.43	—	-9.04	—	-4.85	—	-8.72	—
Deviation, B (%)	1.85	—	-2.57	—	-8.98	—	-4.97	—	-9.40	—
Experimentally Identified Solid Phases*										
Na ₂ B ₄ O ₇ ·10H ₂ O	—	Yes	—	Yes	—	—	—	—	—	—
Na ₂ B ₄ O ₇ ·4H ₂ O	—	—	—	—	—	Yes	—	Yes	—	Yes
Input parameters: H ₂ O: 55.508 mol; Na ₂ B ₄ O ₇ : 2 mol.										
*Expl – experimental. †Nies, N.P. and R.W. Hulbert. "Solubility Isotherms in the System Sodium Oxide-Boric Oxide-Water." <i>Journal of Chemical Engineering Data</i> . Vol. 12, No. 3. pp. 303-313. 1967.										

Table A-4. StreamAnalyzer Version 1.2[®] Speciation Results and Comparison of the Calculated Borax Solubilities with the Experimental Values at Different Temperatures

Temperature °C [°F]	20 [68]		40 [104]		60 [140]		75 [167]		94 [201]	
Phase	Aqueous	Solid	Aqueous	Solid	Aqueous	Solid	Aqueous	Solid	Aqueous	Solid
pH	9.30	—	9.16	—	9.08	—	9.01	—	—	—
Unit	mol	mol	mol	mol	mol	mol	mol	mol	mol	mol
H ₂ O	36.09	—	36.97	—	48.44	—	48.70	—	—	—
B(OH) ₃	0.03	—	0.05	—	0.08	—	0.09	—	—	—
Na ₂ B ₄ O ₇ ·10H ₂ O	0.00	1.91	0.00	1.79	0.00	0.00	0.00	0.00	0.00	0.00
Na ₂ B ₄ O ₇ ·4H ₂ O	0.00	0.00	0.00	0.00	0.00	1.21	0.00	0.97	0.00	0.00
NaB(OH) ₄	3.2 × 10 ⁻³	—	1.2 × 10 ⁻²	—	6.0 × 10 ⁻²	—	8.97 × 10 ⁻²	—	—	—
B(OH) ₄ ⁻	4.26 × 10 ⁻²	—	8.8 × 10 ⁻²	—	2.03	—	2.51	—	—	—
B ₂ O(OH) ₅ ⁻	2.69 × 10 ⁻³	—	1.17 × 10 ⁻²	—	5.21 × 10 ⁻²	—	8.82 × 10 ⁻²	—	—	—
B ₃ O ₃ (OH) ₄ ⁻	1.76 × 10 ⁻²	—	5.36 × 10 ⁻²	—	1.81	—	2.47	—	—	—
B ₄ O ₅ (OH) ₄ ⁻	5.29 × 10 ⁻²	—	1.30	—	5.41	—	6.89	—	—	—
H ⁺	4.79 × 10 ⁻¹⁰	—	7.48 × 10 ⁻¹⁰	—	1.35 × 10 ⁻⁹	—	1.63 × 10 ⁻⁹	—	—	—
Na ⁺	1.69	—	4.13	—	1.52	—	1.96	—	—	—
OH	1.23 × 10 ⁻⁵	—	4.13 × 10 ⁻⁵	—	1.48 × 10 ⁻⁴	—	2.77 × 10 ⁻⁴	—	—	—
Total Mole, mol	36.4	—	37.7	—	51.1	—	52.1	—	—	—
Total Volume, L	0.65	—	0.68	—	0.91	—	0.93	—	—	—

Table A-4. StreamAnalyzer Version 1.2 [®] Speciation Results and Comparison of the Calculated Borax Solubilities with the Experimental Values at Different Temperatures (continued)										
Temperature °C [°F]	20 [68]		40 [104]		60 [140]		75 [167]		94 [201]	
Phase	Aqueous	Solid	Aqueous	Solid	Aqueous	Solid	Aqueous	Solid	Aqueous	Solid
Total Mass, g	672.46	—	720.75	—	1,071.60	—	1,136.50	—	—	—
Density, g/L	1,029.85	—	1,066.48	—	1,183.57	—	1,228.28	—	—	—
Solubilities in Borax in Water										
Calc. Na (M)	0.26	—	0.63	—	1.74	—	2.22	—	—	—
Calc. B (M)	0.53	—	1.26	—	3.49	—	4.44	—	—	—
Exp. Na (M)*	0.25	—	0.63	—	1.84	—	2.23	—	3.52	—
Exp. B (M)*	0.51	—	1.26	—	3.70	—	4.47	—	7.08	—
Deviation, Na (%)	3.56	—	0.47	—	-5.45	—	-0.51	—	—	—
Deviation, B (%)	3.45	—	0.16	—	-5.87	—	-0.71	—	—	—
Experimentally Identified Solid Phases*										
Na ₂ B ₄ O ₇ ·10H ₂ O	—	Yes	—	Yes	—	—	—	—	—	—
Na ₂ B ₄ O ₇ ·4H ₂ O	—	—	—	—	—	Yes	—	Yes	—	Yes
Input parameters: H ₂ O: 55.508 mol; Na ₂ B ₄ O ₇ : 2 mol.										
*Nies, N.P. and R.W. Hulbert. "Solubility Isotherms in the System Sodium Oxide-Boric Oxide-Water." <i>Journal of Chemical Engineering Data</i> . Vol. 12, No. 3. pp. 303-313. 1967.										

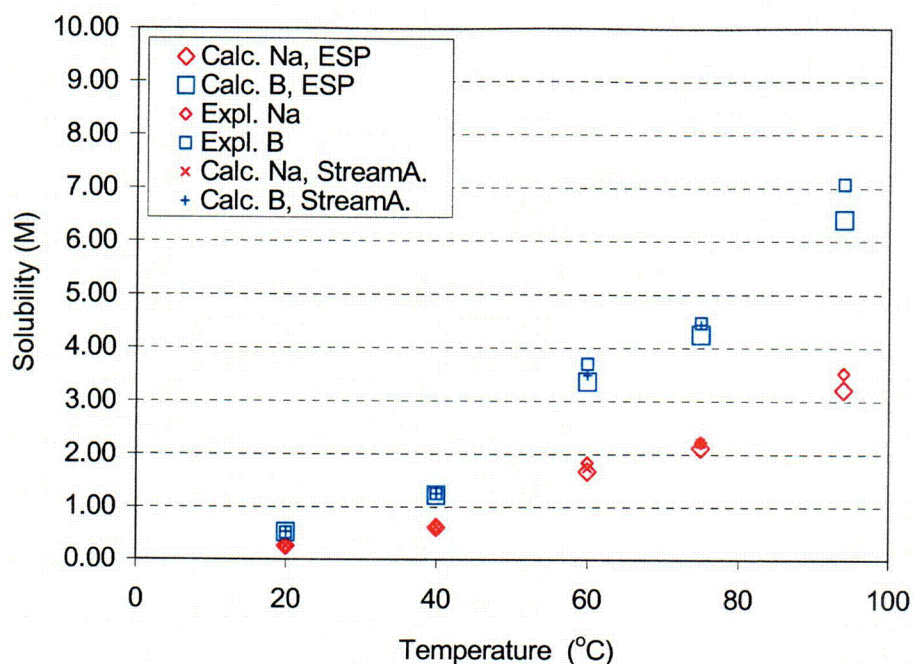


Figure A-4. Comparison of the Calculated Solubilities of Sodium and Boron in Borax-Water Systems Using ESP Version 6.6[®] and StreamAnalyzer Version 1.2[®] with the Experimental Values at Different Temperatures (Note: °F = 1.8 × °C + 32).

A.2.3.2 Test Procedure

The test was run by specifying the calculation as constant pressure isotherm. The input stream contains 0.5 mol [30.9 g] of boric acid [B(OH)₃] and 55.508 mol [1 kg] of water, 3 mol [175.3 g] of NaCl, and an appropriate amount of NaOH to adjust the pH of the solution to the neutral range.

A.2.3.3 Test Results

The calculations with ESP Version 6.6[®] provides a full range of parameters similar to those discussed in Test Case 1. A partial list of these parameters is given in Table A-5. The calculated dissociation constants of boric acid in the 3-M [175.3g] sodium chloride solution are slightly lower than those experimentally measured by Spessard (1970). The differences of $[\log K_1(\text{calc}) - \log K_1(\text{exp})]$ are -0.46 at 25 °C [77 °F] and -0.22 at 90 °C [194 °F].

Table A-5. ESP Version 6.6[®] Speciation Results and Comparison of the Calculated Equilibrium Constant for Dissociation of Boric Acid in Concentrated NaCl Solution at Different Temperatures

Temperature, °C [°F]	25 [77]	40 [104]	58 [136]	90 [194]
pH	5.86	5.94	6.01	6.09
Flow Units	molality	molality	molality	molality
H ₂ O	55.51	55.51	55.51	55.51
HCl	1.01×10^{-12}	2.11×10^{-12}	5.05×10^{-12}	2.12×10^{-11}
NaB(OH) ₄	1.91×10^{-4}	3.09×10^{-4}	4.92×10^{-4}	8.79×10^{-4}
B(OH) ₃	3.54×10^{-1}	3.54×10^{-1}	3.55×10^{-1}	3.59×10^{-1}
OH ⁻	6.19×10^{-9}	2.41×10^{-8}	9.44×10^{-8}	6.32×10^{-7}
B ₃ O ₃ (OH) ₄ ⁻	4.56×10^{-2}	4.58×10^{-2}	4.51×10^{-2}	4.24×10^{-2}
B ₃ O ₅ (OH) ₄ ⁻	1.62×10^{-3}	1.14×10^{-3}	8.59×10^{-4}	6.98×10^{-4}
B(OH) ₄ ⁻	3.18×10^{-4}	5.33×10^{-4}	8.68×10^{-4}	1.59×10^{-3}
Cl ⁻	2.99	2.99	2.99	2.99
H ⁺	1.04×10^{-6}	9.05×10^{-7}	8.14×10^{-7}	7.51×10^{-7}
Na ⁺	3.04	3.04	3.04	3.04
B ₂ O(OH) ₅ ⁻	4.95×10^{-4}	9.38×10^{-4}	1.70×10^{-3}	3.59×10^{-3}
Dissociation Constant for B(OH)₃ + H₂O = H⁺ + B(OH)₄⁻				
log K ₁ (Calc)	-9.03	-8.87	-8.70	-8.48
log K ₁ (Exptl)*†	-8.56	-8.47	-8.47	-8.26
Difference	-0.46	-0.39	-0.23	-0.22
*Exptl – experimental.				
†Spessard, J.E. "Investigation of Borate Equilibria in Neutral Salt Solutions." <i>Journal of Inorganic and Nuclear Chemistry</i> . Vol. 32. p. 2,607. 1970.				

A.3 Experimental Validation Tests and Analyses

Three sets of experiments were performed to support validation of the OLI Systems, Inc. software for borated water. The validation tests involved determination of solubility of compounds by mixing 0.259 mol H₃BO₃, 0.17 mol NaOH, and 0.01 mol ZnCO₃ or CaCO₃ in 1,000 mL water. The validation test matrix is shown in Table A-6.

A.3.1 Validation Test Method

The 25 and 60 °C [77 and 140 °F] tests were performed in open polytetrafluoroethylene beakers. The 90 °C [194 °F] tests were performed in a sealed glass cell to avoid excessive evaporation. The water–solid mixtures were stirred for 4 hours and held for another 4 hours to allow the solid to settle at the bottom of the polytetrafluoroethylene beakers or the glass cell. At the end of the 4-hour hold, samples were taken from the upper section of the beaker or glass cell using a syringe through a 0.45- μ m [1.77×10^{-5} -in] filter to prevent the suspended solid particles from entering the sample. Because of the high water pressure of the solid–water mixture, the 130 °C [266 °F] tests were conducted in a polytetrafluoroethylene-lined autoclave composed of a nickel-based alloy that allowed the mixing by a polytetrafluoroethylene-sheathed magnetic stir bar. At the end of the 4-hour hold, approximately 80 mL [2.7 oz] of liquid were siphoned from the upper section of the autoclave to a beaker through a 3.18-mm [0.125-in]-diameter stainless steel tubing. The tubing was slightly cooled so that the liquid temperature exiting the tubing was lower than 100 °C [212 °F] to avoid evaporation. A syringe was used to take the sample from the beaker, while the liquid was still hot, through a 0.45- μ m [1.77×10^{-5} -in] filter to prevent the suspended solid particle from entering the sample.

Two types of analyses were performed in supporting validation of the OLI Systems, Inc. software for borated water. The primary method was inductively coupled plasma emission spectrophotometry analysis, and the second method was atomic absorption spectrophotometry analysis. Brief descriptions of the analysis methods are given in the following paragraphs.

The inductively coupled plasma spectrophotometer utilizes plasma to excite elemental electrons that produce photons unique to each element (Vela, et al., 1993; Winge, 1985). Advantages of using inductively coupled plasma include its ability to identify and quantify all metallic and

Table A-6. Validation Test Matrix					
	Solution	Temperature (°C) [°F]			
		25 [77]	60 [140]	90 [194]	130 [266]
Test 1	1,000 mL H ₂ O, 0.259 mol H ₃ BO ₃ , 0.17 mol NaOH	X	X	X	—
Test 2	1,000 mL H ₂ O, 0.259 mol H ₃ BO ₃ , 0.17 mol NaOH, 0.01 mol ZnCO ₃	X	X	X	X
Test 3	1,000 mL H ₂ O, 0.259 mol H ₃ BO ₃ , 0.17 mol NaOH, 0.01 mol CaCO ₃	X	X	X	X

nonmetallic elements in an aqueous solution with the exception of argon. In this method, elements entering the hot plasma are vaporized and excited, resulting in the emission of characteristic wavelengths of the element. The intensity of that emission can be used to quantify the amount of the element. Two inductively coupled plasmas were utilized, a Thermo Jarrell Ash Inductively Coupled Plasma Spectrometer Model ICAP 61 Trace Analyzer and a Spectro Inductively Coupled Plasma Spectrometer Model FME-05. The instruments were calibrated daily using traceable standards from the National Institute of Standards and Technology. The detection limit by inductively coupled plasma is 2.5×10^{-6} mol [0.1 ppm] for calcium and 1.5×10^{-6} mol [0.01 ppm] for zinc.

Atomic-absorption spectroscopy was employed on selected samples to verify the zinc and calcium results from inductively coupled plasma. The method uses the absorption of light to measure the concentration of gas-phase atoms in a sample solution (Elwell and Gidley, 1966; Perkin-Elmer Corporation, 1971). Concentrations are determined from a working curve after calibrating the instrument with standards of known concentrations. The calcium and zinc contents of the 25 °C [77 °F] samples were analyzed using a Perkin-Elmer Model 3100 Atomic Absorption Spectrophotometer. Calcium and zinc elements were analyzed independently. Calcium analyses were performed with a copper-iron-manganese-zinc hollow cathode lamp at a 422.7-nm [16.64×10^{-6} -in] wavelength using an air-acetylene flame. The detection limits are 5.0×10^{-6} mol [0.2 ppm] for calcium and 7.6×10^{-7} mol [0.05 ppm] for zinc. Zinc analyses were performed using a calcium-magnesium hollow cathode lamp at 213.9-nm [8.42×10^{-6} -in] wavelength, using an air-acetylene flame. Five absorbency measurements were recorded for each sample, and the average values were reported.

Table A-7 compares the measured values from inductively coupled plasma and atomic absorption analyses on two calcium-containing solutions and one zinc-containing solution. For the calcium-containing solutions, samples were taken after 4 hours and after 360 hours hold times. Identical solutions were submitted for atomic absorption and inductively coupled plasma analysis for comparison. For the 4-hour samples, the atomic absorption and inductively coupled plasma measurements yield an identical value of 8.03×10^{-4} mol. For the 360-hour samples, the

Test Solution in 1,000 mL Water at 25 °C [77 °F]	Component	Atomic Absorption Measurement (mol)	Inductively Coupled Plasma Measurement (mol)	Percent Difference (%)
0.259 mol H ₃ BO ₃ , 0.17 mol NaOH, 0.01 mol CaCO ₃	Calcium	$8.03 \times 10^{-4*}$	$8.03 \times 10^{-4*}$	0
		$8.33 \times 10^{-4}\dagger$	$8.08 \times 10^{-4}\dagger$	3.0
0.259 mol H ₃ BO ₃ , 0.17 mol NaOH, 0.01 mol ZnCO ₃	Zinc	$4.89 \times 10^{-6}\dagger$	$4.6 \times 10^{-6}\dagger$	5.9

*Samples taken after 4 hours.
†Samples taken after 360 hours.

inductively coupled plasma measurement yields 8.08×10^{-4} mol while the atomic absorption measurement yields 8.33×10^{-4} mol, a difference of approximately 3 percent. For the zinc-containing solution, samples were taken after the solution was settled for 360 hours. The inductively coupled plasma measurement yields a zinc content of 4.6×10^{-6} mol, while the atomic absorption yields a measurement of 4.89×10^{-6} mol. The measurement difference from the two methods is approximately 6 percent. The results show that the zinc and calcium measurements by inductively coupled plasma and atomic absorption are consistent.

A.3.2 Comparison of OLI Systems, Inc. Simulation with Experimental Results

Inductively coupled plasma analyses were performed on all solutions listed in Table A-6 to support validation of the OLI Systems, Inc. software. The OLI simulation results for the soluble and insoluble phases for sodium and boron in zinc- and calcium-containing solutions are presented in Tables A-8, A-9, A-10, and A-11 for 25, 60, 90, and 130°C [77, 140, 194, and 266 °F] tests. The inductively coupled plasma analysis results are also shown in the corresponding tables for comparisons. In the tables, the amount of solid phase for calcium and zinc was obtained as a difference between the amount added to the solution and its soluble component.

The results show good agreement between OLI Systems, Inc. simulations and experimental data for sodium and boron in borated water containing zinc or calcium. Except for 130 °C [266 °F], the results also show a good agreement for the insoluble phases of CaCO_3 and ZnCO_3 . The amount of insoluble phase was estimated by subtracting the amount of soluble phase from the total amount added to the test solution. However, significant variance was observed between OLI Systems, Inc. simulations and experimental data for the soluble phases of CaCO_3 and ZnCO_3 . The variance observed for the soluble phases of CaCO_3 is attributed to the large degree of variation in the published solubility data used in the OLI database. For example, the solubility of CaCO_3 in water at about 16 °C [60 °F] was 0.9991×10^{-4} mol/kg-water from one published source and 1.449×10^{-4} mol/kg-water from another published source.² The variance observed for the soluble ZnCO_3 is probably also due to the variations in the published data used in the OLI database. The calculated results for the soluble phases of CaCO_3 and ZnCO_3 are approximately the same orders of magnitude as the measured results except for ZnCO_3 at 130 °C [266 °F]. At 130 °C [266 °F], the measured amount of soluble ZnCO_3 was two orders of magnitude lower than that predicted by the OLI Systems, Inc simulation. Detailed analysis of the simulation indicated that the insoluble phase was present as Zn(OH)_2 below 105 °C [221 °F] and as ZnCO_3 above 105 °C [221 °F]. This discrepancy may be due to error(s) in the ZnCO_3 database or the uncertainty of the ZnCO_3 thermodynamic data at temperatures above 105 °C [221 °F]. The results also show that the calculated trends for the dependence of the solubilities of both CaCO_3 and ZnCO_3 on temperature are the same as the measured trends.

It should be noted, however, that the estimation of insoluble phases by the subtraction of the soluble phases from added amounts of CaCO_3 and ZnCO_3 shows a good agreement between OLI Systems, Inc simulation and experimental data. This indicates that despite large variance in the soluble phase, both CaCO_3 and ZnCO_3 are expected to have low solubility.

²Personal communication with Andre Anderko, OLI Systems, Inc., July 2004.

Table A-8. Distribution of Soluble and Insoluble Phases in Boric Acid and Sodium Hydroxide Solutions Containing Zinc and Calcium at 25 °C [77 °F]

Test Solution in 1,000 mL Water at 25 °C [77 °F]	Element	Amount (mol)	OLI Systems, Inc. Simulation (mol)		Inductively Coupled Plasma Analyses (mol)		Percent Difference	
			Soluble Phase	Insoluble Phase	Soluble Phase	Insoluble Phase*	Soluble Phase	Insoluble Phase
0.259 mol H ₃ BO ₃ , 0.17 mol NaOH	Boron	0.259	0.259	0	0.239	—	7.7	—
	Sodium	0.17	0.17	0	0.147	—	13.5	—
0.259 mol H ₃ BO ₃ , 0.17 mol NaOH, 0.01 mol ZnCO ₃	Boron	0.259	0.259	0	0.247	—	4.6	—
	Sodium	0.17	0.17	0	0.151	—	11.2	—
	Zinc	0.01	9.8×10^{-6}	9.99×10^{-3}	$1.85 \times 10^{-6}\dagger$	9.99×10^{-3}	81.1	0
0.259 mol H ₃ BO ₃ , 0.17 mol NaOH, 0.01 mol CaCO ₃	Boron	0.259	0.259	0	0.249	—	3.9	—
	Sodium	0.17	0.17	0	0.15	—	11.8	—
	Calcium	0.01	5.2×10^{-4}	9.48×10^{-3}	8.0×10^{-4}	9.2×10^{-3}	-53.8	-3

*Estimated from the analysis of soluble species.
†Number close to detection limit, indicating extremely low solubility.

Table A-9. Distribution of Soluble and Insoluble Phases in Boric Acid and Sodium Hydroxide Solutions Containing Zinc and Calcium at 60 °C [140 °F]

Test Solution in 1,000 mL Water at 60 °C [140 °F]	Element	Amount (mol)	OLI Systems, Inc. Simulation (mol)		Inductively Coupled Plasma Analyses (mol)		Percent Difference	
			Soluble Phase	Insoluble Phase	Soluble Phase	Insoluble Phase*	Soluble Phase	Insoluble Phase
0.259 mol H ₃ BO ₃ , 0.17 mol NaOH	Boron	0.259	0.259	0	0.229	—	11.6	—
	Sodium	0.17	0.17	0	0.141	—	17.1	—
0.259 mol H ₃ BO ₃ , 0.17 mol NaOH, 0.01 mol ZnCO ₃	Boron	0.259	0.259	0	0.287	—	-10.8	—
	Sodium	0.17	0.17	0	0.174	—	-2.4	—
	Zinc	0.01	2.4×10^{-5}	9.98×10^{-3}	$6.0 \times 10^{-6}\dagger$	9.99×10^{-3}	-74.0	-0.1
0.259 mol H ₃ BO ₃ , 0.17 mol NaOH, 0.01 mol CaCO ₃	Boron	0.259	0.259	0	0.292	—	-12.7	—
	Sodium	0.17	0.17	0	0.169	—	0.6	—
	Calcium	0.01	4.5×10^{-4}	9.55×10^{-3}	8.3×10^{-4}	9.2×10^{-3}	-84.4	4.0

*Estimated from the analysis of soluble species.
†Number close to detection limit, indicating extremely low solubility.

Table A-10. Distribution of Soluble and Insoluble Phases in Boric Acid and Sodium Hydroxide Solutions Containing Zinc and Calcium at 90 °C [194 °F]								
Test Solution in 1,000 mL Water at 90 °C [194 °F]	Element	Amount (mol)	OLI Systems, Inc. Simulation (mol)		Inductively Coupled Plasma Analyses (mol)		Percent Difference	
			Soluble Phase	Insoluble Phase	Soluble Phase	Insoluble Phase*	Soluble Phase	Insoluble Phase
0.259 mol H ₃ BO ₃ , 0.17 mol NaOH	Boron	0.259	0.259	0	0.240	—	7.3	—
	Sodium	0.17	0.17	0	0.147	—	13.5	—
0.259 mol H ₃ BO ₃ , 0.17 mol NaOH, 0.01 mol ZnCO ₃	Boron	0.259	0.259	0	0.257	—	0.8	—
	Sodium	0.17	0.17	0	0.161	—	5.3	—
	Zinc	0.01	3.07×10^{-5}	9.97×10^{-3}	1.76×10^{-5}	9.98×10^{-3}	43.7	-0.1
0.259 mol H ₃ BO ₃ , 0.17 mol NaOH, 0.01 mol CaCO ₃	Boron	0.259	0.259	0	0.259	—	0	—
	Sodium	0.17	0.17	0	0.16	—	5.9	—
	Calcium	0.01	3.72×10^{-4}	9.63×10^{-3}	5.36×10^{-4}	9.46×10^{-3}	-44.1	1.8

*Estimated from the analysis of soluble species.

Table A-11. Distribution of Soluble and Insoluble Phases in Boric Acid and Sodium Hydroxide Solutions Containing Zinc and Calcium at 130 °C [266 °F]

Test Solution in 1,000 mL Water at 130 °C [266 °F]	Element	Amount (mol)	OLI Systems, Inc. Simulation (mol)		Inductively Coupled Plasma Analyses (mol)		Percent Difference	
			Soluble Phase	Insoluble Phase	Soluble Phase	Insoluble Phase*	Soluble Phase	Insoluble Phase
0.259 mol H ₃ BO ₃ , 0.17 mol NaOH, 0.01 mol ZnCO ₃	Boron	0.259	0.259	0	0.226	—	12.7	—
	Sodium	0.17	0.17	0	0.14	—	17.6	—
	Zinc	0.01	4.21×10^{-3}	5.79×10^{-3}	2.54×10^{-5}	9.97×10^{-3}	99.4	72.2
0.259 mol H ₃ BO ₃ , 0.17 mol NaOH, 0.01 mol CaCO ₃	Boron	0.259	0.259	0	0.241	—	6.9	—
	Sodium	0.17	0.17	0	0.148	—	12.9	—
	Calcium	0.01	2.88×10^{-4}	9.71×10^{-3}	3.34×10^{-4}	9.67×10^{-3}	-16.0	0.4

*Estimated from the analysis of soluble species.

A.4 Summary

Computational thermodynamics simulation calculations were conducted using Environmental Simulation Program (ESP) Version 6.6[®] (OLI Systems, Inc., 2002a) and StreamAnalyzer Version 1.2[®] (OLI Systems, Inc., 2002b). OLI Systems, Inc. software was validated by comparing simulation results with data on borated water published in the literature and with results of solubility type experiments using borated water containing CaCO₃ or ZnCO₃ in the temperature range of 25°C [77°F] to 130°C [266°F]. Data showed a good agreement between published literature and OLI Systems, Inc. simulation. Except for ZnCO₃ at 130°C [266°F], the experimentally measured solubility data agreed with the OLI Systems, Inc. simulation results for the dominant solid or soluble phases, including aqueous H₃BO₃, aqueous NaOH, and solid CaCO₃ or solid ZnCO₃. A large variation was observed for soluble phases of zinc and calcium and was attributed to variation and uncertainty in published data used in OLI Systems, Inc. software database.

A.5 References

Bromley, L.A. "Approximate Individual Ion Values of β (or B) in Extended Debye-Huckel Theory for Uni-Univalent Aqueous Solutions at 298.15 K." *Journal of Chemical Thermodynamics*. Vol. 4. p. 669. 1972.

Elwell, W.T. and J.A.F. Gidley. *Atomic Absorption Spectrophotometry*. 2nd Edition. New York City, New York: Pergamon Press. 1966.

Helgeson, H.C., D.H. Kirkham, and G.C. Flowers. "Theoretical Prediction of the Thermodynamic Behavior of Aqueous Electrolytes at High Pressures and Temperatures IV Calculation of Activity Coefficients, Osmotic Coefficients, and Apparent Molal and Standard and Relative Partial Molal Properties to 600 °C and 5 Kb." *American Journal of Science*. Vol. 281. p. 1,249. 1981.

Nies, N.P. and R.W. Hulbert. "Solubility Isotherms in the System Sodium Oxide-Boric Oxide-Water," *Journal of Chemical Engineering Data*. Vol. 12, No. 3. pp. 303–313. 1967.

OLI Systems, Inc. "StreamAnalyzer Version 1.2." Morris Plains, New Jersey: OLI Systems, Inc. 2002a.

———. "Environmental Simulation Program Version 6.6." Morris Plains, New Jersey: OLI Systems, Inc. 2002b.

Perkin-Elmer Corporation. "Analytical Method for Atomic Absorption Spectrophotometry." Norwalk, Connecticut: Perkin-Elmer Corporation. 1971.

Pitzer, K.S. *Activity Coefficients in Electrolyte Solutions*. K.S. Pitzer, ed. 2nd Edition. Boston, Massachusetts: Chemical Rubber Company, CRC Press. pp. 75–153. 1991.

———. "Thermodynamics of Electrolytes 1: Theoretical Basis and General Equations." *Journal of Physics and Chemistry*. Vol. 77. p. 268. 1973.

Spessard, J.E. "Investigation of Borate Equilibria in Neutral Salt Solutions." *Journal of Inorganic and Nuclear Chemistry*. Vol. 32. p. 2,607. 1970.

Vela, N.P., L.K. Olson, and J.A. Caruso. "Elemental Speciation with Plasma Mass Spectrometry." *Analytical Chemistry*. Vol. 65, No. 13. pp. 584A–597A. 1993.

Winge, R.K. *Inductively Coupled Plasma-Emission Spectroscopy: An Atlas of Spectral Information*. New York City, New York: John Wiley and Sons. 1985.

Yang, L. "Software Validation Report for Environmental Simulation Program (ESP) Version 6.6, Corrosion Simulation Program (CSP) Version 2.3, Environmental Simulation Program for Concentrated Brines (ESPCB) Version 7.0 Alfa, and Stream Analyzer Version 1.2." San Antonio, Texas: Center for Nuclear Waste Regulatory Analyses. 2003.

APPENDIX B

TYPICAL OLI SIMULATION OUTPUT

Calculation Summary

T60C Calculation for Work1

Automatic Chemistry Model

Databanks:

Corrosion

Geochemical

Public

Redox selected

Unit Set: Default

Isothermal Calculation

Temperature 60.000 °C

Pressure 1.0000 atm

B-1

Stream Inflows

H2O	55.508	mol
Zn	1.6000e-6	mol
Al	1.5000e-5	mol
Cu	1.2000e-6	mol
Fe	2.8000e-5	mol
B(OH)3	0.20000	mol
NaOH	0.0	mol
Ca2SiO4	1.0000e-4	mol
SiO2	5.9000e-3	mol
Al2O3	2.0000e-4	mol
MgO	8.3000e-4	mol
Na2O	1.4400e-3	mol
CaB2O4	4.0000e-4	mol
CaO	7.9000e-4	mol

Speciation Summary

Total number of species: 402

User Inflows	Related Inflows	Aqueous Species	Vapor Species	Solid Species	Second Liquid Species
H2O	12CaO.7Al2O3	H2O	H2O - Vap	12CaO.7Al2O3	
Zn	Al(OH)3	Al(OH)2+1	H2 - Vap	Al	
Al	Al2Si2O5(OH)4	Al(OH)3 - Aq	O2 - Vap	Al(OH)3	
Cu	Al2Si2O5(OH)4	Al(OH)4-1		Al2O3	
Fe	Al2Si4O10(OH)2	Al+3		Al2Si2O5(OH)4	
B(OH)3	Al2SiO5	AlOH+2		Al2Si4O10(OH)2	
NaOH	Al2SiO5	B(OH)3 - Aq		Al2SiO5	
Ca2SiO4	Al2SiO5	B(OH)4-1		Al2SiO5	
SiO2	Al2SiO5(OH)4	B2O(OH)5-1		Al2SiO5	
Al2O3	Al4Fe5Si6O22(OH)2	B3O3(OH)4-1		AlO(OH)	
MgO	AlO(OH)	B4O5(OH)4-2		AlO(OH)	
Na2O	AlO(OH)	Ca+2		B(OH)3	
CaB2O4	Ca(Al2Si4O12).2H2O	CaH2BO3+1		Ca(Al2Si4O12).2H2O	
CaO	Ca(Al2Si5O14).5H2O	CaHSiO3+1		Ca(OH)2	
	Ca(Al2Si6O16).5H2O	CaOH+1		CaO .165Al2.33Si3.67O 10(OH)2	
	Ca(OH)2	CaSiO2(OH)2 - Aq		Ca12Al14O33	
	CaO .165Al2.33	Cu(OH)2 - Aq		Ca2Al2Si3O10(OH)2	
	Si3.67O10(OH)2			Ca2Al2SiO7	
	Ca12Al14O33	Cu(OH)3-1		Ca2Al2SiO7	
	Ca2Al2Si3O10(OH)2	Cu(OH)4-2		Ca2Al3Si3O12(OH)	
	Ca2Al2SiO7	Cu+1		Ca2Al3Si3O12(OH)	
	Ca2Al2SiO7	Cu+2		Ca2B2O5	
	Ca2Al3Si3O12(OH)	CuOH+1		Ca2Fe2O5	
	Ca2Al3Si3O12(OH)	Fe(OH)2 - Aq		Ca2Mg5Si8O22(OH)2	
	Ca2Al4Si8O24 .7H2O	Fe(OH)2+1		Ca2MgSi2O7	
	Ca2B2O5	Fe(OH)3 - Aq		Ca2Si3O7(OH)2 .1.5H2O	
	Ca2Fe2O5	Fe(OH)3-1		Ca2SiO3(OH)2 .0.17H2O	
	Ca2Fe5Si8O22(OH)2	Fe(OH)4-1		Ca2SiO4	
	Ca2Mg5Si8O22(OH)2	Fe(OH)4-2		Ca2SiO4	
	Ca2MgSi2O7	Fe+2		Ca3(BO3)2	
	Ca2Si3O7(OH)2 .1.5H2O	Fe+3		Ca3Al2(SiO4)3	
	Ca2SiO3(OH)2 .0.17H2O	Fe2(OH)2+4		Ca3Al2O6	
	Ca2SiO4	FeO4-2		Ca3Fe2Si3O12	
	Ca3(BO3)2	FeOH+1		Ca3MgSi2O8	
	Ca3Al2(SiO4)3	FeOH+2		Ca3Si2O4(OH)6	
	Ca3Al2O6	H+1		Ca3Si2O7	
	Ca3Fe2Si3O12	H2 - Aq			

Ca3MgSi2O8	H2SiO4-2
Ca3Si2O4(OH)6	H3SiO4-1
Ca3Si2O7	Mg+2
Ca3SiO5	MgHSiO3+1
Ca4Al2Fe2O10	MgOH+1
Ca4Si3O9(OH)2 .0.5H2O	MgSiO2(OH)2 - Aq
Ca5Si6H11O22.5	Na+1
Ca5Si6H21O27.5	NaB(OH)4 - Aq
Ca5Si6H6O20	NaHSiO3 - Aq
Ca6Si6O17(OH)2	O2 - Aq
CaAl2(Al2Si2O10)(OH)2	OH-1
CaAl2O4	SiO2 - Aq
CaAl2Si2O7(OH)2	Zn(OH)2 - Aq
CaAl2Si2O7(OH)2.1H2O	Zn(OH)3-1
CaAl2Si2O8	Zn(OH)4-2
CaAl2Si3O10.3H2O	Zn+2
CaAl2Si4O12	ZnOH+1
CaAl2Si4O12	
CaAl2Si4O12.4H2O	
CaAl2Si4O12.6H2O	
CaAl2Si7O18.6H2O	
CaAl2SiO6	
CaB4O7	
CaFe2O4	
CaFeSi2O6	
CaMgSi2O6	
CaMgSi2O6	
CaMgSiO4	
CaSi2O4(OH)2 .H2O	
CaSiO2(OH)2	
CaSiO3	
CaSiO3	
Cu(OH)2	
Cu2O	
CuO	
CuOH	
Fe(OH)2	
Fe(OH)3	
Fe0.947O	
Fe2Al2SiO5(OH)4	
Fe2Al9Si4O23(OH)	
Fe2Fe(FeSiO5)(OH)4	
Fe2O3	

Ca3SiO5
Ca4Al2Fe2O10
Ca4Si3O9(OH)2 .0.5H2O
Ca5Si6H11O22.5
Ca5Si6H21O27.5
Ca5Si6H6O20
Ca6Si6O17(OH)2
CaAl2(Al2Si2O10)(OH)2
CaAl2O4
CaAl2Si2O7(OH)2 .1H2O
CaAl2Si2O8
CaAl2Si3O10.3H2O
CaAl2Si4O12.4H2O
CaAl2SiO6
CaB2O4
CaB4O7
CaFe2O4
CaFeSi2O6
CaMgSi2O6
CaMgSiO4
CaO
CaSi2O4(OH)2 .H2O
CaSiO3
CaSiO3
Cu
Cu(OH)2
Cu2O
CuO
Fe
Fe(OH)2
Fe(OH)3
Fe0.947O
Fe2Al2SiO5(OH)4
Fe2O3
Fe2SiO4
Fe3O4
Fe3Si2O5(OH)4
Fe3Si4O10(OH)2
FeAl2O4
FeO
FeO
FeO(OH)
FeSiO3

Fe₂SiO₄
 Fe₃Al₂Si₃O₁₂
 Fe₃O₄
 Fe₃Si₂O₅(OH)₄
 Fe₃Si₄O₁₀(OH)₂
 Fe₃Si₄O₁₀(OH)₂
 Fe₅Al₂Si₃O₁₀(OH)₈
 Fe₇Si₈O₂₂(OH)₂
 FeAl₂O₄
 FeAl₂SiO₅(OH)₂
 FeNaSi₂O₆
 FeO
 FeO
 FeO(OH)
 FeSiO₃
 H₀.33Al₂.33Si₃.67O₁₀(OH)₂
 H₀.33Fe₂Al₀.33Si₃.67O₁₀(OH)₂
 H₀.33Mg₃Al₀.33Si₃.67O₁₀(OH)₂
 H₂
 H₂FeO₄
 H₄SiO₄
 Mg(OH)₂
 Mg₀.165Al₂.33Si₃.67O₁₀(OH)₂
 Mg₀.495Al₁.67Si₄O₁₀(OH)₂
 Mg₂Al₂SiO₅(OH)₄
 Mg₂Al₃(AlSi₅O₁₈)
 Mg₂Al₃(AlSi₅O₁₈)
 Mg₂Al₃(AlSi₅O₁₈).1H₂O
 Mg₂Al₄Si₅O₁₈.H₂O
 Mg₂SiO₄
 Mg₂SiO₄
 Mg₃.165Al₀.33Si₃.67O₁₀(OH)₂
 Mg₃Al₂Si₃O₁₂
 Mg₃Si₂O₅(OH)₄
 Mg₃Si₂O₅(OH)₄
 Mg₃Si₄O₁₀(OH)₂
 Mg₄[Si₆O₁₅(OH)₂(H₂O)₂].3H₂O

 Mg₄₈Si₃₅O₈₅(OH)₆₂
 Mg₄Al₄Si₂O₁₀(OH)₈
 Mg₅Al(AlSi₃O₁₀)(OH)₈
 Mg₅Al[AlSi₃O₁₀(OH)₂](OH)₆
 Mg₇Si₂O₈(OH)₂

H₀.33Al₂.33Si₃.67O₁₀(OH)₂
 H₀.33Fe₂Al₀.33Si₃.67O₁₀(OH)₂
 H₀.33Mg₃Al₀.33Si₃.67O₁₀(OH)₂
 Mg(OH)₂
 Mg₀.165Al₂.33Si₃.67O₁₀(OH)₂
 Mg₀.495Al₁.67Si₄O₁₀(OH)₂
 Mg₂Al₃(AlSi₅O₁₈)
 Mg₂Al₃(AlSi₅O₁₈).1H₂O
 Mg₂Al₄Si₅O₁₈.H₂O
 Mg₂SiO₄
 Mg₃.165Al₀.33Si₃.67O₁₀(OH)₂
 Mg₃Al₂Si₃O₁₂
 Mg₃Si₂O₅(OH)₄
 Mg₃Si₄O₁₀(OH)₂
 Mg₄[Si₆O₁₅(OH)₂(H₂O)₂].3H₂O
 Mg₄₈Si₃₅O₈₅(OH)₆₂
 Mg₄Al₄Si₂O₁₀(OH)₈
 Mg₅Al(AlSi₃O₁₀)(OH)₈
 Mg₅Al[AlSi₃O₁₀(OH)₂](OH)₆
 Mg₇Si₂O₈(OH)₂
 MgAl₂O₄
 MgFe₂O₄
 MgO
 MgSiO₃
 Na₀.33Al₂.33Si₃.67O₁₀(OH)₂
 Na₂Al₂Si₃O₁₀.2H₂O
 Na₂B₄O₇
 Na₂B₄O₇.10H₂O
 Na₂B₄O₇.4H₂O
 Na₂B₄O₇.5H₂O
 Na₂O
 Na₂.Al₂O₃.2.5H₂O
 Na₂Si₂O₅
 Na₂SiO₃
 Na₂SiO₃.5H₂O
 Na₂SiO₃.6H₂O
 Na₂SiO₃.8H₂O

 Na₂SiO₃.9H₂O
 Na₄SiO₄
 Na₆Si₂O₇
 NaAl₃Si₃O₁₀(OH)₂
 NaAlO₂

Mg7Si8O22(OH)2
MgAl2O4
MgFe2O4
MgSiO2(OH)2
MgSiO3
MgSiO3
Na0.33Al2.33Si3.67O10(OH)2
Na2Al2Si3O10.2H2O
Na2Al2Si5O14.5H2O
Na2B4O7
Na2B4O7.10H2O
Na2B4O7.4H2O
Na2B4O7.5H2O
Na2O.Al2O3
Na2O.Al2O3.2.5H2O
Na2Si2O5
Na2Si5O11
Na2SiO3
Na2SiO3.5H2O
Na2SiO3.6H2O
Na2SiO3.8H2O
Na2SiO3.9H2O
Na4SiO4
Na6Si2O7
NaAl3Si3O10(OH)2
NaAlO2
NaAlSi2O6
NaAlSi2O6
NaAlSi2O6.1H2O
NaAlSi3O8
NaAlSi3O8
NaAlSi3O8
NaAlSi3O8
NaAlSi3O8
NaAlSiO4
NaB(OH)4
NaB3O5
NaB5O8
NaB5O8.5H2O
NaBO2
NaBO2.0.5H2O
NaBO2.2H2O
NaBO2.4H2O

NaAlSi2O6
NaAlSi2O6
NaAlSi2O6.1H2O
NaAlSi3O8
NaAlSi3O8
NaAlSi3O8
NaAlSi3O8
NaAlSi3O8
NaAlSiO4
NaB3O5
NaB5O8.5H2O
NaBO2
NaBO2.0.5H2O
NaBO2.2H2O
NaBO2.4H2O
NaFeO2
NaFeSi2O6
NaOH
NaOH.1H2O
SiO2
SiO2
SiO2
SiO2
SiO2
Zn
Zn(OH)2
Zn(OH)2
Zn2SiO4
ZnO
ZnO.FE2O3
ZnSiO3

NaFeO2
 NaFeSi2O6
 NaH2BO3
 NaHSiO3
 NaOH.1H2O
 O2
 SiO2
 SiO2
 SiO2
 SiO2
 Zn(OH)2
 Zn(OH)2
 Zn2SiO4
 ZnO
 ZnO.FE2O3
 ZnSiO3

Stream Parameters

B-6

Stream Amt	55.718	mol
Temperature	60.000	°C
Pressure	1.0000	atm
pH	6.9771	pH
Ionic Strength	8.9402e-3	mol/kg H2O
ORP	-0.39942	V (SHE)
Osmotic Pressure	0.10217	atm
Electrical Cond, specific	1.3289e-3	1/ohm
Electrical Cond, molar	6.4930	cm2/ohm-mol
Viscosity, absolute	0.46731	cP
Viscosity, relative	1.0017	cP/cP H2O

	Total	Aqueous	Vapor	Solid	2nd Liquid
Density	--	g/ml	g/ml	g/ml	g/ml
	--	0.98827	0.0	2.4234	0.0
Enthalpy	Total	Aqueous	Vapor	Solid	2nd Liquid
	cal	cal	cal	cal	cal
	-3.8105e6	-3.8092e6	0.0	-1354.3	0.0

Total and Phase Flows (Amounts)

	Total	Aqueous	Vapor	Solid	2nd Liquid
Mole	mol 55.718	mol 55.713	mol 0.0	mol 4.8162e-3	mol 0.0
Mass	g 1013.0	g 1012.6	g 0.0	g 0.37692	g 0.0
Volume	L 1.0248	L 1.0246	L 0.0	L 1.5553e-4	L 0.0

Scaling Tendencies

solids within temperature range

Temperature Range

B-7

Species Output (True Species)

	Total	Aqueous	Vapor	Solid	2nd Liquid
H2O	mol 55.516	mol 55.516	mol 0.0	mol 0.0	n/a 0.0
Cu	1.2000e-6	0.0	0.0	1.2000e-6	0.0
B(OH)3	0.18521	0.18521	0.0	0.0	0.0
SiO2	3.2483e-4	3.2483e-4	0.0	0.0	0.0
Al(OH)3	7.7473e-15	7.7473e-15	0.0	0.0	0.0
CaSiO2(OH)2	9.1827e-11	9.1827e-11	0.0	0.0	0.0
Cu(OH)2	1.2978e-22	1.2978e-22	0.0	0.0	0.0
Fe(OH)2	1.3646e-10	1.3646e-10	0.0	0.0	0.0
Fe(OH)3	1.2148e-13	1.2148e-13	0.0	0.0	0.0
Fe3Si4O10(OH)2	7.2270e-6	0.0	0.0	7.2270e-6	0.0
H2	5.2100e-5	5.2100e-5	0.0	0.0	0.0
Mg3Si4O10(OH)2	1.9126e-6	0.0	0.0	1.9126e-6	0.0
MgSiO2(OH)2	5.6683e-10	5.6683e-10	0.0	0.0	0.0
NaAlSi3O8	4.1500e-4	0.0	0.0	4.1500e-4	0.0
NaB(OH)4	2.8294e-6	2.8294e-6	0.0	0.0	0.0
NaHSiO3	1.1638e-7	1.1638e-7	0.0	0.0	0.0

O2	4.2048e-74	4.2048e-74	0.0	0.0	0.0
SiO2	4.3905e-3	0.0	0.0	4.3905e-3	0.0
Zn(OH)2	7.2373e-9	7.2373e-9	0.0	0.0	0.0
Zn2SiO4	3.3908e-7	0.0	0.0	3.3908e-7	0.0
Al(OH)2+1	2.3194e-17	2.3194e-17	0.0	0.0	0.0
Al(OH)4-1	5.9853e-14	5.9853e-14	0.0	0.0	0.0
Al+3	1.8743e-22	1.8743e-22	0.0	0.0	0.0
AlOH+2	1.0088e-19	1.0088e-19	0.0	0.0	0.0
B(OH)4-1	2.0856e-3	2.0856e-3	0.0	0.0	0.0
B2O(OH)5-1	6.8893e-4	6.8893e-4	0.0	0.0	0.0
B3O3(OH)4-1	3.9794e-3	3.9794e-3	0.0	0.0	0.0
B4O5(OH)4-2	2.2016e-5	2.2016e-5	0.0	0.0	0.0
Ca+2	1.2870e-3	1.2870e-3	0.0	0.0	0.0
CaH2BO3+1	1.0301e-4	1.0301e-4	0.0	0.0	0.0
CaHSiO3+1	2.1910e-8	2.1910e-8	0.0	0.0	0.0
CaOH+1	2.6960e-8	2.6960e-8	0.0	0.0	0.0
Cu(OH)3-1	4.0581e-27	4.0581e-27	0.0	0.0	0.0
Cu(OH)4-2	5.4646e-32	5.4646e-32	0.0	0.0	0.0
Cu+1	1.6469e-14	1.6469e-14	0.0	0.0	0.0
Cu+2	1.2536e-23	1.2536e-23	0.0	0.0	0.0
CuOH+1	2.4129e-23	2.4129e-23	0.0	0.0	0.0
Fe(OH)2+1	2.4208e-16	2.4208e-16	0.0	0.0	0.0
Fe(OH)3-1	1.7902e-13	1.7902e-13	0.0	0.0	0.0
Fe(OH)4-1	3.4405e-15	3.4405e-15	0.0	0.0	0.0
Fe(OH)4-2	3.6573e-20	3.6573e-20	0.0	0.0	0.0
Fe+2	6.1804e-6	6.1804e-6	0.0	0.0	0.0
Fe+3	2.3319e-24	2.3319e-24	0.0	0.0	0.0
Fe2(OH)2+4	1.8849e-40	1.8849e-40	0.0	0.0	0.0
FeO4-2	1.0206e-63	1.0206e-63	0.0	0.0	0.0
FeOH+1	1.3855e-7	1.3855e-7	0.0	0.0	0.0
FeOH+2	4.3989e-19	4.3989e-19	0.0	0.0	0.0
H+1	1.1721e-7	1.1721e-7	0.0	0.0	0.0
H2SiO4-2	2.9909e-12	2.9909e-12	0.0	0.0	0.0
H3SiO4-1	2.6300e-6	2.6300e-6	0.0	0.0	0.0
Mg+2	8.2412e-4	8.2412e-4	0.0	0.0	0.0
MgHSiO3+1	2.1532e-8	2.1532e-8	0.0	0.0	0.0
MgOH+1	1.2808e-7	1.2808e-7	0.0	0.0	0.0
Na+1	2.4621e-3	2.4621e-3	0.0	0.0	0.0
OH-1	9.9003e-7	9.9003e-7	0.0	0.0	0.0
Zn(OH)3-1	7.9899e-12	7.9899e-12	0.0	0.0	0.0
Zn(OH)4-2	7.2306e-17	7.2306e-17	0.0	0.0	0.0
Zn+2	6.2688e-7	6.2688e-7	0.0	0.0	0.0
ZnOH+1	2.8772e-7	2.8772e-7	0.0	0.0	0.0

Molecular Output (Apparent Species)

	Total	Aqueous	Vapor	Solid	2nd Liquid
	mol	mol	mol	mol	n/a
H2O	55.534	55.534	0.0	0.0	0.0
Cu	1.2000e-6	0.0	0.0	1.2000e-6	0.0
B(OH)3	0.18291	0.18291	0.0	0.0	0.0
MgO	8.2426e-4	8.2426e-4	0.0	0.0	0.0
CaB4O7	1.3900e-3	1.3900e-3	0.0	0.0	0.0
Fe2O3	6.2583e-14	6.2583e-14	0.0	0.0	0.0
Fe3Si4O10(OH)2	7.2270e-6	0.0	0.0	7.2270e-6	0.0
FeO	6.3190e-6	6.3190e-6	0.0	0.0	0.0
H2	5.2100e-5	5.2100e-5	0.0	0.0	0.0
Mg3Si4O10(OH)2	1.9126e-6	0.0	0.0	1.9126e-6	0.0
NaAlSi3O8	4.1500e-4	0.0	0.0	4.1500e-4	0.0
NaB5O8	2.4650e-3	2.4650e-3	0.0	0.0	0.0
SiO2	4.3905e-3	0.0	0.0	4.3905e-3	0.0
SiO2	3.2762e-4	3.2762e-4	0.0	0.0	0.0
Zn2SiO4	3.3908e-7	0.0	0.0	3.3908e-7	0.0
ZnO	9.2183e-7	9.2183e-7	0.0	0.0	0.0

B-9

Element Balance

	Total	Aqueous	Vapor	Solid	2nd Liquid
	mol	mol	mol	mol	n/a
AL(+3)	0.0	6.7623e-14	0.0	4.1500e-4	0.0
AL(0)	0.0	0.0	0.0	0.0	0.0
B(+3)	0.0	0.20080	0.0	0.0	0.0
CA(+2)	0.0	1.3900e-3	0.0	0.0	0.0
CU(+1)	0.0	1.6469e-14	0.0	0.0	0.0
CU(+2)	0.0	1.6645e-22	0.0	0.0	0.0
CU(0)	1.2000e-6	0.0	0.0	1.2000e-6	0.0
FE(+2)	0.0	6.3191e-6	0.0	2.1681e-5	0.0
FE(+3)	0.0	1.2517e-13	0.0	0.0	0.0
FE(0)	0.0	0.0	0.0	0.0	0.0
Fe(+6)	0.0	1.0206e-63	0.0	0.0	0.0
H	0.0	1.0420e-4	0.0	0.0	0.0
H(+1)	0.0	111.62	0.0	1.8279e-5	0.0
MG(+2)	0.0	8.2427e-4	0.0	5.7377e-6	0.0
NA(+1)	0.0	2.4650e-3	0.0	4.1500e-4	0.0
O	0.0	8.4095e-74	0.0	0.0	0.0

O(-2)	0.0	56.113	0.0	0.012212	0.0
Si(+4)	0.0	3.2762e-4	0.0	5.6724e-3	0.0
ZN(+2)	0.0	9.2184e-7	0.0	6.7817e-7	0.0
Zn(0)	0.0	0.0	0.0	0.0	0.0

Species Activity Coefficients

H2O	0.0	Activity
Al(OH)2+1	0.0	Act-Coeff
Al(OH)3 - Aq	0.0	Act-Coeff
Al(OH)4-1	0.0	Act-Coeff
Al+3	0.0	Act-Coeff
AlOH+2	0.0	Act-Coeff
B(OH)3 - Aq	0.0	Act-Coeff
B(OH)4-1	0.0	Act-Coeff
B2O(OH)5-1	0.0	Act-Coeff
B3O3(OH)4-1	0.0	Act-Coeff
B4O5(OH)4-2	0.0	Act-Coeff
Ca+2	0.0	Act-Coeff
CaH2BO3+1	0.0	Act-Coeff
CaHSiO3+1	0.0	Act-Coeff
CaOH+1	0.0	Act-Coeff
CaSiO2(OH)2 - Aq	0.0	Act-Coeff
Cu(OH)2 - Aq	0.0	Act-Coeff
Cu(OH)3-1	0.0	Act-Coeff
Cu(OH)4-2	0.0	Act-Coeff
Cu+1	0.0	Act-Coeff
Cu+2	0.0	Act-Coeff
CuOH+1	0.0	Act-Coeff
Fe(OH)2 - Aq	0.0	Act-Coeff
Fe(OH)2+1	0.0	Act-Coeff
Fe(OH)3 - Aq	0.0	Act-Coeff
Fe(OH)3-1	0.0	Act-Coeff
Fe(OH)4-1	0.0	Act-Coeff
Fe(OH)4-2	0.0	Act-Coeff
Fe+2	0.0	Act-Coeff
Fe+3	0.0	Act-Coeff
Fe2(OH)2+4	0.0	Act-Coeff
FeO4-2	0.0	Act-Coeff
FeOH+1	0.0	Act-Coeff
FeOH+2	0.0	Act-Coeff
H+1	0.0	Act-Coeff

B-10

H2 - Aq	0.0	Act-Coef
H2SiO4-2	0.0	Act-Coef
H3SiO4-1	0.0	Act-Coef
Mg+2	0.0	Act-Coef
MgHSiO3+1	0.0	Act-Coef
MgOH+1	0.0	Act-Coef
MgSiO2(OH)2 - Aq	0.0	Act-Coef
Na+1	0.0	Act-Coef
NaB(OH)4 - Aq	0.0	Act-Coef
NaHSiO3 - Aq	0.0	Act-Coef
O2 - Aq	0.0	Act-Coef
OH-1	0.0	Act-Coef
SiO2 - Aq	0.0	Act-Coef
Zn(OH)2 - Aq	0.0	Act-Coef
Zn(OH)3-1	0.0	Act-Coef
Zn(OH)4-2	0.0	Act-Coef
Zn+2	0.0	Act-Coef
ZnOH+1	0.0	Act-Coef
H2O - Vap	0.0	Fug-Coef
H2 - Vap	0.0	Fug-Coef
O2 - Vap	0.0	Fug-Coef

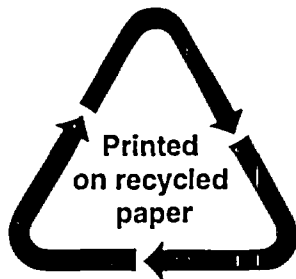
B-11

Species K(eq)-Values

Species Mobilities

Species Self Diffusivities

NRC FORM 335 (9-2004) NRCM 3.7	U.S. NUCLEAR REGULATORY COMMISSION	1. REPORT NUMBER (Assigned by NRC Add Vol. Supp. Rev. and Addendum Numbers If any.)
BIBLIOGRAPHIC DATA SHEET (See instructions on the reverse)		NUREG/CR-6873
2. TITLE AND SUBTITLE Corrosion Rate Measurements and Chemical Speciation of Corrosion Products Using Thermodynamic Modeling of Debris Components to Support GSI-191	3. DATE REPORT PUBLISHED	
	MONTH April	YEAR 2005
	4. FIN OR GRANT NUMBER N6061	
5. AUTHOR(S) B.P. Jain/U.S. Nuclear Regulatory Commission (NRC) V. Jain, X. He, and Y.-M. Pan/Center for Nuclear Waste Regulatory Analyses (CNWRA)	6. TYPE OF REPORT	
	7. PERIOD COVERED (Inclusive Dates) August 2004-April 2005	
8. PERFORMING ORGANIZATION - NAME AND ADDRESS (If NRC provide Division Office or Region U.S. Nuclear Regulatory Commission, and mailing address; if contractor, provide name and mailing address.) Center for Nuclear Waste Regulatory Analyses Southwest Research Institute® 6220 Culebra Road San Antonio, TX 78228-0510		
9. SPONSORING ORGANIZATION - NAME AND ADDRESS (If NRC type "Same as above"; if contractor provide NRC Division Office or Region U.S. Nuclear Regulatory Commission and mailing address) Division of Engineering Technology Office of Nuclear Regulatory Research U.S. Nuclear Regulatory Commission Washington, DC 20555-0001		
10. SUPPLEMENTARY NOTES B.P. Jain, NRC Project Manager		
11. ABSTRACT (200 words or less) <p>This report documents thermodynamic simulations conducted to determine whether post loss-of-coolant-accident (LOCA) debris generation and consequent sump screen head loss in a pressurized water reactor containment can be affected by chemical interactions between the emergency core cooling system/containment spray water and exposed materials. Based on the measured corrosion rates, estimated exposed surface area, and exposure time, the thermodynamics simulations indicated that the formation of dominant solid phases was controlled by the presence of Nukon® low-density fiber insulation, aluminum, and concrete. The predicted dominant solid phases consisted of potentially amorphous silicate phases such as sodium aluminum silicate (NaAlSi₃O₈), calcium magnesium silicate [Ca₂Mg₅Si₈O₂₂(OH)₂], calcium silicate (CaSiO₃), and silica (SiO₂). The results were based on the solid phases included in the thermodynamic simulation program database. The formation of actual solid phases may be different depending on the reaction kinetics. Although some constituents decreased proportionally with increasing time, the solid NaAlSi₃O₈ phase continued to be a dominant solid phase at all times. The formation of NaAlSi₃O₈ in the presence of alkaline solutions could lead to gel formation, which could result in clogging of containment area sump pump suction strainers. Thermodynamic simulations indicate that in alkaline simulated containment water at pH 10 there is no significant difference in corrosion product formation as high-temperature and pressure conditions during the initial stages of a LOCA event approach steady-state atmospheric pressure conditions. This report provides insight to and is useful in understanding the evolution of solution chemistry and the formation of solid phases in integrated chemical effects tests at the University of New Mexico.</p>		
12. KEY WORDS/DESCRIPTORS (List words or phrases that will assist researchers in locating the report.) corrosion thermodynamic modeling LOCA chemical speciation fiber insulation metals GSI-191	13. AVAILABILITY STATEMENT unlimited	
	14. SECURITY CLASSIFICATION (This Page) unclassified	
	(This Report) unclassified	
	15. NUMBER OF PAGES	
16. PRICE		



Federal Recycling Program

**UNITED STATES
NUCLEAR REGULATORY COMMISSION
WASHINGTON, DC 20555-0001**

OFFICIAL BUSINESS